Reservoir-induced control and learning in quantum and classical systems

Zakari Denis

▶ **To cite this version:**

Zakari Denis. Reservoir-induced control and learning in quantum and classical systems. Quantum Physics [quant-ph]. Université Paris Cité, 2021. English. NNT : 2021UNIP7152 . tel-03749730v2

HAL Id: tel-03749730
https://theses.hal.science/tel-03749730v2

Submitted on 17 Nov 2022

HAL is a multi-disciplinary open access archive for the deposit and dissemination of scientific research documents, whether they are published or not. The documents may come from teaching and research institutions in France or abroad, or from public or private research centers.

L'archive ouverte pluridisciplinaire **HAL**, est destinée au dépôt et à la diffusion de documents scientifiques de niveau recherche, publiés ou non, émanant des établissements d'enseignement et de recherche français ou étrangers, des laboratoires publics ou privés.
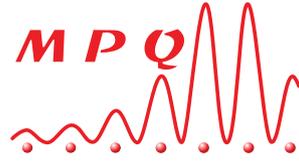
Université de Paris

École doctorale 564 : Physique en Île-de-France

Laboratoire Matériaux et Phénomènes Quantiques (UMR 7162)

Thèse de doctorat en physique

Reservoir-induced control and learning in quantum and classical systems

présentée par

Zakari Denis

sous la direction de

Cristiano Ciuti et Ivan Favero

Jury

PR	Cristiano Ciuti	Université de Paris	Directeur de thèse
DR	Ivan Favero	CNRS (MPQ)	Codirecteur de thèse
PR	Sylvain Gigan	Sorbonne Université	Président
DR	Julie Grollier	Unité Mixte de Physique CNRS/Thalès	Examinatrice
PR	Timothy C. H. Liew	Nanyang Technological University	Rapporteur
DR	Anna Minguzzi	CNRS (LPMMC)	Examinatrice
PR	Giovanna Morigi	Saarland University	Examinatrice
PR	Mauro Paternostro	Queen's University Belfast	Rapporteur

Présentée et soutenue publiquement à Paris le 28 septembre 2021

El plazer de la ciencia — es conplido plazer;
obra syn rependençia — ella del bien fazer.
   — Sᴇᴍ Tᴏʙ de Carrión, *Proverbios morales*

Acknowledgements

Résumé

Cette thèse est consacrée à l'étude de la dynamique induite par réservoir dans les systèmes quantiques ouverts ainsi qu'à l'apprentissage automatique au moyen de réservoirs photoniques classiques. Nous étudions la problématique générale de la dynamique d'ensembles bipartis comprenant un système dont des modes d'intérêt indépendants sont couplés à un réservoir dissipatif pompé doté d'une certaine extension spatiale. En particulier, nous abordons le cas des réservoirs étendus quantiques, cohérents et markoviens. Dans le cadre du formalisme de l'équation maîtresse de Lindblad, nous dérivons des expressions générales, indépendantes du modèle considéré, décrivant les processus cohérents et incohérents médiés par de tels réservoirs dissipatifs et pompés et fournissons une description effective de la dynamique réduite des modes du système. En nous servant d'unités optomécaniques comme de cellules fondamentales, nous étudions le contrôle du transport de particules médié par cavité dans des réseaux de résonateurs optomécaniques dont seules les cavités sont mutuellement couplées et où les modes optiques se comportent comme un réservoir non-local contrôlé. En particulier, nous montrons que le flux de phonons thermiques à travers de telles structures peut être contrôlé et dirigé par un réglage approprié de la phase du pompage du réservoir. Nous donnons également une description quantique détaillée des nano-résonateurs à disque en semi-conducteur, en modélisant le couplage fort entre les excitons d'un puits quantique intégré en leur sein et leur déformation mécanique. Nous présentons ensuite un nouvel algorithme pour la simulation numérique de l'évolution en temps continu de systèmes quantiques ouverts à entropie modérée qui surmonte la complexité de l'équation maîtresse de Lindblad par une représentation efficace de la matrice densité. Nous appliquons cette méthode à la modélisation d'algorithmes quantiques bruités. Enfin, nous présentons les machines à noyaux photoniques, des dispositifs optiques capables d'effectuer des tâches d'apprentissage automatique au moyen de réservoirs photoniques. Nous en décrivons analytiquement le mécanisme d'apprentissage par des concepts issus de la théorie des machines à noyaux, en en dévoilant les représentations internes. Nous appliquons ce procédé à l'analyse spectrale ultrarapide de signaux radiofréquence bruités par une mesure d'intensité optique des modes d'un réseau photonique, tant sur des tâches de régression que de classification.

Mots-clés : optomécanique, systèmes quantiques ouverts, optique quantique, ingénierie de réservoir, transport, équation maîtresse de Lindblad, méthodes numériques, simulation de systèmes ouverts, circuits quantiques, calcul optique, calcul par réservoir, apprentissage automatique, machines à noyau, traitement du signal.

Summary

This thesis is devoted to the study of reservoir-induced dynamics in open quantum systems and to machine learning with classical photonic reservoirs. We study the broad problem of the dynamics of bipartite ensembles consisting of a set of independent system modes of interest that are coupled to some spatially extended driven-dissipative reservoir. In particular, we address the case of Markovian coherent quantum extended reservoirs. Within the Lindblad master equation framework, we derive general model-independent expressions for the coherent and incoherent processes mediated by such controlled driven-dissipative reservoirs and provide an effective description of the reduced dynamics of the system modes. By considering optomechanical units as our pivotal building block, we investigate the control of cavity-mediated particle transport in lattices of cavity-coupled optomechanical resonators, where the optical modes behave as a controlled nonlocal reservoir. In particular, we show that the flow of thermal phonons across such structures can be controlled and directed by a proper tuning of the reservoir's driving phase. We also provide a detailed quantum description of semiconductor optomechanical nanodisc resonators, modelling the strong coupling between excitons of an embedded quantum well and their mechanical strain. We then present a novel algorithm for the numerical simulation of the continuous-time evolution of open quantum systems with moderate entropy that gets over the complexity of the Lindblad master equation by an efficient representation of the density matrix. We apply such a method to model noisy quantum algorithms. Finally, we introduce photonic kernel machines, learning devices capable of performing machine-learning tasks on fast photonic reservoirs. We analytically describe the learning mechanism with kernel-method concepts, unveiling the internal representations such a photonic hardware relies upon. We apply this scheme to the ultrafast spectral analysis of noisy radio-frequency signals from single-shot optical intensity measurements of photonic lattices, on both regression and classification tasks.

Keywords: optomechanics, open quantum systems, quantum optics, reservoir engineering, particle transport, Lindblad master equation, numerical methods, simulation of open systems, quantum circuits, optical computing, reservoir computing, machine learning, kernel methods, signal processing.

Publications

The works of scientific and technical nature produced in the course of this thesis are listed below and will be referred to with Greek characters in the main text. The present manuscript is structured mostly around the results reported in $[\alpha]$, $[\gamma]$, $[\delta]$ and two papers currently in preparation $[\epsilon]$ and $[\zeta]$.

$[\alpha]$ Z. Denis, A. Biella, I. Favero and C. Ciuti,
"Permanent Directional Heat Currents in Lattices of Optomechanical Resonators",
Physical Review Letters **124**, 083601 (2020).

$[\beta]$ S. Pautrel, Z. Denis, J. Bon, A. Borne and I. Favero,
"Optomechanical discrete-variable quantum teleportation scheme",
Physical Review A **101**, 063820 (2020).

$[\gamma]$ K. Donatella*, Z. Denis*, A. Le Boité and C. Ciuti,
"Continuous-time dynamics and error scaling of noisy high-entangling quantum circuits",
arXiv: 2102.04265 (2021).

$[\delta]$ Z. Denis, I. Favero and C. Ciuti,
Dispositif d'analyse de spectre de signaux radiofréquences,
EU Patent application EP21173660, 2021.

$[\gamma]$ Z. Denis, I. Favero and C. Ciuti,
"Photonic kernel machine learning for ultrafast spectral analysis",
arXiv: 2110.15241 (2021).

$[\zeta]$ N. Carlon Zambon*, Z. Denis*, S. Ravets, I. Favero, C. Ciuti and J. Bloch,
"Light, matter and sound in semiconductor microresonators",
in preparation (2021).

---

* Both authors equally contributed to this work.

Contents

General introduction

Effective description

Physics was still in its infancy when the intractable many-body problem, readily identified by Newton at the very end of his *Principia* [1], frustrated the reductionist approach to the practical understanding of nature. Ever since, the confirmation of the many-body discrete nature of the constituent elements of matter, both in diluted media, as shown by Perrin [2] in his experimental confirmation of Einstein's hypothesis on the atomic origin of Brownian motion [3], and condensed matter, as elucidated in the Geiger-Marsden [4] and von Laue's [5] experiments, made it clear that the many-body problem was not restricted to astrophysics but ubiquitous instead, casting doubt on the possibility of giving an exhaustive description of the world around us. Rather fortunately, universe is highly structured and presents strong hierarchies between well-delimited energy scales that adiabatically uncouple. At low energy scales, self-organisation mechanisms, such as synchronisation or phase transitions, shape interacting particles into simpler ordered phases of higher symmetry whose phenomenology significantly differs from that of their constituents, as was very clearly expressed by Anderson in his famous *More is different* [6]. This is for instance the case of atoms organised into crystalline structures, that acquire novel mechanical, optical and electric properties absent from their building blocks. Associated to these emergent symmetries are novel collective excitations that can be accounted for by introducing quantised fields with proper quantum statistics just as for elementary particles. This effective description greatly simplifies the problem. In the aforementioned case of a solid, for instance, the complex description of the motional degrees of freedom of the macroscopic amount of interacting ions that compose its bulk can be replaced by continuous displacement fields that effectively account for mechanical vibrations at wavelengths much larger than the lattice parameter. Under some coherence conditions, elementary excitations of these effective fields exhibit their quantised nature; in this example, such quanta, known as *phonons*, display very simple bosonic statistics.

Nowadays, tremendous advances in the fabrication of micro- and nanodevices make it possible to shape matter into structures that behave as elementary particles with desired quantum statistics. Such *macroscopic quantum systems* [7] can be realised with a great degree of control and isolation from the environment. Micro- and nanomechanical resonators that effectively behave as resolved bosonic modes—phonons—can be fabricated with angular frequencies ranging from $10\,\text{kHz}$ to $10\,\text{GHz}$ in a broad variety of geometries [8]. In circuit quantum electrodynamics, where quantum coherence extends over macroscopic superconducting electric circuits, artificial atoms can be engineered to simulate quantum optics and atomic physics [9–12]. These artificial quantum systems can be assembled into

quantum circuits and used as building blocks of quantum computers and simulators. In semiconductor heterostructures, the confinement of electron-hole pairs leads to effective bosonic and spin-1/2 statistics in quantum wells and quantum dots, respectively. While in vacuum photon-photon interactions would only be observed for gamma radiation at energies of the order of the megaelectronvolt, in these materials such pairs mediate strong optical self-interactions in the near infrared, that is at energies of the order of the ectronvolt. This makes it a formidable playground for the practical study of quantum fluids of light dressed by matter collective excitations [13].

However, because such excitations are supported by macroscopic objects, these often cannot be described as completely isolated from their environment. Fortunately, this can be yet again faithfully accounted for through a further level of effective description, by modelling the environment as a *reservoir* composed of (infinitely) many degrees of freedom that are allowed to exchange energy with the system. While this generally induces thermalisation effects that have detrimental consequences on its coherence, it may be used to one's advantage. Indeed, by a clever design of the reservoir, a process known as *reservoir engineering*, the dynamics of the system under consideration can be controlled and peculiar quantum states of interest can be stabilised [14–21]. In this context, the environment is seen as a resource rather than as an inconvenience.

These ideas will be mobilised throughout the first part of this thesis. A resonator consisting of a disk-shaped micrometric piece of semiconductor will be first addressed. In such a system, the great degree of spatial confinement leads to the emergence of well-resolved optical and mechanical modes, that interact through radiation pressure. These will be shown to be describable as parametrically coupled photon and phonon quanta in weak interaction with their own thermal baths. The study of this standard optomechanical setting will be complemented by the addition of a quantum well embedded in the disk [ζ]. Therein, the dressing of the photons by electron-hole pairs will be shown to yield a significant increase of the bare optomechanical coupling, a feature of great interest in a wide variety of quantum applications ranging from sensing [22–25] to quantum teleportation [β, 26, 27].

In the above optomechanical resonators, the optics and the mechanics have very different time scales, the former being much faster. This makes it possible to interpret the optical mode as an externally tunable reservoir. By driving the optical mode close to certain mechanical resonances, the motion of the mechanical degree of freedom can be controlled to a great extent. This effective description will be lifted to a many-disk scenario where resonators are arranged into lattices whose neighbouring sites are cavity-coupled. In this geometry, the coupled optical modes may be regarded as a spatially extended reservoir that mediates coherent and incoherent interactions between distant mechanical modes. By giving a general description of the effective dynamics induced by such driven-dissipative *extended reservoirs*, we will identify particular conditions upon which a permanent heat flow running through the structure may be stabilised and controlled in the absence of thermal bias [α].

Efficient representation

In some situations, however, over-simplistic effective descriptions may fail in grasping the physics of systems interacting with their environment. In such cases, one is generally left with the problem of numerically simulating a many-body *open quantum system*. Due to the exponential scaling of the Hilbert-space dimension with the number of units composing the system, simulating quantum many-body problems on a classical computer is, in general, a formidable task. The size of the density matrix that encodes the state of open quantum systems poses severe bounds on the system sizes that can be handled in practice by a naive brute-force approach.

Several ideas have been put forward to overcome these limitations by introducing efficient representations of this state. Among the most fruitful approaches, variational methods [28] have recently furthered the investigation of large open quantum systems by encoding their density matrices with parametrised variational ansätze. This was achieved with a wide variety of ansätze, such as matrix-product states [29], tensor networks for Markovian [30–35] and non-Markovian [36] environments, and, more recently, neural-network architectures such as restricted Boltzmann machines [37–41] or autoregressive models [41]. However, such representations usually rely on implicit assumptions about the quantum correlations and/or the geometry of the system.

In many relevant situations, the state of the system under consideration is close to pure, either because of the weakness of the coupling to the environment or because the state is stabilised by reservoir engineering. Then, the density matrix has a very low entropy. Much in the same way as low-entropy digital data can be efficiently compressed by choosing a suitable encoding [42, 43], the density matrix can be faithfully represented by a truncated set of carefully chosen base state vectors. This controlled lightweight representation of the density matrix is at the core of the so-called *corner-space renormalisation method* [44], that has been successfully applied to the steady-state determination of open quantum systems with unprecedented sizes [44–48].

In the second part of this thesis, the *dynamical corner-space method* [γ], that extends this approach to the continuous-time simulation of low-entropy open quantum systems will be introduced. Thanks to this novel method, the spurious effects of noise on the performance of highly entangling quantum circuits will be investigated within a realistic description of their coupling to the environment, a situation relevant in today's so-called noisy intermediate-scale quantum era [49].

Feature-space representation

Another domain where high dimensionality can be an obstacle is that of data analysis. In this context, being able to extract relevant refined information from raw data at high throughput can be compromised by their dimensionality. A clear example of this is the processing of ultrashort analogue pulsed signals containing some information of interest. This involves two costly operations. Firstly, the signal has to be converted from analogue to digital. This step involves the sampling of the input signal by some apparatus with an adapted bandwidth and the storage of the raw digital data. Secondly, the digital data have to be read from memory and treated by some processing unit to extract the features of interest. Both operations can easily become a bottleneck. The state-of-the-art sampling

rate, for instance, fundamentally limits the rate at which input signals can be supplied to the processing chain as well as the band over which the analysis can be carried out. Depending on the time resolution, the finite rate at which the memory can be accessed for writing and reading also might limit the rate at which information can enter the pipeline. Finally, the time involved in the actual digital processing operation can also entail a limit on the final throughput.

A way around this may be found in *reservoir computing*. This machine-learning paradigm is based upon a shallow architecture that well lifts to actual physical hardware [50]. This scheme harnesses computing power from the (fast) nonlinear dynamics of a physical system, viewed as a reservoir. The measure of the non-trivial response of such reservoirs to the input signals of interest realises an embedding of the input data to a so-called *feature space*. The device is then able to learn from example to identify the structure of the input data in this abstract space. Once trained, it is capable of extracting the sought high-level information contained in the raw data from simple measurements. Since it can be implemented on actual analogue hardware, it does not suffer from the analog-to-digital encoding bottleneck. As a matter of fact, quantum reservoirs should be capable of interfacing intrinsically analogue quantum inputs, as has been recently proposed [51–56].

A closely related scheme will be explored in the third part of this thesis, by introducing photonic kernel machines [δ, γ]. These are learning devices capable of performing signal analysis tasks on fast photonic reservoirs. Their feature space will be shown to be directly accessible from empirical data, unveiling the internal representations such a photonic hardware relies upon. This scheme will be numerically proven efficient in performing ultrafast spectral analysis of noisy radio-frequency signals from single-shot optical intensity measurements of photonic lattices, on both regression and classification tasks.

Structure of the manuscript

The thorough derivation of the quantum description of nanodisk optomechanical resonators will be addressed in Chapter 1. In this chapter, the modelling of the unitary dynamics of a standard resonator as well as that induced by the coupling to its environment will be discussed from first principles in Sec. I. Then, a hybrid disk resonator embedding a quantum well will be introduced in Sec. II. Following our work [ζ], some of the results of ongoing research on this hybrid structure to be soon submitted for publication will be briefly presented therein. The various interactions between the optical, electronic and acoustic modes present in this tripartite system will be discussed. Finally, the description of this hybrid resonator will be brought to that of a polariton-mechanical resonator with an enhanced radiation-pressure-like coupling.

In Chapter 2, the nonequilibrium dynamics induced by spatially extended reservoirs will be discussed. The case of a generic bosonic reservoir under single-body external driving and dissipation will be considered, both in discrete and continuous geometries. General analytical expressions for the Liouvillian ruling the reduced dynamics of a system in contact with such extended reservoirs will be derived in Sec. I within the Born-Markov approximation. In Sec. II, this effective Liouvillian description will be completed by an equivalent quantum Langevin-equation approach.

Chapter 3 will elaborate on the results of our work [α] on reservoir-induced permanent heat currents in lattices of cavity-coupled optomechanical resonators. This system will be studied within the framework introduced in Chapter 2. Under particular driving conditions, the optical extended reservoir will be shown to be capable of stabilising states exhibiting ever circulating cavity-mediated heat currents running through the optomechanical structure.

In Chapter 4, several numerical methods for simulating open quantum systems with varying degrees of "quantumness" will be reviewed. Some of them will be adapted to the treatment of systems interacting with extended reservoirs.

Chapter 5 will be devoted to the dynamical corner-space method for efficiently simulating low-entropy open quantum systems. Its algorithm will first be presented in Sec. II; its complexity will be compared to that of the state of the art. Following our work [γ], we will apply this method to the continuous-time simulation of noisy entangling quantum circuits and study the detrimental consequences of the environment on the fidelity of such processors within realistic models of noise.

Photonic kernel machines will be discussed in Chapter 6. After presenting some general theoretical concepts on kernel methods in Sec. II, physical kernel machines will be introduced in Sec. III. The similarity measure and the feature-space representations at the core of their learning mechanism will be first analytically discussed. Then, following our work [δ, γ], some applications to the ultrafast analysis of radiofrequency signals will be presented in Sec. IV by numerically simulating a possible implementation based on photonic lattices.

Finally, the results obtained in the course of this thesis will be summarised in the general conclusion, together with possible perspectives.

1 Single-cavity quantum optomechanics

This chapter is devoted to the study of single-cavity quantum optomechanics [8, 57] in semiconductor nanodisk resonators [58]. These are micrometric disk-shaped structures engineered from a semiconducting material acting as both high-finesse cavities for photons at telecom wavelength and mechanical resonators with high quality factors at gigahertz frequencies. Thanks to the strong spatial confinement, the colocalised optical and acoustic modes of the structure become significantly coupled by a radiation-pressure-like interaction, giving rise to a very rich dynamics. This parametric interaction between the optical intensity held within the disk and its mechanical motion is at the core of many applications ranging from sensing [22–25] and laser cooling of a mechanical resonator to its ground state [59–63] to optics-to-mechanics quantum-state teleportation [β, 26, 27] and mechanically mediated superconducting qubit-to-photon transduction [64], including mechanically assisted squeezed-light generation [65, 66], quantum mechanical-state preparation [67–69], entanglement generation [70–73] or light-mediated quantum communication between remote mechanical resonators [74]. This parametric coupling can be combined with additional degrees of freedom, opening even further perspectives [75–86].

We will give a thorough quantum description of the optical and mechanical modes supported by such devices, bringing out the quantised nature of their elementary optical and acoustic excitations. Photons will emerge as electromagnetic-field quanta from the quantisation of the classical electromagnetic energy stored in the disk. Phonons will arise as mechanical-motion quanta from the quantisation of the elastic energy of the disk's material. The wave functions associated to these particles as well as the Hamiltonian operators that describe their unitary dynamics will then be identified. By describing the environment as an uncorrelated reservoir and considering a harmonic external driving of the optical mode, the fundamental phenomenology exhibited by the mechanical degree of freedom will be reviewed.

Moreover, we will explore the possibility of enhancing the single-photon optomechanical coupling factor by exploiting the strong coupling between the mechanical strain field and the excitons of a quantum well embedded in the nanodisk resonator. We will present a theoretical model describing this tripartite system where light, matter and sound are all mutually coupled. The Hamiltonian of this hybrid resonator will be shown to be analogous to that of the canonical optomechanical system with exciton polaritons playing the role formerly held by photons and an improved optomechanical coupling.

This chapter is organised as follows. In Sec. I, the resonator's optical whispering-gallery modes and mechanical radial breathing modes will be described. Their quantum

Hamiltonian operators will be derived from first principles in Subsecs. I.1 and I.2, respectively. The action of the environment will be given an effective description within the Lindblad master equation approach in Subsec. I.3. In Subsec. I.4, the optomechanical interaction will be introduced; some of the resulting standard phenomenology will be discussed in Subsec. I.5. The sideband cooling and heating mechanisms addressed therein will serve to introduce the concepts of *sideband* and *(anti-)Stokes scattering*, that will emerge as crucial in the next chapters. In Sec. II, a hybrid optomechanical resonator embedding a quantum well will be theoretically described. A theory of the coupling between the quantum-well excitons and the resonator resolved phonons will be presented in Subsec. II.2. This will finally lead to a simpler description of the disk as a polariton-mechanical resonator with an enhanced coupling strength in Subsec. II.3. Finally, Sec. III will summarise the main results, concluding the chapter.

I Quantum description of an optomechanical resonator

Let us consider a piece of a semiconducting material of typical dimension L characterised by some energy gap E_{gap}. Because of the great difference in refractive index at either sides of its boundary, the material may confine a certain set of modes of the electromagnetic field within the bulk. Since no linear absorption is to be expected from the material for photons of energy lower than that of the gap, such a piece of material can be regarded as a transparent cavity for electromagnetic modes at wavelengths ranging from hc/E_{gap} to roughly L. Due to the elasticity of the material it is made of, such an object bears elastic vibrational modes as well. The latter are several orders of magnitude lower in energy than the former and thus likely to be thermally populated under coupling to a thermal bath.

By shrinking the typical dimension L to the order of the micron, the cavity's optical spectrum becomes well-resolved and only a finite discrete set of optical modes in the telecom band remains isolated from the exterior. This goes hand in hand with a similar effect for the object's vibrational spectrum, which goes from the continuous spectrum of the bulk and its characteristic linear dispersion relation to a set of well-resolved mechanical modes. Upon cooling down such a hybrid high-quality-factor resonating structure towards its ground state, quantum effects enter into play, exhibiting the resonator's quantised nature.

By considering the pivotal example of a nanodisk resonator, we here give a derivation of the quantum Hamiltonian describing the unitary dynamics of a resonator's optical and mechanical modes by combining Dirac's canonical quantisation prescription [87, 88] and first-principle electromagnetism and elasticity theory. We extend this to the case of a nanoring optomechanical resonators in Appendix A. We complete this description by treating the interaction between these modes and their environment, thereby introducing the Lindblad master equation, that combines both the unitary dynamics of the system and the irreversible evolution induced by the environment onto the system into a unified formalism.

This will later prove of crucial importance in Section II, when discussing the microscopical theory of polariton optomechanics.
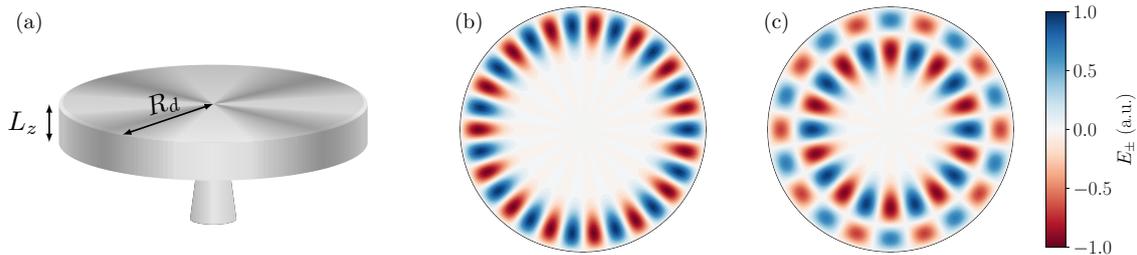
Figure 1.1: (a) Semiconducting optomechanical nanodisk resonator on its pedestal. In-plane view of its optical whispering-gallery modes, as given by Eq. (1.6), for (b) $p = 1$, $\ell = 15$, and (c) $p = 2$, $\ell = 10$.

I.1 Photons: quantisation of the electromagnetic field

Many concave resonators exhibit normal modes travelling at their inner periphery, bearing the name of whispering-gallery modes (WGM) and first described by Lord Rayleigh [89–91] more than a century ago. We will here describe the WGMs of a semiconducting disk of radius R_d and thickness L_z, as represented in Fig. 1.1 (a).

The electromagnetic energy density within the disk is given by

$$\mathcal{U}_c = \frac{1}{2}\Big(\epsilon\|\boldsymbol{E}\|^2 + \frac{1}{\mu}\|\boldsymbol{B}\|^2\Big), \tag{1.1}$$

where ϵ and μ denote the permittivity and the permeability of the medium, and where the electric field $\boldsymbol{E} = -\partial_t \boldsymbol{A}$ and the magnetic field $\boldsymbol{B} = \nabla \times \boldsymbol{A}$ can be expressed in terms of the vector potential $\boldsymbol{A}$. One may distinguish two possible polarisations of the WGM under consideration: transverse-electric (TE) polarisation, corresponding to an in-plane polarisation of the electric field; and transverse-magnetic (TM) polarisation, corresponding to an electric field polarised along the direction orthogonal to the plane. For reasons that will become clear in Sec. II, we will consider the former. For this choice of polarisation, one has $A_z = 0$ and thus $\boldsymbol{A} = A_r \boldsymbol{e}_r + A_\theta \boldsymbol{e}_\theta \equiv \sum_{\sigma=\pm} A_\sigma \boldsymbol{e}_\sigma$, with circularly polarised components $A_\pm$ and the associated rotating unit vectors $\boldsymbol{e}_\pm = e^{\pm i\theta}(\boldsymbol{e}_r \pm i\boldsymbol{e}_\theta)/\sqrt{2}$. It follows that

$$\|\boldsymbol{E}\|^2 = \sum_\sigma \dot{A}_\sigma^2, \quad \|\boldsymbol{B}\|^2 = \sum_\sigma \Big\{(\partial_z A_\sigma)^2 + \frac{1}{r^2}(\partial_\theta A_\sigma)^2 + (\partial_r A_\sigma)^2\Big\}. \tag{1.2}$$

This implies that the electric and magnetic contributions here play a role analogous to the kinetic and potential energies, respectively:

$$\mathcal{T}_c = \frac{1}{2}\epsilon\|\boldsymbol{E}\|^2, \qquad \mathcal{V}_c = \frac{1}{2}\epsilon c^2\|\boldsymbol{B}\|^2, \tag{1.3}$$

where $c = c_0/n$ is the speed of light in the material, with n its refractive index. For a given circular polarisation σ and upon integrating the Lagrangian density $\mathcal{L}_c = \mathcal{T}_c - \mathcal{V}_c$ over the

domain of the disk, that will be henceforth denoted by Ω, the classical Lagrangian reads[1]

$$L_c = \int_\Omega \mathrm{d}\boldsymbol{r}\left\{\frac{1}{2}\epsilon\dot{A}_\sigma^2 + \frac{1}{2}\epsilon c^2 A_\sigma\left(\partial_z^2 + \frac{1}{r^2}\partial_\theta^2 + \frac{1}{r}\partial_r[r]\partial_r\right)A_\sigma\right\}. \tag{1.4}$$

Our goal is here to perform the canonical quantisation of its associated classical Hamiltonian. To do so, one first needs to bring this Lagrangian to a diagonal form. This can be done by expanding the in-plane components of the vector potential on the eigenbasis of the differential operator in the second member of the right-hand side. Equivalently, one may instead seek for the solutions of the Helmholtz equation, obtained via the Euler-Lagrange equations. The latter here reads:

$$\ddot{A}_\sigma = -c^2\left(\partial_z^2 + \frac{1}{r^2}\partial_\theta^2 + \frac{1}{r}\partial_r[r]\partial_r\right)A_\sigma. \tag{1.5}$$

By separation of variables, this can be split into harmonic equations for the out-of-plane and azimuthal dependences and a Bessel equation for the radial one, yielding the following set of base wave functions

$$\phi_{p,\ell}^{(c)}(r,\theta,z) = N_{p,\ell}f_q(k_qz)J_\ell(k_{p,\ell}r)\cos(\ell\theta), \qquad \ddot{\phi}_{p,\ell} = -c^2 k_{p,\ell}^2\phi_{p,\ell}^{(c)}, \tag{1.6}$$

where the wavevector $k_{p,\ell} = \alpha_{\ell,p}/R_d$ is a function of the disk radius and the pth root of the ℓth Bessel function of the first kind $\alpha_{\ell,p}$. Rather unsurprisingly, we recover exactly Rayleigh's solution [90]. These are the so-called whispering-gallery modes. Their normalisation is given by

$$N_{p,\ell} = \frac{\sqrt{2/V}}{|J_{\ell+1}(k_{p,\ell}R_d)|}\left(\int\frac{\mathrm{d}z}{L_z}|f_q(k_qz)|^2\right)^{-1/2}. \tag{1.7}$$

It follows from the above that WGMs are characterised by a radial index p and an azimuthal index ℓ, being $p-1$ their number of internal nodes along the radial direction and ℓ their number of azimuthal maxima. The profile of the mode along the out-of-plane direction will be disregarded in the following, as it has no incidence on the optical spectrum of the WGMs. A few examples of the electric-field amplitudes associated to such modes are shown in Fig. 1.1 for different orders. As illustrated therein, the relevant azimuthal orders are usually much higher than $\ell = 1$. This confines most of the electromagnetic energy at the periphery of the disks.

The field can thus be expanded in the WGM basis as follows:

$$A_\sigma(r,\theta,z) = \sum_{\substack{p=1\\\ell=0}}^{+\infty} A_{p,\ell}\phi_{p,\ell}^{(c)}(r,\theta,z). \tag{1.8}$$

By making use of the orthonormality relation $\int_\Omega \mathrm{d}\boldsymbol{r}\,\phi_{p\ell}^{(c)\star}(\boldsymbol{r})\phi_{p'\ell'}^{(c)}(\boldsymbol{r}) = \delta_{p,p'}\delta_{\ell,\ell'}$, the Lagrangian can be brought into a suitable diagonal form

$$L_c = \sum_{p,\ell}\left(\frac{1}{2}\dot{u}_{p\ell}^2 - \frac{1}{2}c^2 k_{p,\ell}^2 u_{p\ell}^2\right), \tag{1.9}$$

---

[1]Here the boundary conditions, $A_\sigma\partial_r A_\sigma|_{\partial\Omega} = 0$, $A_\sigma\partial_\theta A_\sigma|_{\partial\Omega} = 0$ and $A_\sigma\partial_z A_\sigma|_{\partial\Omega} = 0$, where $\partial\Omega$ denotes the boundary of the domain Ω, were used to write the potential energy under the form of a differential operator.

where $u_{p,\ell} = \sqrt{\epsilon} A_{p,\ell}$. By identifying the conjugated momentum $\pi_{p,\ell} = \partial_{\dot{u}_{p,\ell}} L_c = \dot{u}_{p,\ell}$ and Legendre-transforming the above Lagrangian, one gets the Hamiltonian of a harmonic oscillator

$$H_c = \sum_{p,\ell} \dot{u}_{p,\ell} \pi_{p,\ell} - L_c = \sum_{p,\ell} \left(\frac{1}{2} \pi_{p,\ell}^2 + \frac{1}{2} \omega_{p,\ell} u_{p,\ell}^2 \right), \tag{1.10}$$

where $\omega_{p,\ell} = c k_{p,\ell}$ is the angular frequency associated to the WGM of orders (p, ℓ). As $k_{p,\ell} = \alpha_{\ell,p}/R_d$, the frequency of a WGM is inversely proportional to the radius of the disk.

One can now apply the canonical quantisation prescription $(u_{p,\ell}, \pi_{p,\ell}) \mapsto (\hat{u}_{p,\ell}, \hat{\pi}_{p,\ell})$, with operators $\hat{u}_{p,\ell}$ and $\hat{\pi}_{p,\ell}$ satisfying the canonical commutation relation $[\hat{u}_{p,\ell}, \hat{\pi}_{p',\ell'}] = i\hbar \delta_{p,p'} \delta_{\ell,\ell'}$, yielding

$$\hat{H}_c = \sum_{p,\ell} \left(\frac{1}{2} \hat{\pi}_{p,\ell}^2 + \frac{1}{2} \omega_{p,\ell} \hat{u}_{p,\ell}^2 \right). \tag{1.11}$$

By introducing the usual photon annihilation operators

$$\hat{a}_{p,\ell} = \sqrt{\frac{\omega_{p,\ell}}{2\hbar}} \hat{u}_{p,\ell} + i \sqrt{\frac{1}{2\hbar \omega_{p,\ell}}} \hat{\pi}_{p,\ell}, \tag{1.12}$$

such that $\hat{a}_{p,\ell}$ and its adjoint $\hat{a}_{p,\ell}^\dagger$ respectively subtract or add one excitation quantum in the WGM of indices (p, ℓ) and satisfy bosonic canonical commutation relations $[\hat{a}_{p,\ell}, \hat{a}_{p',\ell'}^\dagger] = \delta_{p,p'} \delta_{\ell,\ell'}$, one finally obtains the standard bosonic Hamiltonian for the harmonic oscillator:

$$\hat{H}_c = \sum_{p,\ell} \hbar \omega_{p,\ell} (\hat{a}_{p,\ell}^\dagger \hat{a}_{p,\ell} + 1/2). \tag{1.13}$$

This completely describes the unitary dynamics of the WGM's elementary excitations: the photons.

Let us clarify a few simplifying assumptions that were implicitly made in the above derivation. Total internal reflection of the electromagnetic field was assumed at the interface of the disk (i.e. strict Dirichlet boundary conditions). Due to the high level of confinement of the electromagnetic field ($R_d \gtrsim \lambda$), this is not exactly the case and, as already noted by Rayleigh [91], part of the field leaks out of the disk's volume. This can be accounted for analytically by solving for the Helmholtz equation at either sides of the boundary and introducing proper field-matching boundary conditions between the solution in the inner domain, as given by Eq. (1.6), and the outwards-propagating *disturbance* field D_ℓ (*ibid.*), beyond. Further details on this approach may be found, for instance, in [92]. Another similar issue relates to the confinement along the out-of-plane direction. For disks too thin, the electromagnetic field may vertically radiate outwards of the disk's domain, impacting the final quality factor. While both of these effects may be integrated into the analytical description, they will be instead effectively treated as a geometric contribution to the loss rate of the cavity in Sec. II.2.

I.2 Phonons: quantisation of the vibrational motion of an elastic solid

Let us now consider the semiconducting disk described above from the mechanical point of view. We will assume the disk to be made out of a homogeneous and isotropic material,

as characterised by the associated pair of Lamé parameters (λ, μ) and its volumetric mass ρ. In order to determine the mechanical eigenmodes of the disk, we shall identify its classical Lagrangian.

An initial perturbation of the disk's radial or vertical deformation profiles induces internal stresses that tend to restore it to its initial equilibrium situation. Inside a continuous elastic material, these conservative forces derive from the following Hooke's potential density [93, Chapter 2]:

$$\mathcal{U}_m = \frac{1}{2}\sigma^{ik}u_{ik} = \frac{1}{2}\lambda u^{ii}u_{ii} + \mu u^{ik}u_{ik}, \tag{1.14}$$

where σ_{ik} is the stress tensor, u_{ik} the strain tensor and summation over repeated indices is implicit. We will consider that, in cylindrical coordinates (r, θ, z), the deformation profile is given by a displacement of the form $\boldsymbol{u}(r, z) = u_r(r)\boldsymbol{e}_r + u_z(r, z)\boldsymbol{e}_z$. While it might seem that within the assumption $\partial_z u_r = 0$ the two acoustic polarisations, radial and vertical, uncouple and can be treated independently, any in-plane stress within the disk results in a sizeable strain u_{zz} along the out-of-plane axis because of the finite Poisson ratio $\nu \equiv \frac{\lambda}{2(\lambda+\mu)}$ of the material. This difficulty can be circumvented by assuming the disk to be in the *plane-stress* condition, routinely used for addressing thin plates. Under this assumption, the state of the disk is such that $\sigma_{zz} = 0$, that is, the vertical strain adapts to the presence of internal in-plane stresses at any point within the volume. By implementing this constraint on Eq. (1.14), one is left with an identical expression for a now two-dimensional disk with a modified first Lamé parameter:

$$\mathcal{U}_m = \frac{1}{2}\tilde{\lambda}u^{ii}u_{ii} + \mu u^{ik}u_{ik} \text{ (2D)}, \quad \tilde{\lambda} = \frac{2\mu}{\lambda + 2\mu}\lambda. \tag{1.15}$$

One accordingly has:

$$\mathcal{U}_m = \frac{\tilde{\lambda} + 2\mu}{2}\Big((\partial_r u_r)^2 + (u_r/r)^2\Big). \tag{1.16}$$

The disk is thus described by a single degree of freedom u_r. By further introducing its associated density of kinetic energy $\mathcal{T}_m = \frac{1}{2}\rho\dot{u}_r^2$, the Lagrangian density is given by $\mathcal{L}_m = \mathcal{T}_m - \mathcal{U}_m$.

Radial breathing modes

Let us treat the identified free radially polarised component. Its associated modes, of great experimental relevance, are known under the name of radial breathing modes (RBMs). Their associated Lagrangian directly follows from Eq. (1.16) and reads

$$L_m = \int_\Omega \mathrm{d}\boldsymbol{r}\Big\{\frac{1}{2}\rho\dot{u}_r^2 - \frac{1}{2}\rho c_s^2\Big((\partial_r u_r)^2 + (u_r/r)^2\Big)\Big\}, \tag{1.17}$$

where

$$c_s = \sqrt{\frac{E}{\rho(1 - \nu)^2}} \tag{1.18}$$

is the propagation speed of longitudinal acoustic waves in the material, expressed in terms of Young's modulus E and Poisson's ratio ν. Up to a constant, integration by parts yields

$$L_m = \int_\Omega \mathrm{d}\boldsymbol{r} \left\{ \frac{1}{2}\rho \dot{u}_r^2 - \frac{1}{2}\rho c_s^2 u_r \left(\frac{1}{r^2} - \frac{1}{r}\partial_r[r]\partial_r \right) u_r \right\}. \tag{1.19}$$

This Lagrangian can be diagonalised by introducing the following Fourier-Bessel expansion of the radial displacement field $u_r(r)$:

$$u_r(r) = \sum_{n=1}^{+\infty} u_n \phi_n^{(m)}(r), \tag{1.20}$$

with

$$\phi_n^{(m)}(r) = \mathcal{N}_n J_1(K_n r), \qquad \mathcal{N}_n^{-1} = \sqrt{J_1^2(K_n R_d) - J_0(K_n R_d)J_2(K_n R_d)}, \tag{1.21}$$

where the normalisation ensures that $\int_\Omega \mathrm{d}\boldsymbol{r}\,\phi_n^{(m)}(r)\phi_m^{(m)}(r) = V_\Omega \delta_{n,m}$. Here, the wave vectors K_n must satisfy a dynamical equilibrium condition at the boundaries of the disk. Indeed, for the modes to correspond to stable stationary vibrational states of the resonating material, the in-plane radial stress of the equivalent two-dimensional problem, $\sigma_{rr} = \tilde{\lambda}(u_{rr} + u_{\theta\theta}) + 2\mu u_{rr} = (\tilde{\lambda} + 2\mu)\partial_r u_r(r) + \tilde{\lambda}u_r(r)/r$, that is induced by the deformation of the material, must vanish at the boundaries of the disk. Substituting therein the base functions of Eq. (1.21), this leads to the following condition:

$$K_n R_d J_0(K_n R_d) - (1 - \nu)J_1(K_n R_d) = 0. \tag{1.22}$$

The wave vectors thus solely depend on the Poisson ratio of the disk's material. We provide the ten lowest wave vectors for GaAs in Table 1.1. Their dependence on the radial order n is roughly linear.

$K_1 R_d$	$K_2 R_d$	$K_3 R_d$	$K_4 R_d$	$K_5 R_d$	$K_6 R_d$	$K_7 R_d$	$K_8 R_d$	$K_9 R_d$	$K_{10} R_d$
2.061	5.393	8.574	11.734	14.885	18.033	21.180	24.325	27.469	30.612

Table 1.1: Wave vectors of a GaAs disk's first ten RBMs ($\nu = 0.32$).

The radial displacement and strain profiles associated to the first two RBMs are shown in Fig. 1.2 (a) and (b). Fig. 1.2 (c) compares the theoretical expression of the radial profile of the first RBM to that obtained by means of axisymmetric finite-element simulations. In the identified basis, the Lagrangian reduces to

$$L_m = \sum_{n=1}^{+\infty} \left\{ \frac{1}{2}M\dot{u}_n^2 - \frac{1}{2}M\Omega_n^2 u_n^2 \right\}, \tag{1.23}$$

where $M = \rho V$ is the mass of the disk and $\Omega_n = c_s K_n$ its angular frequency. For a typical disk of radius $R_d \sim 2$–$5\,\mu\mathrm{m}$ and thickness $L_z \sim 300\,\mathrm{nm}$, one has $M \sim 10\,\mathrm{pg}$ and $\Omega_n/2\pi \sim$

1 GHz. As for the WGM, the mechanical angular frequency is inversely proportional to the radius of the disk. By identifying $\pi_n = \partial L_m / \partial \dot{u}_n = M\dot{u}_n$ and Legendre-transforming the above, one obtains the classical Hamiltonian of a set of independent harmonic oscillators:

$$H_m = \sum_n \dot{u}_n \pi_n - L_m = \sum_n \left\{ \frac{1}{2M}\pi_n^2 + \frac{1}{2}M\Omega_n^2 u_n^2 \right\}. \tag{1.24}$$

One can now apply the canonical quantisation prescription as for the WGM according to $(u_n, \pi_n) \mapsto (\hat{u}_n, \hat{\pi}_n)$, with $[\hat{u}_n, \hat{\pi}_m] = i\hbar\delta_{n,m}$, yet again obtaining the customary quantum harmonic-oscillator Hamiltonian:

$$\hat{H}_m = \sum_n \left\{ \frac{1}{2M}\hat{\pi}_n^2 + \frac{1}{2}M\Omega_n^2\hat{u}_n^2 \right\}. \tag{1.25}$$

This may be brought to the usual bosonic form by expressing the quantum conjugated coordinates as quadratures of the bosonic creation and annihilation operators

$$\begin{cases} \hat{u}_n = x_n^{\mathrm{ZPF}}(\hat{b}_n + \hat{b}_n^\dagger), \\ \hat{\pi}_n = -iMx_n^{\mathrm{ZPF}}(\hat{b}_n - \hat{b}_n^\dagger), \end{cases} \tag{1.26}$$

with the zero-point fluctuations $x_n^{\mathrm{ZPF}} := \sqrt{\langle 0|\, \hat{u}_n^2\, |0\rangle} = \sqrt{\hbar/2M\Omega_n}$, finally resulting in

$$\hat{H}_m = \sum_n \hbar\Omega_n(\hat{b}_n^\dagger\hat{b}_n + 1/2). \tag{1.27}$$

This completely describes the unitary dynamics of the RBM's elementary excitations: the phonons.

The advantage of carrying out the above derivation from first principles, as compared to assuming Eq. (1.27), lies on being now able to relate explicitly the mechanical displacement and the bosonic picture. Indeed, the mechanical displacement can now be given the following operatorial expression:

$$\hat{\boldsymbol{u}}_r(r) = \sum_n \phi_n^{(m)}(r)\hat{u}_n\boldsymbol{e}_r = \sum_n \phi_n^{(m)}(r)x_n^{\mathrm{ZPF}}(\hat{b}_n + \hat{b}_n^\dagger)\boldsymbol{e}_r, \tag{1.28}$$

This will become important in Sec. II, when discussing the strong coupling between the radial mechanical strain and a quantum well's excitons.

The consistency of the normalisation may be verified by comparing the (infinite) energy of the vacuum fluctuations $\langle \mathbf{0}|\, \hat{H}\, |\mathbf{0}\rangle$ in the three pictures—direct, reciprocal and bosonic—

$$\langle \mathbf{0}| \left\{ \int_\Omega \mathrm{d}\boldsymbol{r}\rho c_s^2 \hat{u}_r(r)\left(\frac{1}{r}\partial_r[r]\partial_r - \frac{1}{r^2}\right)\hat{u}_r(r) \right\} |\mathbf{0}\rangle = \langle \mathbf{0}| \sum_n M\Omega_n^2\hat{u}_n^2 |\mathbf{0}\rangle = \sum_n \frac{\hbar\Omega_n}{2}, \tag{1.29}$$

where the Virial theorem [94] was employed.
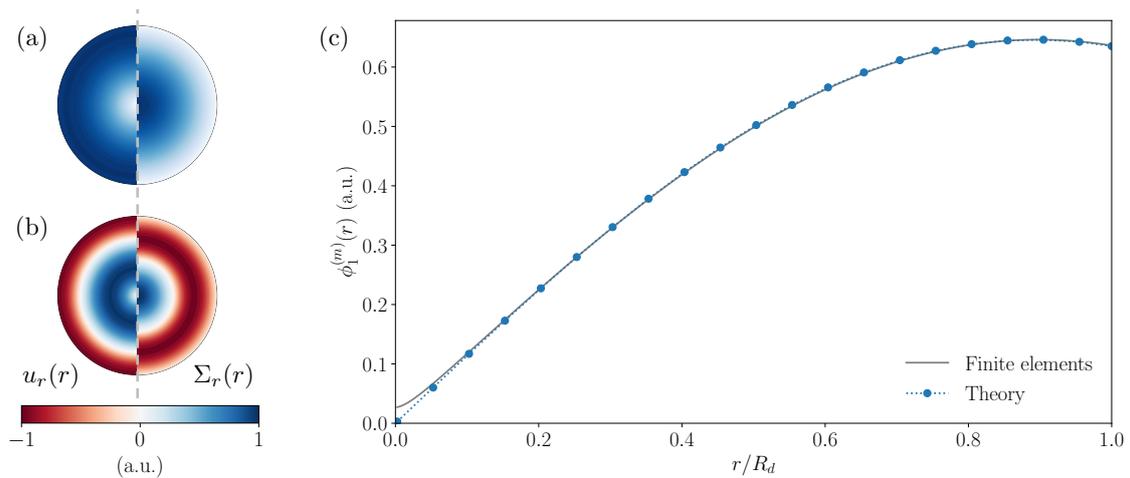
Figure 1.2: Radial displacement $u_r(r)$ and strain $\Sigma_r(r) = \nabla_{\boldsymbol{r}} \cdot \boldsymbol{u}(r)$ associated to the (a) $n = 1$ and (b) $n = 2$ radial breathing modes. (c) Comparison of the theoretically derived phonon wave function and that obtained by finite-element calculations for a GaAs disk of radius $R_d = 2\,\mu\text{m}$ and thickness $L_z = 300\,\text{nm}$.

I.3 Modelling the environment

The system we described so far cannot be faithfully described as completely isolated. Indeed, many ways exist in which it may interact with its environment. As already sketched, the optical-mode photons may radiate out of the disk as a result of the absence of total inner reflection, whether due to a high confinement or to geometrical imperfections at the boundaries [95]. Photons may also be lost through nonlinear scattering processes in the material. Indeed, while linear absorbance in the bulk is in principle suppressed at the relevant wavelengths, surface impurities may lead to the presence of levels in the band gap of the semiconducting material, hence restoring linear absorption channels. Finally, in any relevant setup, information about the optical field is retrieved by some experimental means, inducing some inevitable interaction with the outside world. Neither can the mechanics be considered independently of its environment. Indeed, a notable incoherent process is the mechanical-mode thermalisation with the substrate via the disk's pedestal. Many other dissipation channels have sizeable contributions to its dynamics, whose effects were shown to exhibit a significant and complex temperature dependence [96].

Fortunately, these effects may be accounted for independently from their microscopical origin. This can be achieved via many approaches, such as the Lindblad master equation or the quantum Langevin equation, that share in common the modelling of the environment as an infinite set of possibly coupled harmonic oscillators at thermal equilibrium that are linearly coupled to the system. In any of these approaches, the aim is to obtain an effective description of the system that does not involve keeping track of the evolution of the reservoir. Throughout this manuscript, the master equation approach will be privileged, this section is no exception.

Let us consider some bosonic mode of our system, be it a photon or a phonon, described by a bosonic operator $\hat{a}$ and vanishingly coupled to some large set of distinct bosonic modes, as described by a set of annihilation operators $\{\hat{c}_\lambda\}_\lambda$ that represent the modes

of an external bath. These modes are described by the following harmonic-oscillator Hamiltonians

$$\hat{H}_{\mathrm{S}} = \hbar\omega_0 \hat{a}^\dagger \hat{a}, \qquad \hat{H}_{\mathrm{B}} = \sum_\lambda \hbar\omega_\lambda \hat{c}_\lambda^\dagger \hat{c}_\lambda, \tag{1.30}$$

that, combined, describe the bare energy of the uncoupled bosons $\hat{H}_0 = \hat{H}_{\mathrm{S}} + \hat{H}_{\mathrm{B}}$. Initially, the system is described by some arbitrary density matrix $\hat{\rho}_{\mathrm{S}}(t)$ while the bath is in a thermal statistical mixture $\hat{\rho}_{\mathrm{B}} = e^{-\beta\hat{H}_{\mathrm{B}}}/Z$, where $\beta = 1/k_{\mathrm{B}}T$ is the usual inverse temperature and $Z = \mathrm{Tr}[e^{-\beta\hat{H}_{\mathrm{B}}}]$ is the canonical partition function. At some reference time t_0, the system and its bath, originally independent, are put in contact and start to exchange quanta by means of an interaction Hamiltonian of the form

$$\hat{H}_{\mathrm{I}} = \hat{S} \otimes \hat{B} \equiv (\hat{a} + \hat{a}^\dagger) \otimes \frac{1}{\sqrt{N}} \sum_\lambda (g_\lambda^\star \hat{c}_\lambda + g_\lambda \hat{c}_\lambda^\dagger). \tag{1.31}$$

The system-reservoir ensemble is considered as a closed system an thus evolves according to the following unitary master equation

$$\partial_t \hat{\rho}_{\mathrm{SB}} = -\frac{i}{\hbar}\left[\hat{H}_0 + \hat{H}_{\mathrm{I}}, \hat{\rho}_{\mathrm{SB}}\right], \tag{1.32}$$

where $\hat{\rho}_{\mathrm{SB}}$ is the density matrix of the bipartite ensemble. By moving to the interaction picture induced by the unitary transform $\tilde{O}(t) = e^{i\hat{H}_0(t-t_0)/\hbar}\hat{O}e^{-i\hat{H}_0(t-t_0)/\hbar}$, the dynamics is solely generated by the interaction Hamiltonian

$$\partial_t \tilde{\rho}_{\mathrm{SB}} = -\frac{i}{\hbar}\left[\tilde{H}_{\mathrm{I}}, \tilde{\rho}_{\mathrm{SB}}\right], \tag{1.33}$$

and the solution may be expressed formally as

$$\tilde{\rho}_{\mathrm{SB}}(t) = \tilde{\rho}_{\mathrm{SB}}(t_0) - \frac{i}{\hbar}\int_{t_0}^t \mathrm{d}t' \left[\tilde{H}_{\mathrm{I}}(t'), \tilde{\rho}_{\mathrm{SB}}(t')\right]. \tag{1.34}$$

By inserting Eq. (1.34) into Eq. (1.33), one arrives to the following integro-differential master equation:

$$\partial_t \tilde{\rho}_{\mathrm{SB}}(t) = -\frac{i}{\hbar}\left[\tilde{H}_{\mathrm{I}}(t), \hat{\rho}_{\mathrm{SB}}(t_0)\right] - \frac{1}{\hbar^2}\int_{t_0}^t \mathrm{d}t' \left[\tilde{H}_{\mathrm{I}}(t), [\tilde{H}_{\mathrm{I}}(t'), \tilde{\rho}_{\mathrm{SB}}(t')]\right]. \tag{1.35}$$

One aims at describing the dynamics of the system, only, irrespective of the state of the bath, as given by the system's reduced density matrix $\hat{\rho}_{\mathrm{S}} = \mathrm{tr}_{\mathrm{B}}\hat{\rho}_{\mathrm{SB}}$. For this purpose, one traces out the bath's degrees of freedom in the above expression to identify the system's effective master equation. By noting that $\mathrm{tr}_{\mathrm{R}}\{[\tilde{H}_{\mathrm{I}}(t), \hat{\rho}_{\mathrm{SB}}(t_0)]\} = 0$ and within the Born approximation, which assumes that the system and its bath remain approximately separable at any time $\hat{\rho}_{\mathrm{SB}} \approx \hat{\rho}_{\mathrm{S}} \otimes \hat{\rho}_{\mathrm{B}}$, straightforward manipulations lead to the following dynamical equation, back to Schrödinger's picture:

$$\partial_t \hat{\rho}_{\mathrm{S}}(t) = -\frac{i}{\hbar}\left[\hat{H}_{\mathrm{S}}, \hat{\rho}_{\mathrm{S}}(t)\right] - \frac{1}{\hbar^2}\int_0^{t-t_0} \mathrm{d}\tau \left\{\mathcal{G}(\tau)\left[\hat{S}, e^{-i\hat{H}_{\mathrm{S}}\tau/\hbar}\left(\hat{S}\hat{\rho}_{\mathrm{S}}(t-\tau)\right)e^{-i\hat{H}_{\mathrm{S}}\tau/\hbar}\right] + \mathrm{H.c.}\right\}, \tag{1.36}$$

with $\mathcal{G}$ a relevant correlation function of the reservoir. Neglecting the backaction of the system on the bath, that is, assuming that the bath is "big" enough with respect to the system, the state of the bath is time-translational invariant and one simply has $\mathcal{G}(\tau) = \langle \hat{B}(\tau)\hat{B}(0) \rangle \equiv \text{tr}_\text{B}[\hat{\rho}_\text{B}\hat{B}(\tau)\hat{B}(0)]$. This acts as a memory kernel of typical support τ_B, that decreases with the amount of available modes in the bath.

Let us examine the second member of Eq. (1.36). The system operator $\hat{S} = \hat{a} + \hat{a}^\dagger$ acts on the density matrix by either destroying or creating an excitation. (i) The term $\hat{S}\hat{\rho}_\text{S}(t-\tau)$ thus corresponds to a scattering event from the system to the reservoir or vice versa happening at time $t - \tau$ in the recent past (note that $\tau \lesssim \tau_\text{B}$). (ii) The resulting perturbed density matrix is then evolved by the bare Hamiltonian up to the present time t and (iii) the operator $\hat{S}$ is actuated again. One thus sees that the reservoir-induced effective dynamics of the system at time t is essentially ruled by all processes involving single-body excursions from the bath (resp. system) into the system (resp. bath) and lasting a time τ within the typical relaxation time of the bath τ_B. By assuming τ_B to be much shorter than the typical timescales of the system, one can perform a partial Markovian approximation consisting in neglecting the unitary evolution of the density matrix during the (short) excursion times. By further taking the reference time to remote past $t_0 \to -\infty$, one obtains the Bloch-Redfield equation

$$\partial_t \hat{\rho}_\text{S} = -\frac{i}{\hbar}\big[\hat{H}_\text{S}, \hat{\rho}_\text{S}\big] + \frac{1}{\hbar^2}\big\{\big[\hat{U}\hat{\rho}_\text{S}, \hat{S}\big] + \big[\hat{S}, \hat{\rho}_\text{S}\hat{U}^\dagger\big]\big\}, \tag{1.37}$$

with dressed system operators $\hat{U} = \int_0^{+\infty} \mathrm{d}\tau \mathcal{G}(\tau)\tilde{S}(-\tau) = \Gamma(\omega_0)\hat{a} + \Gamma(-\omega_0)\hat{a}^\dagger$, where $\Gamma(\omega) = \int_0^{+\infty} \mathrm{d}\tau \mathcal{G}(\tau)e^{i\omega\tau}$. While preserving the trace 1 of the density matrix, this master equation does not preserve its semipositivity due to the partial Markovian approximation that breaks the causality of the evolution. This can be fixed by retaining only resonant terms in the second member. By splitting bath's spectrum into its Hermitian and anti-Hermitian parts as $\Gamma(\omega) = \frac{1}{2}\gamma(\omega) + i\hbar S(\omega)$, this so-called secular or rotating-wave approximation yields the celebrated Lindblad master equation [97–99]

$$\partial_t \hat{\rho}_\text{S} = -\frac{i}{\hbar}\big[\hat{H}'_\text{S}, \hat{\rho}_\text{S}\big] + \gamma(\omega_0)\mathcal{D}[\hat{a}]\hat{\rho}_\text{S} + \gamma(-\omega_0)\mathcal{D}[\hat{a}^\dagger]\hat{\rho}_\text{S}, \tag{1.38}$$

where $\hat{H}'_\text{S}$ denotes the Lamb-shifted Hamiltonian, with an angular frequency renormalised by the interaction with the reservoir as $\omega'_0 = \omega_0 + S(\omega_0) + S(-\omega_0)$, and where, for any Lindblad jump operator $\hat{L}$, $\mathcal{D}[\hat{L}]$ is a trace-preserving completely positive superoperator acting on the density matrix as

$$\mathcal{D}[\hat{L}]\hat{\rho} = \hat{L}\hat{\rho}\hat{L}^\dagger - \frac{1}{2}\{\hat{L}^\dagger\hat{L}, \hat{\rho}\}, \tag{1.39}$$

where curly brackets denote the anticommutator $\{\hat{A}, \hat{B}\} = \hat{A}\hat{B} + \hat{B}\hat{A}$.

By introducing the bath's density of states $D_\text{B}(\omega) = \frac{1}{N}\sum_\lambda \delta(\omega - \omega_\lambda)$, the Lamb shift and the dissipation rates may be expressed explicitly as

$$S(\omega) = \text{p.v.} \int \mathrm{d}\omega' D_\text{B}(\omega')|g(\omega')|^2\Big\{\frac{\bar{N}(\omega') + 1}{\omega - \omega'} + \frac{\bar{N}(\omega')}{\omega + \omega'}\Big\}, \tag{1.40}$$

$$\gamma(\omega) = \begin{cases} 2\pi D_\text{B}(\omega)|g(\omega)|^2(\bar{N}(\omega) + 1), & \omega \geq 0; \\ 2\pi D_\text{B}(-\omega)|g(-\omega)|^2\bar{N}(\omega), & \omega \leq 0. \end{cases} \tag{1.41}$$

This yields the final master equation driving the dynamics of the system's bosonic mode:

$$\partial_t \hat{\rho}_{\mathrm{S}} = -\frac{i}{\hbar}\left[\hat{H}'_{\mathrm{S}}, \hat{\rho}_{\mathrm{S}}\right] + \gamma(\bar{N}+1)\mathcal{D}[\hat{a}]\hat{\rho}_{\mathrm{S}} + \gamma\bar{N}\mathcal{D}[\hat{a}^{\dagger}]\hat{\rho}_{\mathrm{S}}, \tag{1.42}$$

with $\gamma = 2\pi D_{\mathrm{B}}(|\omega_0|)|g(|\omega_0|)|^2$ the relaxation rate and $\bar{N} = 1/(\exp(\beta\hbar\omega_0)-1)$ the Planck distribution at the bare oscillator energy. In this expression, $\mathcal{D}[\hat{a}]$ is responsible for the leakage of excitations from the system to the bath at a rate $\gamma(\bar{N}+1)$ while $\mathcal{D}[\hat{a}^{\dagger}]$ incoherently injects excitations into the system from the bath at a rate $\gamma\bar{N}$. This is illustrated in Fig. 1.3. As may be trivially checked from the detailed-balance condition, the steady state of the above Lindblad master equation is found to be a thermal state $\hat{\rho}_{\mathrm{S}}(t \to +\infty) = e^{-\beta\hat{H}_{\mathrm{S}}}/Z$ whose thermal occupation is indeed $\mathrm{Tr}[\hat{\rho}_{\mathrm{S}}\hat{a}^{\dagger}\hat{a}] = \bar{N}$.
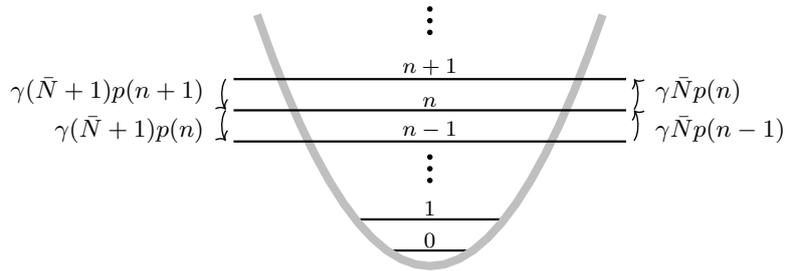
Figure 1.3: Schematic illustration of the action of the dissipator on the diagonal elements of the system's density matrix $p(n) = \langle n|\hat{\rho}_{\mathrm{S}}|n\rangle$.

Photon's master equation

Let us now adapt the general result presented above to the case of a nanodisk's WGM. From Eq. (1.10) one has $\omega_{p,\ell} = \frac{c_0 \alpha_{\ell,p}}{n R_d}$. For a typical WGM of radial and azimuthal orders of $(p, \ell) = (1, 10)$ hosted by a disk of radius $R_d = 1.5\,\mu\mathrm{m}$, one has $\hbar\omega_{1,10} \approx 0.5\,\mathrm{eV}$ and thus at room temperature $\bar{N} \approx 6.3 \times 10^{-10}$. The second dissipator in Eq. (1.42) can thus be safely neglected. The optical master equation will thus henceforth take the simpler form

$$\partial_t \hat{\rho} = -\frac{i}{\hbar}[\hbar\omega_c \hat{a}^{\dagger}\hat{a} + \hat{V}_p(t), \hat{\rho}] + \kappa\mathcal{D}[\hat{a}]\hat{\rho}, \tag{1.43}$$

where ω_c is the bare cavity angular frequency (the Lamb shift is typically negligible), κ is the optical decay rate and $\hat{V}_p(t)$ is a time-dependent Hamiltonian describing the driving of the cavity by means of an external monochromatic coherent optical field. This takes the form

$$\hat{V}_p(t) = \hbar F(\hat{a}e^{+i\omega_p t} + \hat{a}^{\dagger}e^{-i\omega_p t}), \tag{1.44}$$

where F is the amplitude of the driving and ω_p the angular frequency of the pump. By moving to a frame rotating with the drive's phase, $\hat{H} \mapsto \hat{U}(t)\hat{H}\hat{U}^{\dagger}(t)$, $\hat{\rho} \mapsto \hat{U}(t)\hat{\rho}\hat{U}^{\dagger}(t)$, where $\hat{U}(t) = e^{i\omega_p \hat{a}^{\dagger}\hat{a}t}$, one finally gets an equivalent time-independent master equation for the cavity photons

$$\partial_t \hat{\rho} = -i[-\Delta\hat{a}^{\dagger}\hat{a} + F(\hat{a} + \hat{a}^{\dagger}), \hat{\rho}] + \kappa\mathcal{D}[\hat{a}]\hat{\rho}, \tag{1.45}$$

where $\Delta = \omega_p - \omega_c$ denotes the detuning of the pump with respect to the cavity's frequency.

The optical mode can thus be seen as a driven harmonic oscillator coupled to a zero-temperature bath. In what follows, the ratio $Q_c = \kappa/\omega_c$ will be referred to as the cavity quality factor.

Phonon's master equation

From Eq. (1.23), the mechanical angular frequency is given by $\Omega_n = c_s K_n$. For the first RBM, of radial order $n = 1$, and a disk of radius $R_d = 1.5\,\mu\text{m}$, one has $\hbar\Omega_1 \approx 4.45\,\mu\text{eV}$ and thus a thermal population of $\bar{N} \approx 5770$ phonons at room temperature. Hence, the finite temperature of the mechanical bath cannot be neglected. The mechanical master equation will henceforth be expressed as

$$\partial_t \hat{\rho} = -i[\Omega_m \hat{b}^\dagger \hat{b}, \hat{\rho}] + \Gamma_m(\bar{N}_m + 1)\mathcal{D}[\hat{b}]\hat{\rho} + \Gamma_m \bar{N}_m \mathcal{D}[\hat{b}^\dagger]\hat{\rho}, \tag{1.46}$$

where Ω_m denotes the angular frequency of the RBM of interest, Γ_m the mechanical relaxation rate and $\bar{N}_m$ the thermal steady-state phonon population. In what follows, the ratio $Q_m = \Gamma_m/\Omega_m$ will be referred to as the mechanical quality factor.

Let us note however that the above derivation relies on a rotating approximation valid in so far as the coherent dynamics of the system's degrees of freedom happens at a much faster timescale than that of the bath. While this situation, known as the quantum optical limit [99], is perfectly legitimate both in the case of the optical mode and that of a mechanical mode with a high mechanical quality factor, the approximation may break down for mechanical resonators with mediocre quality factors. In particular, this model can easily be shown to not match the classical dynamical equations of a thermalised harmonic oscillator in the semiclassical limit. In such cases, one should fall back to the Caldeira-Leggett model [100, 101] to faithfully account for the action of the environment on the mechanical motion of the resonator.

I.4 The optomechanical coupling

So far, the optical WGM and the mechanical RBM under consideration were treated as independent modes. Let us now describe the optomechanical interaction between these two bosonic fields.

The most direct way photons and phonons may couple is through radiation pressure. Indeed, we have seen that the angular frequency of some WGM of interest is inversely proportional to the radius of the disk, $\omega_{p,\ell} = \frac{c_0 \alpha_{\ell,p}}{n R_d}$; then, as the disk boundaries move outwards (inwards) due to the mechanical motion of the RBM, the energy of the photon is decreased (increased). The WGM's photons are thus sensitive to the mechanical mode. Reciprocally, the optical field exerts some radiation pressure at the boundaries of the disk, leading to a mechanical displacement.

This is most easily understood by considering a unidimensional Fabry-Pérot cavity in which one of the mirrors is movable and harmonically confined around its initial equilibrium position, as depicted in Fig. 1.4. The effect of the displacement x of the mobile mirror on the angular frequency of the fundamental mode of the cavity can be classically

written [8] as

$$\omega[x] = 2\pi c/(L+x) = \omega_c + x\,\partial_x\omega[x]|_{x=0} + \mathcal{O}(x^2), \tag{1.47}$$

where $\omega[x]$ denotes the parametric dependence of ω in the displacement x of the mirror from its initial position $x = 0$. The quantised version of this is obtained by using the same prescription as before. Defining $g = -x_{\mathrm{ZPF}}\partial_x\omega[x]|_{x=0} = \omega_c x_{\mathrm{ZPF}}/L$, the bare optical Hamiltonian is modified as $\hbar\omega_c\hat{a}^\dagger\hat{a} \mapsto \hbar(\omega_c - g\hat{x}/x_{\mathrm{ZPF}})\hat{a}^\dagger\hat{a}$. Then, the supplemental term can be extracted into an optomechanical interaction Hamiltonian:

$$\hat{H}_{cm} = -\hbar g\hat{a}^\dagger\hat{a}(\hat{b} + \hat{b}^\dagger). \tag{1.48}$$

This mechanism is here explained by simple common arguments but can be treated by a rigorous canonical quantisation of the exact cavity and resonator modes with time-dependent boundary conditions [102, 103]. We shall here sketch the derivation for the radiation-pressure interaction between a nanodisk's WGM and RBM.
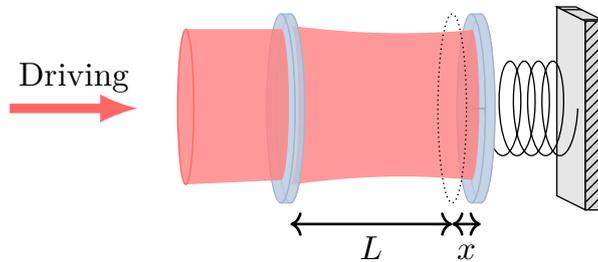
Figure 1.4: Schematic representation of a Fabry-Pérot-based cavity optomechanical system. Photons circulate between the harmonically confined mobile end mirror and the input mirror through which photons are pumped into the cavity.

Geometric contribution to the optomechanical coupling

Let us consider a TM-polarised WGM of order (p, ℓ) and the nth RBM. These are completely described from the expressions of the associated vector potential operator and mechanical displacement operator

$$\hat{\boldsymbol{A}}(\boldsymbol{r}) = \phi_c(\boldsymbol{r})\sqrt{\frac{\hbar}{2\epsilon c k_c}}(\hat{a} + \hat{a}^\dagger)\boldsymbol{e}_z, \quad \hat{\boldsymbol{u}}(r) = \phi_m(r)x_{\mathrm{ZPF}}(\hat{b} + \hat{b}^\dagger)\boldsymbol{e}_r, \tag{1.49}$$

with $\phi_c = \phi_{p,\ell}^{(c)}$, $k_c = k_{p,\ell}$, $\phi_m = \phi_n^{(m)}$, $x_{\mathrm{ZPF}} = x_n^{\mathrm{ZPF}}$.

The density of work exerted by the electromagnetic field on the dielectric takes the form

$$\mathcal{W}_{cm} = \sigma^{ij}u_{ij} = \sigma_{rr}u_{rr} + \sigma_{\theta\theta}u_{\theta\theta}, \tag{1.50}$$

where **u** is the usual mechanical strain tensor introduced in Subsec. I.2 and $\boldsymbol{\sigma}$ denotes Maxwell's stress tensor, as given by (see [104, Section 6.7], for instance)

$$\sigma_{ij} = \epsilon E_i E_j + \frac{1}{\mu}B_i B_j - \frac{1}{2}\Big(\epsilon\|\boldsymbol{E}\|^2 + \frac{1}{\mu}\|\boldsymbol{B}\|^2\Big)\delta_{ij}. \tag{1.51}$$

Let us remark that, contrary to the common intuition, the strength of the radiation-pressure coupling here depends upon the overlap between the optical energy density and the mechanical *strain*, not the absolute mechanical *displacement*. This was already the case for the paradigmatic Fabry-Pérot example, where $\hbar g = \hbar \omega_c x_{\mathrm{ZPF}}/L$ could be seen as proportional to the "strain" (relative displacement) x_{ZPF}/L induced by a single vibrational quantum, and now becomes explicit in expression (1.50). By specialising Maxwell's tensor to the considered WGM, one finally gets the optomechanical coupling Hamiltonian:

$$\hat{H}_{cm} = -\hbar g \hat{a}^\dagger \hat{a}(\hat{b} + \hat{b}^\dagger), \tag{1.52}$$

with the optomechanical constant g given by[2]

$$\frac{g}{\omega_c} = \int_\Omega \mathrm{d}\boldsymbol{r} \left\{ \left(\frac{1}{k_c} \partial_r \phi_c(\boldsymbol{r}) \right)^2 x_{\mathrm{ZPF}} \partial_r \phi_m(r) + \left(\frac{1}{k_c r} \partial_\theta \phi_c(\boldsymbol{r}) \right)^2 \frac{x_{\mathrm{ZPF}}}{r} \phi_m(r) \right\}. \tag{1.53}$$

The strength of this contribution to the optomechanical coupling is proportional to the optical angular frequency, and thus inversely proportional to the radius of the disk. It depends on the radial orders of the mechanical and optical modes under consideration. Upon choosing some specific set of modes, this contribution as well as that of the photoelasticity can be numerically evaluated [105, 106].

I.5   The optomechanical master equation

This thorough quantum modelling process finally results in the following master equation for the optomechanical resonator

$$\begin{aligned}
\partial_t \hat{\rho} &= -\frac{i}{\hbar}[\hat{H}, \hat{\rho}] + \kappa \mathcal{D}[\hat{a}]\hat{\rho} + \Gamma_m(\bar{N}_m + 1)\mathcal{D}[\hat{b}]\hat{\rho} + \Gamma_m \bar{N}_m \mathcal{D}[\hat{b}^\dagger]\hat{\rho}, \\
\hat{H}/\hbar &= -\Delta \hat{a}^\dagger \hat{a} + F(\hat{a} + \hat{a}^\dagger) - g\hat{a}^\dagger \hat{a}(\hat{b} + \hat{b}) + \Omega_m \hat{b}^\dagger \hat{b},
\end{aligned} \tag{1.54}$$

that summarises Eqs. (1.45), (1.46) and (1.52).

A rich phenomenology emerges from the interplay between the various distinctive features of this model. Among these, let us first highlight the usually strong hierarchy between the short optical and the long mechanical timescales. As a consequence, by acting on the coherent drive at the optical timescale $1/\kappa$ one may avoid the dynamical backaction of the mechanical subsystem onto the optics, thus allowing one to control the mechanics through the external optical driving. A second feature is the strong dependence on the detuning of the effective dynamics induced by the optomechanical coupling in the so-called resolved-sideband regime ($\kappa \ll \Omega_m$). In this regime, the optical spectrum presents additional resonances corresponding to Stokes and anti-Stokes scattering processes between the mechanical and the optical modes. These can thus be excited and either enhanced or suppressed by proper tuning of the pump angular frequency. This has found applications ranging from the ubiquitous sideband cooling scheme for cooling down the mechanical oscillator [107–117] to quantum teleportation schemes [β, 26, 27]. Another very interesting feature derives directly from the form of the optomechanical

---

[2]Here, the Virial theorem was used.

coupling. This coupling, by making intervene the optical population $\hat{n}$, couples dynamically its conjugated quantity, the optical phase $\hat{\phi}$ [118], to the mechanical displacement, $i\partial_t \hat{\phi}|_{\hat{H}} = \omega_c - g\hat{x}/x_{\text{ZPF}}$. The optomechanical coupling can therefore be interpreted as the extent to which a mechanical displacement that is commensurate with the mechanical zero-point fluctuations impacts the angular frequency of the optical state. This interfacing ability of optomechanical resonators to optically perform the readout of a mechanical element's microscopic displacements very soon generated interest in the field of sensing [22–25].

Sideband cooling and heating

Let us thereafter briefly discuss some of the basic optomechanical phenomenology that will later prove useful to understand the main results of Chapter 2.

The master equation (1.54) can be greatly simplified by a suitable unitary transformation. Indeed, operators can be displaced thanks to the following unitary transformation $\hat{U} = \hat{D}(\alpha)\hat{D}(\beta)$, where $\hat{D}(\alpha) = e^{\alpha\hat{a}^\dagger - \alpha^*\hat{a}}$ and $\hat{D}(\beta) = e^{\beta\hat{b}^\dagger - \beta^*\hat{b}}$. This eliminates all linear terms in the Hamiltonian for the following choice of displacement:

$$\alpha = \frac{F}{\widetilde{\Delta} + i\kappa/2}, \quad \beta = \frac{g|\alpha|^2}{\Omega_m - i\Gamma_m/2}, \tag{1.55}$$

where $\widetilde{\Delta} = \Delta + 2g^2|\alpha|^2/\Omega_m$ is the nonlinearly shifted cavity detuning[3]. This can be seen as a shift of the origin of the phase-space coordinates, $(\hat{a}, \hat{a}^\dagger, \hat{b}, \hat{b}^\dagger) \mapsto (\hat{a} - \langle\hat{a}\rangle, \hat{a}^\dagger - \langle\hat{a}\rangle^\star, \hat{b} - \langle\hat{b}\rangle, \hat{b}^\dagger - \langle\hat{b}\rangle^\star)$, to the mean-field solutions $\alpha = \langle\hat{a}\rangle$ and $\beta = \langle\hat{b}\rangle$. In this displaced frame, $\hat{a}$ and $\hat{b}$ become annihilation operators of the fluctuation quanta around the mean-field solutions.

Some non-trivial physics can readily be observed on the steady-state mean-field populations. Indeed, squaring Eqs. (1.55), many stable solutions for the coherent optical population $N_c = |\alpha|^2$ may exist to the nonlinear equation

$$\left[\left(\Delta + \frac{2g^2}{\Omega_m}N_c\right)^2 + \left(\frac{\kappa}{2}\right)^2\right]N_c = |F|^2, \tag{1.56}$$

yet, in the following, we will assume that one remains in the stable manifold.

The trivial quadratic Hamiltonian terms can also be absorbed into yet another unitary transformation $\hat{U} = e^{-i\Delta\hat{a}^\dagger\hat{a}t + i\Omega_m\hat{b}^\dagger\hat{b}t}$. This finally yields, to second order in the fluctuation operators:

$$\hat{H} \approx -\hbar g\sqrt{N_c}\left\{(\hat{a}e^{+i(\widetilde{\Delta}-\Omega_m)t} + \hat{a}^\dagger e^{-i(\widetilde{\Delta}+\Omega_m)t})\hat{b} + \text{H.c.}\right\}. \tag{1.57}$$

Only one term is left in this linearised Hamiltonian driving the dynamics of quantum fluctuations. This is responsible for the Stokes and anti-Stokes scattering processes. Indeed,

---

[3]The quantum optical limit (see comment below Eq. (1.46)) actually gives $\widetilde{\Delta} = \Delta + 2g^2|\alpha|^2\Omega_m/[\Omega_m^2 + (\Gamma_m/2)^2]$, which is slightly off with respect to the semiclassical picture. Yet, this is negligible for $Q_m = \Omega_m/\Gamma_m \gg 1$ as will be the case throughout this thesis and may be fixed by using a Caldeira-Legget approach for modelling the mechanical environment.

in the well-resolved-sideband regime $\kappa \ll \Omega_m$, rapid non-resonant terms can be eliminated within the rotating-wave approximation (RWA), finally yielding

$$\hat{H} \approx \begin{cases} -g\sqrt{N_c}(\hat{a}^\dagger \hat{b}^\dagger + \text{H.c.}), & \widetilde{\Delta} \sim +\Omega_m; \\ -g\sqrt{N_c}(\hat{a}^\dagger \hat{b} + \text{H.c.}), & \widetilde{\Delta} \sim -\Omega_m. \end{cases} \tag{1.58}$$

Thus, by driving the cavity in tune with the blue-shifted sideband ($\widetilde{\Delta} \sim \Omega_m$) or the red-shifted sideband ($\widetilde{\Delta} \sim -\Omega_m$), one may inject excitations into the mechanical resonator through Stokes processes, $\hat{a}^\dagger \hat{b}^\dagger$, or retrieve thermal phonons via anti-Stokes processes, $\hat{a}^\dagger \hat{b}$. In the latter case, the scattered phonons are optically dissipated at a much higher rate than that at which they are refilled from the mechanical thermal bath, thereby cooling down the mechanical degree of motion. This is explained in Fig. 1.5, which well illustrates the necessity of being in the resolved-sideband regime ($\kappa \ll \Omega_m$) in order to be able to selectively pump phonons either in or out of the mechanical mode.

This intuition can be formalised in various ways. We will stick to the effective master equation framework and perform an adiabatic elimination of the optical degree of freedom. Details about the elimination of a driven-dissipative reservoir can be found, for instance, in Refs. [20, 119] or, in optomechanics, in Refs. [120, 121] and [α, SM]. This approximation relies on the Markovian assumption that there is hardly any backaction of the mechanics onto the optics ($\kappa \gg \Gamma_m$) and that no significant entanglement builds up between the two modes of the resonator. This is true for very low values of the coupling. The result of this process yields

$$\partial_t \hat{\rho}_m = -i[\widetilde{\Omega}_m \hat{b}^\dagger \hat{b}, \hat{\rho}_m] + \Gamma_m(\bar{N}_m + 1)\mathcal{D}[\hat{b}]\hat{\rho}_m + \Gamma_m \bar{N}_m \mathcal{D}[\hat{b}^\dagger]\hat{\rho}_m$$
$$+ \Gamma_{\text{Opt}}^{(\downarrow)} \mathcal{D}[\hat{b}]\hat{\rho}_m + \Gamma_{\text{Opt}}^{(\uparrow)} \mathcal{D}[\hat{b}^\dagger]\hat{\rho}_m, \tag{1.59}$$

where $\widetilde{\Omega}_m = \Omega_m + S(\Omega_m) + S(-\Omega_m)$ is the Lambd-shifted mechanical angular frequency, a feature known as optical-spring effect in this context, and where $\Gamma_{\text{Opt}}^{(\downarrow)} = \Gamma_{\text{Opt}}(+\Omega_m)$ and $\Gamma_{\text{Opt}}^{(\uparrow)} = \Gamma_{\text{Opt}}(-\Omega_m)$ are mechanical dissipation and gain rates induced by the optics. These parameters have a crucial dependence on the detuning of the external drive and are given hereafter:

$$S(\omega) = g^2 N_c \frac{\widetilde{\Delta} + \omega}{(\widetilde{\Delta} + \omega)^2 + (\kappa/2)^2}, \quad \Gamma_{\text{Opt}}(\omega) = g^2 N_c \frac{\kappa}{(\widetilde{\Delta} + \omega)^2 + (\kappa/2)^2}. \tag{1.60}$$

Several conclusions can be drawn from this result. Even though a driven-dissipative cavity is very different from a continuous thermal bath, the new terms in the mechanical master equation bear a resemblance to those obtained in Sec. I.3; by defining $\Gamma_{\text{Opt}} = \Gamma_{\text{Opt}}^{(\downarrow)} - \Gamma_{\text{Opt}}^{(\uparrow)}$ and $\bar{N}_{\text{Opt}} = \Gamma_{\text{Opt}}^{(\uparrow)}/\Gamma_{\text{Opt}}$, the mechanical mode may indeed be interpreted as in contact with two thermal baths at different temperatures

$$\partial_t \hat{\rho}_m = -i[\widetilde{\Omega}_m \hat{b}^\dagger \hat{b}, \hat{\rho}_m] + \Gamma_m(\bar{N}_m + 1)\mathcal{D}[\hat{b}]\hat{\rho}_m + \Gamma_m \bar{N}_m \mathcal{D}[\hat{b}^\dagger]\hat{\rho}_m$$
$$+ \Gamma_{\text{Opt}}(\bar{N}_{\text{Opt}} + 1)\mathcal{D}[\hat{b}]\hat{\rho}_m + \Gamma_{\text{Opt}}\bar{N}_{\text{Opt}}\mathcal{D}[\hat{b}^\dagger]\hat{\rho}_m. \tag{1.61}$$

The final thermal occupation being given by the weighted average over those of the two baths:

$$\bar{N}_m^{\text{eff}} = \frac{\Gamma_m \bar{N}_m + \Gamma_{\text{Opt}} \bar{N}_{\text{Opt}}}{\Gamma_m + \Gamma_{\text{Opt}}} < \bar{N}_m \iff \bar{N}_{\text{Opt}} < \bar{N}_m. \tag{1.62}$$
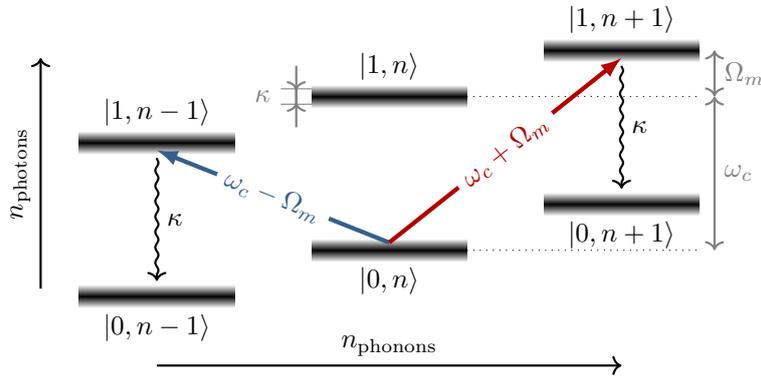
Figure 1.5: Stokes (red) and anti-Stokes (blue) irreversible scattering processes involved in sideband heating and cooling schemes. States $|n_{\text{photons}}, n_{\text{phonons}}\rangle$ are expressed in the displaced basis, n_{photons} being the number of quantum-optical fluctuation quanta on top of the "classical" optical coherent population, and n_{phonons} the thermal phonon occupation. In the resolved-sideband regime ($\kappa \ll \Omega_m$), for $\omega_p = \omega_c \pm \Omega_m$ ($\Delta = \pm\Omega_m$), the only resonant processes are given by $|0, n\rangle \leftrightarrow |1, n \pm 1\rangle \rightarrow |0, n \pm 1\rangle$, where the last path is made irreversible thanks to the optical dissipation.
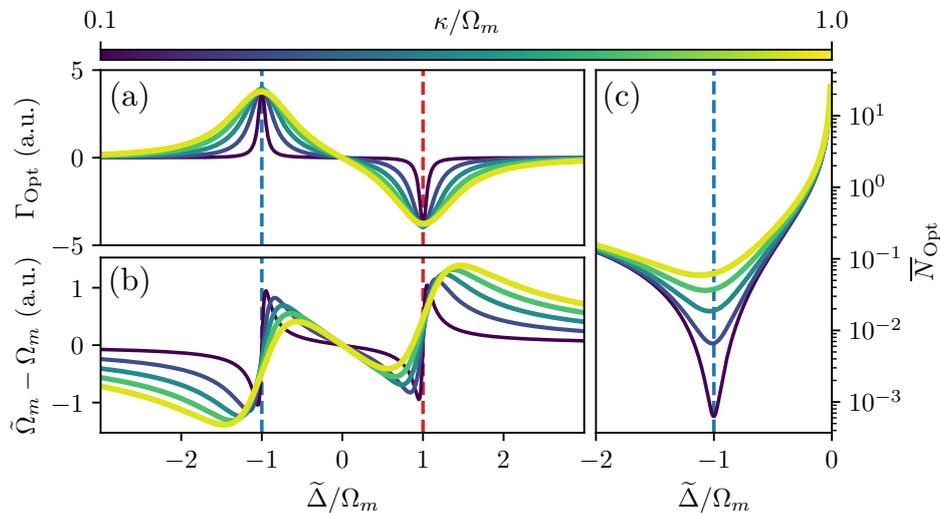
Figure 1.6: (a) Optical damping rate Γ_{Opt} as a function of the nonlinearly shifted detuning. Negative values correspond to positive gain. Cooling is maximal at the anti-Stokes sideband (dashed blue line); conversely, heating is maximal at the Stokes sideband (dashed red line). (b) Optical spring effect (Lamb shift) as a function of the nonlinearly shifted detuning. (c) Effective Planck thermal population associated to the optical "thermal bath" around the anti-Stokes sideband.

These quantities are plotted as a function of the nonlinearly shifted detuning in Fig. 1.6 for various values of the ratio κ/Ω_m. One sees that the optically induced dissipation rate is maximum around the anti-Stokes sideband and all the more peaked that the resolved-sideband condition is met. The Lamb shift instead vanishes at the sidebands and at resonance with the cavity frequency ($\widetilde{\Delta} = 0$). The strength of this coherent shift decreases slower than the optically induced dissipation; as a consequence, one may optically shift the mechanical angular frequency without adding significant dissipation to the system by driving the cavity off the sidebands. Finally, one observes that the thermal phonon occupation associated to the optical bath is very sensitive to κ/Ω_m. This implies that one should be in the well-resolved sideband regime $\kappa \ll \Omega_m$ for sideband-cooling applications. In this regime, the minimal thermal occupation obtained by resonantly driving the system at the anti-Stokes sideband is roughly given by $\bar{N}_m^{\mathrm{eff}} \approx \frac{1}{1+C}\bar{N}_m$, where C denotes the cooperativity:

$$C = \frac{\Gamma_{\mathrm{Opt}}}{\Gamma_m}\bigg|_{\widetilde{\Delta}=-\Omega_m} \simeq N_c \times C_0, \qquad C_0 = \frac{4g^2}{\kappa\Gamma_m}. \tag{1.63}$$

Here, C_0 denotes the single-photon cooperativity, a good figure of merit for characterising the magnitude of the dissipative coupling between the optical and the mechanical modes. It follows from the above that, for $C_0 \sim 1$, one could in principle cool the resonator down to its ground state with only $N_c \gtrsim \bar{N}_m$ photons. This has motivated a quest for realising optomechanical resonators with large single-photon cooperativities, yet, with the exception of cold atomic ensembles, the state of the art remains well below $C_0 = 1$ [8].

Richness of the optomechanical coupling

We just gave the intuition and the theoretical description of some of the phenomenology our theoretical findings will be elaborated on in the next chapter. But optomechanical resonators can exhibit many other peculiar behaviours stemming from the radiation-pressure interaction such as self-induced optomechanical oscillations [122–126] or phase-locking and synchronisation of coupled optomechanical resonators in a variety of configurations [127–135]. The optomechanical Hamiltonian is also an excellent tool for reservoir engineering and the basic ideas briefly presented above may be advantageously exploited to design *ad hoc* models. For the sake of example, let us design a toy model for a phonon laser.

We shall begin with a very simple Hamiltonian describing an optomechanical resonator, consisting of an optical mode described by $\hat{a}$ and a mechanical mode described by $\hat{b}$, to which an auxiliary cavity, of operator $\hat{c}$, is linearly coupled:

$$\hat{H}/\hbar = \omega\hat{a}^\dagger\hat{a} - g\hat{a}^\dagger\hat{a}(\hat{b}+\hat{b}^\dagger) + \Omega\hat{b}^\dagger\hat{b} - \frac{\lambda}{2}(\hat{a}^\dagger\hat{c} + \hat{c}^\dagger\hat{a}) + \omega\hat{c}^\dagger\hat{c}, \tag{1.64}$$

where λ is the coupling constant between the nanodisk's cavity and the external optical mode and where we chose the two optical modes to have the exact same angular frequency for simplicity. By introducing the bonding and antibonding modes $\hat{a}_\pm = (\hat{a}\pm\hat{c}^\dagger)/\sqrt{2}$, with associated angular frequencies $\omega_\pm = \omega \mp \lambda/2$, and going to a rotating frame through the rotation $\hat{U}(t) = \exp(i\omega_-\hat{a}_-^\dagger\hat{a}_- t + i(\omega_- - \Omega)\hat{a}_+^\dagger\hat{a}_+ t + i\Omega_m\hat{b}^\dagger\hat{b}t)$, the Hamiltonian can be written equivalently, within the rotating-wave approximation, as

$$\hat{H} = -\delta\hat{a}_+^\dagger\hat{a}_+ + \frac{g}{2}(\hat{a}_+^\dagger\hat{a}_-\hat{b}^\dagger + \mathrm{H.c.}), \tag{1.65}$$

where $\delta = \lambda - \Omega$ is the detuning of the angular frequency of the antibonding-to-bonding transition with respect to the bare mechanical angular frequency.

Under non-resonant driving of the optics at some frequency higher than ω_-, the dissipative part of the system's dynamics is described by

$$\partial_t \hat{\rho}|_{\text{diss.}} = \Gamma \mathcal{D}[\hat{b}] + \kappa_+ \mathcal{D}[\hat{a}_+] + \kappa_- \mathcal{D}[\hat{a}_-] + P \mathcal{D}[\hat{a}_-^\dagger], \qquad (1.66)$$

where the mechanical mode was supposed in contact with a cryostat, for simplicity, and P is the (pumping) rate at which non-resonant driving photons relax into the system. Upon assuming $\kappa_+ \gg g$, as is natural in optomechanics, one may adiabatically eliminate the bonding mode $\hat{a}_+$, which (yet in the rotating frame) yields the final master equation[4]:

$$\partial_t \hat{\rho} = -\frac{i}{\hbar} \left[\frac{K}{2} \hat{a}_-^\dagger \hat{a}_- \hat{b}^\dagger \hat{b}, \hat{\rho} \right] + \Gamma \mathcal{D}[\hat{b}] \hat{\rho} + \beta \mathcal{D}[\hat{b}^\dagger \hat{a}_-] \hat{\rho} + \kappa_- \mathcal{D}[\hat{a}_-] \hat{\rho} + P \mathcal{D}[\hat{a}_-^\dagger] \hat{\rho}. \qquad (1.67)$$

where $K = -\delta \frac{g^2/2}{\delta^2 + (\kappa_+/2)^2}$ is an effective cross-Kerr interaction and $\beta = \frac{\kappa_+ g^2/4}{\delta^2 + (\kappa_+/2)^2}$ and effective rate of stimulated emission. The dynamical equations of motion satisfied by the occupation operators $\hat{n} = \hat{b}^\dagger \hat{b}$ and $\hat{N} = \hat{a}_-^\dagger \hat{a}_-$ directly follow from this:

$$\begin{aligned} \gamma^{-1} \partial_t \hat{n} &= +\tilde{\beta} \hat{N}(\hat{n} + 1) - \tilde{\Gamma} - \hat{n}, \\ \gamma^{-1} \partial_t \hat{N} &= -\tilde{\beta} \hat{N}(\hat{n} + 1) - \hat{N} + \tilde{P}, \end{aligned} \qquad (1.68)$$

where $\gamma \equiv \kappa_- - P$, and, for any parameter, $\tilde{x} \equiv x/\gamma$. These are exactly the dynamical equations of the famous Rice's and Carmichael's quantum theory for a semiconductor laser [136]. In the context they were introduced in, $\langle \hat{n} \rangle$ corresponds to the laser's photon population and $\langle \hat{N} \rangle$ to the number of carriers. In contrast, here the lasing mode is of purely phononic nature. Within a mean-field approach, one easily verifies that the steady-state phonon population experiences a second-order phase transition in the (thermodynamical) limit of $\tilde{\beta}^{-1} \to +\infty$:

$$\langle \hat{n} \rangle = \frac{1}{2\tilde{\beta}} \left(R - 1 + \sqrt{(R-1)^2 + 4\tilde{\beta}R} \right) \xrightarrow{\tilde{\beta}^{-1} \to +\infty} \tilde{\beta}^{-1} \max(0, R - 1), \qquad (1.69)$$

with $R = \tilde{\beta}\tilde{P}/\tilde{\kappa}$. It follows that the critical pump power is given by $P_c = \kappa_-$. Past this threshold, the phonon population rises linearly with the pump power and acquires Poissonian statistics.

The example presented above is not to be confused with what is commonly referred to as *mechanical lasing* in the optomechanical context, which is associated to a linewidth narrowing of the mechanical mode in the regime of self-oscillations. This should convince the reader of the wide range of phenomena hidden behind the seemingly simple optomechanical coupling of Eq. (1.52) and of its convenience in the domain of reservoir engineering.

---

[4]Notice that the effective dynamics of the system became U(1)-symmetric, which is crucial for the emergence of a second order lasing transition.

II   Beyond photons and phonons: polariton optomechanics

Many recent optomechanical applications involve the manipulation of the quantum state of the mechanical degree(s) of freedom through Stokes and anti-Stokes processes resonant at the sidebands. This encompasses ground-state sideband cooling [59–63], mechanically assisted squeezed-light generation [65, 66], quantum mechanical-state preparation [67–69], entanglement generation between photons [70], photons and phonons [71, 72], and distant phonon modes [73], mechanically mediated superconducting-qubit-to-photon transduction [64], optics-to-mechanics quantum-state teleportation [β, 26, 27], or light-mediated quantum communication between remote mechanical resonators [74]. The peculiar dynamics involved in such applications is driven by the aforementioned parametric optomechanical interaction. In this context, the figure of merit that quantifies the efficiency of the Stokes and anti-Stokes processes occurring at the sidebands is the single-photon cooperativity $C_0 = 4g^2/\kappa\Gamma_m$. Yet the bare optomechanical coupling strength g is typically very small as compared to the optical relaxation rate κ. For a typical micrometric GaAs disk, for instance, this is of the order of a few megahertz [58, 105, 106, 137], as compared to $\kappa \sim 1\,\mathrm{GHz}$ and $\Omega_m \sim 1$–$10\,\mathrm{GHz}$. Analogue figures are found in optomechanical crystals [138, 139]. One could in principle increment the number of photons in the cavity by increasing the optical pump power so as to linearly enhance the effective cooperativity $C = N_c \times C_0$. Working with such large photonic populations, however, can lead to a significant heating of the material and degrade both the cavity's quality factor and the mechanical coherence, thereby limiting the maximum optomechanical cooperativity that can be reached in practice [140].

In this section, we will explore the possibility of overcoming this bottleneck by exploiting the strong interaction between a resonator's phonons and quantum-well excitons in order to boost the bare optomechanical coupling strength in hybrid nanodisk polariton-mechanical resonators (see Refs. [81, 83] for a related scenario). Indeed, in the last couple of decades, evidences of strong parametric optomechanical interactions were reported in planar microcavities embedding quantum wells [141–145], first interpreted as an enhancement of the optomechanical coupling and later as an interaction between phonons and *polaritons*, hybrid exciton-photon quasiparticles. Very recently, resonances corresponding to hybrid quasiparticles of excitonic, optical and acoustic nature were identified in *ab initio* numerical simulations [146]. We shall here give a first-principle theoretical description of this interaction.

II.1   Quantum-well excitons

Let us describe a GaAs nanodisk optomechanical resonator of radius R_d and thickness L_z embedding a quantum well of thickness $L_{\mathrm{QW}} \ll L_z$ made from a alloy of GaAs and InAs, as illustrated in Fig. 1.8 (a). We will here simply outline some standard concepts. A detailed theoretical description of such semiconducting heterostructures may be found elsewhere [148–152].
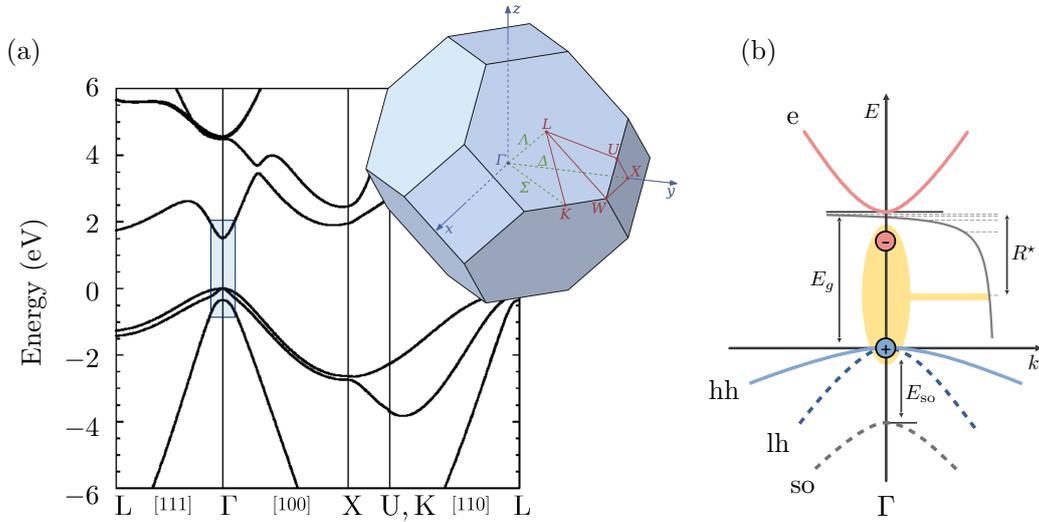
Figure 1.7: (a) Band structure of bulk GaAs, as computed in [147] with a 30-band $\mathbf{k} \cdot \mathbf{p}$ method. (b) First Brillouin zone, as highlighted in (a), within a parabolic band approximation. The relevant conduction and heavy-hole bands are represented with plain lines. The first five electron-hole bound states are represented as dashed lines in the Coulomb potential. Adapted with permission from [148].
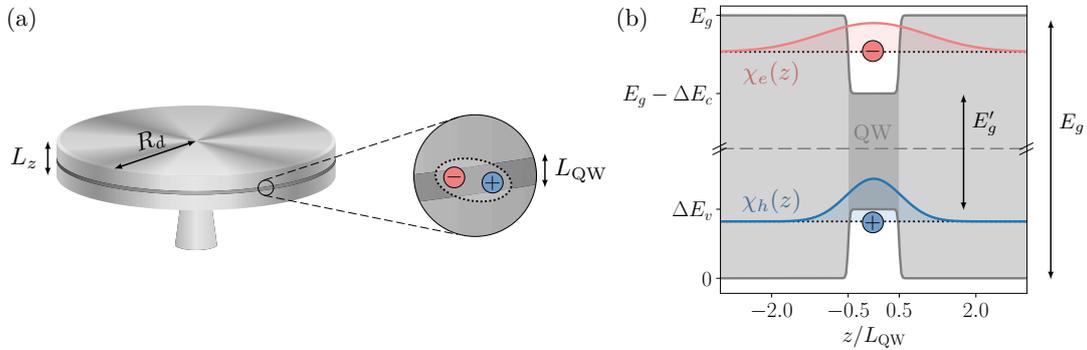
Figure 1.8: (a) Schematic representation of a GaAs hybrid nanodisk resonator embedding a $\text{In}_x\text{Ga}_{1-x}\text{As}$ quantum well. Scales have been adapted for better readability; in practice one typically has $R_d \sim 2\,\mu\text{m}$, $L_z \sim 300\,\text{nm}$ and $L_{\text{QW}} \sim 10\,\text{nm}$. (b) Conduction- and valence-band profiles at the Γ point as a function of the out-of-plane coordinate for a quantum well of thickness $L_{\text{QW}} = 8\,\text{nm}$ and indium fraction $x = 5\,\%$ held at $T = 4\,\text{K}$. First electron and heavy-hole envelopes along the out-of-plane direction are shown at their associated energies, $E_e = 1.499\,\text{eV}$ and $E_h = 28.625\,\text{meV}$, respectively. For these parameters, $E_g = 1.519\,\text{eV}$, $\Delta E_c = 41.750\,\text{meV}$, $\Delta E_v = 34.801\,\text{meV}$, so that $E_g'/E_g \approx 95\,\%$.

Excitons in bulk GaAs

The electronic band structure of bulk GaAs is shown in Fig. 1.7 (a). At proximity of the Γ point ($\boldsymbol{k} = 0$), it exhibits an energy gap of $E_g = 1.519\,\mathrm{eV}$ that opens between the three highest valence bands and the first conduction band. As depicted in Fig. 1.7 (b), close to this point, the material is well described in terms of a parabolic four-band structure. Hence, close to the centre of the Brillouin zone, one has the following quadratic dispersion relations for the conduction and valence bands:

$$E_c(\boldsymbol{k}) \simeq E_g + \frac{\hbar^2 k^2}{2m_c^\star}, \qquad E_{v,i}(\boldsymbol{k}) \simeq -E_{v,i}(\boldsymbol{k}) - \frac{\hbar^2 k^2}{2m_i^\star}. \tag{1.70}$$

Here, $m_c^\star$ denotes the effective mass of the conduction-band electron. The light- (lh) and heavy-hole (hh) bands are degenerate at Γ, that is $E_{v,\mathrm{lh}}(\boldsymbol{0}) = E_{v,\mathrm{hh}}(\boldsymbol{0}) \equiv 0$, but have different effective masses $m_{\mathrm{hh}}^\star > m_{\mathrm{lh}}^\star$. Finally, the split-off (so) band, of angular momentum $J = 1/2$, lies below the two other valence bands, of angular momentum $J = 3/2$, as a consequence of a significant spin-orbit energy splitting ($E_{v,\mathrm{so}} = 341\,\mathrm{meV}$ in bulk GaAs). In what follows the light-hole and split-off bands will be disregarded.

An elementary excitation of this system results from the promotion of one electron from either of the upper valence bands to the conduction band, thereby generating a positively charged hole quasiparticle (h) and a negatively charged electron (e) at either sides of the gap around $\boldsymbol{k} \approx \boldsymbol{0}$. This pair is subject to the attractive Coulomb interaction that mutually couples its oppositely charged components. The resulting two-body problem can be separated as usual into the centre-of-mass and relative-motion single-body ones, yielding the following Hamiltonian

$$\hat{H} = \frac{\hbar^2}{2M}\nabla_{\boldsymbol{R}}^2 + \left\{ E_g + \frac{\hbar^2}{2\mu}\nabla_{\boldsymbol{\rho}}^2 - \frac{1}{2}\frac{hcR^\star}{\rho/a_B} \right\}, \tag{1.71}$$

where $\boldsymbol{R} = \frac{m_e^\star}{M}\boldsymbol{r}_e + \frac{m_h^\star}{M}\boldsymbol{r}_h$ is the position of the centre of mass of the electron-hole pair, of mass $M = m_e^\star + m_h^\star$, and $\boldsymbol{\rho} = \boldsymbol{r}_e - \boldsymbol{r}_h$ is the relative position of the electron, with associated relative mass $\mu = m_e^\star m_h^\star / M$. The first term of this Hamiltonian correspond to the kinetic energy associated to the free motion of the pair within the volume V of the bulk and can thus be solved by introducing plane-wave wave functions with momentum $\boldsymbol{K}$, of the form $V^{-1/2}e^{-i\boldsymbol{K}\cdot\boldsymbol{R}}$. The second term corresponds to the Hamiltonian of a hydrogen-like atom with an effective reduced mass μ, an effective Rydberg constant $hcR^\star = \hbar^2/2\mu a_B^2 = 4.8\,\mathrm{meV}$ and an effective Bohr radius $a_B = 4\pi\epsilon\hbar^2/\mu e^2 = 12\,\mathrm{nm}$. Much in the same way as for the hydrogen-atom problem, this gives rise to bound electron-hole states, as represented in Fig. 1.7 (b), whose energies $E_x^{\mathrm{pot}}(n) = E_g - hcR^\star/n^2$ are quantised by the principal quantum number $n \in \mathbb{N}^\star$ and that spatially confine both particles within a distance of $n^2/2 \times a_B$. These bound states are known as *excitons*. The associated wave functions are nothing more than the usual hydrogen-like atomic orbitals. In what follows, we shall restrict ourselves to the lowest-energy exciton. This is described by the following 1s-exciton wave function:

$$\phi_{\boldsymbol{K}}^{(x)}(\boldsymbol{R}, \boldsymbol{r}) = \frac{2}{\sqrt{Va_B^3}}e^{-i\boldsymbol{K}\cdot\boldsymbol{R}}e^{-2\rho/a_B}. \tag{1.72}$$

Excitons in a quantum well

Let us now briefly describe how the presence of an $\text{In}_x\text{Ga}_{1-x}\text{As}$ quantum well embedded in the disk's GaAs modifies the simple picture sketched above.

InAs has a lower energy gap than that of GaAs. Because of this, the energy gap of the material is locally lowered within the quantum well, as represented in Fig. 1.8 (b). This acts as a confining potential well in the vertical direction for both the electron and the hole. Several consequences derive from this. Firstly, the degeneracy of light- and heavy-holes at the Γ point is lifted and elementary excitations of the material no longer involve the former. Secondly, excitons become partially localised in a two-dimensional domain of thickness $\sim L_{\text{QW}}$ comparable to the exciton Bohr radius. While the two-body problem can still be split into two single-body problems for the centre-of-mass and relative degrees of freedom, the partial vertical confinement breaks the isotropy of the latter, that can thus no longer be solved in terms of hydrogen-like atomic orbitals.

Let us first proceed with the in-plane centre-of-mass degree of freedom. Its wave function must be an eigenstate of the Hamiltonian

$$\hat{H}_{\text{c.o.m}} = \frac{\hbar^2}{2M}\nabla^2_{\boldsymbol{R}_\parallel} + V_{\text{c.o.m}}(\boldsymbol{R}_\parallel) + \text{cst.}, \tag{1.73}$$

where $V_{\text{c.o.m}}(\boldsymbol{R}_\parallel \in \Omega) = 0$ inside of the disk's domain and infinite outside of it. This amounts to solving the same Helmholtz equation as for the electromagnetic field. The exciton's in-plane centre-of-mass motion is thus described by the WGM wave function of the disk's photons:

$$F_{p,\ell}(\boldsymbol{R}_\parallel) \propto J_\ell(k_{p,\ell}R_\parallel)\cos(\ell\theta), \tag{1.74}$$

where we used the same radial and azimuthal quantum numbers p and ℓ as for the photonic wave function.

The remaining (coupled) degrees of freedom are described by the following Hamiltonian:

$$\hat{H}_{\text{rel}} = \frac{\hbar^2}{2m_e^\star}\partial^2_{z_e} + \frac{\hbar^2}{2m_h^\star}\partial^2_{z_h} + \frac{\hbar^2}{2\mu}\nabla^2_{\boldsymbol{\rho}_\parallel} + V_c(z_e) + V_v(z_h) + V_C(\rho), \quad V_C(\rho) = \frac{-hcR^\star a_B}{2\sqrt{\rho_\parallel^2 + (z_e - z_h)^2}}, \tag{1.75}$$

where $V_{v,c}$ are square potentials associated to the shift of the valence and conduction bands in the quantum well, as depicted in Fig. 1.8 (b). This can be dealt with perturbatively by first solving for the vertical dependence of the electron and hole wave functions $\chi_{e,h}(z_{e,h})$, as shown in Fig. 1.8 (b), and then projecting the Coulomb potential on this zeroth-order wave functions to obtain a new effective pseudo-potential $V_C^{\text{eff}}(\rho_\parallel)$ for the in-plane relative distance only [152, 153]. This may be iterated until convergence is reached, leading to a separable wave function for the relative and out-of-plane dependences. As shown in [148], the radial dependence of the lowest bound state's wave function can be very well approximated by a two-dimensional hydrogen-like atomic orbital with a reduced in-plane Bohr radius and a higher binding energy. For a quantum well of thickness $L_{\text{QW}} = 8\,\text{nm}$ and indium fraction $x = 5\,\%$, these are given by $a_B = 8.3\,\text{nm}$ and $hcR^\star = 7.1\,\text{meV}$. One finally has the following 1s-exciton wave function:

$$\phi_{p,\ell}^{(x)}(\boldsymbol{R}, \boldsymbol{\rho}) = F_{p,\ell}(\boldsymbol{R}_\parallel)\phi(\rho_\parallel)\chi_h(z_h)\chi_e(z_e), \tag{1.76}$$

with $\phi(\rho_{\parallel}) \sim \exp(-2\rho_{\parallel}/a_B)$.

In the following, we shall adopt a second quantisation approach. In this framework, the exciton ladder operator $\hat{c}_{p,\ell}^{\dagger}$ is defined such that it acts on the ground state by adding an exciton to the system:

$$\left|\phi_{p,\ell}^{(x)}\right\rangle = \hat{c}_{p,\ell}^{\dagger} \left|\text{GS}\right\rangle. \tag{1.77}$$

In two dimensions, this operator satisfies quasi-bosonic commutation rules $[\hat{c}_{p,\ell}, \hat{c}_{p',\ell'}^{\dagger}] = \delta_{p,p'}\delta_{\ell,\ell'} - O(n_S a_B^2)$ [154, 155], where n_S is the surface exciton density. We will henceforth assume low excitonic densities, $n_S a_B^2 \ll 1$, and therefore treat QW excitons as bosons.

Now that the exciton wave function was identified, the exciton many-body Hamiltonian can be expressed in second quantisation:

$$\hat{H}_x = \hbar\omega_{p,\ell}^{(x)}\hat{c}_{p,\ell}^{\dagger}\hat{c}_{p,\ell} + \hat{V}_{xx}, \tag{1.78}$$

where $\omega_{p,\ell}^{(x)}$ denotes the angular frequency of the 1s excitons. Here, $\hat{V}_{xx}$ accounts for the two-body Coulomb repulsive interactions between distinct excitons. This term was shown to be quartic in bosonic operators and to induce scattering processes between excitonic modes with distinct wave vectors [156, 157]. However, in the limit $a_B \ll 2\pi/k_{p,\ell} \sim R_d$, this simplifies and bears the form a Kerr nonlinearity of strength $U_{p,\ell}$ [158, 159]:

$$\hat{H}_{xx} = \frac{\hbar U_{p,\ell}}{2}\hat{c}_{p,\ell}^{\dagger}\hat{c}_{p,\ell}^{\dagger}\hat{c}_{p,\ell}\hat{c}_{p,\ell}. \tag{1.79}$$

The optoelectronic Hamiltonian

Quantum-well excitons and TE-polarised cavity photons have similar energies. Thanks to their colocalised and strong confinement, these strongly couple in the considered resonator. In second quantisation, the minimal light-matter coupling for this system reads [152, 160]:

$$\hat{H}_{cx} = -\left\langle\text{GS}\middle|e\sum_i \hat{\boldsymbol{A}}(\boldsymbol{r}_i)\cdot\dot{\boldsymbol{r}}_i\middle|\phi_{p,\ell}^{(x)}\right\rangle\hat{c}_{p,\ell} + \text{H.c.}, \tag{1.80}$$

where the sum is carried over all electrons, with positions $\boldsymbol{r}_i$, and the vector potential is that identified in Eq. 1.8, $\hat{\boldsymbol{A}}(\boldsymbol{r}) = \hat{A}_{p,\ell}\phi_{p,\ell}^{(c)}(\boldsymbol{r})\boldsymbol{e}_{\pm}$. Upon neglecting counter-rotating terms and up to a $\pi/2$ rotation of exciton's field, this Hamiltonian reduces to the linear Rabi coupling [158]:

$$\hat{H}_{cx} = \hbar\Omega_{\text{R}}\left(\hat{a}_{p,\ell}^{\dagger}\hat{c}_{p,\ell} + \text{H.c.}\right), \tag{1.81}$$

where $\hbar\Omega_{\text{R}}$ denotes the Rabi energy splitting. Analytical expressions for this coupling for the exact same wave functions can be found in Ref. [92]. In the alloy here considered, this is typically found around $\Omega_{\text{R}} \sim 1\,\text{THz}$.

This modelling process leads to a standard expression for the Hamiltonian of the coupled quantum-well excitons and cavity photons. Neglecting the saturable anharmonic exciton-photon interaction and the self-interaction of the optical field, this reads [159]:

$$\hat{H}/\hbar = \omega_c\hat{a}^{\dagger}\hat{a} + \omega_x\hat{c}^{\dagger}\hat{c} + \Omega_{\text{R}}(\hat{a}^{\dagger}\hat{c} + \hat{c}^{\dagger}\hat{a}) + \frac{U}{2}\hat{c}^{\dagger}\hat{c}^{\dagger}\hat{c}\hat{c}, \tag{1.82}$$

where quantum numbers were dropped and notations were simplified for the cavity and exciton angular frequencies, ω_c and ω_x, respectively.

II.2 Theory of the coupling between quantum-well excitons and resolved phonons

So far, we have described the acoustic, optical and excitonic modes of the hybrid nanodisk resonator as well as the exciton self-interaction, the optoelectronic interaction and the optomechanical interaction. The missing element in this description is the interaction between the resonator's phonons and the quantum-well excitons. As mentioned in the introduction, this is expected to clearly dominate the bare optomechanical coupling from both experimental and numerical evidence. We shall now derive the form of this interaction and closed-form expressions for its strength.

The coupling between excitons and phonons originates from the effect of the mechanical strain of the semiconducting material on its band structure as the result of a local modulation of the lattice constant. As very soon identified [161–165], this induces an energy shift well captured by the deformation potential [166]

$$U(\boldsymbol{r}_e, \mathbf{r}_h) = a_e \Sigma_n(\boldsymbol{r}_e) - a_h \Sigma_n(\boldsymbol{r}_h), \tag{1.83}$$

where $\boldsymbol{r}_e$ and $\boldsymbol{r}_h$ are the positions of the carriers, and a_e and a_h are the values of the electron and hole deformation potentials in the material. In bulk GaAs, $a_e = -7.0\,\mathrm{eV}$ for electrons and $2.7\,\mathrm{eV}$ for holes [167, 168]. $\Sigma_n(\boldsymbol{r}) = \nabla_{\boldsymbol{r}} \cdot \boldsymbol{u}_n(\boldsymbol{r})$ denotes the mechanical strain at $\boldsymbol{r}$ imputable to the presence of a phonon in the mechanical mode n under consideration. Here, $\boldsymbol{u}_n(\boldsymbol{r}) = x_n^{\mathrm{ZPF}} \phi_n^{(m)}(\boldsymbol{r})$ denotes the corresponding displacement, where $x_n^{\mathrm{ZPF}} = \sqrt{\hbar/2M_m\Omega_n}$ is the magnitude of the zero-point fluctuations of the mechanical degree of freedom, of mass M_m and angular frequency Ω_n, and $\phi_n^{(m)}$ its associated wavefunction, normalised to $\int_V \mathrm{d}\boldsymbol{r}|\phi_n^{(m)}(\boldsymbol{r})|^2 = V$, as given by Eq. (1.21) for RBMs. We now dispose of all the necessary quantities to express this Hamiltonian for some given excitonic and mechanical modes of quantum numbers $\lambda = (p, \ell)$ and n, respectively. The second quantisation prescription yields a parametric coupling of the optomechanical form [166, 169]:

$$\hat{H}_{xm} = -\hbar g_{xm}^{\lambda,n} \hat{b}_\lambda^\dagger \hat{b}_\lambda \hat{c}_n + \mathrm{H.c.}, \tag{1.84}$$

with the exciton-phonon coupling factor:

$$-\hbar g_{xm}^{\lambda,n} := \left\langle 0, \phi_\lambda^{(x)} \middle| \hat{U} \middle| \phi_n^{(m)}, \phi_\lambda^{(x)} \right\rangle = \int_V \mathrm{d}\boldsymbol{r}_e \mathrm{d}\boldsymbol{r}_h \phi_\lambda^{(x)\star}(\boldsymbol{r}_e, \boldsymbol{r}_h) U(\boldsymbol{r}_e, \mathbf{r}_h) \phi_\lambda^{(x)}(\boldsymbol{r}_e, \boldsymbol{r}_h)$$

$$= \int \mathrm{d}\boldsymbol{R}_\parallel \mathrm{d}\boldsymbol{\rho}_\parallel \mathrm{d}z |F_\lambda(\boldsymbol{R}_\parallel)|^2 |\phi(\boldsymbol{\rho}_\parallel)|^2 \Big(a_e \Sigma_n(\boldsymbol{R}_\parallel + \tfrac{m_h}{M}\boldsymbol{\rho}_\parallel + z\boldsymbol{e}_z)|\chi_e(z)|^2 \tag{1.85}$$

$$- a_h \Sigma_n(\boldsymbol{R}_\parallel + \tfrac{m_e}{M}\boldsymbol{\rho}_\parallel + z\boldsymbol{e}_z)|\chi_h(z)|^2 \Big).$$

This expression can be greatly simplified by neglecting the exciton's Bohr radius over the mechanical in-plane wavelength, as already considered on writing Eq. (1.82), and the thickness of the quantum well $L_{\mathrm{QW}} \lesssim 10\,\mathrm{nm}$ over the typical out-of-plane variations of the strain, none for an ideal RBM. Indeed, within these approximations, the exciton-phonon coupling reduces to solely the overlap between the exciton's envelope and the single-phonon strain at the location of the well:

$$\hbar g_{xm}^{\lambda,n} \simeq (a_h - a_e) \int_S \mathrm{d}\boldsymbol{R}_\parallel |F_\lambda(\boldsymbol{R}_\parallel)|^2 \Sigma_n(\boldsymbol{R}_\parallel, z_{\mathrm{QW}}). \tag{1.86}$$
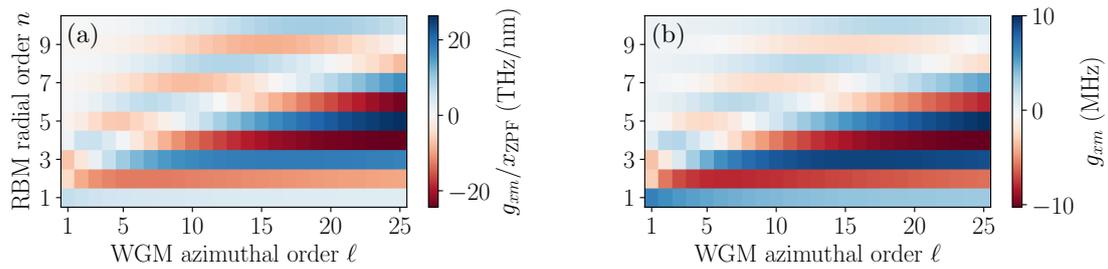
Figure 1.9: Electromechanical coupling in units of x_n^{ZPF} (panel (a)) and frequency units (panel (b)) for a disk of radius $R_d = 1\,\mu\mathrm{m}$ and thickness $L_z = 320\,\mathrm{nm}$ bearing a mechanical radial breathing mode of order n and an excitonic whispering gallery mode of order $(p, \ell) = (1, \ell)$.

Here, the in-plane exciton mode amplitude $F_\lambda(\boldsymbol{R})$ exactly corresponds to the WGM's, given in Eq. (1.6). The single-phonon mechanical strain Σ_n can be easily obtained from the phonon wave function of Eq. (1.21) as $\Sigma_n(R) = (1/R_\parallel)\partial_{R_\parallel}[R_\parallel]\phi_n^{(m)}(R_\parallel) = K_n x_n^{\mathrm{ZPF}}\mathcal{N}_n J_0(K_n R_\parallel)$. Thus, for the disk, one finally has:

$$\hbar g_{xm}^{p,\ell;n} \simeq (a_h - a_e)\frac{x_n^{\mathrm{ZPF}}}{R_d}\mathcal{I}_{p,\ell;n}, \quad \mathcal{I}_{p,\ell;n} := \frac{2K_n R_d \mathcal{N}_n}{J_{\ell+1}^2(\alpha_{\ell,p})}\int_0^1 \mathrm{d}\xi\,\xi J_\ell^2(\alpha_{\ell,p}\xi) J_0(K_n R_d \xi), \quad (1.87)$$

where the relative deformation potential $(a_e - a_h)$ can be measured directly by applying hydrostatic pressure on the material [167], x_n^{ZPF}/R_d quantifies the deformation of the disk induced by the zero-point fluctuations and $\mathcal{I}_{p,\ell;n}$ is a dimensionless geometric overlap integral between the exciton distribution and the strain field. Note that the latter does not depend on the radius of the disk, as $K_n R_d$ only depends on the Poisson ratio of the material (see Table 1.1 for GaAs). Much in the same way as for the optomechanical coupling, the ratio $\hbar g_{xm}^{p,\ell;n}/x_n^{\mathrm{ZPF}}$ gives a good characterisation of the coupling strength that is independent from the resonator's mass and angular frequency. This is found inversely proportional to the radius of the disk, as for the geometric contribution to the disk's optomechanical coupling [106]. The linear dependence of its strength on the zero-point deformation of the resonator is also very reminiscent of the radiation-pressure interaction of the Fabry-Pérot cavity discussed in Subsec. I.4, whose rate was shown to be indeed proportional to the relative displacement of its bounding mirror: $g_{cm} = \omega_c x^{\mathrm{ZPF}}/L$.

The value of the electromechanical coupling is reported in Fig. 1.9 for various pairs of excitonic and mechanical modes. The geometry of the disk is chosen as in Ref. [105]. The electromechanical coupling is here found one order of magnitude higher than that computed therein for the bare photoelastic and geometric contributions to the optomechanical coupling. In semiconducting nanoring resonators [170, 171] (see App. A for their mode description) and micropillars [172] embedding a quantum well, where the overlap between the strain field and quantum-well excitons is close to optimal, this improvement could be of two orders of magnitude, as calculations not shown here suggest [ζ]. As shown in Fig. 1.9, the electromechanical coupling presents an interesting dependence on the radial order n of the mechanical RBM. Indeed, the coupling of even RBMs has opposite sign with respect to the optomechanical one. For mechanical wave vectors too large with respect to the WGM's, the strain exhibits oscillations within the support of the WGM. The

effect of the strain on the exciton energy is thus averaged out, resulting into vanishingly small coupling factors.

II.3   Effective polaritonic description

In the rotating frame, the Hamiltonian of the entire tripartite system finally reads:

$$\hat{H}/\hbar = \omega_c \hat{a}^\dagger \hat{a} + \omega_x \hat{c}^\dagger \hat{c} + \Omega_\mathrm{R}(\hat{a}^\dagger \hat{c} + \hat{c}^\dagger \hat{a}) + \Omega_m \hat{b}^\dagger \hat{b}$$
$$+ \frac{U}{2}\hat{c}^{\dagger 2}\hat{c}^2 - g_{cm}\hat{a}^\dagger \hat{a}(\hat{b} + \hat{b}^\dagger) - g_{xm}\hat{c}^\dagger \hat{c}(\hat{b} + \hat{b}^\dagger). \tag{1.88}$$

where ω_c, ω_x and Ω_m are the cavity, exciton and mechanical angular frequencies, respectively, Ω_R the Rabi splitting, g_{cm} and g_{xm} the bare optomechanical and electromechanical coupling rates, and U the exciton-exciton Kerr nonlinearity. The single-body part of the optoelectronic Hamiltonian (first line) can be readily diagonalised in terms of two bosonic fields:

$$\hat{H}_1/\hbar = \omega_- \hat{p}_-^\dagger \hat{p}_- + \omega_+ \hat{p}_+^\dagger \hat{p}_+. \tag{1.89}$$

These normal quasimodes are hybrid exciton-photon excitations known as *polaritons*. These split into two branches: the lower (LP) and upper (UP) polariton branches whose energies split with the optoelectronic interaction according to:

$$\omega_\pm = \frac{\omega_c + \omega_x}{2} \pm \sqrt{\left(\frac{\omega_c - \omega_x}{2}\right)^2 + \Omega_\mathrm{R}^2}. \tag{1.90}$$

These polariton operators can be expressed in terms of the original exciton and photon operators by means of the following unitary transformation:

$$\begin{bmatrix} \hat{p}_- \\ \hat{p}_+ \end{bmatrix} = \begin{bmatrix} X & C \\ -C & X \end{bmatrix} \begin{bmatrix} \hat{c} \\ \hat{a} \end{bmatrix}, \quad X = 1/\sqrt{1 + \left(\frac{\Omega_\mathrm{R}}{\omega_- - \omega_c}\right)^2}, \quad C = -1/\sqrt{1 + \left(\frac{\omega_- - \omega_c}{\Omega_\mathrm{R}}\right)^2}. \tag{1.91}$$

Here, X^2 and $C^2 \equiv 1 - X^2$ respectively correspond to the exciton and cavity fractions of the lower polariton, and reciprocally for the upper polariton. The avoided crossing of Eq. (1.90) is shown in Fig. 1.10. At $\omega_x = \omega_c$, both polaritons are exactly half-exciton half-photon and split in energy by $\omega_+ - \omega_- = 2\Omega_\mathrm{R}$; out of resonance, they recover their purity.

We shall now express the hybrid disk Hamiltonian in this natural basis. Two distinct cases are to be considered.

Polariton transition resonant with the phonon energy

For very low values of the Rabi splitting, the transition between the upper and lower polariton branches might become resonant with the angular frequency of the mechanical oscillator: $2\Omega_\mathrm{R} \sim \Omega_m$. In this scenario and within the rotating-wave-approximation, the hybrid disk Hamiltonian reads:

$$\hat{H}/\hbar = \sum_\pm \left(\omega_\pm \hat{p}_\pm^\dagger \hat{p}_\pm + \frac{U_\pm}{2}\hat{p}_\pm^{\dagger 2}\hat{p}_\pm^2\right) - \frac{K}{2}\hat{p}_+^\dagger \hat{p}_+ \hat{p}_-^\dagger \hat{p}_- + \Omega_m \hat{b}^\dagger \hat{b} + g_\mathrm{twm}(\hat{p}_-^\dagger \hat{p}_+ \hat{b}^\dagger + \mathrm{H.c.}). \tag{1.92}$$
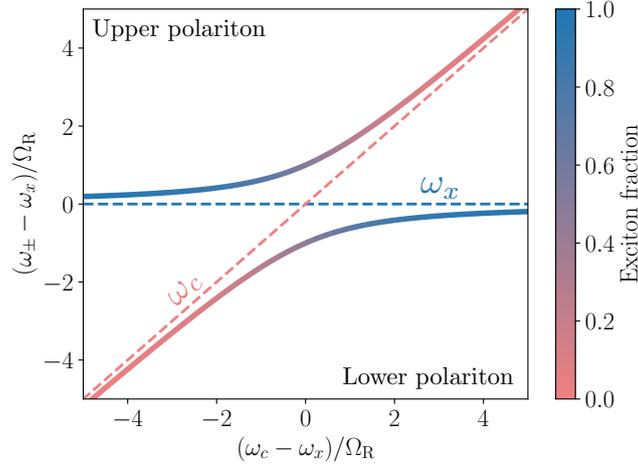
Figure 1.10: Upper and lower polariton angular frequencies as a functions of the frequency mismatch between the cavity photons and the quantum-well excitons. At $\omega_c \approx \omega_x$, the spectrum exhibits an avoided crossing due to the optoelectronic interaction that separates the two branches by twice the Rabi splitting Ω_R.

Here, $U_+ = X^4 U$ and $U_- = C^4 U$ correspond to Kerr nonlinearities, each polariton mode inherits the exciton repulsive interactions in proportion to its exciton fraction. $K = 4XC$ is a cross-Kerr interaction between the two polariton branches. Finally, the resulting effective polariton-phonon interaction is a three-wave mixing term of strength $g_{\mathrm{twm}} = |XC|(g_{xm} - g_{cm})$ that allows for upper polaritons to be down-converted to the lower mode by emitting one phonon in the mechanical resonator. This is of the form of the Hamiltonian (Eq. (1.65)) of the model for phonon lasing proposed in Subsec. I.5. However, this is a rather unnatural situation as the Rabi splitting is typically in the terahertz range while the disk's mechanical frequency lies around the gigahertz.

Quasiresonant driving of a polariton mode

The most experimentally relevant regime corresponds to a single polariton mode σ under quasiresonant driving by some external coherent pump in the band $\omega_p \sim \omega_\sigma \pm \Omega_m$. In this situation, the hybrid disk Hamiltonian reads:

$$\hat{H}/\hbar = \omega_\sigma \hat{p}_\sigma^\dagger \hat{p}_\sigma + \frac{U_\sigma}{2} \hat{p}_\sigma^{\dagger 2} \hat{p}_\sigma^2 + \Omega_m \hat{b}^\dagger \hat{b} - g_{pm} \hat{p}_\sigma^\dagger \hat{p}_\sigma (\hat{b}^\dagger + \hat{b}). \qquad (1.93)$$

Up to the Kerr nonlinearity, this amounts to the usual optomechanical Hamiltonian where the considered polariton mode acts as the optical field with an enhanced interaction strength:

$$g_{pm} = \begin{cases} X^2 g_{xm} + C^2 g_{cm}, & \sigma = - \quad \text{(lower polariton)} \\ C^2 g_{xm} + X^2 g_{cm}, & \sigma = + \quad \text{(upper polariton)} \end{cases}. \qquad (1.94)$$

This expression can be easily understood, the electromechanical and optomechanical inter-action strengths are weighted by the exciton and photon fractions in either polariton mode.

This yields an effective *polariton-mechanical* parametric interaction; the phenomenology of the system can thus to a great extent be understood as an optomechanical model where now polaritons play the role of the usual photons and the bare optomechanical coupling is enhanced by the presence of excitons coupling to the mechanics through the deformation potential. This picture well agrees with the interpretation of the early experiments [141–144].

The enhancement factor by which the single-photon cooperativity of the disk is increased due to the presence of the quantum well reads, for the lower polariton:

$$\frac{C_0^{pm}}{C_0^{om}} = \frac{(X^2 \frac{g_{xm}}{g_{cm}} + C^2)^2}{X^2 \frac{\gamma_x}{\kappa} + C^2}, \tag{1.95}$$

where γ_x denotes the exciton linewidth. For a mechanical quality factor of $Q_m = 10^5$ ($\Omega_m = 1.6\,\mathrm{GHz}$), a poor exciton linewidth of $\gamma_x = 200\,\mathrm{GHz}$, an optical linewidth of $\kappa = 60\,\mathrm{GHz}$, parametric couplings of strength $g_{xm} = 10\,\mathrm{MHz}$ and $g_{om} = 1\,\mathrm{MHz}$, and an exciton fraction of $X^2 = 35\,\%$, the enhancement is of exactly one order of magnitude. Calculations to be soon submitted [ζ] show that the single-polariton cooperativity could exceed unity in micropillar optomechanical resonators [172].

III   Conclusion

In this chapter, we derived from first principles the master equation describing an optomechanical nanodisk resonator. We discussed some of the phenomenology induced by scattering processes occurring at the mechanical sidebands, both by addressing the standard sideband cooling mechanism and a more elaborated model for mechanical lasing.

A hybrid semiconducting nanodisk resonator embedding a quantum well was then introduced and given a quantum description. In particular, an analytical expression for the coupling between the quantum-well excitons and the resolved phonons of the disk was derived. This tripartite resonator, comprising mutually coupled modes of both light, matter and acoustic nature, was then shown to be describable as an effective optomechanical system with exciton polaritons playing the role of photons in standard cavity optomechanics with an enhanced parametric coupling, in qualitative agreement with experimental observations [141–145] and *ab initio* numerical simulations [146].

Several interesting points remain to be addressed. In order to determine the maximal enhancement of the parametric interaction in hybrid nanodisk resonators, a comprehensive optimisation of the parameters of the disk and the orders of the relevant modes is yet necessary. Calculations suggest that annular disks/rings [170, 171] and micropillars [172] present very high degrees of spatial confinement of the strain and the quantum-well excitons that could lead to cooperativities above unity for moderately high exciton fraction [ζ]. These will soon be submitted for publication. Finally, the inhomogeneous broadening of the exciton's linewidth can pose severe limitations on the exciton fraction that can be practically reached without strongly reducing the polaritonic quality factor. These detrimental effects should also be investigated in order to explore the limits of the increase in cooperativity here reported.

The original results of this chapter are contained in Ref. [ζ].

2 Dynamics induced by extended reservoirs

The present chapter is devoted to the theoretical study of the dynamics induced by spatially extended correlated reservoirs.

When discussing the sideband-cooling mechanism in Subsec. I.5 of the first chapter, we saw how a driven-dissipative optical mode treated as a reservoir could induce a sensitive change in the dynamics of the mechanical mode of interest. In this situation, we identified particular resonance conditions between *local* mechanical energies and *local* optical transition energies upon which one could precisely control the dynamics of the mechanical motion. We later extended this picture to the treatment of a system composed of three interacting modes and identified that, by properly tuning the transition energy between antibonding and bonding collective modes to that of the mechanical element, *nonlocal* scattering events could be exploited in order to induce a lasing phase transition in which an initially thermal mechanical oscillator would start to exhibit coherent oscillations and Poissonian statistics.

We shall now address a slightly more complex situation where a set of local modes of interest, our *system*, is put in local contact with a spatially extended *reservoir*. This is illustrated in Fig. 2.1, where a set of local system modes is either in contact with a lattice of interacting reservoir modes or immersed into some continuous field. Much in the same way as before, the effective dynamics of the system will be driven by scattering of local excitations of the system through the reservoir. The novelty here stems from the possibility for a local excitation to be transduced into a reservoir fluctuation quantum, scatter away from its initial position within the reservoir's typical relaxation time, and finally re-enter back into the system at another site.

This situation raises a number of fundamental conceptual issues. Firstly, on the possibility of engineering a reservoir-mediated coupling between distant and initially mutually independent resonators. Secondly, on the role of a new parameter, the spatial correlation length of the reservoir, in the effective dynamics induced on the system. Finally, whether the time-irreversible nature of the Stokes and anti-Stokes scattering events translates into a breaking of the spatial reversibility, that may generate reservoir-mediated directional currents flowing between distant system modes. These, and in particular the link between time and spatial irreversibility, will be the main subject of Chapter 3. The numerical treatment of such spatially extended reservoirs will be addressed in Chapter 4.

This chapter is organised as follows. In Sec. I, spatially extended reservoirs will be first introduced and their associated effective master equation will be derived in a general driven-dissipative setting, both in the discrete and the continuous cases. The general res-

ults of this section will then be translated to the quantum-Langevin-equation framework in Sec. II.
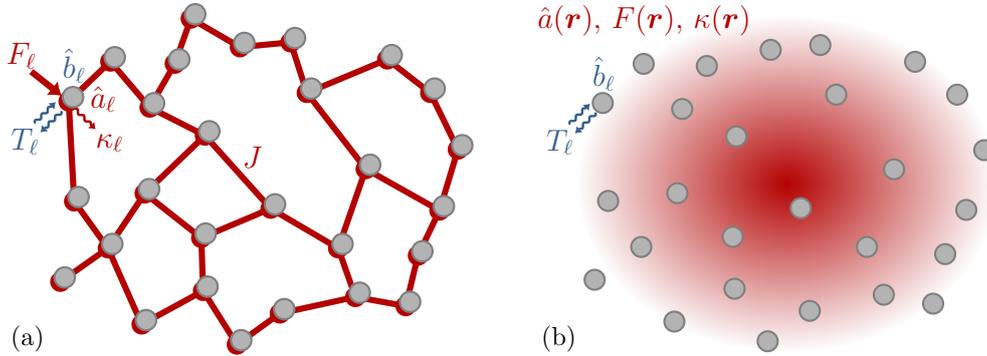
Figure 2.1: Schematic illustration of a set of system modes in contact with either a discrete or a continuous driven-dissipative extended reservoir. (a) Discrete case: the reservoir (in red) is described as a discrete set of bosonic operators $\hat{a}_\ell$ colocalised with the system's modes (in grey) and arranged into some arbitrary lattice geometry. (b) Continuous case: the reservoir (in red) is described by some continuous delocalised bosonic mode $\hat{a}(\mathbf{r})$. The system's modes are in local contact with the reservoir.

I   Adiabatic elimination of a generic extended reservoir

Let us consider a bipartite configuration where a set of local modes of interest, henceforth referred to as *system*, is in local contact with a spatially extended *reservoir*, as illustrated in Fig. 2.1. The reservoir and system ensemble can be described by a Lindblad master equation of the form[1]

$$\partial_t \hat{\rho}_{\mathrm{RS}} = -i[\hat{H}_{\mathrm{R}} + \hat{H}_{\mathrm{S}} + \hat{H}_{\mathrm{I}}, \hat{\rho}_{\mathrm{RS}}] + \mathcal{D}_{\mathrm{R}}\hat{\rho}_{\mathrm{RS}} + \mathcal{D}_{\mathrm{S}}\hat{\rho}_{\mathrm{RS}}, \qquad (2.1)$$

where $\hat{\rho}_{\mathrm{RS}}$ is the density matrix of the ensemble, $\hat{H}_{\mathrm{R(S)}}$ the reservoir (system) Hamiltonian, $\mathcal{D}_{\mathrm{R(S)}}$ the reservoir (system) dissipators, and $\hat{H}_{\mathrm{I}}$ a local coupling Hamiltonian.

The discrete and continuous cases can be worked out similarly. In the following we will treat in detail the case of a discrete extended reservoir and then briefly address how the result generalises to the continuum.

I.1   Discrete extended reservoirs

We shall restrict our discussion to reservoirs that are subject to single-body loss and single-body external harmonic driving, a situation relevant for photonic applications. In

---

[1]From now on, we switch to natural units, such that $\hbar = c_0 = k_{\mathrm{B}} = G = 1$.

the rotating frame, this can be described by the following Hamiltonian and dissipator

$$\hat{H}_{\mathrm{R}} = \hat{H}_{\mathrm{R}}^{(0)} + \sum_i (F_i^\star \hat{a}_i + F_i \hat{a}_i^\dagger), \quad \mathcal{D}_{\mathrm{R}} \hat{\rho}_{\mathrm{R}} = \sum_i \kappa_i \mathcal{D}[\hat{a}_i] \hat{\rho}_{\mathrm{R}}, \tag{2.2}$$

where $\hat{H}_{\mathrm{R}}^{(0)} \equiv H_{\mathrm{R}}^{(0)}[\hat{\boldsymbol{a}}, \hat{\boldsymbol{a}}^\dagger]$ denotes the reservoir's Hamiltonian in the absence of driving, parametrised by the set of reservoir-mode bosonic operators $\{\hat{a}_i\}_i$, and where F_i and $\kappa_i > 0$ are the driving and dissipation strengths at site i, respectively. Without loss of generality we will assume the operators $\hat{H}_{\mathrm{R}}^{(0)}$ and $\hat{R}$ to be expressed as normally ordered products of bosonic operators [173, 174], that is, where all annihilation operators are placed on the right and all creation operators on the left.

In order to be able to perform the elimination of the reservoir's degrees of freedom, one needs to ensure that it behaves as a purely dissipative system. Indeed, the crucial Markovian approximation the following derivation relies upon requires the reservoir correlation functions to decay to zero fast enough. We shall therefore express the reservoir's master equation in terms of suitable fluctuation operators whose correlation functions decay at the relaxation rate κ. To do so we introduce the following unitary transformation $\hat{U} = \prod_i \hat{D}(\alpha_i)^\dagger$, with the usual displacement operator $\hat{D}(\alpha_i) = \exp(\alpha_i \hat{a}_i^\dagger - \alpha_i^\star \hat{a}_i)$. This transformation operates a shift of the phase-space coordinates of the reservoir. In terms of the transformed coordinates, the Hamiltonian admits the following second-order truncated Taylor expansion:

$$\hat{H}_{\mathrm{R}} \approx E_0 + \sum_i \left\{ \left(F_i - i\alpha_i \kappa_i/2 + \partial_{\alpha_i^\star} H_{\mathrm{R}}^{(0)}[\boldsymbol{\alpha}, \boldsymbol{\alpha}^\star] \right) \hat{a}_i^\dagger + \mathrm{H.c.} \right\} + \frac{1}{2} \hat{\boldsymbol{A}}^\dagger \mathbf{H} \hat{\boldsymbol{A}}, \tag{2.3}$$

where $\hat{\boldsymbol{A}} = (\hat{a}_1, \ldots, \hat{a}_1^\dagger, \ldots)^T$, $\hat{\boldsymbol{A}}^\dagger = (\hat{a}_1^\dagger, \ldots, \hat{a}_1, \ldots)$, and $\mathbf{H}$ is the following (Hermitian) Hessian matrix:

$$\mathbf{H} = \begin{bmatrix} \mathrm{H}^{(\mathrm{I})} & \mathrm{H}^{(\mathrm{II})} \\ \mathrm{H}^{(\mathrm{II})\star} & \mathrm{H}^{(\mathrm{I})T} \end{bmatrix}, \quad H_{ij}^{(\mathrm{I})} = \frac{1}{2} \partial_{\alpha_i^\star} \partial_{\alpha_j} H_{\mathrm{R}}^{(0)}[\boldsymbol{\alpha}, \boldsymbol{\alpha}^\star], \quad H_{ij}^{(\mathrm{II})} = \partial_{\alpha_i^\star} \partial_{\alpha_j^\star} H_{\mathrm{R}}^{(0)}[\boldsymbol{\alpha}, \boldsymbol{\alpha}^\star]. \tag{2.4}$$

Let us note that in the case of a quadratic Hamiltonian, the expansion in Eq. (2.3) introduces no approximation. By choosing the parameters of the shift to correspond to some stable solution $\tilde{\boldsymbol{\alpha}}$ of the eventually nonlinear equation

$$F_i - i\tilde{\alpha}_i \kappa_i/2 + \partial_{\tilde{\alpha}_i^\star} H_{\mathrm{R}}^{(0)}[\tilde{\boldsymbol{\alpha}}, \tilde{\boldsymbol{\alpha}}^\star] = 0, \tag{2.5}$$

the reservoir becomes described, to second order in the fluctuation operators, by simply:

$$\hat{H}_{\mathrm{R}} = \frac{1}{2} \hat{\boldsymbol{A}}^\dagger \mathbf{H} \hat{\boldsymbol{A}}, \quad \mathcal{D}_{\mathrm{R}} \hat{\rho}_{\mathrm{R}} = \sum_i \kappa_i \mathcal{D}[\hat{a}_i] \hat{\rho}_{\mathrm{R}}, \tag{2.6}$$

where all linear driving terms exactly cancelled, leaving only dissipation.

Let us analyse this result. The steady-state solution of Eq. (2.6) is simply the vacuum $|0, 0, \ldots\rangle$. Indeed, all linear terms responsible for the driving of the reservoir disappeared from the Hamiltonian, making the master equation purely dissipative (notice $\mathbf{H} = \mathbf{H}^\dagger$). In the original frame, the steady state thus reads $\hat{U} |0, 0, \ldots\rangle = |\tilde{\alpha}_1, \tilde{\alpha}_2, \ldots\rangle$, where $|\alpha\rangle$ denotes a coherent state [175], that is, the solution of Eq. (2.5) corresponds to the mean-field

steady-state solution of the original master equation (2.2). In the displaced frame, operators $\hat{a}_i$ and $\hat{a}_i^\dagger$ thus correspond to the annihilation or creation of a fluctuation quantum on top of the coherent solution we just identified. Then, Eq. (2.6) describes the decay of any quantum fluctuation that enters the reservoir. Due to the simple form of the fluctuation's master equation, one may now solve it for any correlation function. In particular, all normally ordered reservoir operators and correlation functions decay to 0 in time; one can proceed further with the adiabatic elimination of the lattice reservoir.

So far we did not yet consider the presence of the system of interest. It couples to the reservoir through the interaction Hamiltonian, which may be written, without loss of generality, as $\hat{H}_\mathrm{I} = \lambda \sum_i \hat{R}_i \otimes \hat{S}_i$, where $\lambda \ll 1$ is a dimensionless scale "bookmark" and where $\hat{R}_i$ and $\hat{S}_i$ are operators acting at site i on the reservoir and the system Hilbert spaces, respectively. Here, $\hat{R}_i$ has the dimension of a frequency. Then, assuming that the reservoir and the system remain separable at any time (Born approximation), one arrives to an expression very similar to Eq. (1.36) for the reduced dynamics of the system [α, Supplemental Material]:

$$\partial_t \hat{\rho}_\mathrm{S}(t) = \mathcal{L}_\mathrm{S} \hat{\rho}_\mathrm{S}(t) - \lambda^2 \sum_{ij} \int_0^{t-t_0} \mathrm{d}\tau \Big\{ \mathcal{G}_{ij}(\tau) \Big[\hat{S}_i, e^{\mathcal{L}_S \tau} \big(\hat{S}_j \hat{\rho}_\mathrm{S}(t-\tau) \big) \Big] + \mathrm{H.c.} \Big\}, \qquad (2.7)$$

where we assumed for simplicity that $\langle \hat{H}_\mathrm{I} \rangle (t \to +\infty) = 0$. The superoperator $\mathcal{L}_\mathrm{S}$ here denotes the system's Liouvillian: $\mathcal{L}_\mathrm{S} \hat{\rho} = -i[\hat{H}_\mathrm{S}, \hat{\rho}] + \mathcal{D}_\mathrm{S} \hat{\rho}$. The reservoir's correlation function $\mathcal{G}$ is now given, in the displaced frame, by

$$\mathcal{G}(\tau) = \langle \hat{R}_i(t) \hat{R}_j(t-\tau) \rangle = \langle \hat{R}_i(\tau) \hat{R}_j(0) \rangle = \langle \mathbf{0} | \hat{R}_i(\tau) \hat{R}_j(0) | \mathbf{0} \rangle, \qquad (2.8)$$

where we used the time-translational invariance of the equilibrium state of the reservoir, under the assumption of no significant backaction of the system on the stabilised reservoir.

The system operators may be decomposed as $\hat{S}_i = \sum_\alpha \hat{s}_i(\omega_\alpha)$ in terms of eigenoperators of the dissipativeless system adjoint Liouvillian $i[\hat{H}_\mathrm{S}, \hat{s}_i(\omega_\alpha)] = -i\omega_\alpha \hat{s}_i(\omega_\alpha)$, where the eigenvalues $\{\omega_\alpha\}_\alpha$ correspond to all the possible transition energies between eigenstates of the system Hamiltonian. $\hat{s}_i(\omega_\alpha > 0)$ acts as a generalised lowering operator that induces a transition from some excited state to some other state lower in energy by ω_α. Conversely, $\hat{s}_i(\omega_\alpha < 0)$ corresponds to a generalised raising operator that increases the system's ernergy by an amount of ω_α. The interpretation of the action of the reservoir on the system then becomes very clear, as illustrated in Fig. 2.2. The correlation function $\mathcal{G}$ is a memory kernel that decays roughly after $\tau_R \sim 1/\kappa$, acting as a cutoff for the time integral. The term $\hat{S}_j \hat{\rho}_\mathrm{S}(t-\tau)$ corresponds to a scattering event happening at time $t - \tau$ in the recent past where the system operator $\hat{S}_j$ acts locally at site j by inducing some transition of energy ω_α. This corresponds to the simultaneous action of $\hat{R}_j$ on the reservoir at this same location, as expressed by the first half of its correlation function $\hat{R}_j(t-\tau) | \mathbf{0} \rangle$. Both the perturbed reservoir and system are then evolved for a time τ and a similar scattering event takes place at present time t at some eventually different site i, corresponding to the operator $\hat{S}_i$ in the commutator and to $\langle \mathbf{0} | \hat{R}_i(t+\tau)$ in the correlator. The master equation therefore amounts to the sum of all such processes happening within the reservoir's typical relaxation time $\tau \lesssim \tau_R$.
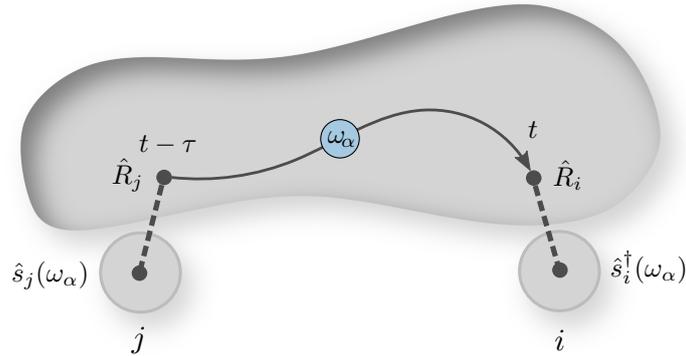
Figure 2.2: Schematic representation of the leading scattering processes involved in the master equation (2.7). At time $t - \tau$, an excitation of energy ω_α is absorbed into the reservoir at site j under the action of the interaction Hamiltonian, thereby inducing a transition between two system energy levels $\omega_i \to \omega_f$ such that $\omega_f - \omega_i = -\omega_\alpha$. The excitation propagates through the reservoir and is either dissipated or scattered back into the system at site j at some later time t. The former is responsible for dissipation whereas the latter preserves the energy of the system and yields a nonlocal Lamb shift.

We shall now assume the reservoir fluctuations to decay much faster than the typical relaxation of the system (Markovian approximation) and, for consistency, that the system was weakly coupled to its own local environment[2] so that $\lambda^2 \exp(\mathcal{L}_S \tau_R)\hat{\rho}_S \approx \lambda^2 \exp(-i\mathcal{K}[\hat{H}_S]\tau_R)\hat{\rho}_S$, where $\mathcal{K}[\hat{H}]\hat{\rho} := [\hat{H}, \hat{\rho}]$. Within this second approximation, one gets

$$\partial_t \hat{\rho}_S(t) = -i\left[\hat{H}_S, \hat{\rho}_S(t)\right] - \lambda^2 \sum_{ij} \int_{\mathbb{R}_+} d\tau \left\{ \mathcal{G}_{ij}(\tau)\left[\hat{S}_i, e^{-i\hat{H}_S\tau}\hat{S}_j e^{+i\hat{H}_S\tau}\hat{\rho}_S(t)\right)\right] + \text{H.c.}\right\}. \quad (2.9)$$

By now using the decomposition $\hat{S}_i = \sum_\alpha \hat{s}_i(\omega_\alpha)$ and performing the secular approximation introduced in Sec. I.3, one finally gets

$$\partial_t \hat{\rho}_S(t) = -i\left[\hat{H}_S, \hat{\rho}_S(t)\right] - \sum_{i,j,\alpha} \left\{ S_{ij}^{(\alpha)}\left[\hat{s}_i^\dagger(\omega_\alpha), [\hat{s}_j(\omega_\alpha)\hat{\rho}_S(t)]\right] + \text{H.c.}\right\}, \quad (2.10)$$

with the two-point reservoir spectrum $S_{ij}^{(\alpha)} := S_{ij}(\omega_\alpha) = \lambda^2 \int_{\mathbb{R}_+} \mathcal{G}_{ij}(\tau)e^{i\omega_\alpha\tau}$. Contrary to the local-reservoir case, its Lindblad form is not yet explicit at this point. This can be achieved by identifying the Hermitian and anti-Hermitian components of the reservoir spectrum at ω_α: $\frac{1}{2}\boldsymbol{\Gamma}^{(\alpha)} = (\mathbf{S}^{(\alpha)} + \mathbf{S}^{(\alpha)\dagger})/2$ and $\boldsymbol{\Omega}^{(\alpha)} = (\mathbf{S}^{(\alpha)} - \mathbf{S}^{(\alpha)\dagger})/2i$, respectively. The final dissipation rates follow from the diagonalisation of the former, as given by

$$\text{diag}(\Gamma_1^{(\alpha)}, \Gamma_2^{(\alpha)}, \ldots) = \mathbf{U}^{(\alpha)}\boldsymbol{\Gamma}^{(\alpha)}\mathbf{U}^{(\alpha)\dagger}, \quad (2.11)$$

---

[2]This condition may be relaxed by expanding the system operators in the eigenbasis of the system's full adjoint Liouvillian $\mathcal{L}_S^\dagger$ instead of solely $i\mathcal{K}[\hat{H}_S]$, where $\mathcal{K}[\hat{H}]\hat{\rho} := [\hat{H}, \hat{\rho}]$.

where $\mathbf{U}^{(\alpha)}$ is the diagonalising unitary matrix; the Lamb shift directly follows from the latter. Finally, Eq. (2.10) simply becomes:

$$\partial_t \hat{\rho}_\mathrm{S}(t) = -i\Big[\hat{H}_\mathrm{S} + \textstyle\sum_{ij\alpha}\Omega_{ij}^{(\alpha)}\hat{s}_i^\dagger(\omega_\alpha)\hat{s}_j(\omega_\alpha), \hat{\rho}_\mathrm{S}(t)\Big] + \sum_{k,\alpha}\Gamma_k^{(\alpha)}\mathcal{D}[\textstyle\sum_j U_{kj}^{(\alpha)}\hat{s}_j(\omega_\alpha)]\hat{\rho}_\mathrm{S}(t). \quad (2.12)$$

The effective dynamics induced by a generic lattice reservoir is therefore completely determined by the spectral matrix $\mathbf{S}^{(\alpha)}(\omega)$ evaluated at the angular frequencies of the system's transitions. This quantity depends solely on the correlation function (2.8), which can be easily computed exactly for any choice of reservoir operator $\hat{R}_i$ in the interaction Hamiltonian, thanks to the state of the reservoir being Gaussian and to the quantum regression theorem [99, 176–178]. Furthermore, one may note that, to second order in the fluctuations, the only terms in the expansion of $\hat{R}_i$ whose correlation functions are not strictly equal to zero are those of zeroth and first order in reservoir fluctuation operators. The most generic non-trivial coupling operator is thus of the form $\hat{R}_i = t_i^\star \hat{a}_i + t_i \hat{a}_i^\dagger \equiv [\mathbf{T}^\dagger \hat{\boldsymbol{A}}]_i$, with $\mathbf{T} = [\begin{smallmatrix}\boldsymbol{\Theta}\\\boldsymbol{\Theta}^\star\end{smallmatrix}]$, where $\boldsymbol{\Theta} = \mathrm{diag}(t_1, t_2, \ldots)$. Then $\mathbf{S}^{(\alpha)}$ depends linearly on the covariance matrix

$$\mathbf{C}(\tau \geq 0) = \langle \hat{\boldsymbol{A}}(\tau)\hat{\boldsymbol{A}}^\dagger(0)\rangle = e^{-iB\tau}\mathbf{C}(0), \quad (2.13)$$

where $\mathbf{B} = \mathbf{H} - i\mathbf{K}/2$, with $\mathbf{K} = \mathrm{diag}(\kappa_1, \ldots, \kappa_1, \ldots)$, is the Bogoliubov operator, that generates the dynamics of the reservoir excitations according to a Bogoliubov-like equation $i\partial_t \hat{\boldsymbol{A}} = \mathbf{B}\hat{\boldsymbol{A}}$; and $\mathbf{C}(0) = [\begin{smallmatrix}\mathbb{1} & \mathbf{0}\\\mathbf{0} & \mathbf{0}\end{smallmatrix}]$ is the covariance matrix of the vacuum stemming from the canonical commutation relations. Then, one finally obtains, in all generality:

$$\mathbf{S}^{(\alpha)} = \lambda^2 \mathbf{T}^\dagger \frac{i\mathbf{C}(0)}{\omega_\alpha \mathbb{1} - \mathbf{B}}\mathbf{T}. \quad (2.14)$$

This last Equation (2.14) together with Equations (2.11) to (2.12) are the main result of the chapter. They describe the dynamics induced by the quantum fluctuations of any generic driven-dissipative possibly nonlinear spatially extended reservoir around some of its Gaussian equilibrium states. Remarkably, no assumption other than the usual Born, Markov and no-backaction approximations was required in the derivation. Another striking finding is that the effective dynamics induced by such a reservoir is of genuine quantum origin. Indeed, it originates from the possibility for the various modes of the system to exchange energy via travelling virtual excitations of the reservoir. This can be seen explicitly in Eq. (2.14), where $\mathbf{S}^{(\alpha)}$ crucially depends on the contribution of the canonical non-commutativity of bosonic operators to the vacuum covariance $\mathbf{C}(0)$, which would otherwise be zero for a reservoir at zero temperature as was here considered.

Let us now examine more in details the general master equation (2.12). The reservoir is responsible for the emergence of both new coherent terms in the Hamiltonian and new dissipators. While this is reminiscent of the reduced dynamics of a system in contact with a local reservoir, as described by Eq. (1.59), some notable differences exist. Indeed, contrary to the case of a local reservoir, the coherent contribution does not merely take the form of a Lamb shift, and instead may couple distant system modes. Furthermore, off-diagonal elements of the form $\Omega_{ij}^{(\alpha)}$ may be complex, accounting for the phase that may be picked up by a system's excitation quantum travelling from site j to i via the reservoir. This opens up an avenue for the design of complex couplings between system

modes, whether they be of bosonic nature or not, allowing for the flexible construction of effective lattice models with high connectivity. The new dissipators stemming from the presence of the reservoir have peculiar properties as well; they are nonlocal in the system operators $\hat{s}_i(\omega_\alpha)$. This has strong consequences on the effective dynamics. Indeed, this may lead to a breaking of the reciprocity of the system [179–181] and induce directional currents between system's modes, as will be investigated in the Chapter 3.

As clearly appears in Eq. (2.14), the range p of the effective interactions and the amount of nonlocality in the dissipative dynamics is related to the magnitude of $S_{i,i+p}^{(\alpha)}$ and thus to the correlation length of the reservoir ξ_c. To illustrate this, let us consider some generic one-dimensional extended reservoir bearing the form of an homogeneous chain of driven-dissipative bosonic modes with a tunnelling rate of $-J$, a drive's detuning of Δ and a dissipation rate of κ. In this simple example, the Bogoliubov operator is tridiagonal and can be explicitly inverted [182]. Then, $|S_{i,i+p}^{(\alpha)}| \sim (J/2)^p/|\Delta + \omega_\alpha - i\kappa/2|^p$, for $J < \kappa$. Upon tuning the external drive to match some system transition ω_α, one has $|S_{i,i+p}^{(\alpha)}| \sim \exp(-p/\xi_c)$, with $\xi_c = 1/\ln(\kappa/J)$, that is the range of the effective interactions exactly corresponds to the system's correlation length.

I.2 Continuous extended reservoirs

The same procedure can be applied to continuous reservoirs. Let us consider the case of some bosonic field $\hat{a}_{\boldsymbol{r}}$ confined into some finite volume $\mathcal{V}$. This could be, for instance, a polariton condensate as described in [13]. By performing the same displacement transformation as that introduced in the previous subsection, one gets that the most general master equation for the quantum fluctuations of the reservoir is of the form

$$\hat{H}_{\mathrm{R}} = \int_{\mathcal{V}} \mathrm{d}\boldsymbol{r}\mathrm{d}\boldsymbol{r}' \hat{\boldsymbol{A}}_{\boldsymbol{r}}^\dagger \mathbf{H}_{\boldsymbol{r}\boldsymbol{r}'} \hat{\boldsymbol{A}}_{\boldsymbol{r}'}, \quad \mathcal{D}_{\mathrm{R}}\hat{\rho}_R = \int_{\mathcal{V}} \mathrm{d}\boldsymbol{r}\kappa_r \hat{a}_r, \tag{2.15}$$

where the modes $\hat{\boldsymbol{A}}_{\boldsymbol{r}} = (\hat{a}_{\boldsymbol{r}}, \hat{a}_{\boldsymbol{r}}^\dagger)$, satisfy some Bogoliubov dynamical equation $i\partial_t \hat{\boldsymbol{A}}_{\boldsymbol{r}} = \int_{\mathcal{V}} \mathrm{d}\boldsymbol{r}' \mathbf{B}_{\boldsymbol{r}\boldsymbol{r}'} \hat{\boldsymbol{A}}_{\boldsymbol{r}'}$ [13], where the Bogoliubov operator $\mathbf{B}_{\boldsymbol{r}\boldsymbol{r}'} = \mathbf{H}_{\boldsymbol{r}\boldsymbol{r}'} - i\begin{bmatrix} \kappa_r/2 & 0 \\ 0 & \kappa_r/2 \end{bmatrix}\delta(\boldsymbol{r} - \boldsymbol{r}')$ typically carries some dependence on the mean fields accounting for the nonlinearity of the reservoir. Just as before, the system is then locally put in contact with these degrees of freedom via an interaction Hamiltonian of the form

$$\hat{H}_{\mathrm{I}} = \lambda \sum_i \hat{R}(\boldsymbol{r}_i) \otimes \hat{S}_i, \tag{2.16}$$

where $\hat{R}(\boldsymbol{r}_i) = t_i^\star \hat{a}_{\boldsymbol{r}_i} + t_i \hat{a}_{\boldsymbol{r}_i}^\dagger \equiv \boldsymbol{T}_i^\dagger \hat{\boldsymbol{A}}$, with now $\boldsymbol{T}_i = \begin{bmatrix} t_i \\ t_i^\star \end{bmatrix}$.

Under the above-discussed approximations, the system's effective master equation is identical to that of the previous subsection, Eq. (2.12), except for the expression of the reservoir spectrum $S_{ij}^{(\alpha)} = \int_{\mathrm{R}_+} \mathrm{d}\tau e^{i\omega_\alpha} \mathcal{G}_{\boldsymbol{r}_i \boldsymbol{r}_j}(\tau)$, that instead takes the following form

$$S_{ij}^{(\alpha)} = \frac{\lambda^2}{\mathcal{V}} \sum_{\boldsymbol{k},\boldsymbol{k}'} \boldsymbol{t}_i^\dagger \frac{i\mathbf{c}(0)\phi_{\boldsymbol{k}}^\star(\boldsymbol{r}_i)\phi_{\boldsymbol{k}'}(\boldsymbol{r}_j)}{\omega_\alpha \mathbb{1} - \mathbf{B}_{\boldsymbol{k}\boldsymbol{k}'}} \boldsymbol{t}_j. \tag{2.17}$$

where $\mathbf{c}(0) = \begin{bmatrix} 1 & 0 \\ 0 & 0 \end{bmatrix}$, $\mathbf{B}_{\boldsymbol{k}\boldsymbol{k}'} = \int_{\mathcal{V}} \mathrm{d}\boldsymbol{r}\mathrm{d}\boldsymbol{r}' \phi_k(\boldsymbol{r}) \mathbf{B}_{\boldsymbol{r},\boldsymbol{r}'} \phi_{\boldsymbol{k}'}^\star(\boldsymbol{r}')$, and $\{\phi_{\boldsymbol{k}}\}_{\boldsymbol{k}}$ denotes any complete basis of $L^2(\mathcal{V})$ that satisfies the boundary conditions imposed by the original Hamiltonian and the normalisation condition $\int_{\mathcal{V}} \mathrm{d}\boldsymbol{r}\phi_{\boldsymbol{k}}^\star(\boldsymbol{r})\phi_{\boldsymbol{k}'}(\boldsymbol{r}) = \mathcal{V}\delta_{\boldsymbol{k},\boldsymbol{k}'}$.

This further highlights the generality of the master equation (2.12).

II   The quantum Langevin approach to extended reservoirs

The above results were derived within the framework of the Lindblad master equation. Even though this Liouvillian approach will be preferred throughout this manuscript, in some contexts, however, an alternative and equivalent approach, the quantum Langevin equation, may be more suitable or customary. This is especially true when dealing with Gaussian or close-to-Gaussian models, such as those usually encountered in the field of optomechanics. For reference, we shall here briefly address how our results translate into this alternative picture.

The quantum Langevin equation

In the derivation of the optical master equation (1.42) in Sec. II.2, we obtained the reduced dynamical equation of the system by tracing out the bath. The quantum Langevin approach instead integrates explicitly the (linear) equations of motion of the bath operators and then substitutes the resulting expressions into the Heisenberg equation of the system operators. Upon neglecting the backaction of the system on the equilibrium state of the bath, the resulting interaction term in the equation of motion of the system operators bears the form of a fluctuating force and the fate of the system becomes completely determined by its two-point correlation function. Under similar Markovian assumptions as those used in the derivation of the optical master equation, the fluctuating force becomes delta-correlated and behaves as an operator-valued random variable whose covariance only depends on the equilibrium state of the bath $\hat{\rho}_{\mathrm{B}}$. The Heisenberg motion of the system can then be described as a stochastic differential equation driven by this fluctuating random force.

A detailed presentation of the theory behind the quantum Langevin equation approach can be found elsewhere [178, 183]. Let us simply recall that, in this picture, a generic thermal master equation in Lindblad form, as defined by the Liouville equation

$$\partial_t \hat{\rho}_{\mathrm{S}} = \mathcal{L}\hat{\rho}_{\mathrm{S}} = -i[\hat{H}_{\mathrm{S}}, \hat{\rho}_{\mathrm{S}}] + \gamma\Big\{(\bar{N}+1)\mathcal{D}[\hat{L}]\hat{\rho}_{\mathrm{S}} + \bar{N}\mathcal{D}[\hat{L}^\dagger]\hat{\rho}_{\mathrm{S}}\Big\}, \tag{2.18}$$

and parametrised by some Lindblad operator $\hat{L}$ acting on the system, translates into the following Heisenberg stochastic dynamics for any given system operator $\hat{O}$ [183]

$$\partial_t \hat{O} = \mathcal{L}^\dagger \hat{O} - \big[\hat{\xi}^\dagger \hat{L} - \hat{\xi}\hat{L}^\dagger, \hat{O}\big], \tag{2.19}$$

where the noise operator satisfies bosonic statistics

$$\langle\hat{\xi}(t)\rangle_{\mathrm{B}} = 0, \quad \langle\hat{\xi}^\dagger(t)\hat{\xi}(t')\rangle_{\mathrm{B}} = \gamma\bar{N}\delta(t-t'), \quad \langle[\hat{\xi}(t),\hat{\xi}^\dagger(t')]\rangle_{\mathrm{B}} = \gamma\delta(t-t'), \tag{2.20}$$

with $\langle\{\ldots\}\rangle_{\mathrm{B}} \equiv \mathrm{tr}_{\mathrm{B}}[\hat{\rho}_{\mathrm{B}}\{\ldots\}]$; and where the adjoint Liouvillian denotes the superoperator such that $\mathrm{Tr}[\hat{O}\mathcal{L}\hat{\rho}] = \mathrm{Tr}[\hat{\rho}\mathcal{L}^\dagger\hat{O}]$ [99].

Local thermal bath

For instance, for a bosonic site $\hat{b}$, of Hamiltonian $\hat{H}_{\mathrm{S}} = \omega \hat{b}^\dagger \hat{b}$, in contact with a thermal reservoir, $\hat{L} = \hat{b}$, this leads to a simple Ornstein-Uhlenbeck process:

$$\partial_t \hat{b} = -(i\omega + \gamma/2)\hat{b} + \hat{\xi} \quad \Leftrightarrow \quad \hat{b}(t) = \int_{-\infty}^{t} \mathrm{d}t' e^{-(i\omega + \gamma/2)(t-t')}\hat{\xi}(t'), \qquad (2.21)$$

where the time at which the bath was put in contact with the system was taken in the remote past $t_0 \to -\infty$, for simplicity. Then, one has indeed that

$$\begin{cases} \langle \hat{b}^\dagger(t)\hat{b}(t) \rangle_{\mathrm{B}} = \int_{\mathbb{R}_+} \mathrm{d}\tau \mathrm{d}\tau' e^{(i\omega - \gamma/2)\tau} e^{-(i\omega + \gamma/2)\tau'} \langle \hat{\xi}^\dagger(t-\tau)\hat{\xi}(t-\tau') \rangle_{\mathrm{B}} = \bar{N}, \\ \langle [\hat{b}(t), \hat{b}^\dagger(t)] \rangle_{\mathrm{B}} = \int_{\mathbb{R}_+} \mathrm{d}\tau \mathrm{d}\tau' e^{-(i\omega + \gamma/2)\tau} e^{(i\omega - \gamma/2)\tau'} \langle [\hat{\xi}(t-\tau), \hat{\xi}^\dagger(t-\tau')] \rangle_{\mathrm{B}} = 1. \end{cases} \qquad (2.22)$$

As just appeared, the quantum noise is essential to capture the thermal population of the bosonic site as well as to preserve the correct canonical commutation relations at any time.

Extended reservoirs

Let us now consider the case of a lattice of bosonic sites all in contact with their respective local thermal baths and with a common extended reservoir. The system is described by a set of annihilation operators $\{\hat{b}_i\}_i$. As we just saw, in the absence of extended reservoir, the system is originally described by the following system of quantum Langevin equations

$$\partial_t \hat{b}_i = i\left[\hat{H}, \hat{b}_i\right] - \frac{\gamma_i}{2}\hat{b}_i + \hat{\xi}_i, \qquad (2.23)$$

where

$$\langle \hat{\xi}_i(t) \rangle_{\mathrm{B}} = 0, \quad \langle \hat{\xi}_i^\dagger(t)\hat{\xi}_j(t') \rangle_{\mathrm{B}} = \gamma \bar{N}_i \delta_{i,j}\delta(t-t'), \quad \langle [\hat{\xi}_i(t), \hat{\xi}_j^\dagger(t')] \rangle_{\mathrm{B}} = \gamma \delta_{i,j}\delta(t-t'). \quad (2.24)$$

We now couple this system to an extended reservoir as described by Eq. (2.12). To simplify matters, we shall here treat only the case of a linear coupling to the reservoir, as described by the following effective Liouvillian:

$$\mathcal{L}_{\mathrm{ER}}\hat{\rho} = -i\left[\sum_{ij}(\Omega_{ij}^{(+)} + \Omega_{ji}^{(-)})\hat{b}_i^\dagger \hat{b}_j, \hat{\rho}\right] + \sum_k \left(\Gamma_k^{(+)}\mathcal{D}[\sum_j U_{kj}^{(+)}\hat{b}_j]\hat{\rho} + \Gamma_k^{(-)}\mathcal{D}[\sum_j U_{kj}^{(-)}\hat{b}_j^\dagger]\hat{\rho}\right), \quad (2.25)$$

where $\Omega_{ij}^{(\pm)}$ are two effective coherent reservoir-mediated hopping rates associated to collective Stokes $(-)$ and anti-Stokes $(+)$ processes and $\Gamma_k^{(\pm)}$ the rates of the corresponding incoherent processes. The latter as well as the unitary matrices $\mathbf{U}^{(\pm)}$ follow from the above-introduced eigendecomposition of the Hermitian matrices $\mathbf{\Gamma}^{(\pm)} = \mathbf{U}^{(\pm)\dagger} \mathrm{diag}(\Gamma_1^{(\pm)}, \ldots)\mathbf{U}^{(\pm)}$. This Liouvillian translates into the following quantum Langevin equation for the system modes:

$$\partial_t \hat{\boldsymbol{b}} = i\left[\hat{H}, \hat{\boldsymbol{b}}\right] - i(\mathbf{\Omega}^{(+)} + \mathbf{\Omega}^{(-)T})\hat{\boldsymbol{b}} - \frac{1}{2}\mathbf{\Gamma}\hat{\boldsymbol{b}} + \hat{\boldsymbol{\xi}}, \qquad (2.26)$$

with now non-local dissipation rates

$$\mathbf{\Gamma} = \mathbf{\Gamma}^{(\uparrow)} - \mathbf{\Gamma}^{(\downarrow)T}, \quad \Gamma_{ij}^{(\uparrow)} = \delta_{i,j}\gamma_i\bar{N}_i + \Gamma_{ij}^{(-)}, \quad \Gamma_{ij}^{(\downarrow)} = \delta_{i,j}\gamma_i(\bar{N}_i + 1) + \Gamma_{ij}^{(+)}, \qquad (2.27)$$

and spatially correlated quantum noise. By introducing $\hat{\boldsymbol{\Xi}} = \begin{bmatrix} \hat{\boldsymbol{\xi}} \\ \hat{\boldsymbol{\xi}}^\dagger \end{bmatrix}$, the noise is now characterised by the following covariance matrix

$$\langle \hat{\boldsymbol{\Xi}}(t)\hat{\boldsymbol{\Xi}}^\dagger(t')\rangle_{\mathrm{ER}} = \boldsymbol{\Gamma} \begin{bmatrix} \bar{\boldsymbol{\sigma}} & \mathbf{0} \\ \mathbf{0} & \bar{\boldsymbol{\sigma}} + \mathbf{1} \end{bmatrix} \delta(t-t'), \qquad (2.28)$$

where $\bar{\boldsymbol{\sigma}} = \boldsymbol{\Gamma}^{-1}\boldsymbol{\Gamma}^{(\uparrow)}$, $\bar{\boldsymbol{\sigma}}+\mathbf{1} = \boldsymbol{\Gamma}^{-1}\boldsymbol{\Gamma}^{(\downarrow)}$. This bears a striking resemblance with the covariance matrix of the noise operators of a local thermal bath as in Eq. (2.20):

$$\left\langle \begin{bmatrix} \hat{\xi}^\dagger(t)\hat{\xi}(t') & \hat{\xi}(t)\hat{\xi}(t') \\ \hat{\xi}^\dagger(t)\hat{\xi}^\dagger(t') & \hat{\xi}(t)\hat{\xi}^\dagger(t') \end{bmatrix} \right\rangle_{\mathrm{B}} = \gamma \begin{bmatrix} \bar{N} & 0 \\ 0 & \bar{N}+1 \end{bmatrix} \delta(t-t'). \qquad (2.29)$$

In fact, $\bar{\boldsymbol{\sigma}}$ indeed corresponds to a thermal population towards which the system relaxes. By considering an arbitrary non-squeezing quadratic Hamiltonian $\hat{H} = \hat{\boldsymbol{B}}^\dagger \mathbf{H} \hat{\boldsymbol{B}}$, where $\hat{\boldsymbol{B}} = \begin{bmatrix} \hat{b} \\ \hat{b}^\dagger \end{bmatrix}$, one finds[3]:

$$\langle \hat{\boldsymbol{B}}(t)\hat{\boldsymbol{B}}^\dagger(t)\rangle_{\mathrm{R}} = \int_{\mathbb{R}_+} \mathrm{d}\tau \mathrm{d}\tau' e^{-(i\tilde{\mathbf{H}}+\boldsymbol{\Gamma}/2)\tau} \langle \hat{\boldsymbol{\Xi}}(t-\tau)\hat{\boldsymbol{\Xi}}^\dagger(t-\tau')\rangle_{\mathrm{BR}} e^{-(i\tilde{\mathbf{H}}+\boldsymbol{\Gamma}/2)\tau'}$$
$$= \begin{bmatrix} \boldsymbol{\Gamma}^{-1}\boldsymbol{\Gamma}^{(\uparrow)} & \mathbf{0} \\ \mathbf{0} & \boldsymbol{\Gamma}^{-1}\boldsymbol{\Gamma}^{(\downarrow)} \end{bmatrix} \equiv \begin{bmatrix} \bar{\boldsymbol{\sigma}} & \mathbf{0} \\ \mathbf{0} & \bar{\boldsymbol{\sigma}}+\mathbf{1} \end{bmatrix}. \qquad (2.30)$$

Thus, $\bar{\sigma}_{ij} = \langle \hat{b}_i^\dagger \hat{b}_j \rangle_{t\to+\infty}$ corresponds to the steady-state single-particle density matrix and can be obtained analytically as $\bar{\boldsymbol{\sigma}} = \boldsymbol{\Gamma}^{-1}\boldsymbol{\Gamma}^{(\uparrow)}$, giving access to the steady-state populations and coherences. This completes the analogy with the single-site thermal bosonic system case.

The quantum Langevin equation (2.26) together with the covariance (2.28) give an alternative complete quantum description of the reservoir-induced dynamics of the system.

---

[3]The Lamb shift was here absorbed into a redefinition of the Hamiltonian.

3 Permanent circulating heat currents in rings of optomechanical resonators

In this chapter, we shall study the effective phonon dynamics in lattices of cavity-coupled optomechanical resonators whose photonic modes are coherently driven and whose mechanical modes are mutually uncoupled and connected to independent thermal baths. This setup, of experimental relevance, furnishes an ideal playground for testing our theoretical findings on spatially extended reservoirs. Indeed, much in the same way as we did in the Subsec. I.5 of Chapter 1 when discussing sideband cooling, the light modes can here be interpreted as playing the role of a fast driven-dissipative reservoir that mediates the phononic out-of-equilibrium dynamics. By applying the prescription derived in the Chapter 2 to optomechanical lattices, we will show that it is possible to stabilise stationary states that exhibit directional heat currents ever flowing through the structure over arbitrary distance, despite the absence of thermal gradients and of direct coupling between distinct mechanical resonators.

The chapter is structured as follows. The introductory Section I will give a general overview of the context of this work. A model describing a set of cavity-coupled optomechanical resonators will then be introduced in Sec. II. In Sec. III, the dynamics of the system's mechanical degrees of freedom will be given an effective description. Building on this reduced picture, permanent circulating heat currents will be identified in the steady-state of rings of optomechanical resonators, in Sec. IV. The effective analytical description will be numerically benchmarked in Sec. V, before concluding the chapter in Sec. VI.

I   Introduction

The emergence of persistent currents in many-body systems is closely related to fundamental concepts in classical and quantum physics. In classical electrodynamics, any permanently magnetised object exhibits persistent electronic currents [184]. A conducting ring in the quantum coherent regime supports a permanent electric current when pierced by an external magnetic field [185]. When pairing interactions are considered, a superconductor cooled below its critical temperature displays persistent currents, and a constant magnetic field builds up through any continuous loop of the material [186]. Systems with nontrivial topology can also give rise to persistent edge currents [187].

These manifestations of persistent currents involve two noticeable ingredients: (i) an

external gauge field and (ii) the presence of a significant coherence extending over the entire sample [188]. Recently, it was shown that these ingredients are not strictly required, and that permanent currents in rings can instead be generated by *reservoir engineering* [179, 188], where specific many-body quantum states with properties of interest are stabilised [16, 189]. More than a mere source of decoherence, the environment becomes then a tool to generate correlated phases, sometimes with no equilibrium counterpart [190]. In this context, the study of systems driven by nonlocal dissipators has emerged, notably in relation to nonreciprocal behaviours [179]. In several nonreciprocal realisations, a direct coupling between two bosonic modes was engineered through a common ancillary degree of freedom [181, 191, 192]. Very recently, the concept of engineered directionality was theoretically scaled up to extended lattices, by tailoring ancilla-assisted interactions [188, 193–195].

Besides nonreciprocity, the coupling of independent mechanical modes to commonly shared optical modes was proposed to transport phonons between distant resonators [120], to model out-of-equilibrium quantum thermodynamics [121], and experimentally implemented to phase-lock adjacent [132] and distant [133, 196] mechanical resonators. Yet, many aspects of the nonlocal quantum dynamics of extended lattices in optomechanics remain to be explored.

In the present chapter, we shall analytically study the effective dynamics of originally independent mechanical resonators coupled to extended lattices of driven-dissipative optical cavities. By specialising the main result of the previous chapter, Eq. (2.12), to lattices of optically coupled optomechanical resonators [8, 197], we will obtain the general effective master equation governing the dynamics of the structure's thermal phonons and compare our predictions with a mean-field approach. Upon examining analytically the steady-state of the model, we will show that, under certain driving conditions, rings of cavity-coupled optomechanical resonators exhibit persistent whirling currents of thermal phonons. This heat transport is uniquely mediated by spatially correlated quantum fluctuations of the optical fields, in the absence of any direct mechanical coupling, and triggered by a proper tuning of the phase of the optical drive. This phenomenon will be shown to persist when mechanical resonators interact with independent thermal baths, over a wide range of temperatures. The magnitude of this current will be expressed analytically within a Born-Markov approximation.

II   Model

The system under consideration consists of a network of L optomechanical resonators whose optical modes are coherently driven by external laser fields. Neighbouring cavities are optically coupled to one another, while mechanical modes are not. This setting is experimentally relevant, for instance, when considering an implementation with optomechanical disk resonators, such as those described in Chapter 1. Indeed, each of these resonators bears two modes of interest, an optical WGM and a mechanical RBM, coupled through a radiation-pressure-like interaction. While no obvious way of directly coupling the RBMs of distincts disks was yet identified that would preserve their remarkable mechanical quality factor, the WGMs of neighbouring resonators couple rather naturally.

Indeed, the periphery of each disk confines much of the electromagnetic field of its whispering gallery modes of high azimutal order. This is accompanied by the presence of an evanescent field radially propagating outwards at the vicinity of the peripheral boundaries of the disk. By engineering the disks side by side, the evanescent optical fields of neighbouring cavities hybridise, giving rise to a significant lateral coupling of the considered WGMs. The same mechanism is exploited in order to couple an external coherent drive of angular frequency ω_p to the disks' WGMs through a near waveguide [198, 199], that brings the optomechanical resonator out of equilibrium. Such resonators can be fabricated with ultralow site-to-site disorder [200]. One optomechanical cell is schematically illustrated in Fig. 3.1 (a).
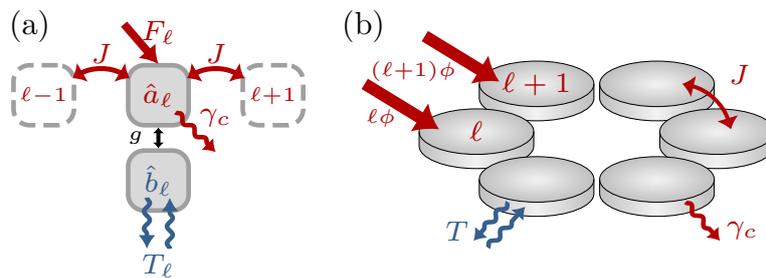
Figure 3.1: (a) Schematic representation of a single optomechanical cell and its nearest-neighbour optical couplings. $\hat{a}_\ell$ ($\hat{b}_\ell$) is the optical (mechanical) mode of index ℓ. (b) Ring of optomechanical disk resonators. Each site is optically driven with a phase that varies as $\ell\phi$, being ℓ the site number. Optical modes are coupled while mechanical ones are not.

While in the following we will focus on one-dimensional (1D) chains, we here consider, for the sake of generality, an arbitrary network where the coupling between adjacent photonic modes is fully specified by some $L \times L$ adjacency matrix $\mathbf{A}$ where $A_{\ell\ell'} = 1$ if the sites ℓ and ℓ' are coupled and $A_{\ell\ell'} = 0$ otherwise. In the frame rotating at the driving frequency ω_p, the unitary part of the dynamics is described by the following Hamiltonian [128]:

$$\hat{H}_{\text{tot}} = \sum_{\ell=1}^{L} \left[-\Delta_\ell \hat{a}_\ell^\dagger \hat{a}_\ell + F_\ell^\star \hat{a}_\ell + F_\ell \hat{a}_\ell^\dagger - g_\ell \hat{a}_\ell^\dagger \hat{a}_\ell (\hat{b}_\ell + \hat{b}_\ell^\dagger) \right] - \frac{J}{2} \sum_{\ell,\ell'=1}^{L} A_{\ell\ell'} \hat{a}_\ell^\dagger \hat{a}_{\ell'} + \sum_{\ell=1}^{L} \Omega_m^{(\ell)} \hat{b}_\ell^\dagger \hat{b}_\ell, \quad (3.1)$$

where $\hat{a}_\ell$ and $\hat{b}_\ell$ are, respectively, the photonic and phononic annihilation operators of the ℓ-th resonator, $\Delta_\ell = \omega_p - \omega_c^{(\ell)}$ denotes the detuning of the driving laser frequency with respect to the local bare cavity frequency $\omega_c^{(\ell)}$, F_ℓ is the (complex) amplitude of the coherent drive, g_ℓ is the optomechanical vacuum coupling rate and J is the hopping rate between connected optical cavities.

Incoherent processes associated to local photon losses (at a rate κ_ℓ) and phonon thermalisation with their respective thermal baths (at a rate Γ_ℓ) are taken into account by means of a Lindblad master equation analogous to that obtained in Eq. (1.54) for a single resonator, which fully determines the system evolution,

$$\partial_t \hat{\rho}(t) = \mathcal{L}_{\text{tot}} \hat{\rho}(t) \equiv -i[\hat{H}_{\text{tot}}, \hat{\rho}(t)] + \mathcal{D}_{\text{tot}} \hat{\rho}(t), \quad (3.2)$$

where

$$\mathcal{D}_{\text{tot}}\hat{\rho} = \sum_{\ell=1}^{L} \left\{ \Gamma_\ell \left[(\bar{N}_\ell + 1)\mathcal{D}[\hat{b}_\ell]\hat{\rho} + \bar{N}_\ell \mathcal{D}[\hat{b}_\ell^\dagger]\hat{\rho} \right] + \kappa_\ell \mathcal{D}[\hat{a}_\ell]\hat{\rho} \right\}, \tag{3.3}$$

with $\mathcal{D}[\hat{L}]\hat{\rho} = \hat{L}\hat{\rho}\hat{L}^\dagger - \frac{1}{2}\{\hat{L}^\dagger\hat{L}, \hat{\rho}\}$ and $\bar{N}_\ell$ the average number of thermal phonons due to the ℓth thermal bath. One here recognises the dissipators previously introduced in Eqs. (1.42), (1.45) and (1.46).

With the notable exception of ultracold atomic ensembles [201, 202], the bare coupling rate between the optical field and the mechanical motion is orders of magnitude lower than that of the optical dissipation. Then, upon driving the optical mode to some stable population of coherent photons, the magnitude of the coupling between photons and thermal phonons becomes enhanced by a factor $\sqrt{N_c} \equiv \langle \hat{a}^\dagger \hat{a} \rangle^{1/2}$ that can be varied by playing on the amplitude of the driving. One can thus always put oneself into a situation where the optomechanical coupling is much lower than the typical optical relaxation time, that is $\kappa \gg 2gN_c^{1/2}$. Under this condition and in a regime where the system is dynamically stable, as we shall assume in the following, the optical fluctuations are negligibly affected by the mechanics and the coupled cavities can be regarded as an extended optical *reservoir*. Such and optical reservoir possesses particularly suitable features for studying the dynamics induced by the spatially extended reservoirs theoretically introduced in Chapter 2, as we shall now see.

III   Effective description

We aim at describing the effective dynamics of the resonators' thermal phonons. To this aim, let us split the fields into their steady-state mean-field values plus zero-mean fluctuations as $\hat{a}_\ell = \tilde{\alpha}_\ell + \hat{c}_\ell$ and $\hat{b}_\ell = \tilde{\beta}_\ell + \hat{d}_\ell$, where $\hat{c}_\ell$ is the operator associated to photonic fluctuation quanta at site ℓ and $\hat{d}_\ell$ that of the thermal phonons thereof. The scalars $\tilde{\alpha}_\ell$ and $\tilde{\beta}_\ell$ are chosen so as to be the steady-state solutions of the mean-field dynamical equations. That is

$$F_\ell - \tilde{\Delta}_\ell \tilde{\alpha}_\ell - i\frac{\kappa_\ell}{2}\tilde{\alpha}_\ell - \frac{J}{2}\sum_{\ell'} A_{\ell\ell'}\tilde{\alpha}_{\ell'} = 0, \quad \tilde{\beta}_\ell = \frac{g_\ell|\tilde{\alpha}_\ell|^2}{\Omega_m^{(\ell)} - i\Gamma_\ell/2}, \tag{3.4}$$

where $\tilde{\Delta}_\ell \simeq \Delta_\ell + 2g_\ell^2|\tilde{\alpha}_\ell|^2/\Omega_m^{(\ell)}$ (for a high mechanical quality factor, see footnote 3) denotes the nonlinearly shifted detuning of the cavity. Because of this shift of the cavity's angular frequency due to the mean mechanical displacement, the system may exhibit multistability, i.e. Eq. (3.4) may have several solutions.

Outside of the multistable region, the Hamiltonian and the dissipator can be safely expanded to second order in the fluctuations around the mean fields, yielding

$$\hat{H}'_{\text{tot}} \simeq \sum_{\ell=1}^{L} \left[-\tilde{\Delta}_\ell \hat{c}_\ell^\dagger \hat{c}_\ell - \frac{J}{2}\sum_{\ell'} A_{\ell\ell'}\hat{c}_\ell^\dagger \hat{c}_{\ell'} + \hat{V}_\ell + \Omega_m^{(\ell)}\hat{d}_\ell^\dagger \hat{d}_\ell \right], \tag{3.5}$$

where now the leading optomechanical interaction is given by $\hat{V}_\ell = (G_\ell^* \hat{c}_\ell + G_\ell \hat{c}_\ell^\dagger)(\hat{d}_\ell + \hat{d}_\ell^\dagger)$, with $G_\ell = g_\ell \tilde{\alpha}_\ell$, and where a term of order $\mathcal{O}(g\hat{c}^2\hat{d})$ was neglected.

As became explicit in this frame, thermal phonons, as represented by $\hat{d}_\ell$, do not interact with the coherent optical populations and are instead sensitive to the quantum optical

fluctuations of the cavities, as represented by $\hat{c}_\ell$. A second linked observation relates to the possibility of tuning both the amplitude and the phase of G_ℓ via the external driving. This feature of the linearised optomechanical coupling makes it a powerful tool to investigate reservoir-induced dynamics and proves crucial in the emergence of permanent heat currents as we will see below. Finally, one remarks that this specific shift in the operators exactly cancels all linear (driving) terms in the Hamiltonian while the dissipator remains that of Eq. (3.3) upon substituting $\hat{a}_\ell, \hat{b}_\ell \to \hat{c}_\ell, \hat{d}_\ell$. It becomes thus clear that, in this displaced frame, finite-lived ($\tau_c = 1/\kappa$) quantum optical fluctuations are not externally driven but may enter the reservoir from the mechanics through the now linear optomechanical coupling ($\hat{V}_\ell$). Such fluctuation quanta can then travel through the lattice by tunnelling from cavity to cavity until they are scattered back into some distant mechanical mode or leak out of the cavities due to optical losses. We will formalise this intuition hereafter by looking at the reduced dynamics of the mechanical degrees of freedom.

One has that any excitation entering the optical reservoir rapidly decays, $\hat{c}_\ell(t \gg \tau_c) \approx 0$, and thus that the state of the optical modes remains roughly the identified coherent state, $\hat{a}_\ell(t \gg \tau_c) \approx \tilde{\alpha}_\ell$. As these optical fluctuations have little memory on timescales larger than τ_c, the single-body two-time correlation functions of the optical reservoir decay in time as those of a thermal bath at $T = 0$, allowing one to treat it within the Markovian approximation. Within the Born-Markov approximation, the adiabatic elimination of the lattice of optical cavities can be performed by applying the general result of Eq. (2.12), yielding the following effective Hamiltonian and dissipator for the mechanical modes:

$$\hat{H}_m^{\text{eff}} = \sum_{\ell=1}^{L} \Omega_m^{(\ell)} \hat{d}_\ell^\dagger \hat{d}_\ell + \sum_{\ell,\ell'=1}^{L} (\Omega_{\ell\ell'}^{(+)} + \Omega_{\ell'\ell}^{(-)}) \hat{d}_\ell^\dagger \hat{d}_{\ell'}, \tag{3.6}$$

$$\mathcal{D}_m^{\text{eff}} \hat{\rho}_m = \sum_{\ell=1}^{L} \Gamma_\ell \left((\bar{N}_\ell + 1) \mathcal{D}[\hat{d}_\ell] \hat{\rho}_m + \bar{N}_\ell \mathcal{D}[\hat{d}_\ell^\dagger] \hat{\rho}_m \right) + \sum_{\ell=1}^{L} \left(\Gamma_\ell^{(+)} \mathcal{D}[\hat{\beta}_\ell^{(\downarrow)}] \hat{\rho}_m + \Gamma_\ell^{(-)} \mathcal{D}[\hat{\beta}_\ell^{(\uparrow)}] \hat{\rho}_m \right), \tag{3.7}$$

where $\mathbf{\Omega}^{(\pm)}$ are the two *nonlocal* Lamb shifts associated to Stokes ($-$) and anti-Stokes ($+$) collective scattering processes, and $\Gamma_\ell^{(\pm)}$ the corresponding dissipation rates, associated to nonlocal lowering and raising jump operators $\hat{\beta}_\ell^{(\updownarrow)}$. As identified in Chapter 2, all of these are determined by the Hermitian and anti-Hermitian parts of the spectrum $\mathbf{S}^{(\pm)}$ of the reservoir:

$$S_{\ell\ell'}^{(\pm)} = G_\ell^\star \left[\frac{i\mathbf{1}}{\pm\Omega_m^{(\ell')}\mathbf{1} - \mathbf{B}} \right]_{\ell\ell'} G_{\ell'}, \tag{3.8}$$

with $\mathbf{B} = -\frac{J}{2}\mathbf{A} - \text{diag}(\{\widetilde{\Delta}_\ell + i\kappa_\ell/2\})$, and in terms of which

$$\mathbf{\Omega}^{(\pm)} = \frac{\mathbf{S}^{(\pm)} - \mathbf{S}^{(\pm)\dagger}}{2i}, \quad \frac{\mathbf{\Gamma}^{(\pm)}}{2} = \frac{\mathbf{S}^{(\pm)} + \mathbf{S}^{(\pm)\dagger}}{2} = \mathbf{U}^{(\pm)\dagger} \text{Diag}(\{\Gamma_\ell^{(\pm)}/2\}) \mathbf{U}^{(\pm)}, \tag{3.9}$$

where $\mathbf{U}^{(\pm)}$ are the unitary matrices that diagonalise the spectral matrix of the reservoir. Finally, the nonlocal jump operators are defined as $\hat{\beta}_\ell^{(\downarrow)} = \sum_{\ell'=1}^{L} U_{\ell\ell'}^{(+)} \hat{d}_{\ell'}$, $\hat{\beta}_\ell^{(\uparrow)} = \sum_{\ell'=1}^{L} U_{\ell\ell'}^{(-)} \hat{d}_{\ell'}^\dagger$. In this effective description, the lattice of cavities modifies the dynamics of the mechanical modes by adding coherent phonon-hopping processes between previously uncoupled mechanical modes and acting as a thermal bath for L extended phononic

modes $\{\hat{\beta}_\ell^{(\downarrow)}\}_\ell$, when $\hat{\beta}_\ell^{(\uparrow)} = \hat{\beta}_\ell^{(\downarrow)\dagger}$. Let us note that this last condition is not met in general. This is in contrast with the reduced mechanical master equation of the single-resonator, Eq. (1.59), where the jump operators corresponding to optically-induced transitions were Hermitian conjugates. This has profound implications in the dynamics, as we will later see.

Cavity-mediated interactions

It follows from Eqs. (3.6) and (3.7) that, as anticipated, originally independent and distant mechanical modes indeed couple through the optical reservoir. To better understand the dynamics described by this reduced master equation, let us look at the dynamical equations of the thermal phonon operators:

$$ i\partial_t \hat{d}_\ell = \Omega_m^{(\ell)} \hat{d}_\ell - i\frac{\Gamma_\ell}{2}\hat{d}_\ell + \sum_{\ell'}(\Omega_{\ell\ell'}^{(+)} + \Omega_{\ell'\ell}^{(-)})\hat{d}_{\ell'} - i\sum_{\ell'}\frac{\Gamma_{\ell\ell'}^{(+)} - \Gamma_{\ell'\ell}^{(-)}}{2}\hat{d}_{\ell'}. \qquad (3.10) $$

From this it becomes clear that $\mathbf{\Omega}^{(\pm)}$ and $\mathbf{\Gamma}^{(\pm)}/2$ respectively describe the coherent and incoherent cavity-mediated coupling between distant mechanical resonators, whose index indicate whether they originate from anti-Stokes $(+)$ or Stokes $(-)$ scattering processes. We illustrate the dependence of both of these cavity-mediated interactions on the detuning of the cavities in Fig. 3.2 (a) and Fig. 3.2 (b), for a periodic chain of optomechanical resonators of length $L = 32$. Interestingly, one observes that the range and the phase pattern of the cavity-mediated interactions crucially depends on the extended reservoir's parameters: (i) its correlation length, $\xi_c \sim J/\kappa$; (ii) its intercavity coupling; and (iii) the detuning of its drive. As briefly sketched in the introduction, two opposite regimes can be distinguished when discussing reservoir-mediated interactions, that of two-body interactions through a local ancilla, as in [188]; and that of all-to-all coupling through well-resolved delocalised modes, as in [120, 121]. One may, by a proper choice of the distance between disks, design interactions with a desired range. This makes it possible to study the cavity-mediated dynamics and transport in a setting with varying connectivity, that interpolates between these two contrasting situations, by simply relying on the correlation length associated to the finite lifetime of the mediating-photon fluctuations.

In the dynamics of single phonons, as described by the adjoint master equation (3.10), the presence of the reservoir induces both a coherent and an incoherent effect. This bears a close resemblance to the single-resonator case, where the former corresponded to the so-called optical spring effect and the latter to the sideband cooling or heating of the mechanical degree of freedom. Here, one observes that due to the coupling J between optical modes of neighbouring cavities, the two sidebands originally located at $\widetilde{\Delta}^{(\pm)} = \pm\Omega_m$ acquire a finer structure, respectively splitting into L sidebands at $\widetilde{\Delta}_{k_n}^{(\pm)} = \pm\Omega_m + J\cos(k_n)$, with $k_n = 2\pi n/L$, comprised within angular frequency intervals of width $2J$. This is illustrated in Fig. 3.2 (c) and Fig. 3.2 (d), that display the on-site optical spring and optical dissipation strengths, around the new sidebands. The behaviour of these two effective quantities is reminiscent from the single-resonator case, as depicted in Fig. 1.4. This can be explained very simply by looking at the reservoir's "density of states" $D_R(\omega)$, plotted in the top panel. Indeed, it follows from Fermi's golden rule that the rate at which a specific single-phonon transition can be induced by the reservoir on the system
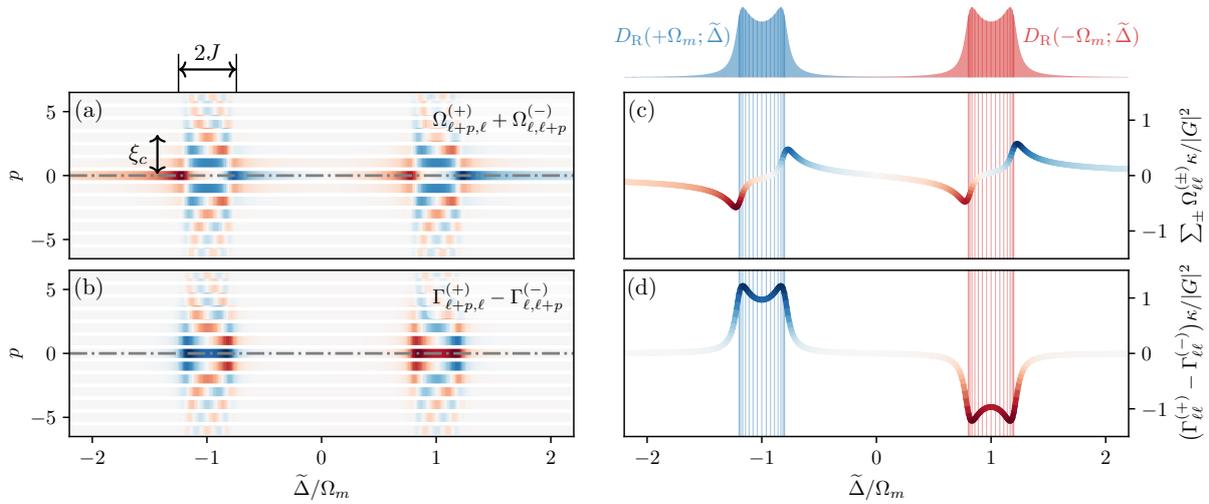
Figure 3.2: (a) Coherent and (b) incoherent coupling between sites ℓ and $\ell + p$ of a periodic chain of optomechanical resonators as a function of the distance p and the nonlinearly shifted detuning of the driving. (c) Local optical spring effect and (d) optical damping rate along the dash-dotted lines of the left panels. Negative values correspond to positive gain. The positions of the Stokes and anti-Stokes sidebands are denoted by red and blue vertical lines, respectively. The "density of states" of the reservoir at the energy of the single-phonon transitions is represented on top as a function of the detuning. Parameters are chosen identical at all sites, with $L = 32$ sites, $G/\Omega_m = 0.2$, $\kappa/\Omega_m = 0.1$, $J/\kappa = 2$.
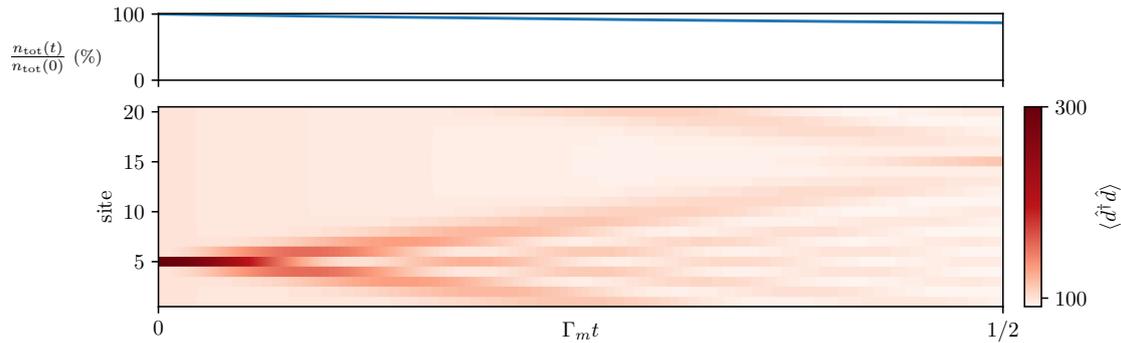
Figure 3.3: Linear cavity-mediated diffusion of an initial 200-thermal-phonon population imbalance in a periodic chain of optomechanical resonators. Top: relative change in global thermal-phonon population due to thermal relaxation and residual sideband cooling. Bottom: time evolution of each site's thermal population. Parameters are chosen identical at all sites, with $L = 20$ sites, $G/\Omega_m = 0.2$, $\kappa/\Omega_m = 10$, $J/\kappa = 2$, $\Gamma_m/\Omega_m = 1 \times 10^{-4}$, and $\bar{N} = 100$.
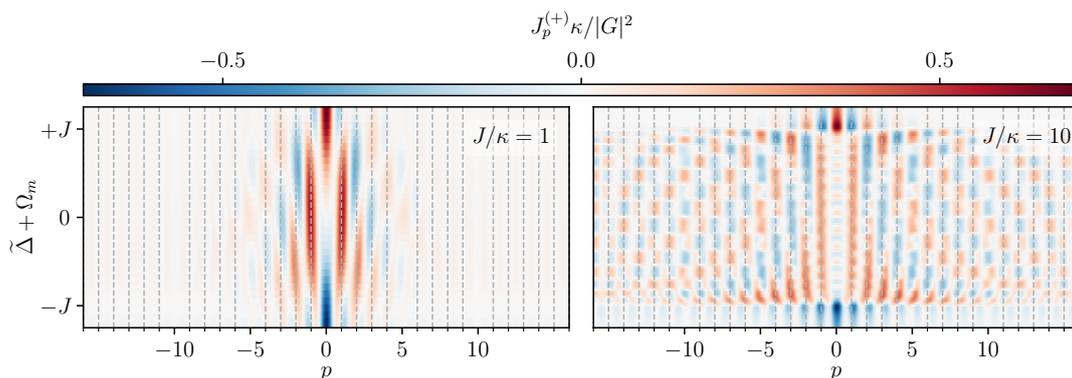
Figure 3.4: Dependence of the range of the cavity-mediated coherent interactions on the intercavity coupling and the detuning of the driving around the anti-Stokes sidebands. $J_p^{(+)}$, as given by Eq. (3.12), is shown for $J/\kappa = 1$ (left panel) and $J/\kappa = 10$ (right panel). The range of the interaction is found to be of the order of J/κ. Here $L = 32$, the rest of parameters are given in the text.

is proportional to $D_{\mathrm{R}}(\omega = \pm\Omega_m)$, where $\omega = +\Omega_m$ corresponds to the absorption of one thermal phonon by the reservoir and $\omega = -\Omega_m$ to the emission of a phonon into the system. This is indeed what is observed in Fig. 3.2 (d), which closely follows the density of states of the reservoir.

Cavity-mediated coherent transport

Let us first focus on the coherent effects induced by the reservoir by looking at the cavity-mediated transport in such a ring. As is well known and may be checked from Fig. 1.4, the best coherent-to-dissipative ratio is found in the bad-cavity limit $\kappa \gg \Omega_m$ far from the sidebands. In Fig. 3.3, we simulate the dynamics of a ring of length $L = 20$, which is initially perturbed at site $\ell = 5$ upon driving the reservoir far below resonance with the anti-Stokes sidebands. Here, each site of the ring is initially prepared in a thermal state containing $\bar{N} = 100$ thermal phonons, at equilibrium with its local thermal bath. At $t = 0$, the fifth site is set out-of-equilibrium by the addition of 200 supplementary phonons. Upon time evolution, one indeed observes the coherent diffusion of the thermal population imbalance due to scattering through the reservoir.

The parity-broken optomechanical ring

As we just saw, the resonators' cavities can indeed mediate reciprocal particle transport. We now exploit the effective description derived above to study the emergence of persistent directional heat currents in such rings. So far, we have discussed the case of a homogeneous ring with identical parameters at every site. Such a lattice is parity symmetric, that is symmetric upon a spatial point reflection $\ell \mapsto -\ell$. For the ring to exhibit directional currents, this parity must be broken. One may think of the common example of a conducting spire, whose electron diffusion becomes directionally biased as the parity is broken by the presence of a magnetic field piercing through the loop. This symmetry can be broken either explicitly or spontaneously, we shall break it explicitly while preserving

space-translational symmetry. To this aim, the cavities are driven individually with the same intensity but with a site-dependent phase such that $|F_\ell| = F$ and $\text{Arg}(F_\ell) = \ell\phi$ with $\phi = 2\pi n/L$ and $n \in \mathbb{Z}$, which creates a homogeneous phase gradient around the ring. This situation is schematically illustrated in Fig. 3.1 (b). A similar strategy has been adopted in Ref. [203] with optomechanical crystals where optical and mechanical modes are strongly hybridised and neighbouring mechanical modes are directly coupled. Following Eqs. (3.6) and (3.7), the unitary part of the mechanical effective dynamics is governed by

$$\hat{H}_m^{\text{eff}} = \sum_\ell (\Omega_m + J_0^{(+)} + J_0^{(-)})\hat{d}_\ell^\dagger \hat{d}_\ell + \Sigma_\pm \sum_{p\geq 1} \frac{J_p^{(\pm)}}{2} \sum_\ell \left(\hat{d}_{\ell+p}^\dagger \hat{d}_\ell e^{\mp i\phi\times p} + \text{H.c.} \right), \qquad (3.11)$$

where

$$J_p^{(\pm)} = \sum_k \frac{e^{ikp}}{L} \frac{|G|^2(\pm\Omega_m + \widetilde{\Delta} + J\cos k)}{(\pm\Omega_m + \widetilde{\Delta} + J\cos k)^2 + (\kappa/2)^2} \qquad (3.12)$$

is the real-valued amplitude of the effective complex coupling between p-distant modes. Interestingly, the interaction between distinct mechanical modes now bears a complex phase such that a phonon scattering between two sites through the reservoir picks up a phase proportional to the signed distance between the exit and entry sites. Thus, the reservoir acts as a synthetic gauge field for the thermal phonons. Such engineered synthetic gauge fields [204, 205] have been well studied both theoretically and experimentally [206, 207] in the context of cold atoms and are connected to the emergence of persistent currents [208–210]. Coherent effects in Eq. 3.11 emerge in terms of two sets of directional couplings, respectively noted by $\pm$. This can be understood from second order perturbation theory by examining the two mechanics-to-mechanics scattering processes having finite overlap $\langle f|\hat{V}_{\ell+p}\hat{V}_\ell|i\rangle$ and preserving the total energy: $\langle f|G_{\ell+p}^\star \hat{c}_{\ell+p}\hat{d}_{\ell+p}^\dagger \times G_\ell \hat{c}_\ell^\dagger \hat{d}_\ell|i\rangle$ and $\langle f|G_{\ell+p}\hat{c}_{\ell+p}^\dagger \hat{d}_{\ell+p}^\dagger \times G_\ell^\star \hat{c}_\ell \hat{d}_\ell|i\rangle$. These respectively correspond to scattering events happening around the anti-Stokes and Stokes resonances. During either process, the transported phonon picks up opposed phases. Therefore, the magnitude of each of these directional hopping channels, and thus the net effective flux of phonons, can be adjusted by setting the drive detuning Δ closer to either of the two sets of sidebands. This dependence is complex in general, as shown in Fig. 3.4 for $J_p^{(+)}$. For this figure, as for all the following ones, parameters are $L = 8$, $\phi = 2\pi/L$, $|\tilde{\alpha}|^2 = 100$, $g/\Omega_m = 2 \times 10^{-3}$, $\kappa/\Omega_m = 1 \times 10^{-1}$, $\Gamma_m/\Omega_m = 1 \times 10^{-3}$, and $\bar{N} = 100$.

The incoherent part of the effective dynamics now reads:

$$\begin{aligned}
\mathcal{D}_m^{\text{eff}}\hat{\rho}_m = \sum_{\ell=1}^{L} \Gamma_m \Big((\bar{N} + 1)\mathcal{D}[\hat{d}_\ell]\hat{\rho}_m + \bar{N}\mathcal{D}[\hat{d}_\ell^\dagger]\hat{\rho}_m \Big) \\
+ \sum_k \Big(\Gamma_k(+\Omega_m)\mathcal{D}[\tilde{d}_k]\hat{\rho}_m + \Gamma_k(-\Omega_m)\mathcal{D}[\tilde{d}_{-k}^\dagger]\hat{\rho}_m \Big).
\end{aligned} \qquad (3.13)$$

The collective jump operators are given by the Fourier modes $\tilde{d}_k = \frac{1}{\sqrt{L}}\sum_\ell e^{-ik\ell}\hat{d}_\ell$ with $k \in \{n \times 2\pi/L\}_{n=0}^{L-1}$ and are responsible for dissipation taking place in the reciprocal space at a rate

$$\Gamma_k(\omega) = \frac{|G|^2\kappa}{(\omega + J\cos(k+\phi) + \widetilde{\Delta})^2 + (\kappa/2)^2}. \qquad (3.14)$$
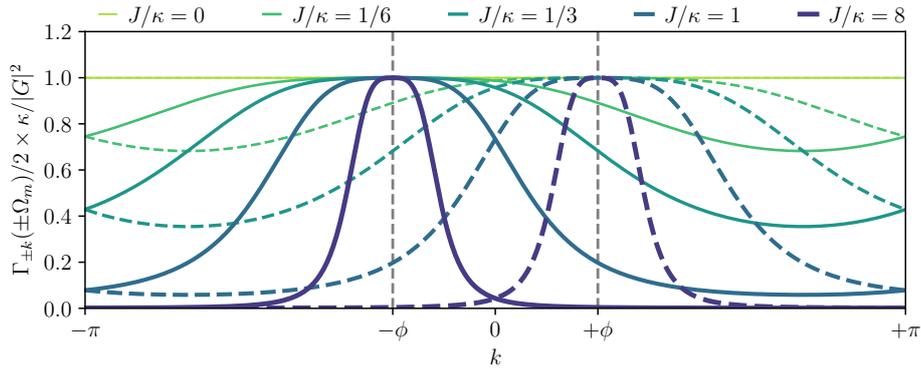
Figure 3.5: Gain $\Gamma_{-k}(-\Omega_m)$ (dashed) and loss $\Gamma_k(+\Omega_m)$ rates induced by the engineered reservoir for various J/κ. $\widetilde{\Delta} = +\Omega_m - J$ for the gain rate and $\widetilde{\Delta} = -\Omega_m - J$ for the loss rate. Here $L = 8$, the rest of parameters are given in the text.

Just as in the homogeneous case, our system has L Stokes sidebands at $\widetilde{\Delta}_k^{(-)} = \Omega_m - J\cos(k - \phi)$ and L anti-Stokes sidebands at $\widetilde{\Delta}_k^{(+)} = -\Omega_m - J\cos(k - \phi)$, that can be employed to respectively amplify or cool down collective mechanical modes. As appears in Eq. (3.13), to any given pair of reservoir resonances $\widetilde{\Delta}_k^{(\pm)}$, correspond an anti-Stokes process at wavevector k and a Stokes process at wavevector $-k$. In Fig. 3.5 we show the k-space asymmetry between the incoherent gain and loss rates for $\phi \neq 0$ around the lowest Stokes and anti-Stokes sidebands. Therefore, depending on the detuning, the engineered optical reservoir acts onto the system by either absorbing collective excitations with pseudomomentum $k \sim -\phi$ (jump operator $\tilde{d}_k$) or creating excitations with opposite momentum $k \sim +\phi$ (jump operator $\tilde{d}_{-k}^\dagger$). Let us stress that this is not the result of the optical driving being at resonance with any particular k mode as it holds when the dissipation rate is of the order of the width of the optical lattice's spectrum ($J \sim \kappa$). In such a regime, the concept of resonance has no longer any operative meaning.

Let us now investigate the steady state properties of this effective model by diagonalising the Liouvillian in the Fourier normal-mode basis as $\hat{H}_m^{\text{eff}} = \sum_k \Omega_k \tilde{d}_k^\dagger \tilde{d}_k$ and $\mathcal{D}_m^{\text{eff}}\hat{\rho}_m = \sum_k \left(\Gamma_k^{(\downarrow)} \mathcal{D}[\tilde{d}_k]\hat{\rho}_m + \Gamma_k^{(\uparrow)} \mathcal{D}[\tilde{d}_k^\dagger]\hat{\rho}_m \right)$, with

$$\Omega_k = \Omega_m + \sum_\pm \frac{|G|^2 (\pm\Omega_m + \widetilde{\Delta} + J\cos(k \pm \phi))}{(\pm\Omega_m + \widetilde{\Delta} + J\cos(k \pm \phi))^2 + (\kappa/2)^2}, \tag{3.15}$$

$$\Gamma_k^{(\downarrow)} = \Gamma_m(\bar{N} + 1) + \Gamma_k(+\Omega_m) , \quad \Gamma_k^{(\uparrow)} = \Gamma_m \bar{N} + \Gamma_{-k}(-\Omega_m). \tag{3.16}$$

Both the unitary and the dissipative parts of the Liouvillian are no longer even in k space for finite ϕ, as a result of having explicitly broken the parity symmetry of the coupling to the reservoir. The unitary effect is illustrated in Fig. 3.6 (a). As the phase gradient ϕ is chosen finite, the dispersion relation of the normal lattice-modes acquires a Lamb frequency shift centered around $k = \mp\phi$ close to either sidebands. In particular, we show in Fig. 3.6 (b) the dispersion relation when the driving laser is operated around the lowest anti-Stokes sideband ($\widetilde{\Delta} = -J - \Omega_m - \kappa/2$). This shows that the ground state of the system has a finite momentum $k_{\text{GS}} = -\phi$ and that it is located at the maximum of the sideband cooling effect. While this has strong consequences in the transport properties of
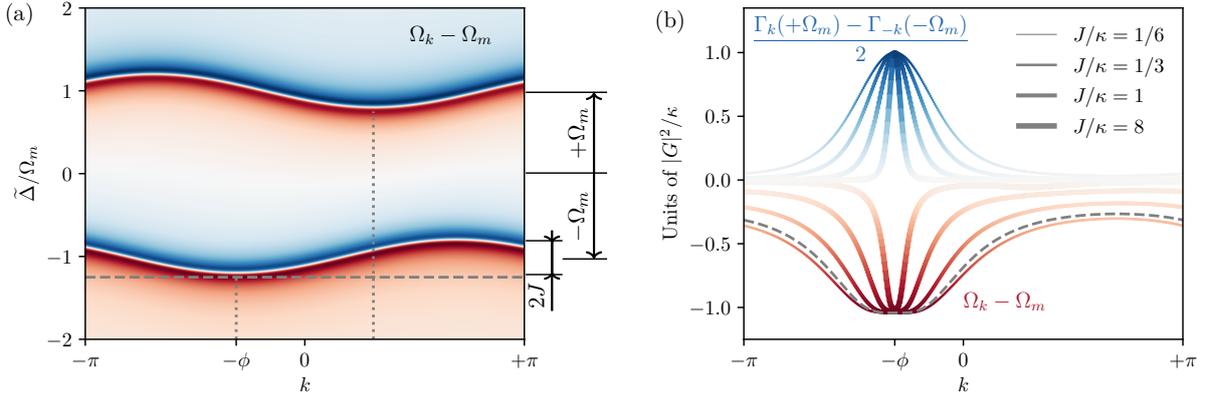
Figure 3.6: Parity asymmetry of the effective model. (a) Effect of the Lamb shift on the dispersion relation of the normal modes of the ring in units of $|G|^2/\kappa$. Here $J = 2\kappa$. (b) Dispersion relation and optically induced damping at $\widetilde{\Delta} = -J - \Omega - \kappa/2$ (dashed cut in panel (a)) for increasing values of the intercavity coupling J. Here $L = 32$, the rest of parameters are given in the text.

closed systems, here the fate of the system is completely ruled by the strong dissipative effects occurring therein. The steady state of the mechanical part reads:

$$\hat{\rho}_{\text{ss}} = \bigotimes_k \frac{e^{-\beta_k \Omega_k \tilde{d}_k^\dagger \tilde{d}_k}}{1 - e^{-\beta_k \Omega_k}}, \quad T_k = \frac{\Omega_k}{\log\left(\Gamma_k^{(\downarrow)}/\Gamma_k^{(\uparrow)}\right)}. \tag{3.17}$$

From this, any operator can be evaluated. In particular, the steady-state thermal-phonon occupations are given by the Planck distribution:

$$\langle \tilde{d}_k^\dagger \tilde{d}_k \rangle_{\text{ss}} = \frac{1}{e^{\beta_k \Omega_k} - 1} = \frac{\Gamma_k^{(\uparrow)}}{\Gamma_k^{(\downarrow)} - \Gamma_k^{(\uparrow)}}. \tag{3.18}$$

IV Discussion

The phase gradient of the drive yields a permanent directional heat flow around the ring of disks. Indeed, the continuity equation satisfied by the phonon number operator,

$$i[\hat{H}_m^{\text{eff}}, \hat{d}_\ell^\dagger \hat{d}_\ell] = -\sum_p (\hat{\jmath}_{\ell \to \ell - p} + \hat{\jmath}_{\ell \to \ell + p}), \tag{3.19}$$

with

$$\hat{\jmath}_{\ell \to \ell + p} = -\sum_\pm \frac{J_p^{(\pm)}}{2i} (\hat{d}_{\ell + p}^\dagger \hat{d}_\ell e^{\mp i \phi p} - \text{H.c.}), \tag{3.20}$$

induces the following definition for a net circulating-current operator for the thermal phonons:

$$\hat{\jmath}_C = \sum_{\ell=1}^L \sum_{p \geq 1} \hat{\jmath}_{\ell \to \ell + p} = -\sum_k \sum_{p \geq 1} \sum_\pm J_p^{(\pm)} \sin(p(k \pm \phi)) \tilde{d}_k^\dagger \tilde{d}_k. \tag{3.21}$$
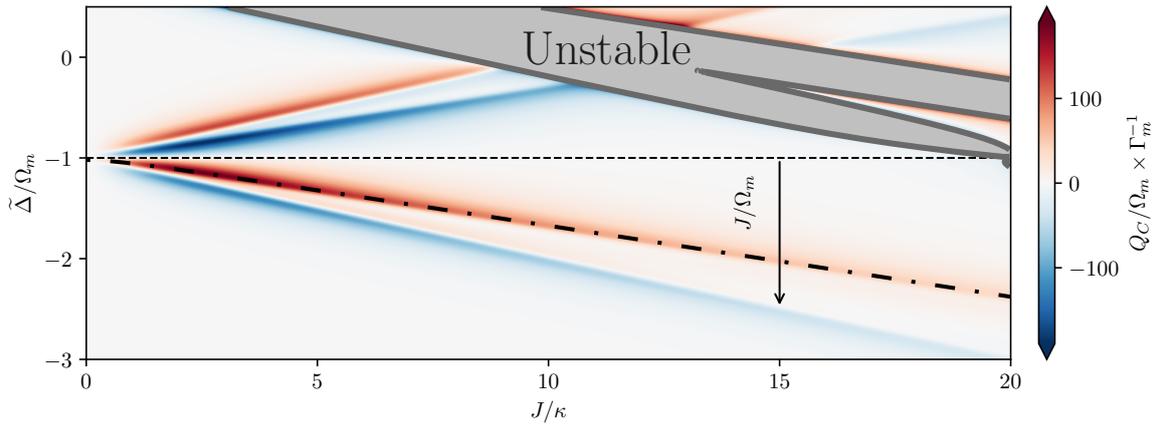
Figure 3.7: Predicted net permanent heat current Q_C in units of $\Omega_m \times \Gamma_m$ around a ring of cavity-coupled optomechanical resonators as a function of the intercavity coupling and the detuning. The system is unstable in the grey region. The maximum current is found through the dash-dotted line. The lowest anti-Stokes sideband lies below, and is here identified by the arrow.

This includes all contributions corresponding to phonons flowing in one sense by jumps between p-distant sites. The expectation value of this operator can be experimentally determined by measuring the thermal populations $\langle \tilde{d}_k^\dagger \tilde{d}_k \rangle$, for example, from the L sidebands in the mechanical noise spectrum measured at the output of some local resonator. In optomechanical disk resonators, a secondary optical mode, such as a higher-order whispering gallery mode of the disk, could be used for that purpose. For our effective model, we get:

$$\langle \hat{j}_C \rangle_{\text{ss}} = -\sum_k \frac{\sum_{p \geq 1} \sum_\pm J_p^{(\pm)} \sin(p(k \pm \phi))}{\Gamma_k^{(\downarrow)} / \Gamma_k^{(\uparrow)} - 1}. \qquad (3.22)$$

The net permanent heat current whirling around the ring is thus simply $Q_C = \Omega_m \langle \hat{j}_C \rangle_{\text{ss}}$. The amount of this heat transported over a phonon lifetime is shown in single-phonon energy units in Fig. 3.7 as a function of $\widetilde{\Delta}/\Omega_m$ and J/κ. Its sign (propagation direction) crucially depends on the detuning. Indeed, as occurred with the local optical spring effect, the cavity-mediated coupling changes sign when crossing a sideband. Regions in gray correspond to sets of parameters for which the system is unstable. This includes the emergence of bistability in the optical reservoir and the dynamical instability of the mechanics close to the Stokes sidebands, wherever the overall gain $\Gamma_k^{(\uparrow)}$ exceeds the dissipation $\Gamma_k^{(\downarrow)}$ at any of the mechanical modes.

In Fig. 3.8 (a), we show the behaviour of each contribution $Q_{\ell \to \ell + p} = \Omega_m \sum_\ell \langle \hat{j}_{\ell \to \ell + p} \rangle$ to the total flow as a function of J when the detuning $\widetilde{\Delta}$ is adjusted to follow its maximum (dash-dotted line of Fig. 3.7). Interestingly, Q_C is nonmonotonic in J/κ. For $J \lesssim \kappa$, optical fluctuation quanta mediating the heat transport are short lived ($\tau_c \lesssim 1/J$) and are thus destroyed before reaching sites farther than their nearest neighbours. This implies that the only sizeable contribution is that flowing by local steps in the clockwise direction. Conversely, for $J \gtrsim \kappa$, optical fluctuation quanta can be scattered farther across the optical lattice before being destroyed by the cavity losses and the permanent heat flow is

Figure 3.8: (a) Contributions $Q_{\ell\to\ell+p} = \Omega_m\sum_\ell\langle\hat{j}_{\ell\to\ell+p}\rangle$ and net directional heat flow $Q_C = \sum_{p\geq 1}Q_{\ell\to\ell+p}$ along the dash-dotted line of Fig. 3.7 as predicted by our effective theory (lines) and mean field (circles). (b) Sketch of the two leading contributions in (a). (c) Gradual triggering of off-diagonal coherence $g_{\ell,\ell+p}^{(1)} = \langle\hat{d}_\ell^\dagger\hat{d}_{\ell+p}\rangle/(\langle\hat{d}_\ell^\dagger\hat{d}_\ell\rangle\langle\hat{d}_{\ell+p}^\dagger\hat{d}_{\ell+p}\rangle)^{1/2}$ along the lowest anti-Stokes sideband $\tilde{\Delta} = -J - \Omega_m$.
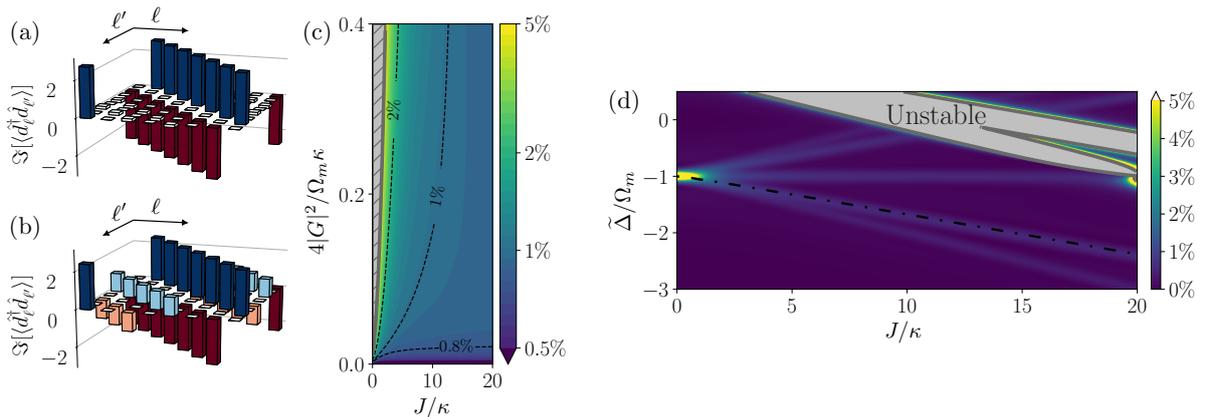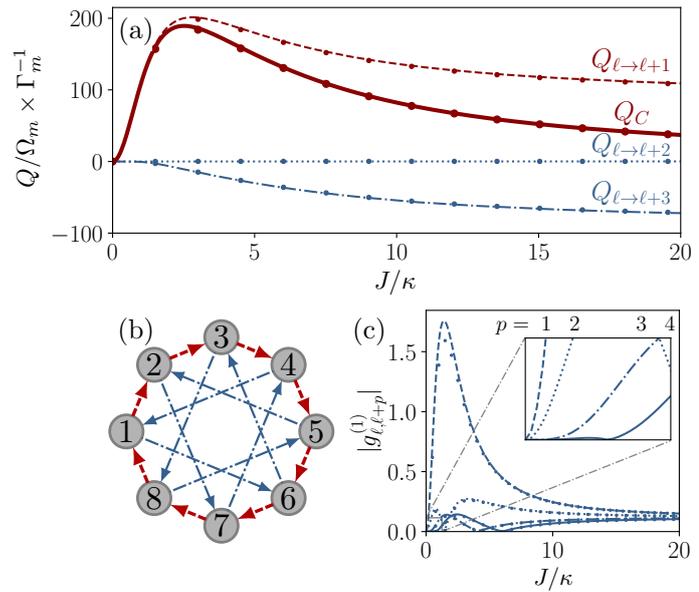
Figure 3.9: Imaginary part of the steady-state single-particle density matrix predicted by the effective theory as given by Eq. 3.24 for $L = 8$, $\phi = 2 \times 2\pi/L$, $|\tilde{\alpha}|^2 = 100$, $\tilde{\Delta} = -J - \Omega_m$, $g/\Omega_m = 1 \times 10^{-2}$, $\kappa/\Omega_m = 1 \times 10^{-1}$, $\Gamma_m/\Omega_m = 1 \times 10^{-3}$, $\bar{N} = 10$ and $J/\kappa = 1$ (a) and $J/\kappa = 5$ (b). Relative errors δ are 1.0% (a) and 0.7% (b). (c) δ as a function of the effective optomechanical coupling and the intercavity coupling for $L = 8$, $\phi = 2\pi/L$, $|\tilde{\alpha}|^2 = 100$, $\tilde{\Delta} = -J - \Omega_m - \kappa/2$, $\kappa/\Omega_m = 1 \times 10^{-1}$, $\Gamma_m/\Omega_m = 1 \times 10^{-3}$ and $\bar{N} = 100$. $\delta \geq 5\%$ in the dashed region. (d) Relative error δ associated to the Fig. 3.7.

supported on supplementary directed graphs (see Fig. 3.8 (b)). In this case, a nonlocal anticlockwise flow contributes to the nonmonotonic dependence on J/κ of the net current. Fig. 3.8 (c) shows how longer-range correlations get gradually triggered as the J/κ ratio is increased following the lowest anti-Stokes sideband (see arrow in Figure 3.7).

V Benchmarking the effective description

In order to benchmark our effective description, we compute the exact steady-state covariance matrix of both optical and mechanical fluctuations for the linearised model described by Eq. (3.5) and extract the exact mean-field single-particle density matrix $\sigma_{\ell\ell'} = \langle \hat{d}_\ell^\dagger \hat{d}_{\ell'} \rangle_{\text{ss}}$ as given by:

$$\sigma_{\ell,\ell'}^{\text{MF}} = \lim_{t\to+\infty} \left\langle \hat{\boldsymbol{\phi}} \, \hat{\boldsymbol{\phi}}^\dagger \right\rangle_{L+\ell,L+\ell'}, \tag{3.23}$$

where $\hat{\boldsymbol{\phi}} = [\hat{c}_1, \ldots, \hat{d}_1, \ldots, \hat{c}_1^\dagger, \ldots, \hat{d}_1^\dagger, \ldots]^T$, and compare it to the single-particle density matrix of the effective description, as explicitly given by

$$\sigma_{\ell\ell'}^{\text{eff}} = \frac{1}{L} \sum_k \frac{e^{-ik(\ell-\ell')}}{\Gamma_k^{(\downarrow)}/\Gamma_k^{(\uparrow)} - 1}, \tag{3.24}$$

by computing the error $\delta = \|\sigma^{\text{eff}} - \sigma^{\text{MF}}\|_2 / \|(\sigma^{\text{eff}} + \sigma^{\text{MF}})/2\|_2$.

As shown in Fig. 3.8 (a), Fig. 3.8 (a), and Fig. 3.9, the analytical results obtained from the effective theory match well the numerical solution of the linearised dynamics in a wide regime of parameters.

VI Conclusion

We have studied the emergence of spatial correlations and permanent directional heat currents across lattices of optomechanical resonators whose mechanical modes are originally uncoupled. In the above picture, quantum fluctuations of the optical fields mediate effective long-range interactions between mechanical sites of both coherent and dissipative nature, whose range is tunable via the correlation length of the reservoir. A remarkable feature is the possibility to flow arbitrary phonon streams in directions and topologies that seem to contradict common thermodynamic intuition, for example, a permanent phonon heat flow can be generated in the absence of thermal gradient.

More generally, this investigation provides a clear instance of a broader class of physical situations for which a weak coupling to an extended reservoir suffices to alter dramatically the fate of an initially trivial set of independent modes. The effective description presented here introduces an analytical tool for understanding quantum systems interacting via extended close-to-Markovian reservoirs, a realm yet to be fully explored.

The results of this chapter are contained in Ref. [α].

4 Numerical methods for tackling nonlocal dissipation

As we have seen throughout Chapters 2 and 3, the study of the dynamics induced by spatially extended reservoirs involves integrating a master equation with nonlocal jump operators. In this chapter, we will review a few of the most natural ways to address this problem from a numerical perspective. The theoretical investigation of such systems can be approached in a number of ways with varying degree of complexity, from a purely mean-field level to a fully quantum picture, and so can their numerical simulation. The structure of this chapter follows this progression. Sec. I will give an overview of the efforts that have been put forward to overcome the challenges of simulating open quantum systems. These difficulties will then be briefly sketched in Sec. II. In Sec. III and IV, we will adapt standard mean-field approaches and the semiclassical truncated Wigner technique, respectively, to the presence of nonlocal dissipation. Finally, the Monte Carlo wave function approach will be introduced in Sec. V. The discussion of this method will serve as a link with the Chapter 5, devoted to the study of the dynamical corner-space method, whose operating principle will be related to the latter.

I Introduction

The simulation of extended closed quantum many-body systems on a classical computer remains in general a quite complex problem as a result of the size of the Hilbert space growing exponentially with the number of subsystems. This difficulty is all the more challenging in the case of open quantum systems [211]. Indeed, the latter are described by a density matrix whose number of elements scales as the square of the number of components of a pure state vector. This object typically being a dense matrix, the simulation of open quantum systems can quickly become extremely demanding in terms of RAM. Moreover, as opposed to the Hamiltonian that generates the unitary dynamics of closed quantum systems, the master equation is driven by a non-Hermitian Liouvillian superoperator, which further increases the computational complexity of the simulations. All this poses severe bounds on the maximum size of the open quantum systems that may be practically simulated by brute-force methods.

This has encouraged a considerable amount of works aimed at developing new algorithms to overcome these limitations. In the past, mean-field methods have proven very effective in the study of Bose-Einstein condensates [212–214], the phase-diagram investigation of correlated systems [215–218] and the simulation of quantum fluids [13, 219].

Close-to-mean-field techniques such as truncated correlation hierarchies [220–223], linked cluster expansions [224], cluster mean field [190, 225], cluster Gutzwiller [226, 227], truncated phase-space representations [228–231] or Gaussian trajectories [232, 233] have been investigated in boson and spin models. Methods able to capture, at least asymptotically, arbitrary degrees of quantum correlations have also been proposed, by exactly reducing the dimensionality of the problem exploiting exact symmetries of the system [234], by stochastic methods such as Monte Carlo wave function [235–241] and real-time full configuration interaction Monte Carlo [242], or by the corner-space renormalisation method [44–48], recently extended to real-time simulations [γ]. Finally, variational methods [28] have recently furthered the investigation of large open quantum systems by reducing the complexity of simulations to a polynomial scaling in the size of the system by efficiently representing their states with parametrised variational ansätze. This was achieved with a wide variety of ansätze, such as matrix-product states [29], tensor networks for Markovian environments [30–35] and beyond [36], and, more recently, neural-network architectures such as restricted Boltzmann machines [37–41] or autoregressive models [41].

II The Lindblad master equation

II.1 Direct picture

As already introduced in previous chapters, the Lindblad master equation that describes the dynamics of an open quantum a system in contact with its environment bears the form

$$\partial_t \hat{\rho} = \mathcal{L}\hat{\rho} = -i[\hat{H}, \hat{\rho}] + \sum_k \gamma_k \mathcal{D}[\hat{L}_k]\hat{\rho}, \qquad (4.1)$$

where the Liouville superoperator $\mathcal{L}$ acts as the generator of the dynamics and is parametrised by a Hamiltonian operator $\hat{H}$, that drives the coherent dynamics of the system, and a set of superoperatorial dissipators $\mathcal{D}[\hat{L}]\hat{\rho} = \hat{L}\hat{\rho}\hat{L}^\dagger - \frac{1}{2}\{\hat{L}^\dagger\hat{L}, \hat{\rho}\}$, with $\{\hat{L}_k\}_k$ a set of Lindblad jump operators and $\{\gamma_k\}_k$ their associated rates.

Time evolution

For finite-dimensional Hilbert spaces of dimension N, this linear ordinary differential equation (ODE) can be numerically integrated by giving all involved operators a $N \times N$ matrix representation. In particular, for a system made of L n-dimensional identical subsystems, for instance spins $1/2$ ($n = 2$), the matrix is characterised by $N^2 = n^{2L}$ real scalars[1]. This scales as the square of the number components of a pure state vector. This exponential trend poses a limit on the size of the systems that can practically be simulated. Moreover, while operators $\hat{H}$ and $\{\hat{L}_k\}_k$ often have very sparse matrix representations, as they typically involve at most two-site operators, the density matrix is in general dense in the computational basis, in the absence of any particular symmetry[2]. This makes brute-force integration of Eq. (4.1) very demanding in terms of RAM resources, as illustrated in

---

[1]Strictly, $N^2 - 1$, due to the constraint on the trace

[2]A simple counterexample is that of U(1)-symmetric density matrices expressed in the Fock basis. Indeed, for any operator $\hat{\rho}$ symmetric under conjugation by $\hat{U}_\varphi \equiv e^{i\varphi\hat{a}^\dagger\hat{a}}$, one has that $\mathrm{Tr}[\hat{\rho}\hat{a}^{\dagger p}] =$

Fig. 4.1. By way of comparison, the state vector of a 20-spin-1/2 system weighs only 16 megabytes whereas its density matrix counterpart exceeds the terabyte. Still, for smaller systems, this can be done by means of standard ODE solvers. In principle, Eq. (4.1) can be integrated with explicit solvers such as Tsitouras' order-5/4 Runge-Kutta method [243]. Yet, this ODE can become *stiff* when dealing with systems exhibiting very different time scales or at the onset of a first-order phase transition, where the system is in a statistical mixture of metastable states [244]. In this situation, stiff-stable implicit solvers can be employed, such as order-2/3 L-stable Rosenbrock-W methods [245], or A-L stable stiffly-accurate ESDIRK methods with splitting [246]. For most use cases, one can choose methods that handle well reasonably stiff equations, such as the Dormand-Prince's order-5/4 Runge-Kutta method [247], as used by default in the `QuantumOptics.jl` suite [248], or auto-switching methods[3].
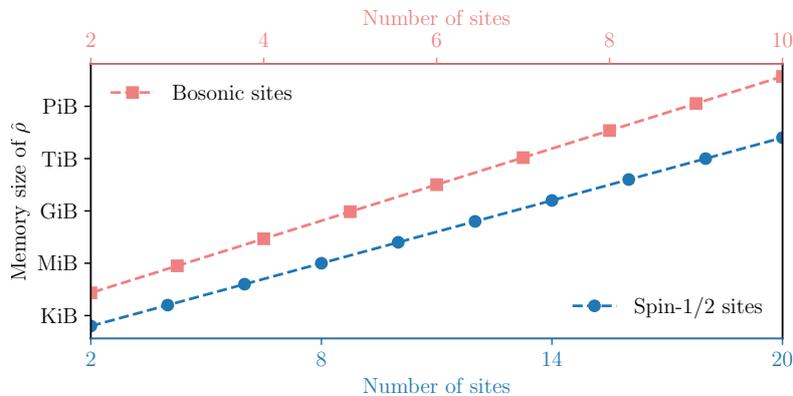
Figure 4.1: Amount of RAM required to store a dense density matrix of an extended system as a function of its number of sites. Light red squares correspond to bosonic sites (top axis), with a local cut-off on the maximum number of excitations per site of $N_{\max} = 5$. Blue circles correspond to spin-1/2 sites (bottom axis). Memory use is expressed in log scale as powers of 1024 bytes.

Steady state solution

In many applications, one only wants to evaluate the steady state of Eq. (4.1). Time-evolving the density matrix for long times, while effective, can be very slow, especially close to a phase transition. Indeed, the long time dynamics of the density matrix, $\hat{\rho}(t) - \hat{\rho}_{\mathrm{ss}} \propto e^{-\mathrm{Re}[\lambda_1]t}$, is governed by the eigenvalue λ_1 of the Liouville superoperator $\mathcal{L}$ with the smallest non-zero real part [250], the steady state being the eigenoperator associated

---

$\mathrm{Tr}[\hat{U}_\varphi \hat{\rho} \hat{a}^{\dagger p} \hat{U}_\varphi^\dagger] = \mathrm{Tr}[\hat{\rho}[\hat{U}_\varphi \hat{a}^\dagger \hat{U}_\varphi^\dagger]^p] = e^{in\varphi}\mathrm{Tr}[\hat{\rho}\hat{a}^{\dagger p}]$, $\forall\varphi$; in particular, by choosing $\varphi = 2\pi/(p+1)$, it follows that $\mathrm{Tr}[\hat{\rho}\hat{a}^{\dagger p}] = 0$, $\forall p$. By now remarking that $\rho_{n,n+p} = \langle n|\hat{\rho}|n+p\rangle = \sqrt{\frac{n!}{(n+p)!}}\mathrm{Tr}[\hat{\rho}\hat{a}^{\dagger p}|n\rangle\langle n|]$ and that $[|n\rangle\langle n|\hat{\rho}, \hat{U}_\varphi] = 0$, for $\hat{\rho}$ U(1)-symmetric, it follows from the first lemma that the density matrix is diagonal: $\rho_{n,n+p} = 0$, $\forall p \neq 0$.

[3]For reference, all these methods may be found under the names of `Tsit5`, `Rosenbrock23`, `KenCarp4` and `DP5`, in order of appearance, in the suite `DifferentialEquations.jl`[249].

to the zero eigenvalue. At a phase transition, this so-called *Liouvillian gap* closes in the thermodynamic limit [244]: $\mathrm{Re}[\lambda_1] \to 0^+$. One has thus to wait for an asymptotically long time. An alternative consists in looking for the solution of the linear system

$$\begin{cases} \mathcal{L}\hat{\rho}_{\mathrm{ss}} = 0, \\ \mathrm{Tr}\hat{\rho}_{\mathrm{ss}} = 1. \end{cases} \tag{4.2}$$

This corresponds to solving for the eigenproblem $\mathcal{L}\hat{\rho} = \lambda\hat{\rho}$ associated to the eigenoperator $\hat{\rho}_{\mathrm{ss}}$ of $\mathcal{L}$ with zero eigenvalue $\lambda = 0$. This can be efficiently solved with matrix-free iterative methods such as BiCGStab(ℓ) [251] or IDR(s) [252, 253] for Hilbert-space sizes typically below ten thousand states.

II.2   Adjoint picture

We just saw some of the intrinsic difficulties related to the classical simulation of the quantum master equation. We saw that direct techniques are very limited in the size of the systems that can be conveniently handled. One simple idea to circumvent the exponential dimensionality of the density matrix is to focus on the time evolution of the expectation values of the observables of interest, simple scalars. We shall now address some of the delicate points that frustrate the scope of this naive approach.

The dynamical equation of any observable $\hat{O}$ is given by the adjoint master equation [99]

$$\partial_t \langle \hat{O} \rangle = \langle \mathcal{L}^\dagger \hat{O} \rangle = \Big\langle i[\hat{H}, \hat{O}] + \sum_k \gamma_k \mathcal{D}^\dagger[\hat{L}_k]\hat{O} \Big\rangle, \tag{4.3}$$

where now $\mathcal{L}^\dagger$ denotes the adjoint Liouville superoperator and $\mathcal{D}^\dagger[\hat{L}]\hat{O} = \hat{L}^\dagger \hat{O}\hat{L} - \frac{1}{2}\{\hat{L}^\dagger\hat{L}, \hat{O}\}$ is the adjoint dissipator, with jump operators in the first term permuted with respect to those in $\mathcal{D}[\hat{L}]$.

The Bogoliubov-Born-Green-Kirkwood-Yvon hierarchy

While this seems to solve completely the issues arising from the high dimensionality of the density matrix, by casting the problem into that of integrating simple scalar fields, the reality is quite different. Indeed, let us consider as an example the time evolution of the second-order moments $\mu_{ij}^{(2)} = \langle \hat{a}_i^\dagger \hat{a}_j \rangle$ of the following many-body toy model:

$$\hat{H} = \frac{U}{2}\sum_i \hat{a}_i^\dagger \hat{a}_i^\dagger \hat{a}_i \hat{a}_i - J(\hat{a}_1^\dagger \hat{a}_2 + \hat{a}_2^\dagger \hat{a}_1), \tag{4.4}$$

with local single-body losses at a rate κ. Here U is the strength of the nonlinearity and J the hopping rate between the two sites. Eq. (4.3) yields

$$\partial_t \mu_{ij}^{(2)} = +iJ(\mu_{\tilde{i}j}^{(2)} - \mu_{i\tilde{j}}^{(2)}) - \kappa\mu_{ij}^{(2)} - iU(\mu_{ijjj}^{(4)} - \mu_{iiij}^{(4)}) \equiv f_2(\mu^{(4)}, \mu^{(2)}), \tag{4.5}$$

with $\tilde{1} = 2$, $\tilde{2} = 1$, and where $\mu_{ijk\ell}^{(4)} = \langle \hat{a}_i^\dagger \hat{a}_j \hat{a}_k^\dagger \hat{a}_\ell \rangle$. From this example, one sees that the system cannot be closed as the nonlinear terms in the adjoint Liouvillian lead to a

hierarchy of coupled dynamical equations of the form

$$\partial_t \mu^{(2)} = f_2(\mu^{(4)}, \mu^{(2)}),$$
$$\vdots \tag{4.6}$$
$$\partial_t \mu^{(n)} = f_n(\mu^{(n+2)}, \ldots).$$

This is known as the Bogoliubov-Born-Green-Kirkwood-Yvon (BBGKY) hierarchy [254–258]. Nonlinear dissipative processes lead to a similar hierarchy [222].

In order to solve this system of coupled equations, one needs to perform a truncation. The simplest truncation scheme corresponds to the mean-field approximation[4]:

$$\mu^{(4)}_{ijk\ell} = \langle \hat{a}_i^\dagger \hat{a}_j \hat{a}_k^\dagger \hat{a}_\ell \rangle \approx \langle \hat{a}_i^\dagger \hat{a}_j \rangle \langle \hat{a}_k^\dagger \hat{a}_\ell \rangle = \mu^{(2)}_{ij} \mu^{(2)}_{k\ell}. \tag{4.7}$$

This approximation assumes the state of the system is close to Gaussian and that its moments can be factorised according to Isserlis' theorem. Truncating next-order moments instead corresponds to the Bogoliubov back-reaction approximation [259–261]:

$$\mu^{(6)}_{ijk\ell mn} = \langle \hat{a}_i^\dagger \hat{a}_j \hat{a}_k^\dagger \hat{a}_\ell \hat{a}_m^\dagger \hat{a}_n \rangle \approx \mu^{(4)}_{ijk\ell} \mu^{(2)}_{mn} + \mu^{(4)}_{ijmn} \mu^{(2)}_{k\ell} + \mu^{(4)}_{k\ell mn} \mu^{(2)}_{ij} - 2\mu^{(2)}_{ij} \mu^{(2)}_{k\ell} \mu^{(2)}_{mn}. \tag{4.8}$$

Higher-order self-consistent truncation schemes can be generated to arbitrary order as described in Ref. [221].

So far, we have seen that simulating open quantum systems from the time evolution of a set of observables of interest is generally subtle. We have then seen that this could be achieved by introducing some simplifying assumptions on the statistics of the density matrix of the system. We shall now see how these ideas translate to the simulation of quantum systems in contact with extended reservoirs. We will first start this discussion from the mean-field level.

III Mean field

Let us consider a bosonic system consisting in a set of sites, described by a set of annihilation operators $\{\hat{a}_i\}_i$, in contact with an extended Markovian reservoir. This is well described by a master equation of the form:

$$\partial_t \hat{\rho} = -i\big[\hat{H}_{\mathrm{S}}, \hat{\rho}\big] + \mathcal{D}_{\mathrm{S}}\hat{\rho} + \mathcal{L}_{\mathrm{ER}}\hat{\rho}, \tag{4.9}$$

where $\hat{H}_{\mathrm{S}}$ and $\mathcal{D}_{\mathrm{S}}$ are the system's bare Hamiltonian and dissipator, and $\mathcal{L}_{\mathrm{ER}}$ the Liouvillian describing all the coherent and incoherent processes induced by the extended reservoir. As identified by Eq. (2.12), the latter is of the following general Lindblad form:

$$\mathcal{L}_{\mathrm{ER}}\hat{\rho} = -i\Big[\textstyle\sum_{ij\alpha}\Omega^{(\alpha)}_{ij}\hat{s}_i^\dagger(\omega_\alpha)\hat{s}_j(\omega_\alpha), \hat{\rho}\Big] + \sum_{k,\alpha}\Gamma^{(\alpha)}_k \mathcal{D}[\textstyle\sum_j U^{(\alpha)}_{kj}\hat{s}_j(\omega_\alpha)]\hat{\rho}. \tag{4.10}$$

Here, $\mathbf{\Omega}^{(\alpha)}$ was a nonlocal Lamb shift, related to the anti-Hermitian part of the two-point susceptibility of the reservoir $\mathbf{S}^{(\alpha)}$. The set of dissipation rates $\{\Gamma^{(\alpha)}_k/2\}_k$ was obtained as

---

[4]Here no squeezing was assumed.

the eigenvalues of the Hermitian part $\mathbf{\Gamma}^{(\alpha)}/2$ of this same susceptibility. These rates were associated to a set of nonlocal jump operators $\{\sum_j U_{kj}^{(\alpha)}\hat{s}_j(\omega_\alpha)\}_k$, expressed in terms of the unitary matrix $\mathbf{U}^{(\alpha)}$ diagonalising $\mathbf{\Gamma}^{(\alpha)}/2$. The operator $\hat{s}_i(\omega_\alpha)$ was a ladder operator acting on the system at site i by inducing a transition $\omega \to \omega' = \omega - \omega_\alpha$ between two eigenstates of the system's bare Hamiltonian. Their specific operatorial expression depends on the specific reservoir-system coupling Hamiltonian under consideration.

For any system operator of interest $\hat{O}$, this Liouvillian results into a very simple dynamical equation:

$$\left\langle \mathcal{L}_{\mathrm{ER}}^\dagger \hat{O} \right\rangle = \left\langle i\left[\sum_{ij\alpha}\Omega_{ij}^{(\alpha)}\hat{s}_i^\dagger(\omega_\alpha)\hat{s}_j(\omega_\alpha), \hat{O}\right] + \sum_{k,\alpha}\Gamma_k^{(\alpha)}\mathcal{D}^\dagger[\sum_j U_{kj}^{(\alpha)}\hat{s}_j(\omega_\alpha)]\hat{O} \right\rangle \tag{4.11}$$

$$= \sum_{ij,\alpha}\left\langle i\left[(\Omega_{ij}^{(\alpha)} - i\Gamma_{ij}^{(\alpha)}/2)\hat{s}_i^\dagger(\omega_\alpha)\hat{s}_j(\omega_\alpha), \hat{O}\right]\right\rangle = \sum_{ij,\alpha}\left\langle \left[S_{ij}^{(\alpha)}\hat{s}_i^\dagger(\omega_\alpha)\hat{s}_j(\omega_\alpha), \hat{O}\right]\right\rangle.$$

Then, one has that the dynamical equation ruling the time evolution of any system operator is given by

$$\partial_t\langle\hat{O}\rangle = \left\langle i\left[\hat{H}_{\mathrm{S}} - i\sum_{ij,\alpha}S_{ij}^{(\alpha)}\hat{s}_i^\dagger(\omega_\alpha)\hat{s}_j(\omega_\alpha), \hat{O}\right] + \mathcal{D}_{\mathrm{S}}^\dagger\hat{O}\right\rangle.$$

Upon setting the ladder operators corresponding to any particular problem of interest and replacing $\hat{O}$ by an nth-order moment, this expression has a form suitable for performing, if necessary, any of the truncation schemes presented above. In particular, by splitting the moments according to Eq. (4.7), one obtains a set of closed mean-field equations.

III.1   Quantum Langevin equation

In practice, truncation schemes such as those presented above can reveal to be cumbersome and inflexible. Another mean-field strategy, of wider interest, relies on the Bogoliubov approximation of the quantum Langevin equation (2.26).

To simplify matters, let us from now on consider the case of a lattice of bosonic sites linearly coupled to an extended reservoir. As given by Eq. (2.26), this is described by a quantum Langevin equation of the form

$$\partial_t\hat{a}_i = i\left[\hat{H}, \hat{a}_i\right] - i\sum_j(\Omega_{ij} - i\Gamma_{ij}/2)\hat{a}_j + \hat{\xi}_i, \tag{4.12}$$

with $\mathbf{\Omega}$ a non-local Lamb shift, $\mathbf{\Gamma} = \mathbf{\Gamma}^{(\downarrow)} - \mathbf{\Gamma}^{(\uparrow)}$ a net nonlocal dissipation rate, both depending on the parameters of the reservoir, and $\{\hat{\xi}_i\}_i$ a set of spatially correlated quantum noise operators whose statistical properties were identified in Eq. (2.28) as

$$\langle\hat{\xi}_i(t)\rangle = 0, \quad \langle[\hat{\xi}_i(t), \hat{\xi}_j^\dagger(t')]\rangle = \Gamma_{ij}\delta(t - t'), \quad \langle\hat{\xi}_i^\dagger(t)\hat{\xi}_j(t')\rangle = \Gamma_{ij}^{(\uparrow)}\delta(t - t'). \tag{4.13}$$

We seek a solution to this system in the form of the Bogoliubov approximation [13]

$$\hat{a}_i(t) = \alpha_i(t) + \delta\hat{a}_i(t), \tag{4.14}$$

where $\alpha_i = \langle\alpha_i|\hat{a}_i|\alpha_i\rangle$ is a complex field accounting for the coherent part of the state of the system and $\delta\hat{a}_i = \hat{a}_i - \alpha_i$ is a Gaussian quantum fluctuation operator. The dynamical

equation for the classical field may be easily obtained by taking the expectation value of
Eq. (4.12) over a coherent-state ansatz $|\boldsymbol{\alpha}\rangle = |\alpha_1, \alpha_2, \ldots\rangle$ as

$$\partial_t \langle\boldsymbol{\alpha}|\hat{a}_i|\boldsymbol{\alpha}\rangle = \dot{\alpha}_i = i \langle\boldsymbol{\alpha}|[\hat{H}, \hat{a}_i]|\boldsymbol{\alpha}\rangle - i \sum_j (\Omega_{ij} - i\Gamma_{ij}/2)\alpha_j. \tag{4.15}$$

By considering, without loss of generality, a Hamiltonian given as a function of normally
ordered strings of bosonic operators $\hat{H} = H[\hat{\boldsymbol{a}}, \hat{\boldsymbol{a}}^\dagger]$, one finally obtains for the classical
part a possibly nonlinear ordinary differential equation reminiscent of the Gross-Pitaevskii
equation:

$$\dot{\alpha}_i = -i\partial_{\alpha_i^\star} H[\boldsymbol{\alpha}, \boldsymbol{\alpha}^\star] - i \sum_j (\Omega_{ij} - i\Gamma_{ij}/2)\alpha_j. \tag{4.16}$$

This classical component completely misses the squeezing of the state of the system as well
as its thermal occupation. This is captured by the dynamical equation of the quantum
fluctuation field:

$$\partial_t \hat{\boldsymbol{A}} \simeq -i(\mathbf{H} + \boldsymbol{\Omega})\hat{\boldsymbol{A}} - \boldsymbol{\Gamma}/2)\hat{\boldsymbol{A}} + \hat{\boldsymbol{\Xi}}. \tag{4.17}$$

where $\hat{\boldsymbol{A}} = (\delta\hat{a}_1, \ldots, \delta\hat{a}_1^\dagger, \ldots)^T$, $\hat{\boldsymbol{\Xi}} = (\hat{\xi}_1, \ldots, \hat{\xi}_1^\dagger, \ldots)^T$, and where anharmonicities of order
$\mathcal{O}(\delta\hat{a}^3)$ were neglected in the Hamiltonian[5]. This is here expressed in terms of the following
(Hermitian) Hessian matrix:

$$\mathbf{H} = \begin{bmatrix} \mathrm{H}^{(\mathrm{I})} & \mathrm{H}^{(\mathrm{II})} \\ \mathrm{H}^{(\mathrm{II})\star} & \mathrm{H}^{(\mathrm{I})T} \end{bmatrix}, \quad H_{ij}^{(\mathrm{I})} = \frac{1}{2}\partial_{\alpha_i^\star}\partial_{\alpha_j} H_{\mathrm{R}}^{(0)}[\boldsymbol{\alpha}, \boldsymbol{\alpha}^\star], \quad H_{ij}^{(\mathrm{II})} = \partial_{\alpha_i^\star}\partial_{\alpha_j^\star} H_{\mathrm{R}}^{(0)}[\boldsymbol{\alpha}, \boldsymbol{\alpha}^\star]. \tag{4.18}$$

Equations (4.16) and (4.17) provide a mean-field description of the system that cap-
tures both the coherent and the (possibly squeezed) thermal populations.

III.2   Lyapunov equation

One is often interested in the steady state of the system under consideration. At mean-
field level, it is described by a Gaussian density matrix and thus the expectation values of
all observables may be determined from the two first moments $\tilde{\alpha}_i = \langle\hat{a}_i\rangle_{\mathrm{ss}}$ and $\langle\hat{\boldsymbol{A}}\hat{\boldsymbol{A}}^\dagger\rangle_{\mathrm{ss}}$.
Both of these may be obtained from the above description.

It follows from Eq. (4.16) that the first can be obtained by solving the possibly non-
linear equation

$$-i\partial_{\tilde{\alpha}_i^\star} H[\tilde{\boldsymbol{\alpha}}, \tilde{\boldsymbol{\alpha}}^\star] - i \sum_j (\Omega_{ij} - i\Gamma_{ij}/2)\tilde{\alpha}_j = 0. \tag{4.19}$$

This can then be substituted into Eq. (4.18) to obtain the steady-state Hamiltonian $\tilde{\mathbf{H}}$ of
the quantum fluctuations. The steady-state solution of the quantum covariance can then
be obtained by setting its time derivative to zero. It follows from Eq. (4.17) that

$$\partial_t \langle\hat{\boldsymbol{A}}\hat{\boldsymbol{A}}^\dagger\rangle_{\mathrm{ss}} = \mathbf{P}\langle\hat{\boldsymbol{A}}\hat{\boldsymbol{A}}^\dagger\rangle_{\mathrm{ss}} + \langle\hat{\boldsymbol{A}}\hat{\boldsymbol{A}}^\dagger\rangle_{\mathrm{ss}}\mathbf{P}^\dagger + \boldsymbol{\Gamma}\mathbf{C} = 0, \tag{4.20}$$

where $\mathbf{P} = -i(\tilde{\mathbf{H}} + \boldsymbol{\Omega}) - i\boldsymbol{\Gamma}/2$ and $\boldsymbol{\Gamma}\mathbf{C} = \mathrm{d}t\langle\hat{\boldsymbol{\Xi}}\hat{\boldsymbol{\Xi}}^\dagger\rangle_{\mathrm{ss}}$, as given by

$$\mathbf{C} = \begin{bmatrix} \boldsymbol{\Gamma}^{-1}\boldsymbol{\Gamma}^{(\uparrow)} & \mathbf{0} \\ \mathbf{0} & \boldsymbol{\Gamma}^{-1}\boldsymbol{\Gamma}^{(\downarrow)} \end{bmatrix}. \tag{4.21}$$

---

[5]Notice that the method induces no approximation in the case of a quadratic Liouvillian.

The form of the Eq. (4.20) is known as the Lyapunov equation and is bound to fundamental concepts in stability analysis [262]; the negativity of the real part of all eigenvalues of $\mathbf{P}$ provides us with a stability criterion for the system. Then, upon introducing the Lyapunov superoperator $\hat{\Lambda}\mathbf{X} = \mathbf{P}\mathbf{X} + \mathbf{X}\mathbf{P}^{\dagger}$, the steady-state covariance can be expressed analytically as follows

$$\langle \hat{\boldsymbol{A}}\hat{\boldsymbol{A}}^{\dagger}\rangle_{\text{ss}} = -\hat{\Lambda}^{-1}\boldsymbol{\Gamma}\mathbf{C}. \tag{4.22}$$

In principle, this solution can be obtained by explicitly inverting the Lyapunov superoperator in matrix representation. This is convenient for small systems. Another approach consists in proceeding as we did for determining the steady-state density matrix of a Liouvillian in Eq. (4.2) by solving for $\hat{\Lambda}\langle \hat{\boldsymbol{A}}\hat{\boldsymbol{A}}^{\dagger}\rangle_{\text{ss}} = -\boldsymbol{\Gamma}\mathbf{C}$ via matrix-free iterative methods such as BiCGStab(ℓ) [251] or IDR(s) [252, 253]. This makes the technique capable of solving for the steady state of several thousand bosonic sites.

This technique captures all of the quantum features of quadratic open quantum models. It has thus been extensively exploited to investigate entanglement of multipartite Gaussian states, notably in the context of optomechanics [79, 263–265], or dynamical effects beyond the rotating wave approximation [266, 267].

IV   Close to mean field

As we have seen this far, the main numerical limitations in the efficient simulation of open quantum systems stems from the high dimensionality of the objects involved, namely the density matrix and the Liouvillian superoperator. The reason for this is that their non-commutativity was encoded into matrix representations whose dimension scales rather unfortunately with the size of the system. A way around this is the phase-space formulation of quantum mechanics [268]. In this picture, the density matrix can be represented by a quasi-probability distribution [175, 269–271] with properties reminiscent from classical statistical mechanics [272, 273]. Accordingly, operators can be expressed as differential operators and their expectation values take the form of an ensemble mean of a scalar field over this quasi-probability distribution [274, 275].

IV.1   Phase-space representation

In this subsection, we will give a phase-space description of the density matrix of a bosonic system and show how its master equation may be expressed as a partial differential equation on a quasi-probability distribution depending on scalar phase-space coordinates.

The density matrix

Let us consider a single quantum (an)harmonic oscillator, as described by bosonic ladder operators $(\hat{a}, \hat{a}^{\dagger})$. The expectation value of an operator $\hat{O}$ on the (mixed) state of the system $\hat{\rho}$, is obtained by the identity

$$\langle \hat{O}\rangle = \text{Tr}[\hat{\rho}\hat{O}]. \tag{4.23}$$

This synthetically encodes both the "classical" ensemble probability, associated to the uncertainty of the specific realisation of the environment the system evolved in contact with, and the "quantum" probability, related to the squared modulus of the coherent components of the wave functions.

Since the seminal work of Wigner [269] in the early thirties, later followed by a set of pioneering papers [270, 272, 273], there has been a significant number of attempts [175, 271] at theorising the correspondence between the above formalism and that of standard statistical mechanics. In a series of papers published in 1969 [274, 275], Cahill and Glauber concluded these efforts in a unified framework. According to this formalism, Eq. (4.23) can be given the following integral expression:

$$\langle \hat{O} \rangle = \overline{O_s} \equiv \int d^2\alpha W_s(\alpha) O_s(\alpha), \tag{4.24}$$

where the first equality is known as the *optical equivalence theorem* [175, 271, 274–277]. Here, $O_s(\alpha)$ is a phase-space representation of the original operator $\hat{O}$, and W_s represents a quasi-probability distribution that associates a weight to each point $(\alpha, \alpha^\star)$ of this phase space. The latter corresponds to a decomposition of the density matrix in the over-complete coherent-state basis $\{|\alpha\rangle\langle\alpha|\}_\alpha$:

$$\hat{\rho} = \int d^2\alpha W_s(\alpha) |\alpha\rangle\langle\alpha|, \tag{4.25}$$

where the index $s \in \{-1, 0, 1\}$ labels three possible equivalent ordering choices leading to such a decomposition. While this distribution is correctly normalised, $\int d^2\alpha W_s(\alpha) = 1$, and Eq. (4.24) bears a great resemblance to a statistical mean, W_s is not a standard probability measure as it violates the first and third Kolmogorov axioms. Indeed, W_s can in principle be non-positive and, as clearly appears from the above decomposition, does not associate probabilities to mutually exclusive states, as $\langle\alpha|\alpha'\rangle \neq 0$, $\forall(\alpha, \alpha') \in \mathbb{C}^2$.

As in standard statistical physics, this quasi-probability distribution and the moment-generating *characteristic function* χ_s are simply related by the following Fourier transform

$$W_s(\alpha) = \int \frac{d^2\alpha'}{\pi^2} \chi_s(\alpha') e^{\alpha'^\star\alpha - \alpha^\star\alpha'}, \quad \chi_s(\alpha) = \text{Tr}[\hat{D}_s(\alpha)\hat{\rho}], \tag{4.26}$$

where $\hat{D}_s(\alpha) = \exp(\alpha\hat{a}^\dagger - \alpha^\star\hat{a} + \frac{1}{2}s|\alpha|^2)$ denotes the *s*-ordered displacement operator:

$$\hat{D}_s(\alpha) = \{\hat{D}(\alpha)\}_s = \sum_{mn} \frac{\alpha^m(-\alpha^\star)^n}{m!n!} \{\hat{a}^{\dagger m}\hat{a}^n\}_s. \tag{4.27}$$

Here, $\{\ldots\}_s$ denotes the *s*-ordering operation that brings strings of ladder operators into anti-normal order ($s = -1$), symmetric ($s = 0$) or normal order ($s = 1$); for instance:

$$\{\hat{a}^\dagger\hat{a}\}_{-1} = \hat{a}\hat{a}^\dagger, \quad \{\hat{a}^\dagger\hat{a}\}_0 = \frac{\hat{a}\hat{a}^\dagger + \hat{a}^\dagger\hat{a}}{2}, \quad \{\hat{a}^\dagger\hat{a}\}_{+1} = \hat{a}^\dagger\hat{a}. \tag{4.28}$$

It follows from Eqs. (4.26) and (4.27) that χ_s is indeed the (*s*-ordered) moment-generating function

$$\langle\{\hat{a}^{\dagger m}\hat{a}^n\}_s\rangle = \partial_\alpha^m(-\partial_{\alpha^\star})^n \chi_s(\alpha)\big|_{\alpha=0}, \tag{4.29}$$

and, thus, that one finally has indeed:

$$\langle \{\hat{a}^{\dagger m}\hat{a}^n\}_s \rangle = \int \mathrm{d}^2\alpha \, W_s(\alpha)\alpha^{\star m}\alpha^n = \overline{\{\hat{a}^{\dagger m}\hat{a}^n\}_s}. \tag{4.30}$$

As we just saw, the quasi-probability function gives a complete scalar description of the state of an open quantum system. The expectation value of any product of ladder operators, and thus any operator, can be evaluated as moments of this distribution. In the following, we will restrict ourselves to the symmetric so-called Wigner distribution, $W \equiv W_0$, whose analytical properties are more adapted to a numerical treatment.

The master equation

We just saw how the density matrix could be expressed as a distribution function of the phase-space coordinates. One now needs to express the master equation in this framework. This requires to identify how the action of an operator onto the density matrix translates in this picture. This can straightforwardly be done from Eq. (4.25), which induces the following simple conversion rules [178]:

$$\begin{aligned} \hat{a}\hat{\rho} &\leftrightarrow (\alpha + \tfrac{1}{2}\partial_{\alpha^\star})W(\alpha), & \hat{\rho}\hat{a} &\leftrightarrow (\alpha - \tfrac{1}{2}\partial_{\alpha^\star})W(\alpha), \\ \hat{a}^\dagger\hat{\rho} &\leftrightarrow (\alpha^\star - \tfrac{1}{2}\partial_{\alpha})W(\alpha), & \hat{\rho}\hat{a}^\dagger &\leftrightarrow (\alpha^\star + \tfrac{1}{2}\partial_{\alpha})W(\alpha). \end{aligned} \tag{4.31}$$

Upon applying this procedure, the master equation finally takes the form of a partial differential equation of the form:

$$\partial_t\hat{\rho} = \mathcal{L}\hat{\rho} \quad \leftrightarrow \quad \partial_t W(\alpha) = \mathcal{F}[\alpha]W(\alpha), \tag{4.32}$$

where the differential operator $\mathcal{F}[\alpha]$ can be interpreted as the quantum counterpart of the Fokker-Planck operator. This approach straightforwardly generalises to the case of many bosonic modes, as we shall next see.

Phase-space representation of the extended-reservoir Liouvillian

Let us consider again the example of the bosonic lattice system linearly coupled to an extended reservoir as we did when discussing the quantum Langevin Eq. (4.12). The associated Liouvillian was given by Eq. (2.25)

$$\mathcal{L}_{\mathrm{ER}}\hat{\rho} = -i\Big[\sum_{ij}\Omega_{ij}\hat{a}_i^\dagger\hat{a}_j, \hat{\rho}\Big] + \sum_k\Big(\Gamma_k^{(+)}\mathcal{D}[\sum_j U_{kj}^{(+)}\hat{a}_j]\hat{\rho} + \Gamma_k^{(-)}\mathcal{D}[\sum_j U_{kj}^{(-)}\hat{a}_j^\dagger]\hat{\rho}\Big). \tag{4.33}$$

By applying the set of rules of Eq. (4.31), this translates as

$$\mathcal{L}_{\mathrm{ER}}\hat{\rho} \quad \leftrightarrow \quad \mathcal{F}_{\mathrm{ER}}W(\boldsymbol{\alpha}), \tag{4.34}$$

with

$$\mathcal{F}_{\mathrm{ER}} = -\partial_{\alpha_i}[(-i\Omega^{ij}-\Gamma^{ij}/2)\alpha_j] - \partial_{\alpha_i^\star}[(+i\Omega^{ij\star}-\Gamma^{ij\star}/2)\alpha_j^\star] + \partial_{\alpha_i}\partial_{\alpha_j^\star}(\Gamma^{(+)ij}+\Gamma^{(-)ji})/2, \tag{4.35}$$

where $\boldsymbol{\Gamma} = \boldsymbol{\Gamma}^{(+)} - \boldsymbol{\Gamma}^{(-)}$.

IV.2 The truncated Wigner approximation

We have seen that the phase-space representation of the master equation takes the form of a partial differential equation (PDE) on a quasi-probability distribution. We determined the representation of the extended-reservoir Liouvillian as a differential operator acting on the Wigner distribution. This was of the form of a complex Fokker-Planck equation. Yet in the presence of non-harmonicities in the Liouvillian, one cannot give it such a simple interpretation. As a matter of example, let us consider the optomechanical master equation:

$$
\begin{aligned}
\partial_t \hat{\rho} &= -i\Big[\hat{H}, \hat{\rho}\Big] + \kappa \mathcal{D}[\hat{a}]\hat{\rho} + \Gamma_m(\bar{N}+1)\mathcal{D}[\hat{b}] + \Gamma_m \bar{N} \mathcal{D}[\hat{b}^\dagger], \\
\hat{H} &= -\Delta \hat{a}^\dagger \hat{a} + F(\hat{a} + \hat{a}^\dagger) - g\hat{a}^\dagger \hat{a}(\hat{b} + \hat{b}^\dagger) + \Omega_m \hat{b}^\dagger \hat{b}.
\end{aligned}
\tag{4.36}
$$

This translates into the following PDE [278]:

$$
\begin{aligned}
\partial_t W(\alpha, \beta) = &- \partial_\alpha \Big[+i\Delta + ig\alpha(\beta + \beta^\star) - \frac{\kappa}{2}\alpha - iF\Big] W(\alpha, \beta) \\
&- \partial_{\alpha^\star} \Big[-i\Delta - ig\alpha^\star(\beta + \beta^\star) - \frac{\kappa}{2}\alpha^\star + iF\Big] W(\alpha, \beta) \\
&- \partial_\beta \Big[-i\Omega_m\beta - ig\Big(|\alpha|^2 - \frac{1}{2}\Big) - \frac{\Gamma_m}{2}\beta\Big] W(\alpha, \beta) \\
&- \partial_{\beta^\star} \Big[+i\Omega_m\beta + ig\Big(|\alpha|^2 - \frac{1}{2}\Big) - \frac{\Gamma_m}{2}\beta^\star\Big] W(\alpha, \beta) \\
&+ \frac{\kappa}{2}\partial_{\alpha^\star}\partial_\alpha W(\alpha, \beta) + \frac{\Gamma_m}{2}(2\bar{N}+1)\partial_{\beta^\star}\partial_\beta W(\alpha, \beta) \\
&+ i\frac{g}{4}\partial_{\alpha^\star}\partial_\alpha\partial_\beta W(\alpha, \beta) - i\frac{g}{4}\partial_{\alpha^\star}\partial_\alpha\partial_{\beta^\star} W(\alpha, \beta).
\end{aligned}
\tag{4.37}
$$

The above expression no longer has the form of a complex Fokker-Planck equation due to the third-order derivatives appearing in the last line. This instead resembles a third-order Kramers-Moyal expansion [239, 279, 280]. The order of the expansion, in general, depends upon the degree of nonlinearity of the Liouvillian. These higher-order terms make it possible for the Wigner function to become negative on phase-space regions of surface $\Delta x \Delta p$ smaller than the Heisenberg uncertainty $\hbar/2$. At a semiclassical level ($\hbar \to 0$), this effect can be neglected. Then, by truncating the expansion to second order only, one obtains a standard Fokker-Planck equation on a positive probability distribution. This is known as the truncated Wigner approximation. For the most general analytic multivariate distribution $W(\boldsymbol{z})$, this has the general form:

$$
\begin{aligned}
\partial_t W(\boldsymbol{z}) = &- \partial_{z_i}[\mu^i(\boldsymbol{z})]W(\boldsymbol{z}) - \partial_{z_i^\star}[\mu^{i\star}(\boldsymbol{z})]W(\boldsymbol{z}) \\
&+ \partial_{z_i^\star}\partial_{z_j}[D^{ij}(\boldsymbol{z})]W(\boldsymbol{z}) + \frac{1}{2}\partial_{z_i}\partial_{z_j}[E^{ij}(\boldsymbol{z})]W(\boldsymbol{z}) + \frac{1}{2}\partial_{z_i^\star}\partial_{z_j^\star}[E^{ij\star}(\boldsymbol{z})]W(\boldsymbol{z}),
\end{aligned}
\tag{4.38}
$$

where $\boldsymbol{\mu}(\boldsymbol{z})$ corresponds to the drift term of the classical Fokker-Planck equation and $\mathbf{D}(\boldsymbol{z})$ and $\mathbf{E}(\boldsymbol{z})$ are diffusion matrices.

Stochastic unravelling of the Fokker-Planck equation

The solution to this Fokker-Planck equation can be sampled by stochastic trajectories, as given by the following Itō equations of motion[6]

$$\mathrm{d}\boldsymbol{z} = \boldsymbol{\mu}(\boldsymbol{z})\mathrm{d}t + \mathrm{d}\boldsymbol{N}, \tag{4.39}$$

with a possibly multiplicative noise characterised by increments $\mathrm{d}\boldsymbol{N}$ with covariances $\mathrm{d}N_i^\star \mathrm{d}N_j = D_{ij}(\boldsymbol{z})\mathrm{d}t$ and $\mathrm{d}N_i \mathrm{d}N_j = E_{ij}(\boldsymbol{z})\mathrm{d}t$.

Therefore, within the truncated Wigner approximation, Eq. (4.37) can be numerically sampled from the numerical integration of the following scalar stochastic differential equations:

$$\begin{aligned}
\mathrm{d}\alpha &= \Big(i\Delta + ig(\beta + \beta^\star) - \frac{\kappa}{2}\Big)\alpha\mathrm{d}t - iF\mathrm{d}t + \sqrt{\kappa/2}\mathrm{d}W_\alpha, \\
\mathrm{d}\beta &= \Big(-i\Omega_m + ig(|\alpha|^2 - 1/2) - \frac{\Gamma_m}{2}\Big)\beta\mathrm{d}t + \sqrt{\Gamma_m(\bar{N} + 1/2)}\mathrm{d}W_\beta,
\end{aligned} \tag{4.40}$$

where $\mathrm{d}W_\lambda$ are Wiener processes satisfying $\overline{\mathrm{d}W_\lambda^\star \mathrm{d}W_{\lambda'}} = \delta_{\lambda,\lambda'}\mathrm{d}t$ and $\overline{\mathrm{d}W_\lambda^n} = 0$, $\forall n$. Symmetrically-ordered observables $\hat{O} = \{O[\hat{a}, \hat{a}^\dagger, \hat{b}^\dagger, \hat{b}^\dagger]\}_s$ can then be evaluated by numerically integrating these complex Langevin equations over many realisations of the noise. Each realisation r yields a particular trajectory $(\alpha^{(r)}, \beta^{(r)})$ with an associated observable expectation value $O_s^{(r)}$. The final quantum-statistical expectation value can then be computed as the average over all these realisations:

$$\langle \hat{O}(t) \rangle = \overline{O_s(t)} = \lim_{N_{\mathrm{traj}} \to +\infty} \frac{1}{N_{\mathrm{traj}}} \sum_{r=1}^{N_{\mathrm{traj}}} O[\alpha^{(r)}(t), \alpha^{(r)\star}(t), \beta^{(r)}(t), \beta^{(r)\star}(t)]. \tag{4.41}$$

Stochastic unravelling of the extended-reservoir Liouvillian

We can now apply this technique to the phase-space representation of the extended-reservoir Liouvillian (4.35), yielding

$$\mathrm{d}\alpha_i\big|_{\mathrm{ER}} = \sum_j (-i\Omega_{ij} - \Gamma_{ij}/2)\alpha_j\mathrm{d}t + \mathrm{d}N_i, \tag{4.42}$$

with again $\overline{\mathrm{d}N_i^n} = 0$, but now instead a spatially correlated diffusion matrix $\overline{\mathrm{d}N_i^\star \mathrm{d}N_j} = \mathrm{d}t(\Gamma_{ij}^{(+)} + \Gamma_{ji}^{(-)})/2$. Symmetrically-ordered observables $\hat{O} = \{O[\hat{\boldsymbol{a}}, \hat{\boldsymbol{a}}^\dagger]\}_s$ can be evaluated just as before:

$$\langle \hat{O}(t) \rangle = \overline{O_s(t)} = \lim_{N_{\mathrm{traj}} \to +\infty} \frac{1}{N_{\mathrm{traj}}} \sum_{r=1}^{N_{\mathrm{traj}}} O[\boldsymbol{\alpha}^{(r)}(t), \boldsymbol{\alpha}^{(r)\star}(t)]. \tag{4.43}$$

---

[6]This can be straightforwardly checked, by remarking that, for any test function f, $\partial_t \langle f(\boldsymbol{z}) \rangle = \int \mathrm{d}\boldsymbol{z} W(\boldsymbol{z})\mathcal{F}^\dagger f(\boldsymbol{z})$, where $\mathcal{F}^\dagger = \boldsymbol{\mu} \cdot \partial_{\boldsymbol{z}} + \boldsymbol{\mu}^\star \cdot \partial_{\boldsymbol{z}^\star} + D^{ij}\partial_{z_i^\star}\partial_{z_j} + \frac{1}{2}E^{ij}\partial_{z_i}\partial_{z_j} + \frac{1}{2}E^{ij\star}\partial_{z_i^\star}\partial_{z_j^\star}$ follows from Itō's lemma. Then, by remarking that one equivalently has that $\partial_t \langle f(\boldsymbol{z}) \rangle = \int \mathrm{d}\boldsymbol{z} f(\boldsymbol{z})\partial_t W(\boldsymbol{z})$, one finally has, by integration by parts, $\int \mathrm{d}\boldsymbol{z} f(\boldsymbol{z})\partial_t W(\boldsymbol{z}) = \int \mathrm{d}\boldsymbol{z} f(\boldsymbol{z})\mathcal{F}W(\boldsymbol{z})$, for any f, and thus the Fokker-Planck equation $\partial_t W(\boldsymbol{z}) = \mathcal{F}W(\boldsymbol{z})$ of Eq. (4.38).

We have seen that within the truncated Wigner approximation, one can simulate bosonic systems dispensing with the computationally costly matrix representation of the master equation. This requires to be able to compute efficiently large sets of trajectories by integrating stochastic differential equations (SDEs) over as many realisations of the quantum noise as necessary. These trajectories being independent from one another, this can be conveniently performed on superscalar computing architectures. While in principle this numerical integration can be performed by using any SDE solver, it was found though that most conventional solvers fail in matching the right result when dealing with metastability [281]. Unlike these, SOSRA2 and SOSRI2 [282] were shown to faithfully approximate the exact quantum results [230], SOSRA2 being the most computationally efficient. Such simulations can conveniently be done up to roughly 2500 bosonic modes.

V Beyond mean field

So far, we have seen how open quantum systems, and in particular bosonic systems in contact with extended reservoirs, could be efficiently simulated on a classical computer. This was made possible at the cost of performing mean-field or semi-classical approximations. We shall now briefly describe the Monte Carlo wave function (MCWF) algorithm, a method relying on an exact stochastic unravelling of the master equation that circumvents the above-identified RAM-usage bottleneck, allowing one to perform the fully-quantum simulation of reasonably large quantum systems.

V.1 Quantum trajectories

Any measurement protocol can be represented as a set of measurement operators $\{\hat{M}_\mu\}_{\mu=0}^m$, satisfying $\sum_\mu \hat{M}_\mu^\dagger \hat{M}_\mu = \mathbb{1}$. At time t, such a measure induces a partial collapse of the system's state. This is given by the normalised average over all possible measurement outcomes:

$$\hat{\rho}(t) \ \to \ \hat{\rho}(t + \mathrm{d}t) = \sum_\mu \frac{\hat{M}_\mu \hat{\rho}(t) \hat{M}_\mu^\dagger}{p_\mu(t)}, \tag{4.44}$$

where $p_\mu = \langle \hat{M}_\mu^\dagger \hat{M}_\mu \rangle(t)$ is the probability of measuring the μth outcome. By introducing the particular choice of measurement operators:

$$\begin{cases} \hat{M}_0 = \hat{\mathbb{1}} - (i\hat{H} + \hat{L}^\dagger \hat{L}/2)\mathrm{d}t, \\ \hat{M}_1 = \hat{L}\mathrm{d}W, \end{cases} \tag{4.45}$$

where $|\mathrm{d}W|^2 = \mathrm{d}t$, one may easily verify that the density matrix gets updated in time as under the action of the Lindblad master equation:

$$\hat{\rho}(t + \mathrm{d}t) - \hat{\rho}(t) = -i[\hat{H}, \hat{\rho}(t)]\mathrm{d}t + \mathrm{d}t \mathcal{D}[\hat{L}]\hat{\rho}(t). \tag{4.46}$$

The dynamics of an open system can thus be interpreted as the result of a continuous weak measurement of the jump operator $\hat{L}$ by the environment. Given the complete measurement record $r(t)$, such that $r = 1$ when the outcome of $\hat{M}_1$ was measured and

$r = 0$ otherwise, the state of the system can be deduced deterministically. For instance, for a cavity subject to single-body loss, as characterised by $\hat{L} = \hat{a}$, the knowledge of the times t_i at which a boson escaped the system ($r(t_i) = 1$) suffices to completely determine the state of the cavity at any time. The times at which such *quantum jumps* take place are non-deterministic; a specific realisation of the monitored evolution of the system, bound to a specific outcome record, is called a *quantum trajectory*. In this picture, known as monitored dynamics, the density matrix is interpreted as a statistical mixture of pure trajectories resulting from our ignorance of the particular realisation of the outcome record $r(t)$.

The outcome record $r(t)$ is a Poisson stochastic process ($r \in \{0, 1\}$). When $\hat{M}_1$ is measured ($r(t) = 1$), with probability $p_1 = \langle \hat{M}_1^\dagger \hat{M}_1 \rangle(t) = \langle \hat{L}^\dagger \hat{L} \rangle(t)\mathrm{d}t$, the state vector of the system evolves according to

$$|\psi_1(t + \mathrm{d}t)\rangle = \frac{\hat{M}_1 |\psi(t)\rangle}{\sqrt{p_1(t)}} = \frac{\hat{L}}{\sqrt{\langle \hat{L}^\dagger \hat{L} \rangle(t)}} |\psi(t)\rangle . \qquad (4.47)$$

This corresponds to the collapse of the wave function upon the environment having successfully measured the outcome of $\hat{L}$. If instead $\hat{M}_0$ had been measured ($r(t) = 0$), with associated probability $p_0 = 1 - p_1$, the system's state vector would have been updated as

$$|\psi_0(t + \mathrm{d}t)\rangle = \frac{\hat{M}_0 |\psi(t)\rangle}{\sqrt{p_0}} = \left\{ \hat{\mathbb{1}} - \mathrm{d}t\left[i\hat{H} - \frac{1}{2}\hat{L}^\dagger \hat{L} + \frac{1}{2}\langle \hat{L}^\dagger \hat{L} \rangle(t)\right] \right\} |\psi(t)\rangle . \qquad (4.48)$$

Interestingly, it here appears that the knowledge of the absence of measurement of $\hat{L}$ induces a slight collapse of the wave function as well.

By combining these two equations, the evolution of the wave function is given by the following stochastic differential equation [183]:

$$\mathrm{d} |\psi(t)\rangle = (1 - \mathrm{d}r(t)) |\psi_0(t + \mathrm{d}t)\rangle + \mathrm{d}r(t) |\psi_1(t + \mathrm{d}t)\rangle - |\psi(t)\rangle$$
$$= \mathrm{d}t\left(\frac{\langle \hat{L}^\dagger \hat{L} \rangle(t) - \hat{L}^\dagger \hat{L}}{2} - i\hat{H} \right) |\psi(t)\rangle + \mathrm{d}r(t)\left(\hat{L}/\sqrt{\langle \hat{L}^\dagger \hat{L} \rangle(t)} - 1 \right) |\psi(t)\rangle . \qquad (4.49)$$

This describes what is known as a piecewise-deterministic process. The dynamics of the wave function is ruled by a deterministic pseudo-unitary evolution between a set of quantum jumps occurring at random times resulting from the statistics of the stochastic Poisson process r. Particular realisations of this process correspond to conditional single trajectories $\{|\psi^{(i)}\rangle\}_i$. It follows from the above that one indeed recovers the solution of the master Eq. (4.46) by averaging over all possible realisations, erasing the knowledge about the measurement outcome:

$$\hat{\rho}(t) = \lim_{N_{\mathrm{traj}} \to +\infty} \frac{1}{N_{\mathrm{traj}}} \sum_{i=1}^{N_{\mathrm{traj}}} |\psi^{(i)}(t)\rangle\langle\psi^{(i)}(t)| . \qquad (4.50)$$

Thus, any observable may be calculated by averaging over enough trajectories:

$$\mathrm{Tr}[\hat{\rho}(t)\hat{O}] = \lim_{N_{\mathrm{traj}} \to +\infty} \frac{1}{N_{\mathrm{traj}}} \sum_{i=1}^{N_{\mathrm{traj}}} \langle\psi^{(i)}(t)|\hat{O}|\psi^{(i)}(t)\rangle . \qquad (4.51)$$

V.2　Monte Carlo wave function

The Monte Carlo wave function method, independently introduced by Mølmer [236] and Carmichael [239], is grounded on this quantum-trajectory approach [183] to quantum dynamics. It starts from a straightforward generalisation of Eq. (4.49) to the case of many dissipative channels:

$$\mathrm{d}\left|\psi(t)\right\rangle = \mathrm{d}t\Big(\sum_i\langle\hat{L}_i^\dagger\hat{L}_i\rangle(t)/2 - i\hat{H}_{\mathrm{nh}}\Big)\left|\psi(t)\right\rangle + \mathrm{d}r(t)\Big(\sum_i\hat{L}_i/\sqrt{\langle\hat{L}_i^\dagger\hat{L}_i\rangle(t)} - 1\Big)\left|\psi(t)\right\rangle. \quad (4.52)$$

The first term corresponds to a pseudo-unitary evolution of the system's state vector under de action of an effective non-Hermitian Hamiltonian $\hat{H}_{\mathrm{nh}} = \hat{H} - \frac{i}{2}\sum_i\hat{L}_i^\dagger\hat{L}_i$; the second, to a set quantum jumps, $\hat{L}_i\left|\psi(t)\right\rangle$, happening with probabilities $\mathrm{d}p_i = \langle\hat{L}_i^\dagger\hat{L}_i\rangle(t)\mathrm{d}t$. This can be numerically integrated between two time steps t and $t + \delta t$ in the following naive manner:

(i) With probability $1 - \sum_i\delta p_i(t)$, the state is evolved according to the Schrödinger equation:

$$\left|\psi(t + \delta t)\right\rangle = e^{-i\hat{H}_{\mathrm{nh}}\delta t}\left|\psi(t)\right\rangle. \quad (4.53)$$

This indeed induces a loss in the norm of the state vector, $\langle\psi(t+\delta t)|\psi(t+\delta t)\rangle = 1 - \sum_i\delta p_i(t) + \mathcal{O}(\delta t^2)$. The rest of the probability is recovered from the complementary possible outcomes.

(ii) With probability $\delta p_i(t) = \langle\hat{L}_i^\dagger\hat{L}_i\rangle(t)\delta t$, the following jump happens instead:

$$\left|\psi(t + \delta t)\right\rangle = \hat{L}_i\left|\psi(t)\right\rangle / \sqrt{\delta p_i(t)/\delta t}. \quad (4.54)$$

While this algorithm converges to the right solution for $\delta t \to 0^+$, it is far from optimal from a numerical perspective. Beyond the obvious overhead of having to generate random numbers at every time step, this is an explicit first-order method with no obvious way of performing adaptive time-stepping. In practice, modern implementations of this method [248, 283, 284] instead rely on a faster-than-the-clock algorithm [285]:

(i) A random number $p_{\mathrm{jump}} \in [0, 1]$ is generated encoding the probability that a jump occurred;

(ii) $\left|\psi(t)\right\rangle$ is then evolved by integrating the Schrödinger equation $i\partial_t\left|\psi(t)\right\rangle = \hat{H}_{\mathrm{nh}}\left|\psi(t)\right\rangle$ by employing an arbitrary ODE solver until the decreasing norm reaches $\langle\psi(t)|\psi(t)\rangle = 1 - p_{\mathrm{jump}}$;

(iii) at this point, the ith jump operator is chosen at random with probability $p_i(t)/p_{\mathrm{jump}}$. A jump is performed by applying the drawn jump operator and normalising the resulting wave function:

$$\left|\psi(t)\right\rangle \; \to \; \left|\psi'(t)\right\rangle = \hat{L}_i\left|\psi(t)\right\rangle / \sqrt{\langle\hat{L}_i^\dagger\hat{L}_i\rangle(t^-)}. \quad (4.55)$$

This cycle is then repeated until the final time of the simulation is attained.

This algorithm allows one to split the problem of simulating the time evolution of the density matrix into that of simulating a possibly large set of independent quantum trajectories with the complexity of evolving a closed system. It lifts well to superscalar implementations and allows one to rather conveniently perform simulations on systems whose Hilbert space dimension lies roughly below one hundred thousand states, for instance an ensemble of 16 spin-1/2 sites. Yet, several drawbacks are to be considered.

V.3   Suboptimality of the Monte Carlo wave function algorithm

The above-presented method may be challenged in several circumstances. We have seen that, for a Hilbert space of size N, this algorithm reduces the complexity of evolving a $N \times N$ matrix to that of evolving N_{traj} state vectors of length N. We shall discuss whether this number of trajectories always scales favourably by considering a very simple situation.

To make our discussion more formal let us introduce a finite-rank benchmarking density matrix that we aim to sample with trajectories:

$$\hat{\rho}(t) = \sum_{m=1}^{M} p_m(t) \, |\phi_m(t)\rangle\langle\phi_m(t)| \,, \quad \langle\phi_m(t)|\phi_n(t)\rangle = \delta_{m,n}, \quad \forall t. \qquad (4.56)$$

For simplicity, we assume this density matrix to preserve its rank and structure upon time evolution. Then, the optimal time evolution scheme would consist in evolving the M base states of this moving frame $\{|\phi_m(t)\rangle\}_m$ while updating their associated probabilities $\{p_m(t)\}_m$ according to some mass equation, M here being roughly the width of the distribution's support. Two situations then pose problems to the Monte Carlo wave function procedure.

High-entropy scenario

First, consider the simple distribution of eigenvalues $p_m = \frac{1}{M}$, $\forall m \in [1, N]$. In this situation, the number of trajectories must clearly scale as the support of the distribution, $N_{\text{traj}} \sim M$. Provided $M \sim N$, the method is of no help in reducing the complexity of the simulation, yet it scales as the optimal scheme and, therefore, no fully quantum alternative may be found to this problem.

Low-entropy scenario

A second scenario where this method fails is all the more problematic as it is of practical relevance. It is that of systems in very weak coupling with their environment whose state is close to pure ($M \sim 1$). This is the case, for instance, of NISQ-era [49] quantum devices. To describe the shortcomings of the method in addressing this situation, let us consider the case of an initially pure state $|\phi_1\rangle$ that evolves under the action of a weak measurement as given by the jump operator $\hat{L} = \sqrt{\kappa}\hat{\ell}$. This could be for instance the case of a highly populated Fock state subject to single-body dissipation, for which $|\phi_1\rangle = |N \gg 1\rangle$ and

$\hat{\ell} = \hat{a}$. After some time Δt, the state of the system is well described by Eq. (4.56) with

$$|\phi_n\rangle \propto \hat{L}^{n-1} |\phi_1\rangle \,, \quad p_{n+1}/p_1 = \frac{\langle \phi_1 | \hat{\ell}^\dagger \hat{\ell} | \phi_1 \rangle^n (\kappa \Delta t)^n}{n!}. \tag{4.57}$$

For $\kappa\Delta t \ll 1$, the spectrum of the density matrix is very peaked Poisson distribution. The density matrix is a mixture of the original pure state $|\phi_1\rangle\langle\phi_1|$ with a weight $p_1 \simeq 1 - \kappa\Delta t$ and a thermal tail of degraded states accounting for the rest of the probability $\kappa\Delta t$. For $\kappa\Delta t = 0.05$, for instance, the distribution can practically be truncated to two states, with probabilities of $p_1 \approx 0.95$ and $p_2 \approx 0.05$, respectively. The optimal integration scheme should thus be able to proceed by evolving only two states. The situation is very different for the Monte Carlo wave function, which converges poorly to the right distribution, requiring a large amount of trajectories. This is due to the fact that, on average, 95% of the trajectories are identical and correspond to the trivial evolution of a same trajectory $|\phi^{(i)}(t)\rangle = |\phi_1\rangle$, while only 5% explore the thermal tail of interest. 95% of the computing resources are therefore wasted in performing a redundant task.

A rather natural way around this bias problem we just identified in low-entropy systems would be to add importance sampling [286] to the Monte Carlo wave function algorithm. We will address this issue from a different perspective in the next chapter by introducing a novel numerical algorithm: the *dynamical corner-space method.*

5

The dynamical corner-space method

In this chapter, we will introduce the dynamical corner-space algorithm for the time evolution of low-entropy open quantum systems. This method efficiently computes the time evolution of intermediate-scale open quantum systems with moderate entropy with controllable accuracy. It will here be applied to the investigation of the continuous-time dynamics of highly-entangling intermediate-scale quantum circuits in the presence of dissipation and decoherence, beyond digital error models. By compressing the Hilbert space to a time-dependent "corner" subspace that supports faithful representations of the density matrix, a noisy quantum Fourier transform processor with up to 21 qubits will be simulated on a classical computer. The large circuit sizes that can be reached in such simulations will allow us to access the scaling behaviour of the error propagation with the dissipation rates and the number of qubits. Moreover, depending on the dissipative mechanisms at play, the choice of input state will be shown to have a strong impact on the performance of the quantum algorithm.

This chapter is structured as follows: Sec. I provides an overview of the context in which the dynamical corner-space method was devised and the challenges that it attempts to address therein; Sec. II gives a detailed description of the algorithm the method builds upon and of its numerical complexity; in Sec. III, the method is used to simulate realistic noisy quantum circuits within a Lindblad master equation approach and investigate their error behaviour; finally, Sec. IV concludes the chapter.

I Introduction

The tremendous advances on the control of artificial quantum systems, such as superconducting Josephson qubits [287] and trapped ions [288], are allowing dramatic progress towards the realisation of devices for quantum computation [289, 290]. The noisy intermediate-scale quantum (NISQ) era [49] was reached, where error correction is not yet possible due to daunting overheads [291], but where quantum advantage might be already exploited for applications in quantum chemistry [292], optimisation [293] and even finance [294]. Scaling up quantum circuits and designing practically efficient quantum correction protocols make it of crucial importance to precisely understand the effects of both incoherent and coherent sources of noise on quantum algorithms [295–298].

To meet these challenges, there is a strong need for accurate numerical simulations of quantum hardware on classical computers [299–303]. In this perspective, the applic-

ation of tensor-network methods to quantum-circuit simulation has been shown to be effective to model circuits, although with restrictions on the amount of entanglement building up through the circuit [304–308]. Modelling tools capable of describing realistic error sources in experimentally relevant platforms are also fundamental, yet most existing simulators of quantum hardware consider only local and digital error models [289, 291, 309, 310]. In such models, the circuit is represented by a series of subsequently applied unitary operations immediately followed by local error gates whose application is supposed to mimic the degradation of the state due to the environment. While in close proximity with classical error models, these two approximations do not necessarily hold, especially for highly-entangling circuits [311], and remain a challenge in quantum error correction [312]. In general, to account for realistic sources of noise in highly-entangling circuits, one should resort to a continuous-time description, where the environment detrimental action is continuously integrated during the application of the quantum gates. Upon neglecting non-Markovian effects, this can be realised within the framework of the Lindblad master equation [99]. However, as explained in Chapter 4, such a description is numerically expensive; for a chain of L qubits with Hilbert space dimension $N = 2^L$, a density matrix of size $N \times N$ must be evolved. Several proposals to reduce the complexity of the task that do not limit entanglement exist, such as the Monte Carlo wave function method [236, 239, 240] discussed therein, which reduces the problem to evolving many wave functions. However, the number of such trajectories is not known in general [313] and, in the case of weak dissipation, the method can quickly become equivalent to a full integration of the master equation as a greater amount of trajectories are needed to reach convergence. In recent years, there has been a growing interest in the idea that for a certain class of low-entropy systems, a limited number of states spanning a so-called "corner" subspace, can provide with a parsimonious and faithful representation of the density matrix [44, 314–316]. Quantum processors, conceived to be as weakly dissipative as possible and thus lowly entropic, belong to this class; so do stabilised arrays [20, 21], cat qubit systems [317] and quantum hardware with state-of-the-art dissipation rates [49, 289].

In this chapter, we will investigate the continuous-time evolution of noisy intermediate-scale quantum circuits. We will describe a time-dependent corner-space method with no restriction on the degree of entanglement, circuit connectivity, physical dimension or noise correlations and provide results with controllable accuracy. The discussion will focus on the analysis of the role of dissipation and decoherence on the quantum Fourier transform (QFT). This is an essential and highly-entangling quantum circuit at the heart of the Shor algorithm [318], quantum phase estimation [319] and many algorithms related to the hidden-subgroup problem [320]. We will demonstrate the capabilities of the dynamical corner-space method by simulating the dissipative QFT up to 21 qubits with a high accuracy, reporting a speedup of at least three orders of magnitude with respect to a full integration of the master equation. We will see that the infidelity of the output state of the dissipative QFT with respect to the output state of a unitary QFT surprisingly scales polynomially with the system size, with an exponent that does not depend on the dissipation rate. Furthermore, we will explore the impact of different dissipative mechanisms on the fidelity and study how the initial state affects the performance of the quantum computation.
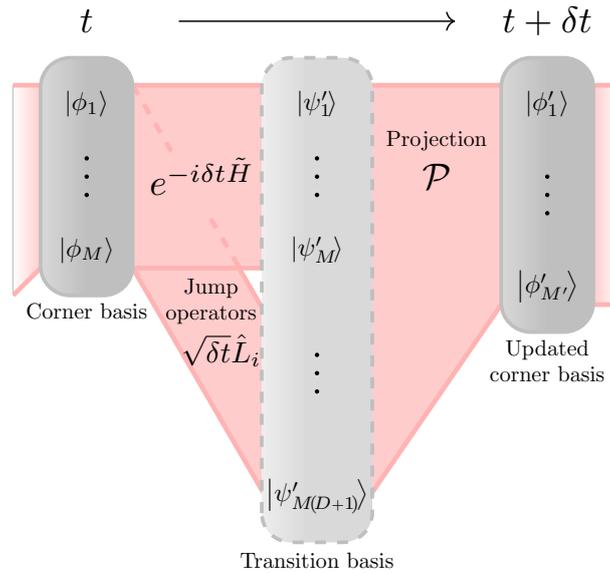
Figure 5.1: Sketch depicting one iteration of the time-dependent corner-space method.

II   The dynamical corner-space method

Let us consider an open quantum system whose dynamics is governed by the following Lindblad master equation [99]:

$$\partial_t \hat{\rho} = \mathcal{L}\hat{\rho} = -\mathrm{i}[\hat{H}, \hat{\rho}] + \sum_{i=1}^{D} \left(\hat{L}_i \hat{\rho} \hat{L}_i^\dagger - \frac{1}{2}\{\hat{L}_i^\dagger \hat{L}_i, \hat{\rho}\} \right), \tag{5.1}$$

where $\hat{H}$ is the system Hamiltonian acting on a Hilbert space $\mathcal{H}$ of dimension N, and $\hat{L}_i$ is the ith jump operator. At any time t, the solution $\hat{\rho}$ may be approximated by

$$\hat{\rho}(t) \simeq \sum_{k=1}^{M(t)} p_k(t) \left|\phi_k(t)\right\rangle\!\left\langle\phi_k(t)\right|, \quad p_k(t) \geq p_{k+1}(t), \ \forall k, \tag{5.2}$$

where $p_k(t)$ are the $M(t)$ largest eigenvalues of $\hat{\rho}$ at the time t and $\left|\phi_k(t)\right\rangle$ their associated eigenvectors. By construction, the controlled truncation error introduced by such an approximation is monotonically decreasing with M and quantified by $\epsilon_M = 1 - \sum_{k=1}^{M} p_k$, so that the decomposition becomes exact for $M(t) = r(t)$, with $r(t)$ denoting the rank of $\hat{\rho}(t)$, equivalent to the $\alpha = 0$ Rényi entropy [321]. Therefore, in a wide class of low-entropy systems including most platforms relevant for quantum computing, $\hat{\rho}$ is very well approximated by $M \ll N$ basis vectors, and even by $M \gtrsim 1$ for close to pure states. Henceforth, this number of components M will be referred to as the *corner dimension*. The accuracy of the calculations will be controlled by a fixed maximum error ϵ with $\epsilon_M \leq \epsilon$ enforced at any time.

It follows from the above that all the information of the density matrix is carried by a set of weighted corner base vectors of the form $\sqrt{p_k}\left|\phi_k\right\rangle$; in some arbitrary computational basis $\{|n\rangle\}_{n=1}^{N}$, these can be represented by a $N \times M$ matrix with elements $C_{nk}(t) =$

$\sqrt{p_k(t)} \langle n | \phi_k(t) \rangle$. It indeed follows from Eq. (5.2) that

$$\hat{\rho}(t) = \sum_{k=1}^{M(t)} p_k(t) | \phi_k(t) \rangle\langle \phi_k(t) | = \hat{C}(t)\hat{C}^\dagger(t). \tag{5.3}$$

Then, the essential goal of this method is to efficiently perform the time-evolution of the low-dimensional weighted corner basis $\hat{C}$ without ever reconstructing $\hat{\rho}$. The evolution $\hat{C}(t) \mapsto \hat{C}(t + \delta t)$ over a small time step δt, schematically illustrated in Fig. 5.1, involves two computational operations: (i) the calculation of the transition basis and (ii) the dimensional reduction by projection onto the new principal components.

Step (i): The weighted corner basis $\hat{C}(t)$ evolves into the weighted transition basis $\hat{T}(t + \delta t)$ as

$$\hat{\rho}(t + \delta t) = \sum_{i=0}^{D} \hat{M}_i \hat{\rho}(t) \hat{M}_i^\dagger = \sum_{m=1}^{M(D+1)} | \psi_m(t + \delta t) \rangle\langle \psi_m(t + \delta t) | = \hat{T}(t + \delta t)\hat{T}^\dagger(t + \delta t). \tag{5.4}$$

Here, the following Kraus map [183], equivalent to Eq. (5.1), was used:

$$e^{\delta t \mathcal{L}} \hat{\rho} = \sum_{i=0}^{D} \hat{M}_i \hat{\rho} \hat{M}_i^\dagger, \quad \hat{M}_0 = \exp(-i\delta t \tilde{H}), \quad \hat{M}_{i \geq 1} = \sqrt{\delta t} \hat{L}_i, \tag{5.5}$$

with $\tilde{H} = \hat{H} - \frac{i}{2} \sum_{i=1}^{D} \hat{L}_i^\dagger \hat{L}_i$ a non-Hermitian operator depending on the Hamiltonian and the quantum jump operators. By construction, the transition basis $\hat{T}(t + \delta t)$ is a $N \times [M(t)(D + 1)]$ rectangular matrix, where D is the number of dissipation channels. Its mth column is given by $| \psi_m(t + \delta t) \rangle = \sqrt{p_\mu} \hat{M}_\nu | \phi_\mu(t) \rangle$, with $\nu = (m - 1) \div M(t)$ and $\mu = (m - 1) \mod M(t) + 1$. This bears close analogy to the monitored-dynamics picture and the Monte Carlo wave function method sketched in Chapter 4. In that formalism, a Kraus operator was drawn at random at every time step according to the probability for an external observer to measure its outcome. This generated a single *stochastic* trajectory conditioned by a specific record of the history of the outcomes. By then averaging over all the realisations of this stochastic process, the density matrix was recovered as a marginal law. We here instead employ a completely deterministic approach. At every time step, all the $(D + 1)$ possible trajectories branching from each of the corner's M base state vectors are generated, naturally weighted by their likelihood. Although exact, no further processing would result in an exponential growth of the corner dimension with time. The second step of the algorithm solves this problem.

Step (ii): The transition matrix is now projected to a new weighted corner basis $\hat{C}(t + \delta t)$ of (lower) dimension $M(t + \delta t) \leq M(t)(D + 1)$ via a new truncated eigendecomposition $\mathcal{P}$ of the form of Eq. (5.3). Importantly, this is possible without ever reconstructing the full density matrix. Indeed, the $N \times N$ matrix $\hat{\rho}(t + \delta t) = \hat{T}(t + \delta t)\hat{T}^\dagger(t + \delta t)$ and the much smaller $[M(t)(D + 1)] \times [M(t)(D + 1)]$ matrix $\hat{\sigma}(t + \delta t) = \hat{T}^\dagger(t + \delta t)\hat{T}(t + \delta t)$ share the same non-zero eigenvalues p_k. Moreover, the associated eigenvectors, $| \phi_{k,\rho}(t + \delta t) \rangle$ and $| \phi_{k,\sigma}(t + \delta t) \rangle$, respectively, are related by the identity [315, 322]:

$$\sqrt{p_k} | \phi_{k,\rho}(t + \delta t) \rangle = \hat{T}(t + \delta t) | \phi_{k,\sigma}(t + \delta t) \rangle. \tag{5.6}$$

The components of the new decomposition can then be judiciously truncated to only retain the leading $M(t + \delta t)$ eigenvalues p_k, yielding an updated weighted corner basis $\hat{C}(t + \delta t)$, with the same structure as the initial one $\hat{C}(t)$.

This procedure can be iterated for an arbitrary time with the possibility of tuning the length of the time step δt and the tolerance parameter ϵ to control the accuracy at the desired level. Crucially, the time evolution of the corner basis involves no explicit reconstruction of the full density matrix. Indeed, the largest representation of the state of the system involved in the process, the transition basis $\hat{T}$, is comparable in size to that of $M(D + 1) \ll N$ closed systems.

II.1   Complexity of the algorithm

The first step of the dynamical corner-space procedure involves computing sparse matrix-dense vector operations of the form $\hat{M}_\nu \ket{\phi_\mu}$, its complexity is thus $M \times (D + 1)$ times that of evolving a closed system's Schrödinger equation for a single time step. For sparse Kraus operators with a maximum number of non-zero entries per row of x, typically a few, the complexity of this step is of order $O(xM[D+1]N)$, that is linear in the Hilbert-space dimension N.

The second step involves three distinct operations. First, the small matrix $\hat{\sigma} = \hat{T}^\dagger \hat{T}$ is constructed, involving a number of operations of order $O(M[D + 1]N/2)$. Then, its diagonalisation is of subleading complexity order $O(M^3[D+1]^3)$. Finally, building up the updated corner from the eigendecomposition of $\hat{\sigma}$ is of complexity $O(M[D+1]N)$.

The overall complexity of the algorithm is thus linear in the density x of the Kraus operators, the corner dimension, the number of dissipation channels and the size of the Hilbert space:

$$O\Big(xM[D + 1]N\Big). \tag{5.7}$$

This is $M[D + 1]$ times the complexity of the time evolution of a closed system. For extended systems with subextensive entropy, this factor scales only polynomially with the number of sites, instead of exponentially, as for the brute-force integration of the density matrix. This represents an extraordinary numerical advantage.

II.2   Complexity of the evaluation of relevant metrics

The evaluation of relevant metrics in quantum information is challenging with quantum-trajectory approaches. These rely on the evolution of N_{traj} stochastic trajectories $\{\ket{\psi_i(t)}\}_{i=1}^{N_{\text{traj}}}$. The density matrix can then be reconstructed as $\hat{\rho}(t) = \frac{1}{N_{\text{traj}}} \sum_{i=1}^{N_{\text{traj}}} \ket{\psi_i(t)}\bra{\psi_i(t)}$. Many metrics, such as fidelity and entanglement measures, namely concurrence, negativity, or entanglement entropy [323], require constructing explicitly the (dense) density matrix of the system and diagonalising it. In practice, the latter operation, of complexity $O(N^3)$, is not feasible for systems larger than ~ 15 qubits. In contrast, the corner-space method yields explicitly both the eigenvalues $\{p_k(t)\}_{k=1}^M$ and the eigenvectors $\{\ket{\phi_k(t)}\}_{k=1}^M$ at every time step, with no need for additional calculations.

To give a concrete example, let us consider the evaluation of the fidelity between two

arbitrary mixed states $\hat{\rho}$ and $\hat{\rho}'$ with rank M and M', respectively, as given by

$$\mathcal{F}(\hat{\rho}, \hat{\rho}') = \text{Tr}\left[\sqrt{\sqrt{\hat{\rho}}\hat{\rho}'\sqrt{\hat{\rho}}}\right] = \sum_{m=1}^{M} \left\langle \phi_m \middle| \left\{ \sum_{k,m=1}^{M} |\phi_k\rangle \, \mathcal{M}_{km} \, \langle\phi_m| \right\}^{1/2} \middle| \phi_m \right\rangle, \qquad (5.8)$$

with

$$\mathcal{M}_{km} = \sum_{k'=1}^{M'} p'_{k'} \sqrt{p_k p_m} \, \langle\phi_k|\phi'_{k'}\rangle \, \langle\phi'_{k'}|\phi_m\rangle \,, \qquad (5.9)$$

where $p_k^{(\prime)}$ and $\phi_k^{(\prime)}$ correspond to the kth eigenvalue and eigenvector of $\hat{\rho}^{(\prime)}$. This involves computations of various degrees of complexity: the diagonalisation of the two density matrices, of order $O(N^3)$; the construction of the matrix $\mathcal{M}_{km}$, of order $O(M' \times N)$; the diagonalisation of the latter, of order $O(M^3)$; and, finally, the trace, of order $O(M \times N)$. When using trajectory-based methods, an additional subleading complexity of order $O(N_{\text{traj}} \times M)$ is to be considered to account for the construction of the density matrices, whereas the leading order $O(N^3)$ stemming from the density-matrix diagonalisations is to be discarded when using the dynamical corner-space method, as the eigendecompositions are known explicitly. A similar discussion can be made for the entropy. Then, for each method, one finally has, to leading order and for $M^{(\prime)} \ll N$, the following scaling figures of merit:

	Monte Carlo wave function	Time-dependent corner-space
$\mathcal{F}(\hat{\rho}, \hat{\rho}')$	$O(N^3)$	$O(\max(M, M') \times N)$
$\mathcal{F}(\hat{\rho}, |\phi\rangle)$	$O(N_{\text{traj}} \times N)$	$O(M \times N)$
$S(\hat{\rho})$	$O(N^3)$	$O(M)$

In practice, the inconvenient scaling of the complexity for the Monte Carlo wave function approach, stemming from the two density-matrix diagonalisations, combined with the necessity of storing dense matrices well beyond the realistically available RAM makes it impossible to compute the fidelity between two mixed states from trajectories for systems larger than ~ 15 sites.

III Discussion

We will now apply the method to the numerical simulation of quantum circuits. These consist of a set of physical two-level systems on which the input state of the circuit is encoded. Similar to classical digital circuits, a set of quantum "logical gates" is then operated on this prepared system by enabling controlled interactions between pairs of such units. These operations take the form of unitary transformations of the state of the qubits. At the end of the process, the result of the quantum computation is encoded in the final state of the system and available for readout.

These two-level systems can be engineered with a great degree of control and isolation from the environment in several platforms, most notably in superconducting circuits [287, 324–326], trapped ions [288] and trapped atoms [327], for which complete sets of single-

and multi-qubit gates were experimentally demonstrated [328–334], with circuits having scaled from few units [334] to several tens of units within the last decade [289, 335–338]. In these physical implementations, the excited and fundamental levels $|\uparrow\rangle$ and $|\downarrow\rangle$ encode the logical states $|0\rangle$ and $|1\rangle$, respectively. While counter-intuitive, this convention is customary in related fields and will thus be employed through this chapter.
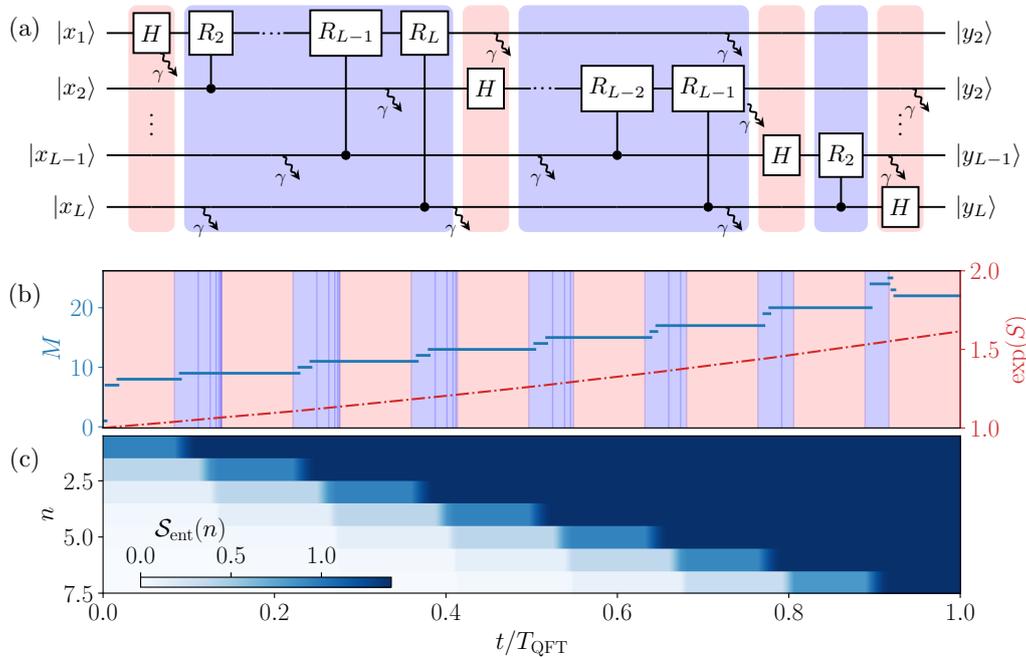
Figure 5.2: (a) Quantum circuit representing the QFT in the presence of dissipation. (b) Continuous-time evolution of the exponential of the von Neumann entropy S (dash-dotted) with the input state $|\psi_0\rangle$ defined in Eq. (5.17), for $L = 8$ qubits and $\gamma/\delta = 1 \times 10^{-3}$. The corner-space dimension $M(t)$ is also plotted (plain line). Temporal intervals corresponding to Hadamard and controlled-phase gates are indicated by lighter (red) and darker (blue) background colors, respectively. (c) Temporal build-up of the entanglement entropy $\mathcal{S}_{\text{ent}}(n)$, as defined in Eq. (5.19), as the different gates of the QFT are performed.

III.1   Application to the noisy QFT

The quantum Fourier transform

As a first application of the method, let us numerically simulate a noisy quantum Fourier transform (QFT) circuit. In doing so, we will consider the architecture depicted in Fig. 5.2 (a). The input state to be Fourier transformed through the circuit is encoded in the state of L qubits. Given an orthonormal computing basis $\{|n\rangle\}_{n=0}^{N}$ spanning the Hilbert space of the system, of dimension $N = 2^L$, this circuit linearly transforms any input of the form

$$|\boldsymbol{x}\rangle = \sum_{j=0}^{N-1} x_j |j\rangle, \tag{5.10}$$

where $\boldsymbol{x}$ is a vector of complex amplitudes, into

$$|\tilde{\boldsymbol{x}}\rangle = \mathrm{QFT}(|\boldsymbol{x}\rangle) = \sum_{k=0}^{N-1} \tilde{x}_k |k\rangle, \quad \mathrm{with} \quad \tilde{x}_k = \frac{1}{\sqrt{N}} \sum_j e^{2i\pi jk/N} x_j. \tag{5.11}$$

This therefore corresponds to the discrete Fourier transform of the N wave-function amplitudes. This operation can be reduced to subsequent applications of only two different types of quantum gates [339], the Hadamard and the controlled-phase gates. In the local basis:

$$\hat{U}_H|_i = \frac{1}{\sqrt{2}} \begin{array}{cc} \langle 0_i| & \langle 1_i| \\ \begin{pmatrix} 1 & 1 \\ 1 & -1 \end{pmatrix} & \begin{array}{c} |0_i\rangle \\ |1_i\rangle \end{array} \end{array}, \qquad \hat{U}_R|_{jk} = \begin{array}{cccc} \langle 0_j 0_k| & \langle 0_j 1_k| & \langle 1_j 0_k| & \langle 1_j 1_k| \\ \begin{pmatrix} 1 & & & \\ & 1 & & \\ & & 1 & \\ & & & e^{2\pi i/2^k} \end{pmatrix} & \begin{array}{c} |0_j 0_k\rangle \\ |0_j 1_k\rangle \\ |1_j 0_k\rangle \\ |1_j 1_k\rangle \end{array} \end{array}. \tag{5.12}$$

The number of involved such elementary gates, $L(L+1)/2$, is only polynomial in $L = \log_2(N)$; the complexity of the QFT algorithm is hence of order $O(L^2)$. In contrast, that of the usual fast Fourier transform (FFT) is exponential: $O(N \log N) \sim O(L2^L)$. This quantum advantage makes the QFT a central building block in many other algorithms.

Modelling the QFT circuit

In the following, the quantum gates introduced above will be executed via a continuous-time evolution defined by an appropriate master equation taking the form of Eq. (5.1). The effect of two types of noise will be addressed. We will first consider dissipative processes induced by a weak coupling to a zero-temperature environment, as described by jump operators of the form:

$$\hat{L}_i = \sqrt{\gamma}\hat{\sigma}_i^-. \tag{5.13}$$

This corresponds to local decay processes from the excited qubit state $|\uparrow\rangle_j \equiv |0\rangle$ to the lower energy qubit state $|\downarrow\rangle_j \equiv |1\rangle$. We will treat the effect of decoherence as well. This will be described by local pure-dephasing jump operators:

$$\hat{L}_i = \sqrt{\gamma}\hat{\sigma}_i^z. \tag{5.14}$$

Let us work in a frame rotating at the frequency of the qubit transition. Then, the Hadamard gate acting on the ith qubit can be realised via the subsequent application of the two following Hamiltonians:

$$\hat{H}_i^1 = \frac{\delta}{2}\hat{\sigma}_i^y, \qquad \hat{H}_i^2 = \frac{\delta}{2}\hat{\sigma}_i^z, \tag{5.15}$$

for a time $\Delta t_{H,1} = \pi/2\delta$ and $\Delta t_{H,2} = \pi/\delta$, respectively. This sequence corresponds to the decomposition of the Hadamard gate into a $\pi/2$-rotation along the y-axis and a π-rotation along the z-axis of the qubit's Bloch sphere. The controlled-phase gates with

control qubit j and target qubit k can instead be performed through the Hamiltonian:

$$\hat{H}_{j,k} = \frac{\delta}{2}\hat{\sigma}_j^z + \frac{\delta}{2}\hat{\sigma}_k^z - \frac{\delta}{2}\left(\hat{\sigma}_j^z\hat{\sigma}_k^z + \hat{\mathbb{1}}\right), \tag{5.16}$$

applied for a time $\Delta t_{R,k} = \pi 2^{-k}/\delta$. For simplicity, we will assume sudden switching between gate Hamiltonians and will not include coherent errors, although both effects could be accurately described by the dynamical corner-space method.

A first example of the dynamics of such a circuit is presented in Fig. 5.2 (b) and Fig. 5.2 (c). There, the initial state is chosen as

$$|\psi_0\rangle = \mathrm{QFT}^{-1}(|\mathrm{GHZ}\rangle) = \frac{1}{\sqrt{2N}}\sum_{n=0}^{N-1}(1 + e^{2i\pi n/N})|n\rangle, \tag{5.17}$$

so as to be the inverse of the Greenberger–Horne–Zeilinger (GHZ) state [340–342]:

$$|\mathrm{GHZ}\rangle = \frac{1}{\sqrt{2}}\left(|00...0\rangle + |11...1\rangle\right). \tag{5.18}$$

The latter is known to be a maximally entangled state and exhibit multipartite entanglement under many entanglement measures. Through this choice, the output state is ensured to be highly entangled, therefore demonstrating that entanglement is not a limiting factor for the corner-space method. In panel (b) of Fig. 5.2, the time evolution of the corner-space dimension M as well as the exponential $\exp(S)$ of the von Neumann entropy $S(\hat{\rho}) = \mathrm{Tr}[\hat{\rho}\ln\hat{\rho}]$ are shown, exhibiting similar trends. Panel (c) depicts the spatial entanglement propagation as the circuit's gates are progressively applied from the first to the last qubit. This is quantified by the following entanglement entropy

$$\mathcal{S}_{\mathrm{ent}}(n) \equiv S(\mathrm{Tr}_{1,\dots,n}[\hat{\rho}]), \tag{5.19}$$

that evaluates the magnitude of the inseparability between contiguous bipartitions of the form $\{\{1,\dots,n\},\{n+1,\dots,L\}\}$. While this is a rigorous measure of entanglement only for pure states [323], it still gives a valid qualitative description of the entanglement temporal build-up for states close to pure, as here treated. Note that $\mathcal{S}_{\mathrm{ent}}(n) > S^1$ is a sufficient condition for proving entanglement between the two subsystems $1 \oplus \dots \oplus n$ and $n+1 \oplus \dots \oplus L$. One sees that the initial localised entanglement spreads through the system in close relation to the architecture of the circuit. As clearly follows from the shading in panel (b), this takes place when the (entangling) controlled-phase gates are applied.

Benchmarking the method

Let us benchmark the accuracy of our calculations against the results of an exact integration of the master equation for small values of L, the numbers of qubits. In what follows, $\hat{\rho}_\gamma$ and $\hat{\rho}_\gamma^{(c)}$ denote the output density matrices of the noisy QFT obtained via the exact integration and via the corner method, respectively. Instead, $\hat{\rho}_0$ denotes the ideal

---

[1]This corresponds to the violation of the classical identity $S_A \leq S_{A \oplus B}$.
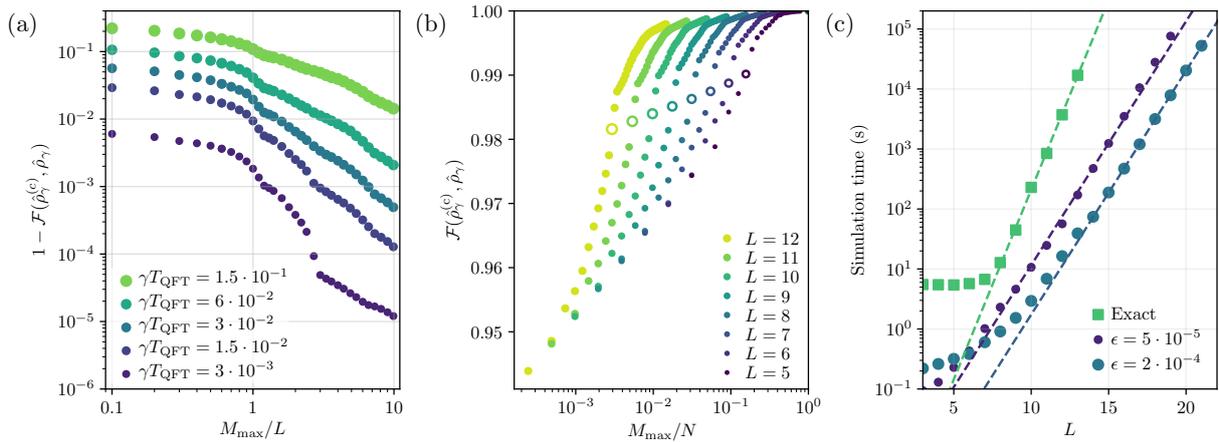
Figure 5.3: (a) Infidelity between the corner $\hat{\rho}_\gamma^{(c)}$ and exact $\hat{\rho}_\gamma$ output density matrices as a function of the maximum corner dimension $M_{\max}$ for different values of γT_{QFT} and $L = 10$ qubits. (b) Fidelity as a function of $M_{\max}$ and L for $\gamma T_{\mathrm{QFT}} = 2.5 \times 10^{-2}$. Values corresponding to $M_{\max} = L$ are highlighted by hollow markers (fidelities $\mathcal{F} \gtrsim 0.997$ are found for $M_{\max} \sim L \ln L$). (c) Simulation time of the noisy QFT circuit versus the number of qubits L for the exact solution of the master equation (squared markers) and the dynamical corner-space method (circles) for two different values of the control parameter ϵ. The dissipation rate is set to $\gamma T_{\mathrm{QFT}} = 2.5 \times 10^{-2}$. The initial state $|\psi_0\rangle$ is that defined in Eq. (5.17) for all three panels.

outcome of the noiseless QFT, which is a pure state. The results of this benchmarking process are presented in Fig. 5.3 for fixed values of γT_{QFT}, where T_{QFT} denotes the physical duration of the QFT operation. This ensures that the output infidelity with respect to $\hat{\rho}_0$ remains constant as the circuit size is increased. In particular, Fig. 5.3 (a) shows the infidelity of the method $1 - \mathcal{F}(\hat{\rho}_\gamma^{(c)}, \hat{\rho}_\gamma)$ as a function of the rescaled maximum corner dimension $M_{\max}/L$ for $L = 10$. One sees that for $M_{\max} \sim 10L$ the exact results are excellently approximated by the time-dependent corner-space method for all the considered values of γT_{QFT}. The method still performs reasonably well for noise rates as high as $\gamma T_{\mathrm{QFT}} = 1.5 \times 10^{-1}$, where the fidelity to the output of the noiseless circuit is as low as $\mathcal{F}(\hat{\rho}_0, \hat{\rho}_\gamma) = 0.758$. Fig. 5.3 (b) shows the fidelity of the method $\mathcal{F}(\hat{\rho}_\gamma^{(c)}, \hat{\rho}_\gamma)$ for different numbers of qubits L as a function of the fraction $M_{\max}/N$ between the dimension of the basis spanning the corner and that of the basis of the entire Hilbert space. These results show that the advantage of the dynamical corner-space method over exact integration of the master equation increases with L. In particular, to match a desired fidelity, the required corner dimension M is found to grow as $L \ln L$ with the system size. For $L = 12$, an excellent agreement of the corner-space method with the exact integration is already obtained for a fraction as low as $M_{\max}/N = 10^{-2}$. Finally, in Fig. 5.3 (c), we compare the computation time of the corner-space method to the exact integration, for two different values of ϵ^2. The corner-space method achieves an exponential speed-up with respect to the master equation integration. This leads to simulations faster by more than three

---

[2]In evaluating these execution times, both the exact integration and corner-space calculations were carried out on a single six-core Intel Xeon E5-2609 v3 processor at 1.9 GHz.

orders of magnitude for $L \sim 15$. Moreover, tuning the tolerance ϵ from 1×10^{-4} down to 5×10^{-5} preserves the scaling of the simulation time with L. Simulations of up to 21 qubits are presented. This represents a Hilbert-space dimension ($N = 2^L$) above 2 million states, corresponding to (dense) density matrices weighting $64\,\mathrm{TiB}$ that could never have been handled with a brute-force integration of the master equation (5.1). The method presented above is thus capable of efficiently evolving such high-dimensional objects by means of parsimonious corner representations of the density matrix.

Scaling laws

One can now evaluate the impact of incoherent processes on intermediate-scale devices via a continuous-time description and determine the scaling of errors. In Fig. 5.4, the fidelity $\mathcal{F}(\hat{\rho}_\gamma^{(c)}, \hat{\rho}_0)$ is shown for up to $L = 21$ qubits, for different values of γ/δ. Here, we consider dissipation channels described by the jump operators $\hat{L}_i = \sqrt{\gamma}\hat{\sigma}_i^-$. Remarkably, the infidelity scales only quadratically as a function of the number of qubits L. This scaling dependence allows one to precisely estimate the impact of $\gamma = 1/T_1$ on the QFT algorithm, T_1 being the energy relaxation time of the considered system.

Impact of initial states

Another key property is the dependence of the fidelity on the initial state, crucial to redesign algorithms that rely preferentially on a certain class of states. In Fig. 5.5, we address this question for the QFT by sampling initial states. Either energy relaxation produced by the jump operators $\hat{L}_i = \sqrt{\gamma}\hat{\sigma}_i^-$ or pure dephasing described by $\hat{L}_i = \sqrt{\gamma}\hat{\sigma}_i^z$ are considered. Only two simple parameters that characterise the initial state are found to be crucial for the considered architecture: the total number n_S of spins up and the spin-up "barycenter"

$$B(\hat{\rho}) = \frac{1}{n_S} \sum_\ell \ell \times \mathrm{Tr}\Big[|\uparrow\rangle\langle\uparrow|_\ell \, \hat{\rho}\Big]. \tag{5.20}$$

Our findings show that, in presence of energy relaxation, the fidelity of the noisy QFT decreases linearly with the number of spins up in the initial state. This is in stark contrast to the case of pure dephasing, which shows no significant dependence on n_S. The fidelity also exhibits a strong dependence on the spin barycenter. Indeed, energy relaxation only affects excited states and the circuit's Hadamard gates are applied one qubit at a time starting from the beginning of the chain. As a result, excited qubit states (spin up) close to the end of the chain are rotated down to the Bloch-sphere equator by the Hadamard gates later than those on the opposite end. Thus, they are globally more affected by dissipation.

IV Conclusion

In this chapter, we investigated the role of dissipation and decoherence in noisy intermediate-scale quantum circuits. Focusing on a circuit implementation of the key QFT algorithm, we revealed the scaling behaviour of a noisy-circuit fidelity with the number of qubits and explored its dependence on the initial state.

To this end, a new numerical algorithm, dubbed dynamical corner-space method, was introduced. By a judicious compression of the density matrix on a reduced corner subspace, this was proven to faithfully reproduce the system's dissipative dynamics. The method was shown to not be limited by entanglement and particularly suitable for systems with moderate entropy. This approach could be combined with efficient representations of the corner-space wave functions, such as neural-network ansätze [343–347], to, ideally, bring the exponential complexity of the simulation from exponential to only polynomial in the number of qubits.

These qualities make the dynamical corner-space approach ideally tailored for the NISQ era, providing a tool to improve our understanding of quantum hardware. The presented method can indeed be applied in many contexts related to quantum information: algorithm design for quantum feedback [348], machine learning for quantum control [349] and quantum error mitigation [350]. Another interesting perspective could be to study the effects of collective dissipation processes [234, 351] on the fidelity of physical quantum circuits, an error that cannot be described within the digital error model framework.

The results of this chapter are contained in Ref. [γ].
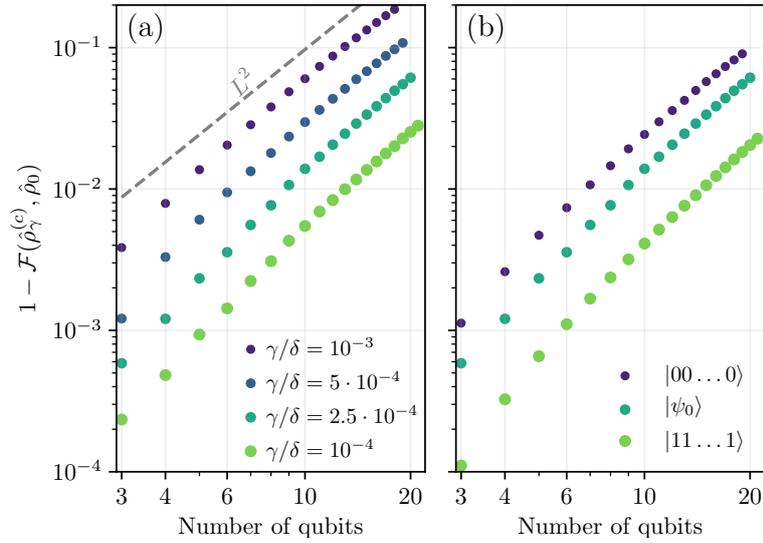
Figure 5.4: (a) Infidelity between the noisy output density matrix $\rho_\gamma^{(c)}$ and the noiseless output $\hat{\rho}_0 = |\text{GHZ}\rangle\langle\text{GHZ}|$ obtained from the initial state $|\psi_0\rangle$ for different values of γ/δ. The dashed line is a guide to the eye showing a growth $\propto L^2$. (b) Infidelity for three different initial states, described in the legend, for the same dissipation rate $\gamma/\delta = 2.5 \times 10^{-4}$.
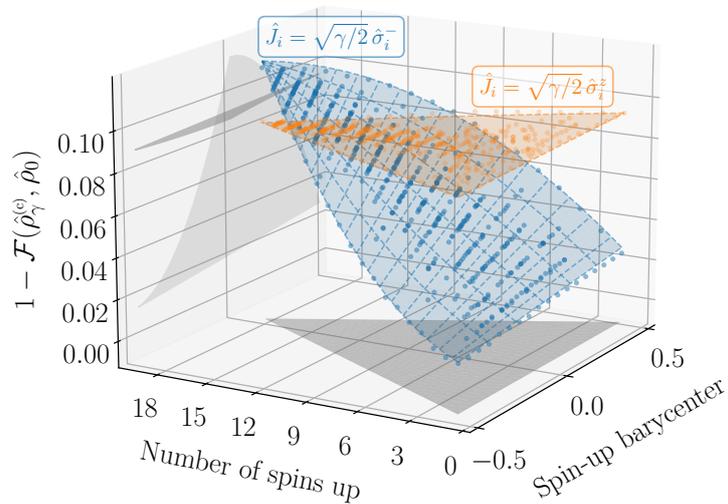
Figure 5.5: Infidelity for $L = 18$ qubits with dissipation (dark blue) or pure dephasing (orange) for 517 initial states per incoherent process, randomly sampled from the canonical basis. The infidelity is plotted versus the total number n_S of spins up in a given state and the spin-up barycenter defined in Eq. 5.20. The infidelity in both cases can be fitted by $\mathcal{I}(n_S, B) = a(n_S - n_{S_0})(B - B_0) + \mathcal{I}_0$. The surface for pure dephasing shows a negligible dependence on the initial state. Parameters: $\gamma/\delta = 3.7 \times 10^{-4}$ ($\gamma T_{\text{QFT}} = 2.5 \times 10^{-2}$) and $\epsilon = 1 \times 10^{-4}$.

6 Photonic kernel machines

In the previous chapters, we considered the general problem of the dynamics induced by optical reservoirs. We first started this discussion by addressing the case of a single optomechanical resonator. This then led us to the study of the reduced dynamics induced by fast optical lattices on a system consisting of a collection of slower mechanical resonators. By eliminating the optical degrees of freedom, we identified that, with great generality, the effective dynamics of the mechanical system was ruled by the spatially correlated quasi-instantaneous response of the optical reservoir to mechanical perturbations. We were able to completely describe this response by introducing a two-point susceptibility $\mathbf{S}(\omega)$. We then interested ourselves to the possibility of controlling the mechanical system by externally tuning this reservoir susceptibility, for instance by modifying its typical correlation length or by playing on the phase and detuning of the drive. In this context, the reservoir was regarded as a valuable resource, able to correlate mechanical inputs and control their effective dynamics. The approach to optical reservoirs that we shall adopt in this chapter differs from that of the previous ones more in its goals than in its means. Instead, we will here use the response of fast optical reservoirs as a resource to generate useful representations of noisy input signals.

This chapter is devoted to the study of photonic kernel machines, learning devices capable of performing machine-learning tasks on fast photonic reservoirs. It is organised as follows. Sec. I will provide a general overview of the context behind this work. After presenting some general concepts from kernel-machine theory in Sec. II, photonic kernel machines will be introduced in Sec. III. Their learning mechanism as well as a physical implementation will be discussed therein. In Sec. IV, this physical model will be applied to the ultrafast spectral analysis of noisy radio-frequency signals from single-shot optical intensity measurements of photonic lattices, on both regression and classification tasks. Finally, conclusions will be drawn in Sec. V.

I Introduction

As a result of its intrinsically faster timescales, photonics was very soon envisioned as a promising tool to outperform integrated electronics in terms of data processing rates [352]. In this perspective, optical setups ranging from matrix-vector multipliers [353], function convolvers [354] and discrete Fourier-transforming processors [355] to non-von Neumann parallel digital processors [356, 357] were proposed.

Although these ideas quickly became outdated as a consequence of the fast rise of silicon-based electronic processors, the latter have started to exhibit some of their limitations. In particular, the emergence of machine learning applications operating on ever increasing amounts of data, involving deeper and deeper neural-network architectures with an increasing degree of complexity [358] has led to a situation where the progress of available digital processor technology no longer keeps pace with the demand in computing capabilities [359]. This trend has moreover gone hand in hand with an increase in the consumption of computational and energy resources, casting doubt on its sustainability [360].

This context has stimulated very interesting proposals aiming at surrogating the realisation of specific tasks that are computationally and energetically very demanding to very specialised (electro-)optical devices. This process, reminiscent of current trends in hardware acceleration technologies, such as graphical (GPUs) and tensor processing units (TPUs), has already led to commercially available optical co-processors [361–364]. In the recent years, this approach was scaled to deep architectures [365] and has proven spectacularly powerful in the field of computer vision, by exploiting diffraction [366] or by optical implementations of convolutional neural networks, both in free-space [367] and on chip [368]. Such architectures are able to extract increasingly abstract representations [369] of the input images fed into the network by subsequent applications of pooled optically-operated linear convolutions.

The most standard neural-network-based machine learning schemes present roughly the following architecture: the digital data to be processed are transformed by a series of consecutive layers that consist in a parametrised affine transformation followed by the point-wise application of an elementary nonlinear activation function. Such a composition of parametrised functions is then expected to approximate some target function of the input upon a proper training process involving the optimisation of the parameters in order to minimise the error of the model on some set of training examples. While this sequential architecture is ideally suited for standard processors, which offer arbitrary levels of programmability by design, the amount of parameters to be addressed during the training process is in practice a hurdle to flexible optical implementations, having progressed from roughly 63 thousands in the paradigmatic LeNet-5 convolutional neural network [370] to several tens of millions on its nowadays counterparts [358]. The number of parameters even exceeds tens of billions in some different modern architectures applied to natural language processing tasks [371, 372].

Therefore, new machine learning paradigms that relax the above constraints, such as echo-state networks [373–377] or reservoir computing [50, 378], have inspired theoretical proposals and experimental realisations in a variety of settings, in optics [379, 380], integrated photonics [381, 382], memristors [383, 384] and beyond [385, 386]. In the context of optics, many fruitful configurations have been investigated, such as delay-line-based setups [387–398], nonlinear polariton lattices [399–401] and backfed systems combining linear light scattering and the measurement nonlinearity [402, 403].

Rather interestingly, together with this surge for harnessing computing power from physical systems in line with the original ideas of optical computing, there has been a resurgence in the criticism of the von Neumann architecture [404], whose limitations had already been raised back then in the same context [357]. Such an architecture relies on

physically separated processing and storage units connected through a bus. The latter's limited bandwidth results into a constant data traffic between the two units. This fundamental limit, coined as the "von Neumann bottleneck" [405], is the main constraint to the energy and processing performance of nowadays processors [406]. This has lead to important developments on in-memory computing in platforms such as memristor crossbars [407–418]. Beyond liquid-state machines/echo-state networks, several proposals have been put forward to reconcile general-purpose machine learning and distributed memory architectures. This, in particular, is the realm of neuromorphic computing, that has led to significant work in the field of spintronics [419–423] and memristors [409, 411, 424–435], notably the one articulated around spike-based machine-learning schemes [436–441]. Such architectures come not without their own technical difficulties. Because they rely on co-located memory and processing resources, standard optimisation algorithms can prove impractical, although novel optimisation procedures have recently been put forward to overcome this obstacle by meeting their peculiar hardware design [442–446].

A second shortcoming of standard software machine learning relates to applications involving analogue data that cannot be suitably interfaced with digital processors. Instances of this problem are, for example, situations where the input data to be analysed are supplied at a throughput too high to be properly sampled in real time. This also occurs when the data are intrinsically analogue, or when direct measurement processes add noise or perturb the system being measured. The utmost example of this is provided by genuinely quantum tasks with no classical counterparts, that involve quantum inputs. This has stimulated many original works, ranging from image recognition tasks [56] to quantum state control [51, 55, 447] and metrology [52, 53], under the name of quantum neuromorphic computing [54].

We here propose to overcome these constraints by taking a distinct machine learning paradigm, namely kernel machines [448, 449], to photonic hardware. We will describe photonic kernel machines as well as the associated theoretical framework under very general assumptions. We will explore the links between key concepts in support-vector-machine (SVM) theory and those of the photonic kernel machine proposed here. We will show that, in contrast with general reservoir computing schemes, knowledge about the underlying internal representations handled by the proposed learning device may be revealed from measurable data, providing direct understanding of the learning process of actual hardware. By introducing a realistic physical model for a photonic kernel machine based on a two-dimensional lattice of coupled linear optical cavities, we will numerically examine the performance of photonic kernel machines on regression and classification tasks involving ultrafast spectral analysis of analogue radio-frequency (RF) signals in the presence of noise, both with continuous and picosecond pulsed signals.

II General concepts

The results of this chapter will be focused on supervised learning problems. These can be formulated as an optimisation problem in which one tries to best approximate a *target* quantity $\boldsymbol{y} = f(\boldsymbol{x})$ of any given input $\boldsymbol{x}$ with a parametrised trial function $\hat{f}$. The input data are distributed according to some possibly unknown distribution $p(\boldsymbol{x})$ from which

only a restricted set of examples $\{(\boldsymbol{x}^{(i)}, \boldsymbol{y}^{(i)})\}_{i=1}^{N}$ is known.

More precisely, in *regression* problems one seeks for the optimal parameters that make $\hat{f}$ the best fit for the known examples by approximating their unknown true functional dependence f. A very simple example of such a task consists in fitting a curve from a set of datapoints. In *classification* problems one aims at determining the function $\hat{f}$ that best associates to the input data $\boldsymbol{x}$ a set of labels $\boldsymbol{y}$ that characterises their belonging to one or more classes. One example of this is determining if a patient is healthy or diseased from a set of measured indicators. These approximation problems are expressed in practice as the minimisation of some cost function J with respect to the parameters of the model to be trained on a given set of examples.

A specific choice of parametrisation defines the architecture of the model. Many architectures exist, ranging from shallow models [450], such as support vector machines (SVM), tree-based models and reservoir computing, to deep-learning models [451], such as feedforward, convolutional or recurrent neural networks. Here, we will exclusively consider kernel machines and reservoir computing models, with a strong emphasis towards the former. In this perspective, let us introduce some fundamental concepts and results from the theory of kernel machines. These notions will reveal particularly useful in the understanding of the physical model presented in Sec. III.2.

Feature-space embedding

In the context of regression, kernel machines approximate the target function by a parametrised linear expansion over a set of well-defined and possibly nonlinear orthogonal transformations ψ_m as

$$\hat{f}(\boldsymbol{x}) = \sum_{m=1}^{M} w_m \tilde{x}_m + b = \boldsymbol{w}^T \tilde{\boldsymbol{x}} + b, \tag{6.1}$$

with

$$\tilde{\boldsymbol{x}} := \boldsymbol{\psi}(\boldsymbol{x}), \tag{6.2}$$

such that $\langle \psi_m, \psi_n \rangle = \int \mathrm{d}\boldsymbol{x}\, p(\boldsymbol{x}) \psi_m(\boldsymbol{x}) \psi_n(\boldsymbol{x}) \propto \delta_{m,n}$. Here, the set of functions $\boldsymbol{\psi} : \boldsymbol{x} \mapsto \tilde{\boldsymbol{x}}$ defines an embedding from the *input space* into a *feature space* of dimension $M \leq +\infty$, with a new associated set of coordinates $\tilde{\boldsymbol{x}}^1$. Then, the parameters $(\boldsymbol{w}, b)$ of the trial function define a hyperplane within this feature space.

As shown in Fig. 6.1(a), a *nonlinear* function in input space can become *linear* when expressed in a higher-dimensional feature space spanned by nonlinear transformations of the inputs. The feature-space embedding maps the original datapoints onto a hyperplane therein. The model of Eq. (6.1) can thus perform regression by approximating the target function as a parametric curve $\tilde{\boldsymbol{x}} = \boldsymbol{\psi}(\boldsymbol{x})$ supported on this possibly infinite-dimensional hyperplane, whose parameters $(\boldsymbol{w}, b)$ are to be determined.

Binary classification can be operated in a similar way. Inputs $\boldsymbol{x}$ are associated to some class a if $\hat{f}(\boldsymbol{x}) > 0$ and to the complementary class b otherwise. While this function might be involuted in input space, it may also become *linear* in some suitable feature space, the frontier between the two classes, $\hat{f}(\boldsymbol{x}) = \boldsymbol{w}^T \tilde{\boldsymbol{x}} + b = 0$, thus becoming the equation of a plane. In this situation, the objective of the optimisation becomes finding the proper plane

---

[1]Note that this in general is not a diffeomorphism and thus *stricto sensu* not a change of coordinates.
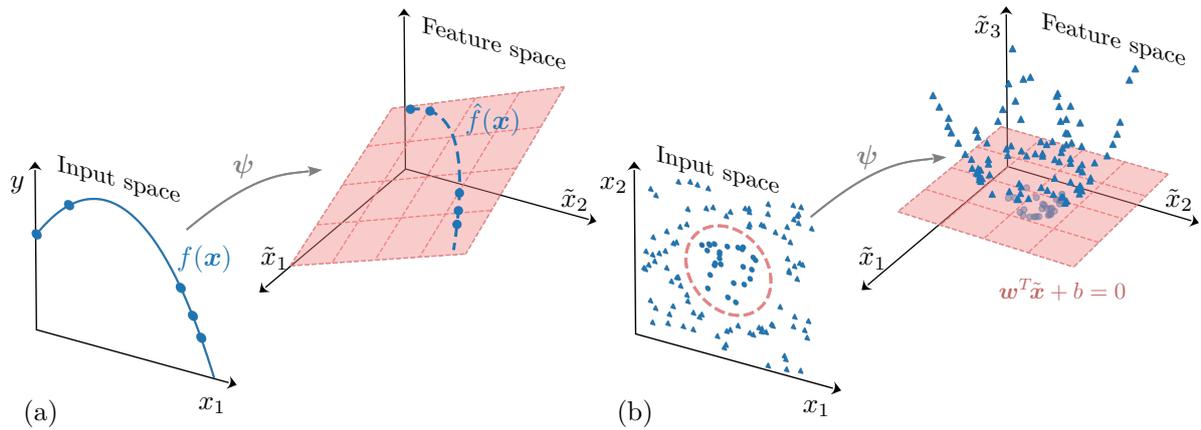
Figure 6.1: Schematic representation of the embedding from input to feature space kernel machines rely upon. (a) An example of regression: the quadratic function $f(x) = 3x - x^2 + 4$ is linearly fitted after performing the embedding of Eq. (6.1), with $\psi_1(x) = x^2$ and $\psi_2(x) = x$. (b) An example of binary classification: after performing the embedding of Eq. (6.1), with $\psi_1(\boldsymbol{x}) = x_1$, $\psi_2(\boldsymbol{x}) = x_2$ and $\psi_3(\boldsymbol{x}) = x_1^2 + x_2^2$, triangles (above the plane) and dots (below the plane) become linearly separable in feature space. The resulting input-space decision boundary $\hat{f}(\boldsymbol{x}) = 0$ is represented by a dashed line. Origins are shifted to improve the legibility.

that well separates data belonging to different classes into two separate clusters lying at either side of this linear decision boundary in feature space, as illustrated in Fig. 6.1 (b). This learned linear decision boundary translates into a potentially non-trivial one back in input space (dashed circle in Fig. 6.1 (b)). The same mechanism can be exploited to perform K-class classification via the one-vs-one and one-vs-rest techniques, which split the problem into respectively $K(K-1)/2$ and K binary-classification problems.

The primal picture

In practice, kernel machines can be trained without explicitly setting some precise feature map (6.1). This is achieved by introducing, under very general conditions, an expansion over some set $\{h_m\}_{m=1}^M$ of $M \leq +\infty$ possibly-nonlinear functions in the form

$$\hat{f}(\boldsymbol{x}) = \sum_{m=1}^M \beta_m h_m(\boldsymbol{x}) = \boldsymbol{\beta}^T \boldsymbol{h}(\boldsymbol{x}), \tag{6.3}$$

where $\boldsymbol{\beta}$ is a vector including the set of parameters of the model [2]. This corresponds to the typical trial function used in the context of reservoir computing, where the readout of the response of a nonlinear dynamical system to an external signal encoding the input is exploited to generate the feature-space embedding. Under some proper choice of loss function, reservoir computing may be strictly interpreted as a kernel machine.

---

[2]For simplicity, no bias is here considered, without loss of generality as one may always write $\hat{f}(\boldsymbol{x}) = \sum_{m=1}^M \beta_m h_m(\boldsymbol{x}) + b = \sum_{m=0}^M \beta_m h_m(\boldsymbol{x})$, with $h_0 = 1$ and $\beta_0 = b$.

Provided a set of training examples $\{(\boldsymbol{x}^{(i)}, y^{(i)})\}_{i=1}^N$, the optimal set of parameters $\hat{\boldsymbol{\beta}}$ is determined by minimising a cost function of the form

$$J(\boldsymbol{\beta}) = \sum_{i=1}^N V\left(y^{(i)}, \hat{f}(\boldsymbol{x}^{(i)})\right) + \frac{\lambda}{2}\|\boldsymbol{\beta}\|^2 \,, \quad \hat{\boldsymbol{\beta}} = \arg\min_{\beta} J(\boldsymbol{\beta}), \qquad (6.4)$$

where $V(y^{(i)}, \hat{f}(\boldsymbol{x}^{(i)}))$ is some pointwise error function on the predictions made by the model that we want to minimise. Here λ is a "bias" hyperparameter that regularises the optimisation in order to prevent the trained model from overfitting the training dataset [450]. This mechanism will be explained in Subsec. II.2.

The dual picture

Thanks to the *representer theorem*, the solution $\hat{f}(\boldsymbol{x}) = \hat{\boldsymbol{\beta}}^T \boldsymbol{h}(\boldsymbol{x})$ to this optimisation problem can be rewritten equivalently [448, 450] as

$$\hat{f}(\boldsymbol{x}) = \sum_{i=1}^N \hat{\alpha}_i K(\boldsymbol{x}, \boldsymbol{x}^{(i)}), \qquad (6.5)$$

where $K(\boldsymbol{x}, \boldsymbol{x}') = \boldsymbol{h}(\boldsymbol{x})\boldsymbol{h}(\boldsymbol{x}')^T = \sum_{m=1}^M h_m(\boldsymbol{x})h_m(\boldsymbol{x}')$ can be seen as a *similarity kernel*, and $\hat{\boldsymbol{\alpha}}$ is the set of optimal parameters of an equivalent dual problem:

$$J(\boldsymbol{\alpha}) = \sum_{i=1}^N V\left(y^{(i)}, \hat{f}(\boldsymbol{x}^{(i)})\right) + \frac{\lambda}{2}\boldsymbol{\alpha}^T \mathbf{K}\boldsymbol{\alpha} \,, \quad \hat{\boldsymbol{\alpha}} = \arg\min_{\alpha} J(\boldsymbol{\alpha}), \qquad (6.6)$$

with the kernel matrix $K_{ij} = K(\boldsymbol{x}^{(i)}, \boldsymbol{x}^{(j)})$. The feature map of Eq. (6.1) can thus also be generated implicitly from a measure of similarity $K(\boldsymbol{x}, \boldsymbol{x}')$ between two inputs.

Upon a proper choice of error function, the training step takes the form of a convex optimisation problem and can be straightforwardly solved. In particular, for a quadratic error $V(\boldsymbol{y}, \hat{\boldsymbol{y}}) = \|\boldsymbol{y} - \hat{\boldsymbol{y}}\|^2$, the optimal parameters are given analytically by

$$\hat{\boldsymbol{\alpha}} = (\mathbf{K} + \lambda\mathbb{1})^{-1}\mathbf{Y} \quad \Leftrightarrow \quad \hat{\boldsymbol{\beta}} = (\mathbf{H}^T\mathbf{H} + \lambda\mathbb{1})^{-1}\mathbf{H}^T\mathbf{Y}, \qquad (6.7)$$

where $H_{im} = h_m(\boldsymbol{x}^{(i)})$ and $Y_{ik} = y_k^{(i)}$.

The equivalence between the primal problem (6.4) and its dual (6.6) has as a strong implication that one can in principle train an infinite-dimensional model ($M = +\infty$) with the optimisation of a finite set of parameters α_i ($N < +\infty$). The model can thus approximate any function in the linear span of $\{\boldsymbol{x} \mapsto K(\boldsymbol{x}, \boldsymbol{x}^{(i)}), \forall i \leq N\}$.

In practice, kernel machine practitioners choose a kernel suitable for their applications; among popular choices are linear kernels, $K(\boldsymbol{x}, \boldsymbol{x}') = \boldsymbol{x}^T\boldsymbol{x}'$; polynomial kernels, $K(\boldsymbol{x}, \boldsymbol{x}') = (1 + \boldsymbol{x}^T\boldsymbol{x}'/c)^d$; radial basis functions (RBF) [452, 453], $K(\boldsymbol{x}, \boldsymbol{x}') = \exp(-\|\boldsymbol{x} - \boldsymbol{x}'\|_2^2/\sigma^2)$; or sigmoid kernels, $K(\boldsymbol{x}, \boldsymbol{x}') = \tanh(\kappa\boldsymbol{x}^T\boldsymbol{x}'+\theta)$; to name a few [454]. Very recently, "quantum" kernels of the form $K(\boldsymbol{x}, \boldsymbol{x}') = \mathrm{Tr}[\hat{\rho}(\boldsymbol{x})^\dagger\hat{\rho}(\boldsymbol{x}')]$ or $K(\boldsymbol{x}, \boldsymbol{x}') = \langle\hat{A}(\boldsymbol{x})^\dagger\hat{A}(\boldsymbol{x}')\rangle$, where $\hat{\rho}(\boldsymbol{x})$ and $\hat{A}(\boldsymbol{x})$ denote quantum operators evolved through some input-dependent unitary transformation $\hat{U}[\boldsymbol{x}]$ were proposed [455, 456] and even experimentally implemented [456–458]. Quantum advantage on a classification task was demonstrated on such kernel machines [459]; more recently, it was shown that circuit-based "quantum neural networks" could be described as such quantum kernel machines [460].

We have seen so far that the "abstract" feature-space embedding of the model $\boldsymbol{\psi}(\boldsymbol{x})$, as defined in Eq. (6.2), can be implicitly generated in two practical ways: either by parametrising an ansatz as a linear combination of known base functions $\boldsymbol{h}(\boldsymbol{x})$ (primal problem), as in Eq. (6.3), or by making a specific choice of similarity kernel $K(\boldsymbol{x}, \boldsymbol{x}')$ (dual problem), as in Eq. (6.5). Both of these approaches lead to equivalent yet different optimisation problems. The trial and regularisation functions as well as the training parameters, as expressed in the primal and dual equivalent pictures, are summarised in Table 6.1.

	Primal	Dual
Trial function $\hat{f}(\boldsymbol{x})$	$\boldsymbol{\beta}^T \boldsymbol{h}(\boldsymbol{x})$	$\sum_i \alpha_i K(\boldsymbol{x}, \boldsymbol{x}^{(i)})$
Regulariser R	$\frac{1}{2}\boldsymbol{\beta}^T\boldsymbol{\beta}$	$\frac{1}{2}\boldsymbol{\alpha}^T\mathbf{K}\boldsymbol{\alpha}$
Training parameters	$\boldsymbol{\beta} \equiv \mathbf{H}^T\boldsymbol{\alpha}$ (dim $= M$)	$\boldsymbol{\alpha}$ (dim $= N$)

Table 6.1: Summary of the main objects discussed in Sec. II in the two introduced pictures.

While the training of the model can be realised using either approach without ever having to access the internal feature-space representations, the associated feature-space embedding $\boldsymbol{\psi}(\boldsymbol{x})$ will be given explicit approximate expressions in the next section. This will allow us to better interpret the learning and regularisation mechanisms in physical kernel machines.

II.1   Feature-space inspection

Let us now identify the feature map (6.1) from a given kernel machine. One advantage of support vector and kernel machines over reservoir computing is that their feature space embedding may be straightforwardly examined. Indeed, for a symmetric positive semidefinite kernel K, Mercer's theorem ensures that it admits an eigendecomposition of the form:

$$K(\boldsymbol{x}, \boldsymbol{x}') = \sum_{m=1}^{M} \gamma_m \phi_m(\boldsymbol{x})\phi_m(\boldsymbol{x}'), \qquad (6.8)$$

with $\gamma_{n+1} \leq \gamma_n$ and $\langle \phi_m, \phi_n \rangle = \int \mathrm{d}\boldsymbol{x}\, p(\boldsymbol{x})\phi_m(\boldsymbol{x})\phi_n(\boldsymbol{x}) = \delta_{m,n}$, where the measure was chosen for convenience. The feature map of Eq. (6.1) can then be easily shown to be given $\psi_m(\boldsymbol{x}) = \sqrt{\gamma_m}\phi_m(\boldsymbol{x})$. We shall now identify the elements of this eigendecompositon.

Empirical eigenvalues and eigenfunctions of the kernel

To identify its eigenvalues and eigenvectors, one has to solve in principle for

$$\int \mathrm{d}\boldsymbol{x}'\, p(\boldsymbol{x}')K(\boldsymbol{x}, \boldsymbol{x}')\phi(\boldsymbol{x}') = \gamma_m \phi_m(\boldsymbol{x}). \qquad (6.9)$$

Yet these may be estimated from the N known training samples by replacing the input distribution $p(\boldsymbol{x})$ with the *empirical* one $\hat{p}(\boldsymbol{x})$, such that $\int \mathrm{d}\boldsymbol{x}\hat{p}(\boldsymbol{x})f(\boldsymbol{x}) = (1/N)\sum_i f(\boldsymbol{x}^{(i)})$ [461].

This yields a tractable discrete eigenvalue problem:

$$\frac{1}{N}\sum_{i=1}^{N} K(\boldsymbol{x},\boldsymbol{x}^{(i)})\hat{\phi}_m(\boldsymbol{x}^{(i)}) = \hat{\gamma}_m\hat{\phi}_m(\boldsymbol{x}), \tag{6.10}$$

in terms of *empirical eigenvalues* $\hat{\gamma}_m$ and *empirical eigenfunctions* $\hat{\phi}_m$. It follows that the empirical eigenvalues correspond to the non-zero eigenvalues of either of the kernel matrices $\mathbf{K} = \mathbf{H}\mathbf{H}^T$ and $\mathbf{k} = \mathbf{H}^T\mathbf{H}$ (let us recall $H_{im} = h_m(\boldsymbol{x}^{(i)})$). Indeed, because of their Gram matrix structure, their eigendecompositions,

$$\mathbf{K} = N\mathbf{U}\mathbf{D}_{\hat{\gamma}}\mathbf{U}^T, \quad \mathbf{k} = N\mathbf{u}\mathbf{d}_{\hat{\gamma}}\mathbf{u}^T, \tag{6.11}$$

with $U_{im} = \hat{\phi}_m(\boldsymbol{x}^{(i)})/\sqrt{N}$, share the same non-zero eigenvalues and can be related through the following simple algebraic identity:

$$\boldsymbol{U}_n = \tfrac{1}{\sqrt{N\hat{\gamma}_n}}\mathbf{H}\boldsymbol{u}_n. \tag{6.12}$$

In the physical model that will be studied below, designed to treat large datasets at a very high rate, one has typically $M \ll N$ and it becomes more suitable to work with the $M \times M$ matrix $\mathbf{k}$.

Similarly, the empirical eigenfunctions can be determined from Eq. (6.10). By making use of the property of Eq. (6.12), these finally read:

$$\hat{\phi}_n(\boldsymbol{x}) = \frac{1}{\sqrt{N\hat{\gamma}_n}}\boldsymbol{u}_n^T\boldsymbol{h}(\boldsymbol{x}). \tag{6.13}$$

Empirical eigen feature map of the kernel

From Eq. (6.8) and Eq. (6.13), the kernel can be expanded into a series of empirical eigen feature maps $K(\boldsymbol{x},\boldsymbol{x}') = \sum_{m=1}^{M}\psi_m(\boldsymbol{x})\psi_m(\boldsymbol{x}')$, with orthogonal feature maps simply given by

$$\hat{\psi}_m(\boldsymbol{x}) = \sqrt{\hat{\gamma}_m}\hat{\phi}_m(\boldsymbol{x}). \tag{6.14}$$

Thus, the internal functional representations of the model are *independent from the optimisation process*, completely determined by the statistics of the training samples and can be estimated by diagonalising the matrix $\mathbf{k}$.

The kernel links the abstract notion of *similarity* between two inputs $\boldsymbol{x}$ and $\boldsymbol{x}'$, as quantified by $K(\boldsymbol{x},\boldsymbol{x}')$, into a *distance* between their feature-space representation $\tilde{\boldsymbol{x}}$ and $\tilde{\boldsymbol{x}}'$. Indeed, $K(\boldsymbol{x},\boldsymbol{x}') = \tilde{\boldsymbol{x}}^T\tilde{\boldsymbol{x}}'$, and thus $d^2(\tilde{\boldsymbol{x}},\tilde{\boldsymbol{x}}') = K(\boldsymbol{x},\boldsymbol{x}) + K(\boldsymbol{x}',\boldsymbol{x}') - 2K(\boldsymbol{x},\boldsymbol{x}')$. Therefore, even in the absence of any training, low-dimensional truncations of the kernel eigen-feature expansion allow one to directly inspect the data $\boldsymbol{x}$ in its feature-space co-ordinates $\tilde{\boldsymbol{x}} = (\hat{\psi}_1(\boldsymbol{x}),\hat{\psi}_2(\boldsymbol{x}),\ldots)$. For simple tasks, the first few leading components of $\tilde{x}$ usually suffice to visually access the structure of the input data.

As we saw in the previous subsection, the predictions of the model in the abstract feature-space picture, $\hat{f}(\boldsymbol{x}) = \boldsymbol{w}^T\tilde{\boldsymbol{x}} \equiv \boldsymbol{w}^T\boldsymbol{\psi}(\boldsymbol{x})$, take the form of a linear combination of features whose weights, determined through training, can be geometrically interpreted

as the parameters of a hyperplane. As a function of the primal parameters, this learned hyperplane is characterised by

$$\hat{\boldsymbol{w}} = \sqrt{N}\boldsymbol{u}^T\hat{\boldsymbol{\beta}}. \tag{6.15}$$

Therefore, provided a set of generating functions $\{h_m\}_m$, we are now able to access to a complete understanding of the model and its feature-space representations.

Further comments can be made about the feature-space structure. First, thanks to the choice of measure, the feature maps may be thought of, up to the centring, as a principal-component decomposition of the kernel [449, 462, 463]. This mean that they embed the data from input space into the principal directions of the corresponding features. Therefore, truncated sets of the features $\tilde{\boldsymbol{x}}$ lie on the feature-space low-dimensional manifolds that are the most statistically relevant to discriminate inputs. As we will see in the next subsection, the regularisation will act as a soft cut-off on the dimension of these manifolds.

II.2 Optimisation

So far, we have seen that the structure of the feature space is completely determined by the kernel and the statistics of the training samples. The trial function then simply consists in a linear combination of these features. The remaining step is to find the parameters of this linear combination that lead to the best accuracy of the model. This optimisation process is done through training.

The training can be performed either in the primal or the dual space, the former is more adapted if the rank M of the kernel is smaller than the number of training examples and conversely. We will here consider for latter convenience only the primal problem. In shallow machine-learning models as that here described, this can performed in the following way:

(i) The total amount of labelled examples $\{\boldsymbol{x}^{(i)}, y^{(i)}\}_i$ is first split into a training set of size N_{train} and a testing set of size N_{test}. The latter solely serves to evaluate the accuracy of the trained model. Therefore, it should not be used at any stage of the training process. For each input $\boldsymbol{x}$ in both sets of samples, the quantities $\{h_m(\boldsymbol{x})\}_m$ are computed. In physical reservoir-computing and kernel-machine schemes, $h_m(\boldsymbol{x}^{(i)})$ corresponds to the measurement of the mth observable resulting from the ith input example. This evaluation is only to be performed once.

(ii) The cost function, as given by Eq. (6.4), is minimised with respect to the parameters of the model $\boldsymbol{\beta}$ for a given value of the hyperparameter λ and for the training set *only*. This cost function involves an error function $V(y^{(i)}, \boldsymbol{\beta}^T\boldsymbol{h}(\boldsymbol{x}^{(i)}))$, whose evaluation only involves the above-precomputed quantities. This function characterises the error in estimating the target of the ith input in the training set. The choice of error function depends on the task and is typically chosen so that the optimisation problem is convex. For regression tasks, a popular choice is simply $V(y, \hat{y}) = \|y - \hat{y}\|^2$, which corresponds to a least-square problem. In binary classification ($y = \pm 1$), it is customary to choose a margin-maximising loss functions [464]. Popular choices [450] are the SVM hinge loss, $V(y, \hat{f}(\boldsymbol{x})) = \max(0, 1 - y\hat{f}(\boldsymbol{x}))$, which makes $\hat{f}$

directly approximate the class label $f(\boldsymbol{x}) = y$, or the binomial deviance $\ln(1 + e^{-y\hat{f}(\boldsymbol{x})})$, which makes $\hat{f}$ instead approximate $f(\boldsymbol{x}) = \ln(\mathbb{P}(y = +1|\boldsymbol{x})/\mathbb{P}(y = -1|\boldsymbol{x}))$. Upon choosing any of these loss functions, the problem is convex and can be solved either analytically, as in Eq. (6.7) for the square error, or by means of a convex optimisation solver. This yields a set of optimal parameters $\hat{\beta}$.

(iii) The trained model now makes estimations of the form $\hat{f}(\boldsymbol{x}) = \hat{\boldsymbol{\beta}}^T \boldsymbol{h}(\boldsymbol{x})$. The final accuracy of the trained model can then be evaluated on the testing data, to which the model was yet never exposed, by comparing the predictions $\hat{y}^{(i)} = \hat{f}(\boldsymbol{x}^{(i)})$ to the actual values $y^{(i)}$. This is done through a metric that may differ from the objective function, in particular if regularisation was employed.

At the end of this process, one obtains a set of parameters $\hat{\boldsymbol{\beta}}$ and an accuracy associated to some value of the regularisation strength λ. Let us now discuss more in details the role of the regularisation on the learning of the model.

Regularisation: overcoming overfitting

The objective of the training procedure is to maximise the accuracy of the model's predictions on data it was never exposed to, that is to be able to generalise. One of the most detrimental obstacles to achieving this is *overfitting*. When the number of free parameters of the model is too large as compared to the size of the training set and the complexity of its statistics, the model can be prone to learn over-specific features of the training set rather than general ones. This translates into a great generalisation error on the testing set. Regularisation allows one to prevent this phenomenon by adding a penalty on the degree of freedom of the model's parameters, reducing its variance at the cost of acquiring a larger bias.

In our case, this specific mechanism may be understood by decomposing the trial function into the orthonormal basis of the kernel:

$$\hat{f}(\boldsymbol{x}) = \sum_m \langle \phi_m, \hat{f} \rangle \phi_m(\boldsymbol{x}) \equiv \sum_m \hat{f}_m \phi_m(\boldsymbol{x}), \tag{6.16}$$

where the components $\hat{f}_m$ may be interpreted as degrees of freedom of the model. It follows from Eqs. (6.5) and (6.8) that $\hat{f}_m = \gamma_m \sum_i \alpha_i \phi_m(\boldsymbol{x}^{(i)})$, then, the regularisation penalty of Eq. (6.6) can be rewritten as

$$\lambda R(\boldsymbol{\alpha}) = \frac{\lambda}{2} \sum_{ijm} \alpha_i \alpha_j \phi_m(\boldsymbol{x}^{(i)}) \gamma_m \phi_m(\boldsymbol{x}^{(j)}) \equiv \sum_m \frac{\lambda_m}{2} |\hat{f}_m|^2, \tag{6.17}$$

where $\lambda_m = \lambda/\gamma_m$. This means that the penalty on the magnitude of the mth component of $\hat{f}$ during the optimisation is inversely proportional to the variance of $\phi_m(\boldsymbol{x})$. Therefore, the effect of the regularisation on the optimisation is to impose a soft cut-off on the dimensionality of the feature-space hyperplane schematically illustrated in Fig. 6.1, while preserving most of the original variance of the inputs by reducing it to only the most statistically relevant directions.

Hyperparameter training

The training of the hyperparameter λ can be done in several ways. For instance, one way of doing this is by grid search, that is by sweeping λ within some bounds and retaining the value at which the performance of the model was maximal. Care must be taken though with the dataset used to assess this performance. Evaluating it on the training set would be of no use in quantifying generalisation. While its evaluation on the testing set would effectively be a measure of generalisation power, it would entail *data leakage* as the optimal parameters and thus future predictions would be conditioned on the knowledge of the test examples, thus compromising the fidelity of the final estimate of the model accuracy in step (iii). One way around this is to partition the training set at step (ii) into a training set and a validation set. Then, the training of the model's parameters is carried out on the former and the tuning of the hyperparameter by benchmarking the accuracy of the model on the latter. Multiple variations around this idea exist. In the following we will use k-fold cross-validation.

III Photonic kernel machines: taking the kernel to optical hardware

The spectral analysis of radio-frequency signals is a very broad field with countless applications. We will mainly focus ourselves on the analysis of ultrashort pulsed signals. This is relevant for instance in the field of pulse-Doppler radars. Such devices emit a pulsed radio-frequency signal around some carrier frequency with some repetition rate and receive it back via an antenna after being reflected by a moving target. This reflected signal is then measured and numerically processed to extract information about the position and the velocity of the tracked target. The distance from the target to the emitter may be estimated from the delay between the emission and reception times while the relative velocity with respect to the receiver can be guessed from the magnitude of the Doppler shift in the reflected signal. The repetition rate is limited by the processing time, which is in turn bounded by the acquisition time.

Nowadays, the state of the art performances are obtained by direct sampling of the signal sensed by the antenna. Yet, the sampling rate of state-of-the-art RF-sampling analogue-to-digital converters (ADCs) lies below 4 GSPS (gigasamples per second), which clearly limits the length of the pulses used. Indeed, to be able to measure 1000 samples of a pulse of interest with such an ADC, one needs the pulse's length to exceed roughly 25 µs. Other strategies proceed by sweeping, yet if the sweep is performed over, for instance, 20 GHz, with a real-time bandwidth of 1 GHz, the analyser is blind 95% of the time. This issue may be circumvented by operating several such analysers in parallel addressing each a separate sub-band. However, the resulting devices are very expensive, heavy and bulky.

Acousto-optical spectrum analysers are also known, in which the signal to be analysed is injected into a piezoelectric crystal (Bragg cell) after being converted into acoustic waves that create variations in the diffraction index. The coherent input light is injected into the transparent medium of the acousto-optical cell, and this light is diffracted according to the spectrum of the initial signal. The laser image is collected by a CCD system. The

amplitude of the outgoing signal is proportional to the amplitude of the radio-frequency signal and the angle of deflection is almost proportional to the frequency of the signal. Such acousto-optic analysers have found applications in astronomy.

In the optical frequency domain, spectral analysis can be performed by means of spectrometers such as monochromators. Such devices perform a frequency sweep with a power measurement at the selected frequency up to a certain spectral resolution. The control of the mechanical element of the spectrometer allowing the frequency sweep greatly limits the rate of acquisition of the spectrum of the signals to be analysed, which can be at best of the order of $10\,\text{kHz}$ for the most efficient devices.

As we have just seen, current electronics pose severe bounds on the achievable processing throughput and on the pulse lengths. This context motivates the quest for technologies that go past these limitations. In what follows, we shall show that these may be lifted by resorting to a learning all-optical processing device based upon the kernel-machine concepts introduced above. We will first introduce a similarity kernel ideally suited for this task although very expensive to evaluate. We will then show that this kernel can be realised rather naturally by means of a single-shot intensity measurement of a photonic lattice, making it possible to process complex radio-frequency signals in times of the order of tens or hundreds of picoseconds.

III.1   Theoretical description

As we have seen above, learning with kernels starts from the introduction of a kernel that serves as a measure of similarity between inputs. In particular, we will focus this discussion on the spectral analysis of ultrashort pulsed signals. The spectral information of such signals $s(t)$ is encoded in their energy spectral density $S[\omega] = |s[\omega]|^2$, where $s[\omega] = (2\pi)^{-1/2} \int \text{d}t e^{-i\omega t} s(t)$. Rather naturally, the similarity between two signals $s(t)$ and $s'(t)$ can thus be given a general expression of the form:

$$K(S, S') = \int \text{d}\omega \text{d}\omega' S[\omega] \mathcal{K}(\omega - \omega') S'[\omega'], \tag{6.18}$$

where $\mathcal{K}(\omega - \omega')$ is a function peaked around $\omega = \omega'$ and with a typical width $\delta\omega$. Such a kernel compares two given input signals by contrasting their energy spectral densities at each frequency with a certain tolerance on their fine structure at frequency scales below $\delta\omega$. While this provides a good and flexible similarity metric, the practical numerical evaluation of such a kernel is rather unsuitable. Indeed, this would require several costly steps: (i) each pulse would have to be sampled in time at similar sampling rates over a time interval larger than $2\pi/\delta\omega$, (ii) the digitised signals would then have to be numerically Fourier-transformed and stored, and, finally, (iii) each kernel evaluation would involve the evaluation of a double integral. We shall next see that the feature-space embedding of this kernel can be computed rather naturally on photonic hardware.

Let us consider an optical system consisting of a set of M generic normal modes, as described in frequency space by their susceptibility to some ith pulsed input signal $s^{(i)}(t)$ of interest:

$$\hat{\alpha}_\ell[\omega] = \chi_\ell[\omega]\left(i s^{(i)}[\omega] + \sqrt{\kappa/2}\,\hat{\alpha}_\ell^{\text{in}}[\omega]\right), \tag{6.19}$$

where $\hat{\alpha}_\ell[\omega] = (2\pi)^{-1/2} \int \mathrm{d}t e^{-i\omega t} \hat{\alpha}_\ell(t)$ is the Fourier-transformed annihilation operator associated to the ℓth normal mode, $\hat{\alpha}_\ell^{\mathrm{in}}$ its associated quantum Langevin input field, $\chi_\ell[\omega]$ its susceptibility at frequency ω, and κ the loss rate.

Optical populations induced by the input pulse are measured via the collected radiated power by a detector with some integration time Δt larger than the length of the pulse, i.e. $\Delta t \gg 1/\Delta\omega$, where $\Delta\omega$ is the bandwidth of the signals to be analysed. The scattered normal-mode populations are thus given by

$$\bar{n}_\ell^{(i)} \propto \frac{1}{\Delta t} \int \mathrm{d}t \langle \hat{\alpha}_\ell^\dagger \hat{\alpha}_\ell \rangle_t = \frac{1}{\Delta t} \int \mathrm{d}\omega \langle \hat{\alpha}_\ell^\dagger \hat{\alpha}_\ell \rangle_\omega = \int \mathrm{d}\omega h_\ell(\omega) S^{(i)}[\omega] \equiv \langle h_\ell | S^{(i)} \rangle, \qquad (6.20)$$

where $h_\ell(\omega) = \Delta t^{-1} |\chi_\ell[\omega]|^2$ is the optical population susceptibility and $S^{(i)}[\omega] = |s^{(i)}[\omega]|^2$ is the energy spectral density of the ith pulse.

From such a population measurement, vector-valued predictions on any input energy spectral density S can thus be made of the form of those of a kernel machine as in Eq. (6.3):

$$\hat{f}_\ell(S) = [\mathbf{B}^T \bar{\boldsymbol{n}}]_\ell \equiv \sum_{\ell'} B_{\ell'\ell} \langle h_{\ell'} | S \rangle, \qquad (6.21)$$

For optical relaxation times of the order of tens of picoseconds, such predictions could in principle be realised for ultrashort pulses at a throughput above the tens of gigahertz.

Let us check that the corresponding dual-picture kernel is indeed of the form of Eq. (6.18) under some general assumptions on the optical-mode density spectrum of the photonic system. This kernel takes the form:

$$K(S, S') = \sum_\ell \langle S | h_\ell \rangle \langle h_\ell | S' \rangle = \int \mathrm{d}\omega \mathrm{d}\omega' S[\omega] \mathcal{K}(\omega, \omega') S'[\omega']. \qquad (6.22)$$

We will focus on $\mathcal{K}(\omega, \omega') = \sum_\ell h_\ell(\omega) h_\ell(\omega')$. By considering that all normal modes of the system share the same susceptibility shape, $h_\ell(\omega) = h(\omega - \omega_\ell)$, and for a continuous optical-mode density spectrum $\rho(\omega)$, this is of the form:

$$\mathcal{K}(\omega, \omega') = \int \mathrm{d}\Omega \rho(\Omega) h(\omega - \Omega) h(\omega' - \Omega). \qquad (6.23)$$

By further assuming a smooth spectral density of spectral width much larger than the normal modes' linewidth, one may finally write:

$$\mathcal{K}(\omega, \omega') \approx \rho\left(\frac{\omega + \omega'}{2}\right) \int \mathrm{d}t h(t) h(-t) e^{-i|\omega - \omega'|t}. \qquad (6.24)$$

The kernel is thus completely determined by the measured-observable susceptibility, here the population: $h(\omega) = |\chi[\omega]|^2/\Delta t$. For instance, the susceptibility of a linear optical mode $\chi_\ell[\omega] = 1/(-i(\omega - \omega_\ell) + \kappa/2)$ translates into a Lorentzian kernel:

$$\mathcal{K}(\omega, \omega') \propto \frac{1}{(\omega - \omega')^2 + \kappa^2}, \qquad (6.25)$$

that was shown to perform better on some tasks than the more common RBF [465]. This kernel indeed bears the desired form introduced in Eq. (6.18), with a spectral tolerance $\delta\omega = \kappa$ given by the mode linewidth.
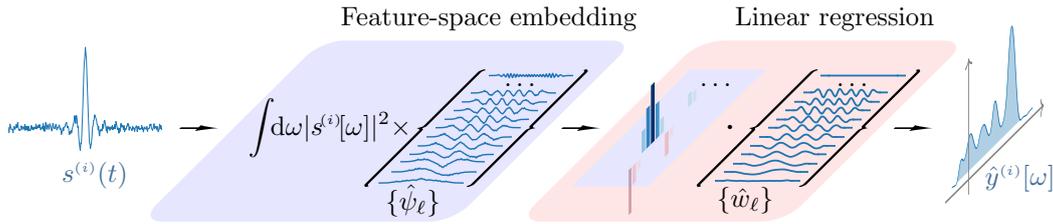
Figure 6.2: Illustration of the photonic kernel machine processing mechanism. Measurement of the pulse-induced optical populations embeds the pulse's energy spectral density into some reciprocal space by projection onto a set of orthogonal base functions $\{\hat{\psi}_\ell\}_\ell$. The spectrum of the ith pulse is reconstructed by a linear combination $\hat{y}^{(i)}[\omega] = \sum_{\ell'} w_{\ell'}[\omega]\langle \hat{\psi}_{\ell'}|S^{(i)}\rangle$ of its reciprocal-space components (features) over some set of learned functions $\{\hat{w}_\ell\}_\ell$. On this example, the learned functions $\{\hat{w}_\ell\}_\ell$ are filtered analogues of $\{\hat{\psi}_\ell\}_\ell$ and the photonic kernel machine is able to extract the spectrum of the incoming pulse from its noisy background.

Inspecting the feature space of photonic kernel machines

One can access to the feature space associated to such a photonic kernel machine as well. Indeed, its kernel admits the following eigendecomposition

$$K(S, S') = \sum_\ell \langle S|h_\ell\rangle \langle h_\ell|S'\rangle = \sum_\ell \gamma_\ell \langle S|\phi_\ell\rangle \langle \phi_\ell|S'\rangle, \tag{6.26}$$

with empirical eigenfunctions and feature maps as given by Eqs. (6.13) and (6.14):

$$\hat{\phi}_n(\omega) = \frac{1}{\sqrt{N\hat{\gamma}_n}}\boldsymbol{u}_n^T \boldsymbol{h}(\omega), \quad \hat{\psi}_n(\omega) = \sqrt{\hat{\gamma}_n}\hat{\phi}_n(\omega), \tag{6.27}$$

where $\boldsymbol{u}_n$ and the empirical eigenvalues $\hat{\gamma}_n$ are obtained following Eq. (6.11) as the nth eigenvector and eigenvalue of the matrix $\mathbf{k}/N = \mathbf{H}^T\mathbf{H}/N$, with $H_{i\ell} = \langle h_\ell|S^{(i)}\rangle = \bar{n}_\ell^{(i)}$, and where $h_\ell(\omega) = |\chi_\ell[\omega]|^2/\Delta t$ is the population susceptibility of the considered normal modes. Strikingly, this kernel matrix, and thus the above feature-map embeddings, can be directly constructed in experiments from the optical-population measurements over the training set as

$$\frac{1}{N}k_{\ell\ell'} = \frac{1}{N}\sum_i \bar{n}_\ell^{(i)}\bar{n}_{\ell'}^{(i)}. \tag{6.28}$$

Now that this set of orthogonal eigenfunctions was identified, feature-space coordinates of the photonic kernel machine can be interpreted as reciprocal-space components $\tilde{S}_\ell = \langle \hat{\psi}_\ell|S\rangle$ of any input spectrum in the span of $\{\hat{\psi}_\ell\}_\ell$.

In particular, let us consider a regression problem with a target of the form $\hat{y}^{(i)}[\omega_\ell] = \hat{f}_\ell(S^{(i)})$. From Eqs. (6.21) and (6.27), one has that the predictions bear the form of an expansion

$$\hat{y}^{(i)}[\omega_\ell] = \sum_{\ell'} w_{\ell'}[\omega_\ell]\langle \hat{\psi}_{\ell'}|S^{(i)}\rangle \tag{6.29}$$

of the feature-space coordinates over a set of learned "functions" $\{w_{\ell'}\}_{\ell'}$, given by

$$w_{\ell'}[\omega_\ell] \equiv \sqrt{N}[\mathbf{u}^T\mathbf{B}]_{\ell'\ell}, \tag{6.30}$$

as directly follows from Eq. (6.15).

In particular, by setting the trainable parameters by hand to $w_{\ell'}[\omega_\ell] = \hat{\psi}_{\ell'}(\omega_\ell)/\hat{\gamma}_{\ell'}$, one sees that $\hat{y}^{(i)}[\omega_\ell] = S^{(i)}[\omega_\ell]$, that is, a photonic kernel machine is, at least, able to reproduce the energy spectral density of a pulse $s(t)$ from a single-shot intensity measurement, provided the energy spectral density belongs to the linear span of $\{\hat{\psi}_\ell\}_\ell$, as will be indeed verified in Sec. IV.1. In practice, the task-dependent "functions" $\{w_{\ell'}\}_{\ell'}$ are learned during the optimisation procedure and may be evaluated explicitly at the chosen frequency bins $\{\omega_\ell\}_\ell$ from the measurement data and the training parameters $\mathbf{B}$ by making use of the above expression. This picture is schematically illustrated in Fig. 6.2.

III.2   Physical implementation

We will apply the above theory to the ultrafast processing of radio-frequency pulsed signals with a photonic lattice. The task consists in analysing a set of baseband radio-frequency signals $\{s^{(i)}(t)\}$ over a bandwidth $\Delta\omega$ around some reference angular frequency ω_0 by extracting some associated quantity of interest $\boldsymbol{y}$, such as the energy spectrum or the peak frequency. To this aim, let us introduce an adapted physical implementation of a photonic-lattice-based kernel machine. The setup is schematically illustrated in Fig. 6.3. It involves four successive elements.

Input signals enter the first unit of the system at an electro-optic modulator through frequency mixing with an optical carrier, $c(t) = c_0 \exp(-i\omega_p t)$, resulting in a modulated signal of the form $F^{(i)}(t) = s^{(i)}(t)e^{-i\omega_p t}$ whose central angular frequency $\omega_p + \omega_0$ may be shifted to accommodate the processing of signals in very different bands. The angular frequency of the local oscillator is set to $\omega_p = \bar{\omega} - \omega_0$, where $\bar{\omega}$ denotes the central angular frequency of the lattice, to maximise the response of the system. The now optical modulated signal is then routed to the photonic lattice, entering the cavities as a coherent drive.

The second unit consists of a $L \times L$ quadratic photonic lattice whose cavities are mutually coupled via near-field nearest-neighbour interactions. These cavities are coupled to the external modulated drive with some arbitrarily spatially-dependent rate v_ℓ. In a frame rotating at the drive's frequency, the dynamics of such a lattice is described by the following set of quantum Langevin equations:

$$\partial_t \hat{a}_\ell(t) = \Big[i(\Delta_\ell + \omega_0) - \kappa_\ell/2\Big]\hat{a}_\ell(t) + i\sum_{m \in v(\ell)} J_{\langle m,\ell\rangle}\hat{a}_m(t) + iv_\ell s(t) + \sqrt{\kappa_\ell/2}\,\hat{a}_\ell^{\mathrm{in}}(t), \quad (6.31)$$

where $\hat{a}_\ell$ is the photon annihilation operator at site ℓ, $\Delta_\ell = \omega_p - \omega_\ell$ is the detuning of the local oscillator, κ_ℓ the optical relaxation rate, $J_{\langle m,\ell\rangle}$ the linear coupling rate between cavities ℓ and m, $s(t)$ the broadband driving signal, and v_ℓ the local weight of the coupling of the ℓth cavity to the external drive. A high degree of control of the parameters is not required. In the following numerical simulations, we will set uniform angular frequencies ω_ℓ for simplicity and $\Delta = -\omega_0$, the rest of the parameters will be random variables. $J_{\langle m,\ell\rangle}$ will be uniformly drawn in the interval $[0, J_{\max}]$, κ_ℓ normally distributed around $\bar{\kappa} = zJ_{\max}/40$ ($z = 4$) with a standard deviation of 10%, $\Delta\omega = zJ_{\max}$ and $\boldsymbol{v}$ will be set to a normalised random real vector.

The third unit consists of a sensor that measures the intensity of the light radiated by the optical cavities as they are externally driven by an input signal. These populations are measured by time-averaging over some detector integration time Δt and collected into a vector $\bar{\boldsymbol{n}}^{(i)} = (\bar{n}_1^{(i)}, \ldots, \bar{n}_{L \times L}^{(i)}, 1)^T$, where a unit entry is added to get a supplementary trainable parameter acting as a bias. In what follows, two measurement settings will be considered:

(i) Measure of the local populations: $\bar{n}_\ell^{(i)} \propto \frac{1}{\Delta t} \int \mathrm{d}t \langle \hat{a}_\ell^\dagger \hat{a}_\ell \rangle_t$. This corresponds, for instance, to the experimental situation where the intensity that is vertically emitted by the cavities is measured by a camera facing the lattice.

(ii) Measure of the normal-mode populations: $\bar{n}_\ell^{(i)} \propto \frac{1}{\Delta t} \int \mathrm{d}t \langle \hat{\alpha}_\ell^\dagger \hat{\alpha}_\ell \rangle_t$. This corresponds, for example, to the experimental situation where the field leaking from the cavities is collected by an evanescently coupled waveguide and frequency-demultiplexed into $L \times L$ frequency channels coupled to photodetectors.

Finally, a fourth unit performs a linear combination of the measured populations by acting with a $n \times (L^2 + 1)$ matrix of parameters $\mathbf{B}$, to be optimised by training. The output of this last unit is thus of the form $\hat{\boldsymbol{y}}^{(i)} = \mathbf{B}^T \bar{\boldsymbol{n}}^{(i)}$, as in Eq. (6.21).
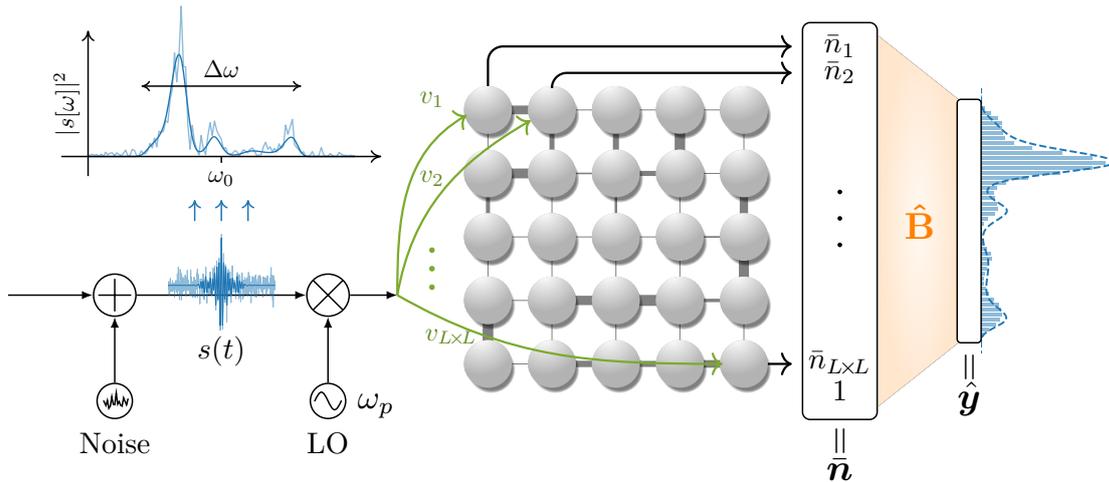

Figure 6.3: Schematic representation of a trained photonic-lattice-based kernel machine estimating the energy spectral density of a noisy pulse from single-shot local intensity measurements. The processing mechanism is the following: (i) A pulsed radio-frequency signal $s^{(i)}(t)$ arrives to the device immersed in white noise, (ii) it is then transferred to an optical carrier of angular frequency ω_p thanks to an electro-optic modulator ($\otimes$) and (iii) coherently injected into a lattice of $L \times L$ linear cavities with random parameters. (iv) The resulting optical populations are then measured through the light radiated by the cavities and, finally, (v) the spectrum of the original noiseless signal is reconstructed by linearly combining the measured quantities thanks to the fixed matrix $\hat{\mathbf{B}}$, obtained from the previous training protocol.

Training the lattice-based photonic kernel

The training starts from a training and a testing sets composed of N_train and N_test signals, respectively, each of the form $\{(s^{(i)}, \boldsymbol{y}^{(i)})\}_i$, where $s^{(i)}$ denotes the ith signal and $\boldsymbol{y}^{(i)}$ a set of known associated features we want our system to learn how to estimate. In regression tasks, these labels $\boldsymbol{y}^{(i)}$ may take arbitrary values, whereas in binary classification tasks $y^{(i)} = \pm 1$ depending on whether the associated input $s^{(i)}$ belongs to a class or not.

The trial function of the untrained model is initially given by $\hat{\boldsymbol{f}}(s^{(i)}) = \mathbf{B}^T \bar{\boldsymbol{n}}^{(i)}$. The training is carried out as follows:

(i) **Construct the matrix Y.** From the known features $\{\boldsymbol{y}^{(i)}\}_i$ associated to the samples of the training set, $\mathbf{Y}$ is first computed as $Y_{in} = y_n^{(i)}$.

(ii) **Obtain the matrix H.** Each input signal $s^{(i)}$ of the training set is fed into the device at the electro-optic modulator and the resulting cavity populations $\bar{\boldsymbol{n}}^{(i)}$ are measured by the sensor. All these measured populations are stored in a matrix $H_{im} = \bar{n}_m^{(i)}$.

(iii) **Determine the optimal parameters $\hat{\mathbf{B}}$.** For a chosen value of the regularisation hyperparameter λ, one obtains the optimal parameters by minimising the objective function as $\hat{\mathbf{B}} = \arg\min_{\mathbf{B}} J(\mathbf{B})$, with $J(\mathbf{B}) = \sum_{i=1}^{N_\text{train}} V(\boldsymbol{y}^{(i)}, \hat{\boldsymbol{f}}(s^{(i)})) + \frac{\lambda}{2}\|\mathbf{B}\|_2^2$, where $\hat{\boldsymbol{f}}(s^{(i)}) = \mathbf{B}^T \bar{\boldsymbol{n}}^{(i)}$, with $\bar{\boldsymbol{n}}^{(i)}$ as obtained in the previous step. For regression tasks, one typically uses square errors $V(y, \hat{y}) = \|y - \hat{y}\|^2$, which directly yields $\hat{\mathbf{B}} = (\mathbf{H}^T\mathbf{H} + \lambda \mathbb{1})^{-1}\mathbf{H}^T\mathbf{Y}$, with $\mathbf{Y}$ and $\mathbf{H}$ as computed at steps (i) and (ii), respectively. For classification tasks, one instead uses the hinge loss $V(y, \hat{f}(\boldsymbol{x})) = \max(0, 1 - y\hat{f}(\boldsymbol{x}))$ and minimises the objective function by standard iterative methods.

(iv) **Evaluate the accuracy of the model.** The model is now trained. For any input signal s fed into the system, features are now estimated according to $\hat{\boldsymbol{f}}(s) = \hat{\mathbf{B}}^T \bar{\boldsymbol{n}}$, from the measurement of the resulting populations $\bar{\boldsymbol{n}}$. Its accuracy can then be tested on the testing set by comparing the predictions $\hat{\boldsymbol{y}}^{(j)} = \hat{\boldsymbol{f}}(s^{(j)})$ to the known features $\boldsymbol{y}^{(j)}$, for every input signal $s^{(j)}$ in the testing set.

Experimentally accessing the feature space

The general feature-space-inspection ideas introduced above can be adapted to the present architecture. We here briefly summarise the main identities that we shall use in the following when studying the learning mechanism from experimentally accessible data.

The prediction associated to some signal $s^{(i)}$ can be written explicitly as an expansion of the feature-space components,

$$\hat{y}_n^{(i)} = \sum_{n'} W_{nn'} \langle \hat{\psi}_{n'} | S^{(i)} \rangle, \tag{6.32}$$

where $S^{(i)}$ is the spectral density of the signal. The dual of the feature map can be easily estimated as $\hat{\psi}_m(\omega) = \sqrt{\hat{\gamma}_m}\hat{\phi}_m(\omega)$ from the empirical eigenvalues $\{\hat{\gamma}_m\}_m$ and eigenfunctions $\{\hat{\phi}_m\}_m$. The former are obtained from the experimental data as the eigenvalues of the matrix $\mathbf{k}/N_\text{train} = \mathbf{H}^T\mathbf{H}/N_\text{train}$ (note that $k_{\ell\ell'}/N_\text{train} = \frac{1}{N_\text{train}}\sum_i \bar{n}_\ell^{(i)}\bar{n}_{\ell'}^{(i)}$); the latter
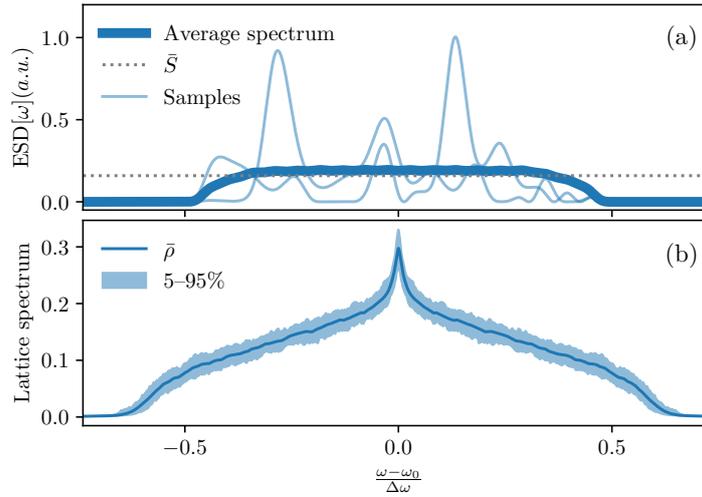
Figure 6.4: (a) Energy spectral density averaged over 10^5 realisations of the noiseless pulses, as given by Eq. (6.34), as well as that of a few individual realisations. (b) Mean and interval between quantiles 5% and 95% for the optical spectra of 100 realisations of a 30×30 random photonic lattice.

are given by $\hat{\phi}_m(\omega) = \boldsymbol{u}_m^T \boldsymbol{h}(\omega)/\sqrt{N_{\text{train}}\hat{\gamma}_m}$, where $\boldsymbol{u}_m$ is the mth eigenvector of $\mathbf{k}$ and $h_\ell(\omega) = |\chi_\ell[\omega]|^2/\Delta t$ is the population susceptibility of the ℓth measured mode. The parameters of the feature-space hyperplanes can be obtained from the trained parameters as $\hat{\mathbf{W}} = \sqrt{N_{\text{train}}}\boldsymbol{u}^T\hat{\mathbf{B}}$. Frequency-dependent features may be defined as $\hat{y}_n = \hat{y}[\omega_n]$. Then one may equivalently write Eq. (6.32) as a mode decomposition over the basis of empirical feature functions as $\hat{y}^{(i)}[\omega] = \sum_{n'} \hat{w}_{n'}[\omega]\langle\hat{\psi}_{n'}|S^{(i)}\rangle$. The hyperplanes can then be interpreted as a set of learned functions, explicitly given by $\hat{w}_{n'}[\omega_n] = \hat{W}_{nn'}$.

Benchmarking the photonic-lattice kernel machine

In the following, two different approaches will be employed to benchmark the above-defined physical implementation of a photonic kernel.

In order to evaluate the ability of the model to estimate the spectrum of pulsed signals, we will first use the modulus square of the fast Fourier transform (FFT) of the input signals as a reference of energy spectral density. We will assume an ideal sampling of the pulse over a centred window of time length $\Delta T = 5 \times 2\pi/\kappa$ at a sampling rate of $f_{\text{s}} = 200 \times \kappa/2\pi$. For cavities with $2\pi/\kappa \sim 10\,\text{ps}$, this corresponds to a sampling rate of $f_{\text{s}} = 10\,\text{THz}$. Note that this is more than three orders of magnitude beyond the state of the art. Yet in the following the photonic kernel will be shown to outperform this rather fictional ideal device.

We will also use a reservoir computing approach based on a nonlinear polaritonic lattice as first introduced in Ref. [399]. This reservoir was numerically proven successful in image and speech recognition tasks and chaotic time-series forecasting, and was recently experimentally tested on an optical character recognition task [400]. This reservoir is

modelled by the following discrete complex Ginzburg-Landau equation:

$$\partial_t \alpha_\ell(t) = \Big[+ i(\Delta_\ell + \omega_0) + \gamma - (\Gamma + ig)|\alpha_\ell(t)|^2 \Big]\alpha_\ell(t) + i \sum_{m \in v(\ell)} J_{\langle m,\ell \rangle} \alpha_m(t) + iv_\ell s(t), \quad (6.33)$$

where $\gamma = P - \kappa/2$ is a gain coefficient that accounts for the single-body decay rate $\kappa/2$ and the magnitude of the external pumping P, that brings the system close to instability. Here, Γ and g respectively account for two-body dissipation and interaction processes. The input signals are coherently injected in the same fashion as for the linear lattice. In the following numerical simulations, we will set $\Delta = -\omega_0$, $J_{\langle m,\ell \rangle}$ uniformly drawn in the interval $[0, J_{\max}]$, $\Gamma = zJ_{\max}/40$ $(z = 4)$, $\gamma/\Gamma = 8 \times 10^{-4}/2\pi$, $g/\Gamma = 1.6/2\pi$, $\Delta\omega = zJ_{\max}$ and $\boldsymbol{v}$ to a normalised random real vector. The output of this model depends on the amplitude of the input. In what follows, the input energy will be set to 50Γ.

The training of this model is realised exactly as for the photonic kernel machine, from local population measurements $\bar{n}_\ell^{(i)} \propto \frac{1}{\Delta t} \int \mathrm{d}t |\alpha_\ell(t)|^2$.

IV   Applications

IV.1   Spectrum estimation

As a first illustration of the learning capabilities of the above-described photonic kernel machine, let us consider the extraction of the noiseless energy spectral density of an ultrashort pulsed signal embedded into a noisy background. Given an input noisy pulsed signal $s(t) + \xi(t)$, this task consists in giving the best possible estimation $\hat{y}_n$ of its frequency-binned energy spectral density $y_n = |s[\omega_n]|^2$ regardless of the noisy background $\xi(t)$.

In order to train and study the performance of the model, we generate training and testing sets of N_{train} and N_{test} pulses, respectively. To do so, we first generate known noiseless random spectra of same total energy $E_0 = \int \mathrm{d}\omega S_{ss}[\omega]$ by cubic B-spline interpolation of a set of N_b signal bins $\tilde{s}_n \equiv \tilde{s}[\omega_n]$, with frequency bins $\{\omega_n\}_n$ equally spaced within the band $[\omega_0 - \Delta\omega/2, \omega_0 + \Delta\omega/2]$ and randomly sampled from a Boltzmann distribution $p[\tilde{s}_n] = (1/Z)e^{-\beta V[\tilde{s}_n]}$ parametrised by the following potential:

$$V[\tilde{s}_n] = \frac{a}{N_b} \sum_{n=1}^{N_b-1} |\tilde{s}_{n+1} - \tilde{s}_n|^2 + b \Big| \max_n |\tilde{s}_n|^2 - S_{\text{peak}} \Big|^2 + c \Big| \mathrm{std}_n |\tilde{s}_n|^2 - \bar{S} \Big|^2, \quad (6.34)$$

with $\tilde{s}_i = 0$, $i = 1, N_b$, $S_{\text{peak}} = 8\bar{S}$, $\bar{S} = E_0/\Delta\omega$. Here, a acts as stiffness parameter whereas the b-term favours peaked spectra. Finally, the c-term prevents the sampled spectra from sharing too similar shapes by favouring the presence of secondary peaks. The parameters used throughout this section are $N_b = 20$, $\beta a = \beta c = 100$ and $\beta b = 50$. The energy spectral densities of the obtained random noiseless spectra are shown in Fig. 6.4 (a), where the average energy distribution is compared to $\bar{S}$ and a few typical examples are plotted, exhibiting various peaks with different heights. The choice of bandwidth ($\Delta\omega = zJ_{\max}$) ensures that all the power of the signal to be analysed can be sensed by the photonic lattice, as shown in Fig. 6.4 (b), where the average optical spectrum of a large random photonic lattice is plotted. The random spectra are then Fourier-transformed to

the time domain and white noise $\xi(t)$ is added to match some signal-to-noise ratio SNR, here defined as the relative contribution of the noise to the total energy in the analysed bandwidth, i.e. $\text{SNR} = E_0^{-1} \int_{\omega_0 - \Delta\omega/2}^{\omega_0 + \Delta\omega/2} d\omega |\xi[\omega]|^2$.

We then simulate the response of the photonic lattice to each of the driving input signals $s^{(i)}(t)$ of the training set by numerically integrating the coupled dynamical equations (6.31). For each signal, either the local and normal-mode populations are then measured yielding a set of time-averaged populations $\bar{\boldsymbol{n}}^{(i)}$. The weights $\mathbf{B}$ are then optimised over the training data so as to minimise the square error between the prediction of the photonic kernel machine $\hat{\boldsymbol{y}}$ and the known spectra of the noiseless pulses $\boldsymbol{y}$. Upon fine-tuning of the hyperparameter λ by 10-fold cross validation, the optimal weights $\hat{\mathbf{B}}$ are obtained analytically as explained above. The error of the trained model is then evaluated on the test set. We here quantify this error by the relative misclassified energy $\Delta E / E_0$, where ΔE represents the energy area between the estimated and the actual energy spectral density curves of the original noiseless spectra. In Fig. 6.5, we use this metric to benchmark our model against the ideal FFT of the input signal and a the nonlinear polariton-based reservoir. For any of the chosen SNR values and lattice sizes, the photonic kernel outperforms the other two approaches. Interestingly, the maximum performance is already reached with lattices as little as 10×10, with an error in the reproduced spectrum about three times smaller than that obtained by the ideal FFT procedure. In addition, Fig. 6.6 shows the error frequency over the testing set for the three values of the SNR and a 20×20 photonic lattice. The (very unlikely) worst-case scenario over the testing set at each value of the SNR is compared to the ideal targeted spectrum and that reconstructed by the FFT in Fig. 6.7.

In order to understand how the device learns from training examples, let us make use of the theoretical concepts introduced above. Regression by the implemented photonic kernel machine is performed by a linear expansion $\hat{y}^{(i)}[\omega_n] = \sum_{n'} \hat{w}_{n'}[\omega_n] \langle \hat{\psi}_{n'} | S^{(i)} \rangle$ of the feature-space components $\langle \hat{\psi}_{n'} | S^{(i)} \rangle$ over a set of learned functions $\hat{\boldsymbol{w}}$. The eigenvalues γ_n and eigenfunctions $\psi_n / \sqrt{\gamma_n}$ of the photonic kernel do not depend on the optimisation procedure and can be given empirical estimations from the measured populations $\bar{\boldsymbol{n}}^{(i)}$ during the training process, as described above. In Fig. 6.8 (a), we show the convergence of the empirical eigenvalues as the amount of training examples is increased, that is already reached for roughly $N_{\text{train}} = 1000$ with our training protocol. Figs. 6.8 (b) and (c) show the leading empirical feature maps as well as the corresponding learned eigenfunctions. On this task, one observes that the optimisation procedure leads to a set of learned functions that correspond to filtered analogues of the empirical eigenfunctions of the kernel. One sees from Fig. 6.8 (b) that the model builds a Fourier-sine expansion with a spectral resolution cut-off at $\Delta\omega / 2\pi L^2$. While in principle the optimisation procedure may be sensitive to any feature-space component within this bound, the ridge regularisation introduced during the optimisation induces a soft cut-off for those whose associated eigenvalues have magnitudes lower than λ. This reduction to only the most statistically relevant components of the functional basis prevents the model from overfitting the training set, which would undermine its generalisation capacity. In Fig. 6.8 (c), the effect of the regularisation is clearly visible on the highest-order represented learned function, that
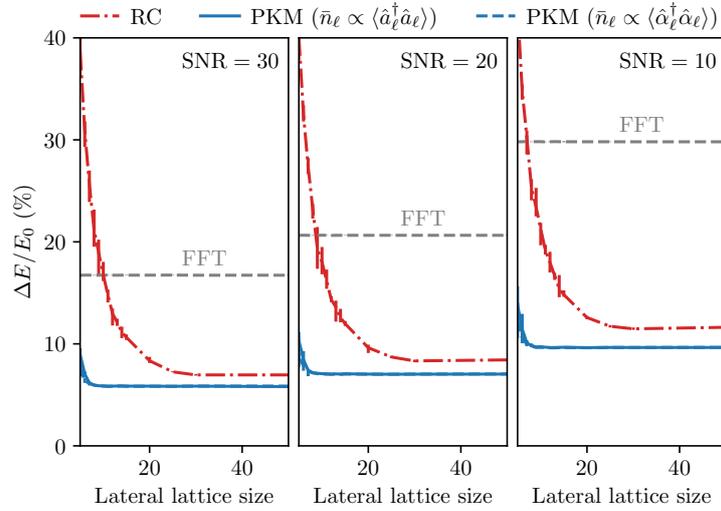
Figure 6.5: Relative misclassified energy $\Delta E/E_0$ on the testing set for three values of the SNR for the FFT (horizontal dashed line), the complex Ginzburg-Landau reservoir computing model (dash-dotted) and the photonic kernel machine where either the local-mode (plain) or the normal-mode (dashed) populations are measured. Data is averaged over 5 realisations of the reservoir, error bars correspond to the intervals between the lowest and highest errors over these realisations. For each realisation: $N_{\text{train}} = 7000$ and $N_{\text{test}} = 3000$.
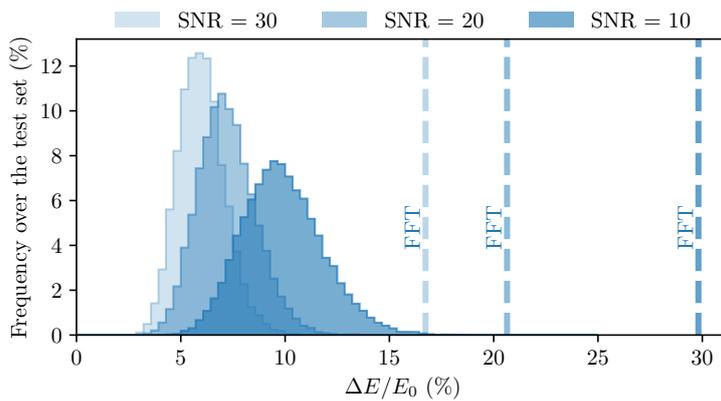

Figure 6.6: Frequency of the error score over the testing set for three SNR values averaged over 5 realisations of a 20×20 photonic kernel machine. $N_{\text{test}} = 3000$ for each realisation. The error score of the FFT is shown as dashed lines for comparison and falls systematically above the upper bound of that of the photonic kernel machine, in spite of being slower and requiring an ideal sampling rate significantly beyond the state of the art.
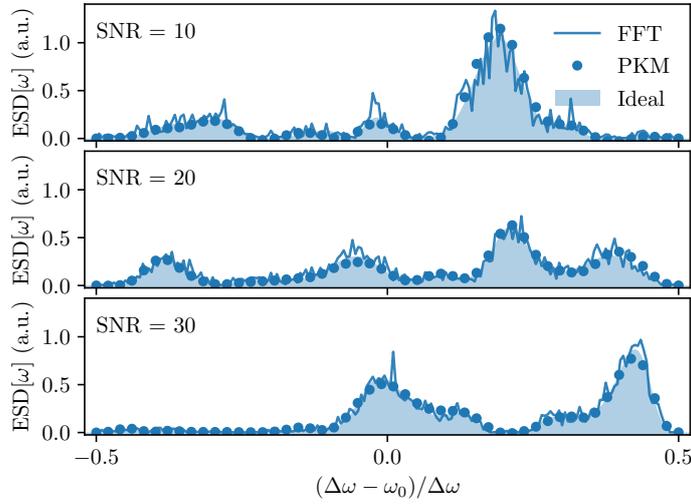
Figure 6.7: Worst-case predictions of a 20×20 photonic kernel machine (dots) over the testing set. The ideal noiseless energy spectral densities to be reconstructed (shaded area) and those obtained by squaring the FFT of the noisy input pulse (plain line) are shown for comparison. Normal-mode populations are measured. $N_{\text{test}} = 3000$.
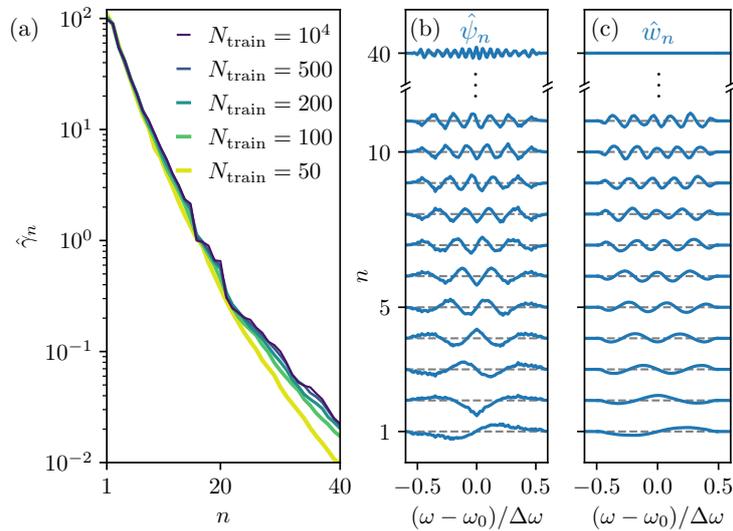

Figure 6.8: (a) Convergence of the empirical spectrum of a photonic kernel for increasing training-set sizes. (b) First empirical eigenfunctions of the photonic kernel for $N_{\text{train}} = 10000$. (c) Functions learned by the photonic kernel machine during the optimisation process. Parameters are $L = 20$, SNR $= 20$ and $\lambda = 10$.

is completely filtered out. Hence, regularisation here manifests itself as a low-pass filter on the learned decomposition.

From this figure, the interpretation of the the photonic kernel machine regression mechanism becomes very clear: (i) the training set determines some optimal Fourier-like decomposition of the spectra, (ii) the regularisation truncates the basis of such a decomposition to its most statistically relevant components, and, finally, (iii) the optimisation finds a set of smooth filtered base functions on which to expand back those components to best reproduce the features, finally reconstructing the noiseless spectrum, from which the noisy background uncorrelated with the training set was regularised out.

IV.2 Pulse shape recognition

We now show the performance of the same photonic kernel machine trained on a noisy-pulse shape classification problem.

The task consists in determining whether the envelope of an input pulse is Gaussian ($y = 1$) or Lorentzian ($y = -1$) from the measurement of the photonic populations of the lattice in the presence of noise at the input port of the system. We prepare a set of pulses with central angular frequencies uniformly drawn at random on the band of interest $[\omega_0 - \Delta\omega/2, \omega_0 + \Delta\omega/2]$ and full widths at half maximum (FWHM) normally distributed around $\overline{\text{FWHM}} = \Delta\omega/20$ with a relative standard deviation of 10%. The induced populations are then time-integrated over some detection time Δt yielding a vector of intensities $\bar{\boldsymbol{n}}$ that are finally linearly combined in such a way that the output of the photonic kernel machine is now a scalar of the form $\hat{f}(S) = \boldsymbol{\beta}^T \bar{\boldsymbol{n}}$. The output of the ith pulse may be equivalently rewritten in terms of components of the feature map as $\hat{f}(S^{(i)}) = \boldsymbol{w}^T \tilde{\boldsymbol{S}}^{(i)} + b$, with $\tilde{S}_n^{(i)} = \langle \psi_n | S^{(i)} \rangle$. As discussed above, $(\boldsymbol{w}, b)$ defines the decision boundary of the model as a hyperplane in feature space. Input pulses are then classified into either of the two classes depending on whether their feature-space coordinates $\tilde{\boldsymbol{S}}^{(i)}$ fall on either sides of this plane. Hence, predictions are of the form $\hat{y}^{(i)} = \text{sign}(\hat{f}(S^{(i)}))$. The optimisation process is realised by minimising the hinge loss $V(y^{(i)}, \hat{f}(S^{(i)})) = \max(0, 1 - y^{(i)}\hat{f}(S^{(i)}))$. This is here achieved by means of a convex optimisation solver [466] for $\lambda \to 0^+$. The classification process is illustrated in Fig. 6.9 for a 20×20 photonic kernel machine and intermediate noise strength (SNR = 20). In panel (a), one observes that features corresponding to either classes indeed cluster at either of the sides of the discriminating hyperplane independently from the value of the FWHM. As it becomes clear in panel (b), the predictions become less accurate as the distance from the separating hyperplane becomes smaller, thereby giving an estimation of the likelihood of the prediction. This can be made more explicit by calibrating the probability of the classifier. This probability is shown in panel (c) as given by $\mathbb{P}(s^{(i)} = \text{``Gaussian''}|\hat{f}(S^{(i)})) = [1 + \exp(-A\hat{f}(S^{(i)}) + B)]^{-1}$, where the calibration parameters A and B were determined by Platt scaling [467].

The performance of a 20×20 trained photonic kernel machine is shown via its receiver operating characteristic (ROC) curve in Fig. 6.10 for increasing noise strengths and the two population measurement scenarios. This displays the sensitivity (true positive rate) as one allows the specificity of the model to drop (higher false positive rates) by playing on some external bias added to the trained model, the best trade-off being found at the top left corner for no external bias. The ROC curve of an unbiased classifier that affects
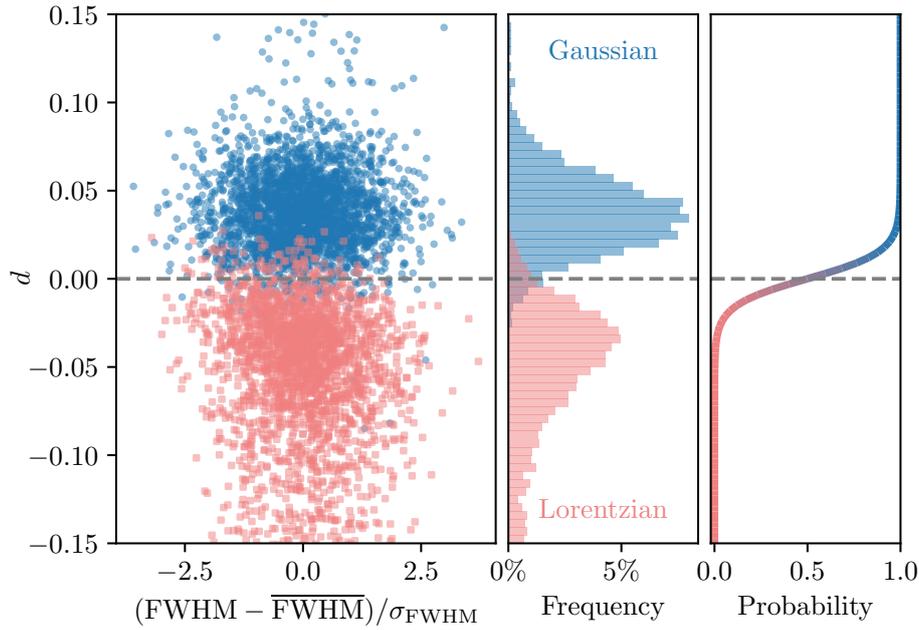
Figure 6.9: (a) Signed distance from the testing pulses' features to the learned hyperplane (decision boundary) as a function of their FWHM for a 20×20 photonic kernel machine under normal-mode measurement of the photonic populations. Dots correspond to Gaussian pulses, squares to Lorentzian ones. Pulses falling above the decision boundary (dashed line) are categorized as Gaussian by the classifier and conversely. SNR = 20, $N_{\text{train}} = 14000$ and $N_{\text{test}} = 6000$. (b) Frequency of each class as a function of the signed distance to the discriminating hyperplane. (c) Probability that a pulse be Gaussian or Lorentzian at any given value of its associated signed distance to the discriminating hyperplane.
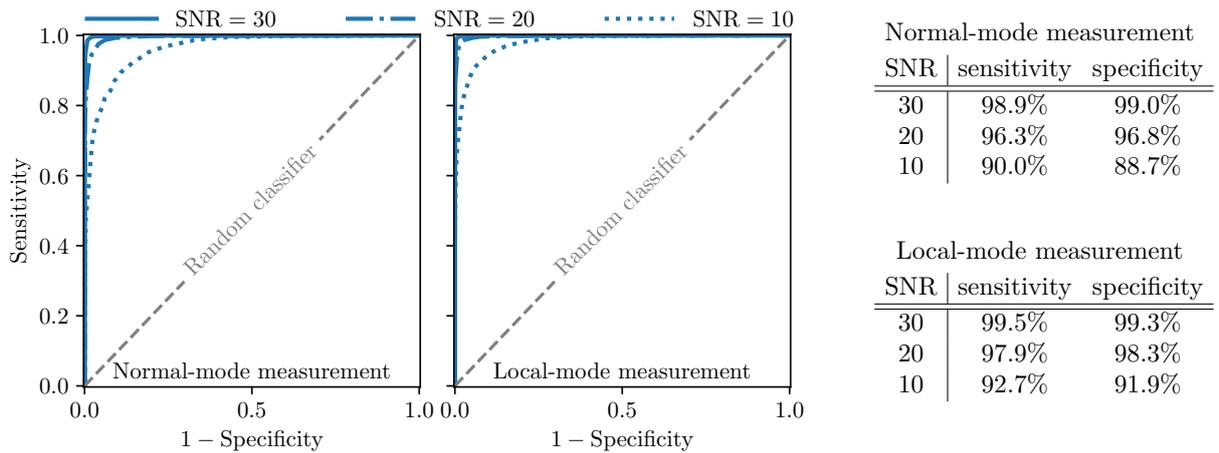

Figure 6.10: Receiver operating characteristic (ROC) curve for a 20×20 photonic kernel machine on the pulse shape classification task for three noise strengths and two measurement scenarios. The closer to the top left corner, the better. The numerical values of their associated sensitivities and specificities are on the right. $N_{\text{train}} = 14000$ and $N_{\text{test}} = 6000$.

pulses randomly to either shape class is plotted as well for comparison. The sensitivity and specificity values of the trained classifier are given in the right panel of Fig. 6.10 for both population-measurement protocols.
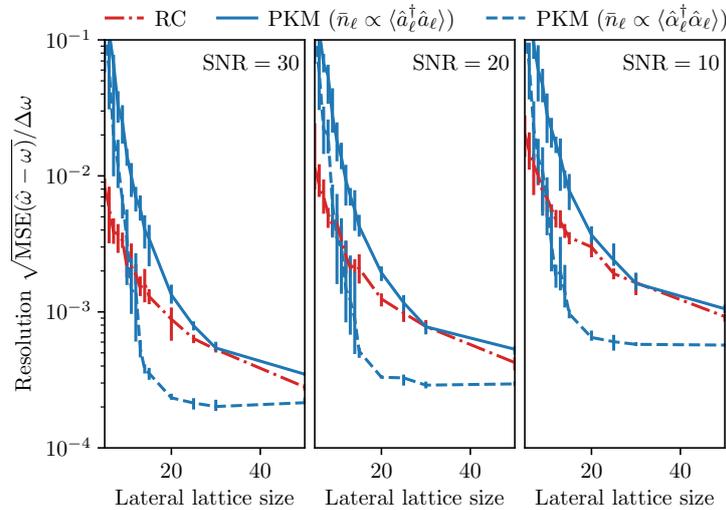

Figure 6.11: Resolution of the photonic kernel machine on the testing set for either local-mode (plain) or normal-mode (dashed) population measurements for increasing lattice sizes L and three values of the signal-to-noise ratio. The performance of the nonlinear polariton-based reservoir-computing scheme (dash-dotted) is shown for comparison. Data is averaged over 5 realisations of the reservoir, error bars correspond to the intervals between the lowest and highest resolutions over these realisations. Parameters are $N_{\text{train}} = 7000$ and $N_{\text{test}} = 3000$.

IV.3   Frequency tracking

Above, only the case of pulsed input signals was investigated. In the following, we illustrate the performance of the photonic kernel machine presented above on the analysis of continuous radio-frequency signals by considering a task of frequency estimation of a noisy sinusoidal signal.

To do so, we first generate a first set of training baseband signals consisting of complex exponentials with random initial phases and angular frequencies ω uniformly drawn between $\omega_0 - \Delta\omega/2$ and $\omega_0 + \Delta\omega/2$, to which white noise is added so as to match some signal-to-noise ratio SNR, here defined as the ratio between the average power of the sinusoidal baseband signal and that of the noise. We then measure the steady-state populations of the cavity resulting from the driving of the coupled cavities by the modulated signals, here after a time $\tau_d = 10/\bar{\kappa}$, and use this vector of populations to make frequency predictions of the form $\hat{f}(S) = \boldsymbol{\beta}^T \bar{\boldsymbol{n}}$. The vector $\boldsymbol{\beta}$ is then optimised so as to minimise the mean squared error between the estimated $\hat{\omega}^{(i)} = \hat{f}(S^{(i)})$ and the actual $\omega^{(i)}$ angular frequencies of all signals in the training set, with a ridge-regularisation hyperparameter determined from 10-fold cross validation.

The performance of the trained photonic kernel machine is finally evaluated on a testing set composed of new random complex exponentials. The achieved average resolution

is shown in Fig. 6.11 as a function of the lattice size for increasing values of the SNR, revealing the performance of the above-described photonic kernel machine on the spectral analysis of continuous radio-frequency signals. For cavities with $2\pi/\kappa \sim 10\,\mathrm{ps}$, the waiting time would be as little as $\tau_d \sim 10\,\mathrm{ps}$.

V   Conclusion

In this chapter, we theoretically proposed photonic kernel machines, a new approach for optical ultrafast spectral analysis of noisy radio-frequency signals that translates kernel methods to photonic hardware. Such devices realise regression or classification tasks on high-dimensional data with throughputs above the gigahertz by utilising the optical response of a set of optical modes to input analogue signals as a measure of similarity.

We first gave a theoretical description of photonic kernel machines under very general assumptions. We analytically investigated the similarity kernel built-in in such devices and were able to express it explicitly from the susceptibility of the measured observables. Furthermore, we explored the feature maps associated to photonic kernel machines and found that their expressions could be experimentally determined from population measurements and the knowledge of the single-mode susceptibility.

We then studied a model describing a physical implementation consisting of a lattice of coupled *linear* optical cavities. We numerically demonstrated its capabilities on various regression and classification tasks, comprising the analysis of both pulsed and continuous radio-frequency signals. In particular, the proposed setup proved efficient in predicting the spectrum of picosecond pulses with nontrivial spectral structure from single-shot intensity measurements. The simulated implementation was shown to be capable of predicting spectra with higher fidelity than the ideal FFT of the noisy input signal. This latter procedure being much slower and involving sampling rates beyond the reach of the state of the art. Moreover, it was shown to be able to discriminate pulses with distinct shapes as well as to estimate the angular frequency of continuous harmonic input signals. We showed that, by adding noise at the input of the device during the training protocol, the spurious effects of background noise on the predictive performance of the device could be successfully mitigated. On a spectrum estimation task, we could extract the actual feature maps associated to the simulated kernel machines as well as the basis of learned functions the photonic kernel machine composes its predictions from. This allowed us to interpret the photonic kernel machine regression mechanism and revealed the ability of the system to filter out the uncorrelated background noise.

We believe that such devices, capable of analysing above one million radio-frequency signals per second, may found applications in a broad variety of domains beyond spectroscopy. In the field of radio-frequency sensing, it could be used in pulse-Doppler radar systems as a way to optically analyse the reflected signals. In this way, the rate of emission could be increased by orders of magnitude, by relaxing the limiting dependence on the sampling rate of analogue-to-digital converters. In telecommunications, these devices could be used, for instance, as a decoding means in frequency-shift keying protocols involving high modulation rates in noisy environments. Finally, photonic kernel machines could be integrated to more conventional machine learning pipelines as a means of extract-

ing non-trivial digital features from analogue signals, acting as both an analogue-to-digital converter and a preprocessing stage.

The original results of this chapter are contained in Refs. $[\delta, \gamma]$.

General conclusion

In this thesis, we studied the reservoir-induced dynamics of open quantum systems as well as the learning mechanism of classical photonic reservoirs. This work was structured around three main axes: the effective description of quantum systems in contact with local and spatially extended engineered reservoirs, the efficient numerical representation and evolution of the state of open quantum systems and the use of photonic reservoirs as hardware capable of realising ultrafast feature-space embeddings of high-dimensional input data for machine learning applications.

In Chapter 1, we gave a quantised description of the coupled optical and mechanical degrees of freedom of a semiconductor nanodisk resonator from first principles. We completed this description by addressing the case of a hybrid resonator embedding a quantum well comprising three mutually coupled degrees of freedom, of electronic, optical and acoustic nature. We derived expressions for numerically evaluating the strong electromechanical coupling between a resonator phonons and its quantum-well excitons. We showed that, in such tripartite resonators, the dressing of photons by electron-hole pairs could induce a significant increase of the bare optomechanical coupling, a feature of great interest in a wide variety of quantum applications. In this regard, a more systematic study of the confinement of the exciton density and the mechanical strain in disk resonators could further enhance the achievable optomechanical cooperativity. Other geometries such as micropillars or annular disks embedding quantum wells could reach cooperativities above 1, as calculations suggest [ζ], opening new perspectives of optomechanics in the strong-coupling regime.

While the coupling of a quantum system of interest to the outside world is generally seen as detrimental in most contexts, structured environments referred to as engineered reservoirs provide a way to externally tweak its fate. In Chapter 1, we gave some clear examples of this in the optomechanical context. We first recalled the standard sideband cooling process and the optical spring effect, mechanisms that allow one to optically control the mechanical motion of a resonator. We then showed that a further ancillary optical degree of freedom could lead to a phonon lasing phase transition, radically changing the statistics of the mechanical mode. On the basis of these optomechanical ideas, we developed a general framework for effectively describing the complex dynamics mediated by spatially extended driven-dissipative reservoirs, in Chapter 2. General analytical expressions for the Liouvillian ruling the reduced dynamics of a system in contact with bosonic such reservoirs were derived within the Born-Markov approximation, both in discrete and continuous geometries.

When studying lattices of cavity-coupled optomechanical resonators within the above framework in Chapter 3, we showed that driven-dissipative extended reservoirs could me-

diate both coherent and incoherent interactions between distant mechanical oscillators. Under particular conditions on the driving of the reservoir, we could stabilise states exhibiting ever circulating cavity-mediated heat currents running through the optomechanical structure [α]. Many extensions of this idea could be studied with the same formalism. Particularly interesting prospects could be, for instance, the study of two-tone-driven [468, 469] extended reservoirs, that would induce many-body squeezing interactions, or the case of nonlinear coupling of the system to the reservoir. An example of the latter is that of parametric coupling, that would lead to effective cross-Kerr models, known for their rich phase diagrams [470, 471].

In Chapter 4, we reviewed several numerical algorithms for simulating open quantum systems, from mean-field to a purely quantum level. Some of these were adapted to the treatment of systems in contact with extended reservoirs, or, more generally, described by nonlocal dissipators. The intrinsic difficulties of simulating the open quantum many-body problem as well as the shortcomings of the existing methods at efficiently simulating very entangled systems led us to introduce the dynamical corner-space method [γ] in Chapter 5. This algorithm proved capable of evolving lightweight parsimonious representations of the density matrix of low-entropy systems. It was successfully applied to the continuous-time simulation of noisy entangling quantum circuits with up to 21 qubits, a situation relevant in today's so-called noisy intermediate-scale quantum era [49]. This allowed us to study the detrimental consequences of the environment on the fidelity of such processors within realistic models of noise. This method opens many new perspectives in the simulation of low-entropy quantum systems. For instance, the robustness to weak dissipation of the quantum advantage recently identified in battery charging processes [472, 473] could be numerically explored. Furthermore, this method could be combined with efficient variational representations of the corner-space wave functions, such as neural-network ansätze [343, 344, 346, 347], to, ideally, bring the exponential complexity of the simulation from exponential down to polynomial in the number of qubits.

Finally, we introduced photonic kernel machines. We first described how usual kernel machines are capable of learning from a similarity measure—the kernel—, and analytically derived prescriptions for accessing to their internal feature-space representations. An ideal similarity measure for comparing two signals was then symbolically introduced *ad hoc*. We showed that the feature-space embeddings characterising this kernel could be naturally obtained from single-shot measurements of the populations of a linear photonic lattice. This motivated the introduction of a photonic-lattice-based kernel machine [δ, γ], powered by physical hardware. The performance of such a device was finally numerically demonstrated on the ultrafast spectral analysis of noisy radio-frequency signals, on both regression and classification tasks. An interesting perspective would be to integrate such devices into more conventional machine learning pipelines as a means of extracting non-trivial digital features from analogue signals, acting as both an analog-to-digital converter and a preprocessing stage.

A Quantum description of an optomechanical nanoring resonator

I Radial breathing modes

Under the plane stress condition $\sigma_{zz} = 0$, the Lagrangian of the radial motion of an annulus of inner and outer radii R_a and R_b takes the form

$$L_r = \int_\Omega \mathrm{d}\boldsymbol{r}\left\{\frac{1}{2}\rho\dot{u}_r^2 + \frac{1}{2}\rho c_{\mathrm{P}}^2 u_r\left(\frac{1}{r}\partial_r[r]\partial_r - \frac{1}{r^2} + \frac{1}{\Gamma^2}\frac{1}{r^2}\partial_\theta^2\right)u_r\right\}, \qquad (A.1)$$

where c_{P} is the sound velocity, as given by Eq. (1.18), $\Gamma \equiv c_{\mathrm{P}}/c_{\mathrm{S}} = \sqrt{\frac{2}{1-\nu}}$ is the sound-velocity ratio in the material for two-dimensional geometries. In GaAs ($\nu = 0.32$) this is given by $\Gamma \approx 1.71$.

This Lagrangian can be diagonalised by expanding the radial displacement into the following basis

$$u_r(r,\theta) = \sum_{\substack{n=1 \\ m=0}}^{+\infty} u_{nm}\phi_{n,m}(r,\theta), \quad \phi_{n,m}(r,\theta) = \mathcal{N}_{nm}R_{nm}(r)\Theta_m(\theta), \quad \int_\Omega \mathrm{d}\boldsymbol{r}|\phi_{n,m}|^2 = V_\Omega,$$
$$(A.2)$$

with

$$R_{nm}(r) = J_{\nu_m}(K_{nm}r) + x_{nm}Y_{\nu_m}(K_{nm}r), \quad \Theta_m(\theta) = \cos(m\theta), \quad \nu_m = \sqrt{1 + (m/\Gamma)^2}, \qquad (A.3)$$

and where K_{nm} is the nth root of

$$(\mathfrak{D}Y_{\nu_m})(kR_a)(\mathfrak{D}J_{\nu_m})(kR_b) - (\mathfrak{D}J_{\nu_m})(kR_a)(\mathfrak{D}Y_{\nu_m})(kR_b) = 0, \qquad (A.4)$$

with $\mathfrak{D}$ the differential operator associated to the considered boundary condition such that $(\mathfrak{D}R)(\boldsymbol{r} \in \partial\Omega) = 0$, and

$$x_{nm} = -\frac{(\mathfrak{D}J_{\nu_m})(K_{nm}R_a)}{(\mathfrak{D}Y_{\nu_m})(K_{nm}R_a)}. \qquad (A.5)$$

These modes have associated angular frequencies $\Omega_{n,m} = K_{nm}c_{\mathrm{P}}$.

The orthogonality of the radial dependence R_{nm} of the eigenfunctions of the differential operator of the Liouvillian follows from it being symmetric. Indeed, one has, for

$K_{nm} \neq K_{n'm'}$,

$$(K_{nm}^2 - K_{n'm'}^2) \int_{R_a}^{R_b} \mathrm{d}r\, r R_{nm}(r) R_{n'm'}(r) = \left[r \Big(R_{nm}(r) \partial_r R_{n'm'}(r) - R_{n'm'}(r) \partial_r R_{nm}(r) \Big) \right]_{R_a}^{R_b}$$

$$\equiv \left[R_{nm}(r) \partial_r [r] R_{n'm'}(r) - R_{n'm'}(r) \partial_r [r] R_{nm}(r) \Big) \right]_{R_a}^{R_b}.$$

$$(A.6)$$

The orthogonality of the base functions then follows from this identity for any choice of boundary conditions among $\mathfrak{D} = 1$, ∂_r, $r^{-1}\partial_r[r]$ and $\alpha \partial_r + \beta r^{-1}$. For a free solid, the latter is the proper boundary condition. Indeed, the radial stress $\sigma_{rr} = \tilde{\lambda}(u_{rr} + u_{\theta\theta}) + 2\mu u_{rr}$ must vanish at the boundaries. One then has $\sigma_{rr} = \frac{2\mu}{1-\nu}(\partial_r + \frac{\nu}{r})u_r$, and thus that $\mathfrak{D} = \partial_r + \frac{\nu}{r}$.

The deformation quantum associated to some excited mode resulting from this decomposition is given by

$$\Sigma(\boldsymbol{r}) = \frac{x_{nm}^{\mathrm{ZPF}}}{R} \partial_R[R] \phi_{n,m}(R,\theta)$$

$$= \frac{x_{nm}^{\mathrm{ZPF}}}{R} \Big((1 - \nu_m)\phi_{n,m}(R,\theta) + K_{nm} R \mathcal{N}_{nm}(J_{\nu_m-1}(K_{nm}R) + x_{nm}Y_{\nu_m-1}(K_{nm}R))\Theta_m(\theta) \Big).$$

$$(A.7)$$

II   Whispering gallery modes

The Hamiltonian density of the annulus' whispering gallery modes is identical to the disk's. The diagonalisation can thus be performed by a decomposition on linear superpositions of Bessel functions of the two kinds

$$A_z(r,\theta) = \sum_{\substack{p=1 \\ \ell=0}}^{+\infty} A_{p\ell}\phi_{p\ell}(r,\theta), \quad \phi_{p,\ell}(r,\theta) = \mathcal{N}_{p\ell}^{\mathrm{cav}} R_{p\ell}^{\mathrm{cav}}(r)\cos(\ell\theta), \quad \int_\Omega \mathrm{d}\boldsymbol{r}|\phi_{p,\ell}|^2 = 1, \quad (A.8)$$

with

$$R_{p\ell}^{\mathrm{cav}}(r) = J_\ell(k_{p\ell}r) + x_{p\ell}Y_\ell(k_{p\ell}r), \tag{A.9}$$

and where $k_{p\ell}$ is the pth root of

$$(\mathfrak{D}Y_\ell)(kR_a)(\mathfrak{D}J_\ell)(kR_b) - (\mathfrak{D}J_\ell)(kR_a)(\mathfrak{D}Y_\ell)(kR_b) = 0, \tag{A.10}$$

with $\mathfrak{D}$ the differential operator associated to the considered boundary condition such that $(\mathfrak{D}R)(\boldsymbol{r} \in \partial\Omega) = 0$, and

$$x_{p\ell} = -\frac{(\mathfrak{D}J_\ell)(k_{p\ell}R_a)}{(\mathfrak{D}Y_\ell)(k_{p\ell}R_a)}. \tag{A.11}$$

These modes have associated angular frequencies $\omega_{p,\ell} = k_{p\ell}c$. Assuming perfect reflection at the boundaries of the material as in Subsec. I.1 of Chap. 1, one simply has Dirichlet boundary conditions. This corresponds to $\mathfrak{D} = 1$.

B | Résumé substantiel

Cette thèse est consacrée à l'étude de la dynamique induite par réservoir dans les systèmes quantiques ouverts ainsi qu'à l'apprentissage automatique au moyen de réservoirs photoniques classiques. Les divers matériaux qui la constituent sont organisés autour de trois grands axes : (i) la description effective d'un système quantique en contact avec son environnement, au cœur des discussions des chapitres 1 à 3 ; (ii) la représentation efficace de l'état d'un système quantique ouvert ainsi que la simulation numérique de son évolution temporelle, sujets abordés aux chapitres 4 et 5 ; et, enfin, (iii) l'extraction de caractéristiques d'un signal au moyen d'un dispositif photonique « classique », faisant l'objet du chapitre 6.

La modélisation quantique d'un nano-résonateur à disque en matériau semi-conducteur est dérivée en détail au chapitre 1 en partant des lois physiques élémentaires de l'électromagnétisme et la théorie de l'élasticité. Un tel dispositif se comporte comme un système biparti comprenant une cavité optique et un mode de déplacement mécanique mutuellement couplés. Dans le formalisme de seconde quantification, cette procédure aboutit à une description effective sous la forme d'une équation maîtresse de Lindblad régissant la dynamique hors-équilibre du résonateur optomécanique ($\hbar = 1$) :

$$
\begin{aligned}
\partial_t \hat{\rho} &= -i[\hat{H}, \hat{\rho}] + \kappa \mathcal{D}[\hat{a}]\hat{\rho} + \Gamma_m(\bar{N}_m + 1)\mathcal{D}[\hat{b}]\hat{\rho} + \Gamma_m \bar{N}_m \mathcal{D}[\hat{b}^\dagger]\hat{\rho}, \\
\hat{H} &= -\Delta \hat{a}^\dagger \hat{a} + F(\hat{a} + \hat{a}^\dagger) - g\hat{a}^\dagger \hat{a}(\hat{b} + \hat{b}) + \Omega_m \hat{b}^\dagger \hat{b};
\end{aligned}
\tag{B.1}
$$

où les opérateurs bosoniques associés aux modes optique et mécanique sont notés respectivement par $\hat{a}$ et $\hat{b}$ et satisfont les relations de commutation canoniques usuelles : $[\hat{a}, \hat{a}^\dagger] = [\hat{b}, \hat{b}^\dagger] = 1$. Ci-dessus, l'opérateur $\hat{\rho}$ désigne la matrice densité du système, donnant une caractérisation complète de son état quantique et statistique. L'hamiltonien $\hat{H}$ décrit quant à lui l'évolution *unitaire* de cette dernière en l'absence d'interaction entre le système et son environnement ; il est paramétré par le désaccord $\Delta = \omega_p - \omega_c$ entre la pulsation de la pompe ω_p et celle de la cavité ω_c, l'amplitude du pompage F, la magnitude du couplage optomécanique g ainsi que la pulsation du mode mécanique Ω_m. Enfin, les effets *dissipatifs* sont intégrés à cette description au moyen de dissipateurs, tels que paramétrés par le superopérateur $\mathcal{D}[\hat{L}]\hat{\rho} = \hat{L}\hat{\rho}\hat{L}^\dagger - \frac{1}{2}\hat{L}^\dagger \hat{L}\hat{\rho} - \frac{1}{2}\hat{\rho}\hat{L}^\dagger \hat{L}$, pour quelque opérateur de saut arbitraire $\hat{L}$. Ces termes modélisent la déperdition de photons de cavité à un taux κ ainsi que la relaxation du mode mécanique à un taux Γ_m vers une population stationnaire composée de $\bar{N}_m$ phonons thermiques.

Dans la plupart des plate-formes expérimentales d'optomécanique, et celle-ci en particulier, le couplage optomécanique, tel qu'évalué par la *cooperativité* $C_0 = 4g^2/\kappa\Gamma_m$, est

extrêmement faible. Ce facteur de mérite quantifie l'efficacité des mécanismes d'interaction optomécanique à proximité des *bandes latérales* ($\Delta \approx \pm\Omega_m$). Dans la perspective de dépasser ces limitations, nous étudions dans ce même chapitre un résonateur hybride comprenant un puits quantique d'un alliage d'arséniure de gallium (GaAs) et d'arséniure d'indium (InAs) intégré dans la matrice de GaAs du disque. Dans un tel système, les paires liées électron-trou du puits — les *excitons* — et les photons de cavité s'hybrident donnant lieu à des *polaritons* excitoniques. Le couplage intense entre ces mêmes excitons et le champ de déformation induit par les *phonons* mécaniques (voir Fig. 1.9) médie une interaction paramétrique entre polaritons et phonons en tout point similaire au couplage optomécanique standard et à la magnitude significativement accrue, améliorant, par là même, la coopérativité du dispositif. Les développements théoriques associés ainsi que des expressions fermées permettant d'évaluer le couplage polariton-mécanique sont compilés dans la section II.

Le chapitre 2 est consacré à la dérivation d'équations générales décrivant la dynamique réduite d'un système en contact avec un réservoir quantique spatialement étendu. Dans le cadre de l'approximation de Born-Markov, de telles expressions y sont dérivées pour un réservoir constitué d'un nombre arbitraire de sites bosoniques et décrit par un hamiltonien pratiquement arbitraire. Chose singulière, en présence de processus de pompage et de dissipation linéaires agissant sur le réservoir, la dynamique effective du système ne dépend que d'une fonction spectrale à deux points :

$$\mathbf{S}^{(\alpha)} = \lambda^2 \mathbf{T}^\dagger \frac{i\mathbf{C}(0)}{\omega_\alpha \mathbb{1} - \mathbf{B}} \mathbf{T}, \tag{B.2}$$

où $\mathbf{T}$ est une matrice ne dépendant que de la forme particulière du couplage entre le réservoir et le système d'intérêt, $\mathbf{C}(0)$ est la matrice de covariance du vide résultant des relations de commutation canoniques, ω_α désigne l'énergie de la α-ième transition entre deux niveaux d'énergie du système et $\mathbf{B}$ est la matrice de Bogoliubov décrivant la dynamique pseudo-hermitienne des excitations élémentaires des champs du réservoir autour de ses solutions de champ moyen. Ainsi, l'équation maîtresse du système prend la forme suivante :

$$\partial_t \hat{\rho}_{\mathrm{S}}(t) = -i\Big[\hat{H}_{\mathrm{S}} + \textstyle\sum_{ij\alpha}\Omega_{ij}^{(\alpha)}\hat{s}_i^\dagger(\omega_\alpha)\hat{s}_j(\omega_\alpha), \hat{\rho}_{\mathrm{S}}(t)\Big] + \sum_{k,\alpha}\Gamma_k^{(\alpha)}\mathcal{D}[\textstyle\sum_j U_{kj}^{(\alpha)}\hat{s}_j(\omega_\alpha)]\hat{\rho}_{\mathrm{S}}(t), \tag{B.3}$$

où $\hat{H}_{\mathrm{S}}$ désigne l'hamiltonien du système seul, la matrice $\mathbf{\Omega}^{(\alpha)} = (\mathbf{S}^{(\alpha)} - \mathbf{S}^{(\alpha)\dagger})/2i$ ainsi que les quantités $\{\Gamma_k^{(\alpha)}/2\}_{k,\alpha}$ et $\{\mathbf{U}^{(\alpha)}\}_\alpha$ décrivent respectivement les processus cohérents et incohérents médiés par le réservoir. Ces dernières correspondent aux valeurs propres et matrices de passage associées à la diagonalisation de $\frac{1}{2}\mathbf{\Gamma}^{(\alpha)} = (\mathbf{S}^{(\alpha)} + \mathbf{S}^{(\alpha)\dagger})/2$. Enfin, $\{\hat{s}_i(\omega_\alpha)\}_{i,\alpha}$ sont des opérateurs du système dont l'expression explicite dépend de $\hat{H}_{\mathrm{S}}$ et du choix spécifique du couplage au réservoir.

Cette étude est étendue aux réservoirs décrits par des champs spatialement continus et complétée par une approche équivalente : l'équation de Langevin quantique.

Au chapitre 3, le formalisme succinctement exposé plus haut est appliqué à l'étude d'un ensemble de résonateurs optomécaniques arrangés en un réseau unidimensionnel périodique de forme annulaire dont seules les cavités sont mutuellement couplées. Dans

un premier temps, un tel système peut être décrit par une équation maîtresse de Lindblad, $\partial_t \hat{\rho}(t) = -i[\hat{H}_{\text{tot}}, \hat{\rho}(t)] + \mathcal{D}_{\text{tot}}\hat{\rho}(t)$, dont les parties cohérente et incohérente sont définies, respectivement, par l'hamiltonien

$$\hat{H}_{\text{tot}} = \sum_{\ell} \left[-\Delta_{\ell}\hat{a}_{\ell}^{\dagger}\hat{a}_{\ell} + F_{\ell}^{\star}\hat{a}_{\ell} + F_{\ell}\hat{a}_{\ell}^{\dagger} - g_{\ell}\hat{a}_{\ell}^{\dagger}\hat{a}_{\ell}(\hat{b}_{\ell} + \hat{b}_{\ell}^{\dagger}) \right] - \frac{J}{2}\sum_{\ell}\left(\hat{a}_{\ell}^{\dagger}\hat{a}_{\ell+1} + \hat{a}_{\ell+1}^{\dagger}\hat{a}_{\ell}\right) + \sum_{\ell}\Omega_m^{(\ell)}\hat{b}_{\ell}^{\dagger}\hat{b}_{\ell},$$ (B.4)

où J désigne l'amplitude du couplage entre cavités adjacentes, et le dissipateur

$$\mathcal{D}_{\text{tot}}\hat{\rho} = \sum_{\ell}\left\{\Gamma_{\ell}\left[(\bar{N}_{\ell} + 1)\mathcal{D}[\hat{b}_{\ell}]\hat{\rho} + \bar{N}_{\ell}\mathcal{D}[\hat{b}_{\ell}^{\dagger}]\hat{\rho}\right] + \kappa_{\ell}\mathcal{D}[\hat{a}_{\ell}]\hat{\rho}\right\}.$$ (B.5)

En choisissant les amplitudes du pompage externe dans un certain rapport $F_{\ell} = Fe^{i\ell\phi}$ et en procédant à l'élimination adiabatique des degrés de liberté optiques conformément à la procédure du chapitre 3, l'on obtient une description effective pour la partie mécanique qui ne dépend plus que des opérateurs associés aux fluctuations thermiques $\hat{d}_{\ell} = \hat{b}_{\ell} - \langle\hat{b}_{\ell}\rangle$. Ainsi, l'hamiltonien mécanique effectif est donné par

$$\hat{H}_m^{\text{eff}} \simeq \sum_{\ell}(\Omega_m + J_0^{(+)} + J_0^{(-)})\hat{d}_{\ell}^{\dagger}\hat{d}_{\ell} + \sum_{\pm}\sum_{p\geq 1}\frac{J_p^{(\pm)}}{2}\sum_{\ell}\left(\hat{d}_{\ell+p}^{\dagger}\hat{d}_{\ell}e^{\mp i\phi\times p} + \text{c.h.}\right).$$ (B.6)

où $J_p^{(\pm)}$, tel qu'exprimé explicitement à l'équation (3.12), est un couplage cohérent effectif entre les sites ℓ et $\ell + p$ médié par les cavités (voir figure 3.4). Cette interaction effective rend possible la circulation de phonons thermiques entre les divers modes mécaniques localisés de la structure ainsi que l'établissement de corrélations spatiales entre ces derniers. Outre ces effets cohérents, le réservoir induit des processus dissipatifs, décrits par le dissipateur effectif suivant :

$$\mathcal{D}_m^{\text{eff}}\hat{\rho}_m \simeq \sum_{\ell}\Gamma_m\left((\bar{N} + 1)\mathcal{D}[\hat{d}_{\ell}]\hat{\rho}_m + \bar{N}\mathcal{D}[\hat{d}_{\ell}^{\dagger}]\hat{\rho}_m\right)$$
$$+ \sum_{k}\left(\Gamma_k(+\Omega_m)\mathcal{D}[\tilde{d}_k]\hat{\rho}_m + \Gamma_k(-\Omega_m)\mathcal{D}[\tilde{d}_{-k}^{\dagger}]\hat{\rho}_m\right),$$ (B.7)

où $\{\Gamma_k(\pm\Omega_m)\}_k$, tels qu'exprimés à l'équation (3.14), sont des taux de gain et de dissipation (voir figure 3.5) associés aux transitions engendrées par le réservoir optique sur les modes de Fourier de la structure, définis par $\tilde{d}_k = \frac{1}{\sqrt{L}}\sum_{\ell}e^{-ik\ell}\hat{d}_{\ell}$ pour quelque pseudo-moment $k \in \{n \times 2\pi/L\}_{n=0}^{L-1}$, L désignant ici le nombre de résonateurs de la chaîne.

L'énergie thermique transitant autour de l'anneau ainsi décrit dans la direction $\ell \to \ell + 1$ peut être exprimé très simplement grâce à l'équation de continuité ; en régime stationnaire :

$$\langle\hat{j}_C\rangle_{\text{ss}} = -\sum_{k}\frac{\sum_{p\geq 1}\sum_{\pm}J_p^{(\pm)}\sin(p(k\pm\phi))}{\Gamma_k^{(\downarrow)}/\Gamma_k^{(\uparrow)} - 1}.$$ (B.8)

Comme on l'observe aux figures 3.7 et 3.8, non seulement cette quantité n'est pas nulle mais encore elle peut être contrôlée au moyen du désaccord Δ de la pompe. Ainsi, de l'action conjuguée de la dynamique hamiltonienne et des processus incohérents induits par les champs optiques, résulte un flux permanent de chaleur tournant au travers de la

structure, et ce malgré l'absence de gradient de température : un constat en contradiction avec l'intuition par trop « naïve » découlant de l'équation (classique) de la chaleur. La validité des approximations ayant abouti à ces résultats peut être vérifiée à la figure 3.9.

Le chapitre 4 est dédié à la discussion de la simulation numérique (classique) de systèmes quantiques ouverts en général, et des systèmes en contact avec des réservoirs étendus en particulier. Diverses méthodes standard, adaptées aux régimes des plus semi-classiques jusqu'aux plus quantiques, sont présentées. Certaines d'entre elles sont généralisées aux liouvilliens présentant des opérateurs de saut non locaux, notamment la méthode dite de Wigner tronquée (*truncated Wigner approximation*).

La discussion des limitations intrinsèques de la méthode de la fonction d'onde Monte Carlo (*Monte Carlo wave function*) nous conduit à l'introduction d'une nouvelle méthode numérique au chapitre 5 : la méthode du sous-espace dynamique (*dynamical corner-space method*). Cette technique est basée sur la possibilité de décomposer la solution de l'équation maîtresse $\hat{\rho}(t)$ sous la forme :

$$\hat{\rho}(t) \simeq \sum_{k=1}^{M(t)} p_k(t) \left| \phi_k(t) \middle\rangle\!\middle\langle \phi_k(t) \right|, \quad p_k(t) \geq p_{k+1}(t), \ \forall k, \tag{B.9}$$

où les $\{p_k(t)\}_k$ sont les $M(t)$ plus grandes valeurs propres à l'instant t et $\{\left| \phi(t) \middle\rangle_k\right\}_k$ les vecteurs propres associés. Lorsque l'entropie du système reste faible au cours de son évolution temporelle, ce qui est notamment le cas lorsque celui-ci n'est que faiblement couplé à son environnement, cette décomposition peut être tronquée à un nombre de composantes M considérablement moindre que la dimension de l'espace de Hilbert originel. La méthode du sous-espace dynamique permet de limiter l'évolution temporelle à ce nombre très limité de composantes sans jamais reconstruire la matrice densité complète. S'ensuit un énorme avantage sur le plan de la complexité numérique de la simulation. À titre d'exemple, pour un ensemble de L spins $1/2$, la complexité est réduite de $O(2^L \times 2^L)$ à $O(M \times 2^L)$. Cette accélération numérique est illustré au tableau de la section II.2 ainsi qu'à la figure 5.3 (c). Dans ce même chapitre, l'algorithme est appliqué à la simulation en temps continu d'un circuit réalisant la transformée de Fourier quantique en présence de dissipation ou de déphasage. Nos simulations montrent (voir la figure 5.4), par exemple, que l'erreur introduite par le couplage du circuit à un environnement extérieur croît quadratiquement avec la taille du système L. Aussi montrons-nous que l'erreur imputable à l'interaction avec l'environnement dépend sensiblement du type d'état à partir duquel l'opération est menée (voir figure 5.5) et en identifions la caractérisation fonctionnelle.

Le chapitre 6, enfin, est dédié aux machines à noyau photonique : des dispositifs opto-électroniques capables de réaliser des tâches d'apprentissage automatique (*machine learning*) grâce à une puce photonique et des photo-détecteurs. Nous dressons tout d'abord un aperçu général des divers concepts issus de la théorie des machines à vecteurs de support utiles à la compréhension des machines à noyau et en présentons les relations analytiques les plus fondamentales. En particulier, il apparaît que les machines à noyau sont capables de tirer parti de la notion abstraite de similarité de leurs réponses à une série de signaux d'entrée afin de s'entraîner à réaliser des tâches bien définies. Nous définissons une mesure de similarité *ad hoc* entre des signaux radio-fréquences puis démontrons qu'elle

peut être mise en œuvre naturellement par un dispositif physique constitué d'une puce photonique couplée à un modulateur électro-optique et un ensemble de photo-détecteurs (se rapporter à la figure 6.3 pour une représentation schématique du système ainsi décrit). Enfin, à la section IV de cet ultime chapitre, nous simulons numériquement un tel dispositif et montrons son efficacité dans l'analyse ultra-rapide de signaux radio-fréquences bruités, tant pour des applications de régression comme de classification. Plus particulièrement, nous l'entraînons à estimer le spectre d'impulsions ultra-courtes en présence de bruit blanc (voir les figures 6.5, 6.6 et 6.7), la forme spectrale d'une série d'impulsions (voir les figures 6.9 et 6.10) et la fréquence d'un signal continu harmonique, et ce en présence de divers niveaux de bruit de fond non corrélé. Aussi examinons-nous les représentations internes et apprises du dispositif entraîné au moyen des outils analytiques développés en première partie de chapitre (voir la figure 6.8).

Bibliography

[α] Z. Denis, A. Biella, I. Favero and C. Ciuti, "Permanent Directional Heat Currents in Lattices of Optomechanical Resonators", Physical Review Letters **124**, 083601 (2020).

[β] S. Pautrel, Z. Denis, J. Bon, A. Borne and I. Favero, "Optomechanical discrete-variable quantum teleportation scheme", Physical Review A **101**, 063820 (2020).

[γ] K. Donatella, Z. Denis, A. Le Boité and C. Ciuti, "Continuous-time dynamics and error scaling of noisy highly-entangling quantum circuits", arXiv: 2102.04265 (2021).

[δ] Z. Denis, I. Favero and C. Ciuti, *Dispositif d'analyse de spectre de signaux radio-fréquences*, EU Patent application EP21173660, 2021.

[γ] Z. Denis, I. Favero and C. Ciuti, "Photonic kernel machine learning for ultrafast spectral analysis", arXiv: 2110.15241 (2021).

[ζ] N. Carlon Zambon, Z. Denis, S. de Oliveira Romain Ravets, I. Favero, C. Ciuti and J. Bloch, *Hybrid polariton optomechanics with semiconductor microresonators*, in preparation, 2021.

[1] I. Newton, "General scholium", in *The principia: mathematical principles of natural philosophy*, trans. by I. B. Cohen, A. Whitman and J. Budenz, first edition (University of California Press, 1999 [1687]), pp. 939–946.

[2] J. Perrin, "Mouvement brownien et molécules", Journal de physique théorique et appliquée **9**, 5–39 (1910).

[3] A. Einstein, "Über die von der molekularkinetischen Theorie der Wärme geforderte Bewegung von in ruhenden Flüssigkeiten suspendierten Teilchen", Annalen der Physik **322**, 549–560 (1905).

[4] H. Geiger, E. Marsden and E. Rutherford, "On a diffuse reflection of the α-particles", Proceedings of the Royal Society of London. Series A, Containing Papers of a Mathematical and Physical Character **82**, 495–500 (1909).

[5] W. Friedrich, P. Knipping and M. Laue, "Interferenzerscheinungen bei Röntgenstrahlen", Annalen der Physik **346**, 971–988 (1913).

[6] P. W. Anderson, "More Is Different", Science **177**, 393–396 (1972).

[7] A. J. Leggett, "Macroscopic Quantum Systems and the Quantum Theory of Measurement", Progress of Theoretical Physics Supplement **69**, 80–100 (1980).

[8]   M. Aspelmeyer, T. J. Kippenberg and F. Marquardt, "Cavity optomechanics", Reviews of Modern Physics **86**, 1391–1452 (2014).

[9]   M. H. Devoret, A. Wallraff and J. M. Martinis, "Superconducting Qubits: A Short Review", arXiv: cond-mat/0411174 (2004).

[10] R. J. Schoelkopf and S. M. Girvin, "Wiring up quantum systems", Nature **451**, 664–669 (2008).

[11] J. Q. You and F. Nori, "Atomic physics and quantum optics using superconducting circuits", Nature **474**, 589–597 (2011).

[12] A. Blais, A. L. Grimsmo, S. M. Girvin and A. Wallraff, "Circuit quantum electrodynamics", Reviews of Modern Physics **93**, 025005 (2021).

[13] I. Carusotto and C. Ciuti, "Quantum fluids of light", Reviews of Modern Physics **85**, 299–366 (2013).

[14] J. F. Poyatos, J. I. Cirac and P. Zoller, "Quantum Reservoir Engineering with Laser Cooled Trapped Ions", Physical Review Letters **77**, 4728–4731 (1996).

[15] B. Kraus, H. P. Büchler, S. Diehl, A. Kantian, A. Micheli and P. Zoller, "Preparation of entangled states by quantum Markov processes", Physical Review A **78**, 042307 (2008).

[16] S. Diehl, A. Micheli, A. Kantian, B. Kraus, H. P. Büchler and P. Zoller, "Quantum states and phases in driven open quantum systems with cold atoms", Nature Physics **4**, 878–883 (2008).

[17] M. Mirrahimi, Z. Leghtas, V. V. Albert, S. Touzard, R. J. Schoelkopf, L. Jiang and M. H. Devoret, "Dynamically protected cat-qubits: a new paradigm for universal quantum computation", New Journal of Physics **16**, 045014 (2014).

[18] G. Morigi, J. Eschner, C. Cormick, Y. Lin, D. Leibfried and D. J. Wineland, "Dissipative Quantum Control of a Spin Chain", Physical Review Letters **115**, 200502 (2015).

[19] F. Minganti, N. Bartolo, J. Lolli, W. Casteels and C. Ciuti, "Exact results for Schrödinger cats in driven-dissipative systems and their feedback control", Scientific Reports **6**, 26987 (2016).

[20] J. Lebreuilly, A. Biella, F. Storme, D. Rossini, R. Fazio, C. Ciuti and I. Carusotto, "Stabilizing strongly correlated photon fluids with non-Markovian reservoirs", Physical Review A **96**, 033828 (2017).

[21] R. Ma, B. Saxberg, C. Owens, N. Leung, Y. Lu, J. Simon and D. I. Schuster, "A dissipatively stabilized Mott insulator of photons", Nature **566**, 51–57 (2019).

[22] V. B. Braginskij, V. I. Panov, V. B. Mitrofanov, K. S. Thorne, E. Gliner and V. B. Braginsky, *Systems with small dissipation* (University of Chicago Press, Chicago, 1985).

[23] V. B. Braginsky, F. Y. Khalili and K. S. Thorne, *Quantum Measurement* (Cambridge University Press, Cambridge, 1992).

[24] Y. Hadjar, P. F. Cohadon, C. G. Aminoff, M. Pinard and A. Heidmann, "High-sensitivity optical measurement of mechanical Brownian motion", EPL (Europhysics Letters) **47**, 545 (1999).

[25] M. D. LaHaye, O. Buu, B. Camarota and K. C. Schwab, "Approaching the Quantum Limit of a Nanomechanical Resonator", Science **304**, 74–77 (2004).

[26] J. Li, A. Wallucks, R. Benevides, N. Fiaschi, B. Hensen, T. P. M. Alegre and S. Gröblacher, "Proposal for optomechanical quantum teleportation", Physical Review A **102**, 032402 (2020).

[27] N. Fiaschi, B. Hensen, A. Wallucks, R. Benevides, J. Li, T. P. M. Alegre and S. Gröblacher, "Optomechanical quantum teleportation", arXiv: 2104.02080 (2021).

[28] H. Weimer, "Variational Principle for Steady States of Dissipative Quantum Many-Body Systems", Physical Review Letters **114**, 040402 (2015).

[29] T. Grujic, S. R. Clark, D. Jaksch and D. G. Angelakis, "Non-equilibrium many-body effects in driven nonlinear resonator arrays", New Journal of Physics **14**, 103025 (2012).

[30] R. Orús and G. Vidal, "Infinite time-evolving block decimation algorithm beyond unitary evolution", Physical Review B **78**, 155117 (2008).

[31] J. Cui, J. I. Cirac and M. C. Bañuls, "Variational Matrix Product Operators for the Steady State of Dissipative Quantum Systems", Physical Review Letters **114**, 220601 (2015).

[32] A. H. Werner, D. Jaschke, P. Silvi, M. Kliesch, T. Calarco, J. Eisert and S. Montangero, "Positive Tensor Network Approach for Simulating Open Quantum Many-Body Systems", Physical Review Letters **116**, 237201 (2016).

[33] A. Kshetrimayum, H. Weimer and R. Orús, "A simple tensor network algorithm for two-dimensional steady states", Nature Communications **8**, 1291 (2017).

[34] D. Jaschke, S. Montangero and L. D. Carr, "One-dimensional many-body entangled open quantum systems with tensor network methods", Quantum Science and Technology **4**, 013001 (2018).

[35] D. Kilda, A. Biella, M. Schiro, R. Fazio and J. Keeling, "On the stability of the infinite Projected Entangled Pair Operator ansatz for driven-dissipative 2D lattices", SciPost Phys. Core **4**, 5 (2021).

[36] A. Strathearn, P. Kirton, D. Kilda, J. Keeling and B. W. Lovett, "Efficient non-Markovian quantum dynamics using time-evolving matrix product operators", Nature Communications **9**, 3322 (2018).

[37] F. Vicentini, A. Biella, N. Regnault and C. Ciuti, "Variational Neural-Network Ansatz for Steady States in Open Quantum Systems", Physical Review Letters **122**, 250503 (2019).

[38] A. Nagy and V. Savona, "Variational Quantum Monte Carlo Method with a Neural-Network Ansatz for Open Quantum Systems", Physical Review Letters **122**, 250501 (2019).

[39] M. J. Hartmann and G. Carleo, "Neural-Network Approach to Dissipative Quantum Many-Body Dynamics", Physical Review Letters **122**, 250502 (2019).

[40] N. Yoshioka and R. Hamazaki, "Constructing neural stationary states for open quantum many-body systems", Physical Review B **99**, 214306 (2019).

[41] D. Luo, Z. Chen, J. Carrasquilla and B. K. Clark, "Autoregressive Neural Network for Simulating Open Quantum Systems via a Probabilistic Formulation", arXiv: 2009.05580 (2021).

[42] C. E. Shannon, "A mathematical theory of communication", The Bell System Technical Journal **27**, 379–423 (1948).

[43] D. J. C. MacKay, *Information Theory, Inference and Learning Algorithms* (Cambridge University Press, 2003).

[44] S. Finazzi, A. Le Boité, F. Storme, A. Baksic and C. Ciuti, "Corner-Space Renormalization Method for Driven-Dissipative Two-Dimensional Correlated Systems", Physical Review Letters **115**, 080604 (2015).

[45] W. Casteels, R. Rota, F. Storme and C. Ciuti, "Probing photon correlations in the dark sites of geometrically frustrated cavity lattices", Physical Review A **93**, 043833 (2016).

[46] A. Biella, F. Storme, J. Lebreuilly, D. Rossini, R. Fazio, I. Carusotto and C. Ciuti, "Phase diagram of incoherently driven strongly correlated photonic lattices", Physical Review A **96**, 023839 (2017).

[47] R. Rota, F. Storme, N. Bartolo, R. Fazio and C. Ciuti, "Critical behavior of dissipative two-dimensional spin lattices", Physical Review B **95**, 134431 (2017).

[48] R. Rota, F. Minganti, C. Ciuti and V. Savona, "Quantum Critical Regime in a Quadratically Driven Nonlinear Photonic Lattice", Physical Review Letters **122**, 110405 (2019).

[49] J. Preskill, "Quantum Computing in the NISQ era and beyond", Quantum **2**, 79 (2018).

[50] G. Tanaka, T. Yamane, J. B. Héroux, R. Nakane, N. Kanazawa, S. Takeda, H. Numata, D. Nakano and A. Hirose, "Recent advances in physical reservoir computing: A review", Neural Networks **115**, 100–123 (2019).

[51] S. Ghosh, T. Paterek and T. C. H. Liew, "Quantum Neuromorphic Platform for Quantum State Preparation", Physical Review Letters **123**, 260404 (2019).

[52] S. Ghosh, A. Opala, M. Matuszewski, T. Paterek and T. C. H. Liew, "Quantum reservoir processing", npj Quantum Information **5**, 1–6 (2019).

[53] S. Ghosh, A. Opala, M. Matuszewski, T. Paterek and T. C. H. Liew, "Reconstructing Quantum States With Quantum Reservoir Networks", IEEE Transactions on Neural Networks and Learning Systems, 1–8 (2020).

[54] D. Marković and J. Grollier, "Quantum neuromorphic computing", Applied Physics Letters **117**, 150501 (2020).

[55] S. Ghosh, T. Krisnanda, T. Paterek and T. C. H. Liew, "Realising and compressing quantum circuits with quantum reservoir computing", Communications Physics **4**, 1–7 (2021).

[56] H. Xu, T. Krisnanda, W. Verstraelen, T. C. H. Liew and S. Ghosh, "Superpolynomial quantum enhancement in polaritonic neuromorphic computing", Physical Review B **103**, 195302 (2021).

[57] P.-F. Cohadon, J. Harris, F. Marquardt and L. Cugliandolo, eds., *Quantum Optomechanics and Nanomechanics: Lecture Notes of the Les Houches Summer School: Volume 105, August 2015*, Lecture Notes of the Les Houches Summer School (Oxford University Press, Oxford, 2020).

[58] L. Ding, C. Baker, P. Senellart, A. Lemaitre, S. Ducci, G. Leo and I. Favero, "High Frequency GaAs Nano-Optomechanical Disk Resonator", Physical Review Letters **105**, 263903 (2010).

[59] J. Chan, T. P. M. Alegre, A. H. Safavi-Naeini, J. T. Hill, A. Krause, S. Gröblacher, M. Aspelmeyer and O. Painter, "Laser cooling of a nanomechanical oscillator into its quantum ground state", Nature **478**, 89–92 (2011).

[60] J. D. Teufel, T. Donner, D. Li, J. W. Harlow, M. S. Allman, K. Cicak, A. J. Sirois, J. D. Whittaker, K. W. Lehnert and R. W. Simmonds, "Sideband cooling of micromechanical motion to the quantum ground state", Nature **475**, 359–363 (2011).

[61] E. Verhagen, S. Deléglise, S. Weis, A. Schliesser and T. J. Kippenberg, "Quantum-coherent coupling of a mechanical oscillator to an optical cavity mode", Nature **482**, 63–67 (2012).

[62] R. W. Peterson, T. P. Purdy, N. S. Kampel, R. W. Andrews, P.-L. Yu, K. W. Lehnert and C. A. Regal, "Laser Cooling of a Micromechanical Membrane to the Quantum Backaction Limit", Physical Review Letters **116**, 063601 (2016).

[63] M. Rossi, D. Mason, J. Chen, Y. Tsaturyan and A. Schliesser, "Measurement-based quantum control of mechanical motion", Nature **563**, 53–58 (2018).

[64] M. Mirhosseini, A. Sipahigil, M. Kalaee and O. Painter, "Superconducting qubit to optical photon transduction", Nature **588**, 599–603 (2020).

[65] T. P. Purdy, P.-L. Yu, R. W. Peterson, N. S. Kampel and C. A. Regal, "Strong Optomechanical Squeezing of Light", Physical Review X **3**, 031012 (2013).

[66] A. H. Safavi-Naeini, S. Gröblacher, J. T. Hill, J. Chan, M. Aspelmeyer and O. Painter, "Squeezed light from a silicon micromechanical resonator", Nature **500**, 185–189 (2013).

[67] C. Galland, N. Sangouard, N. Piro, N. Gisin and T. J. Kippenberg, "Heralded Single-Phonon Preparation, Storage, and Readout in Cavity Optomechanics", Physical Review Letters **112**, 143602 (2014).

[68] S. Hong, R. Riedinger, I. Marinković, A. Wallucks, S. G. Hofer, R. A. Norte, M. Aspelmeyer and S. Gröblacher, "Hanbury Brown and Twiss interferometry of single phonons from an optomechanical resonator", Science **358**, 203–206 (2017).

[69] M. Brunelli, O. Houhou, D. W. Moore, A. Nunnenkamp, M. Paternostro and A. Ferraro, "Unconditional preparation of nonclassical states via linear-and-quadratic optomechanics", Physical Review A **98**, 063801 (2018).

[70] V. C. Vivoli, T. Barnea, C. Galland and N. Sangouard, "Proposal for an Optomechanical Bell Test", Physical Review Letters **116**, 070405 (2016).

[71] R. Riedinger, S. Hong, R. A. Norte, J. A. Slater, J. Shang, A. G. Krause, V. Anant, M. Aspelmeyer and S. Gröblacher, "Non-classical correlations between single photons and phonons from a mechanical oscillator", Nature **530**, 313–316 (2016).

[72] I. Marinković, A. Wallucks, R. Riedinger, S. Hong, M. Aspelmeyer and S. Gröblacher, "Optomechanical Bell Test", Physical Review Letters **121**, 220404 (2018).

[73] R. Riedinger, A. Wallucks, I. Marinković, C. Löschnauer, M. Aspelmeyer, S. Hong and S. Gröblacher, "Remote quantum entanglement between two micromechanical oscillators", Nature **556**, 473–477 (2018).

[74] S. Felicetti, S. Fedortchenko, R. Rossi, S. Ducci, I. Favero, T. Coudreau and P. Milman, "Quantum communication between remote mechanical resonators", Physical Review A **95**, 022322 (2017).

[75] G. De Chiara, M. Paternostro and G. M. Palma, "Entanglement detection in hybrid optomechanical systems", Physical Review A **83**, 052324 (2011).

[76] G. Heinrich, M. Ludwig, H. Wu, K. Hammerer and F. Marquardt, "Dynamics of coupled multimode and hybrid optomechanical systems", Comptes Rendus Physique, Nano- and Micro-Optomechanical Systems **12**, 837–847 (2011).

[77] S. Singh, H. Jing, E. M. Wright and P. Meystre, "Quantum-state transfer between a Bose-Einstein condensate and an optomechanical mirror", Physical Review A **86**, 021801 (2012).

[78] B. Rogers, M. Paternostro, G. M. Palma and G. De Chiara, "Entanglement control in hybrid optomechanical systems", Physical Review A **86**, 042323 (2012).

[79] B. Rogers, N. L. Gullo, G. D. Chiara, G. M. Palma and M. Paternostro, "Hybrid optomechanics for Quantum Technologies", Quantum Measurements and Quantum Metrology **2** (2014).

[80] O. Kyriienko, T. C. H. Liew and I. A. Shelykh, "Optomechanics with Cavity Polaritons: Dissipative Coupling and Unconventional Bistability", Physical Review Letters **112**, 076402 (2014).

[81] J. Restrepo, C. Ciuti and I. Favero, "Single-Polariton Optomechanics", Physical Review Letters **112**, 013601 (2014).

[82] P.-B. Li, Y.-C. Liu, S.-Y. Gao, Z.-L. Xiang, P. Rabl, Y.-F. Xiao and F.-L. Li, "Hybrid Quantum Device Based on *NV* Centers in Diamond Nanomechanical Resonators Plus Superconducting Waveguide Cavities", Physical Review Applied **4**, 044003 (2015).

[83] J. Restrepo, I. Favero and C. Ciuti, "Fully coupled hybrid cavity optomechanics: Quantum interferences and correlations", Physical Review A **95**, 023832 (2017).

[84] V. Bergholm, W. Wieczorek, T. Schulte-Herbrüggen and M. Keyl, "Optimal control of hybrid optomechanical systems for generating non-classical states of mechanical motion", Quantum Science and Technology **4**, 034001 (2019).

[85] X. Han, W. Fu, C. Zhong, C.-L. Zou, Y. Xu, A. A. Sayem, M. Xu, S. Wang, R. Cheng, L. Jiang and H. X. Tang, "Cavity piezo-mechanics for superconducting-nanophotonic quantum interface", Nature Communications **11**, 3237 (2020).

[86] M. Marchese, H. McAleese, A. Bassi and M. Paternostro, "A macrorealistic test in hybrid quantum optomechanics", Journal of Physics B: Atomic, Molecular and Optical Physics **53**, 075401 (2020).

[87] P. A. M. Dirac and R. H. Fowler, "The fundamental equations of quantum mechanics", Proceedings of the Royal Society of London A **109**, 642–653 (1925).

[88] P. A. M. Dirac, *The Principles of Quantum Mechanics*, fourth edition, International Series of Monographs on Physics (Oxford University Press, Oxford, New York, 1981).

[89] J. W. Strutt, *The Theory of Sound*, Vol. 2, Cambridge Library Collection - Physical Sciences (Cambridge University Press, Cambridge, 2011 [1878]).

[90] L. Rayleigh, "CXII. The problem of the whispering gallery", The London, Edinburgh, and Dublin Philosophical Magazine and Journal of Science **20**, 1001–1004 (1910).

[91] L. Rayleigh, "IX. Further applications of Bessel's functions of high order to the Whispering Gallery and allied problems", The London, Edinburgh, and Dublin Philosophical Magazine and Journal of Science **27**, 100–109 (1914).

[92] G. Panzarini and L. C. Andreani, "Quantum theory of exciton polaritons in cylindrical semiconductor microcavities", Physical Review B **60**, 16799–16806 (1999).

[93] L. D. Landau, E. M. Lifšic and L. D. Landau, *Theory of elasticity*, third English edition, Vol. 7, Course of Theoretical Physics (Elsevier, Amsterdam, 2008).

[94] V. Fock, "Bemerkung zum Virialsatz", Zeitschrift für Physik **63**, 855–858 (1930).

[95] D. Parrain, C. Baker, G. Wang, B. Guha, E. G. Santos, A. Lemaitre, P. Senellart, G. Leo, S. Ducci and I. Favero, "Origin of optical losses in gallium arsenide disk whispering gallery resonators", Optics Express **23**, 19656–19672 (2015).

[96] M. Hamoumi, P. E. Allain, W. Hease, E. Gil-Santos, L. Morgenroth, B. Gérard, A. Lemaître, G. Leo and I. Favero, "Microscopic Nanomechanical Dissipation in Gallium Arsenide Resonators", Physical Review Letters **120**, 223601 (2018).

[97] V. Gorini, A. Kossakowski and E. C. G. Sudarshan, "Completely positive dynamical semigroups of N-level systems", Journal of Mathematical Physics **17**, 821–825 (1976).

[98] G. Lindblad, "On the generators of quantum dynamical semigroups", Communications in Mathematical Physics **48**, 119–130 (1976).

[99] H.-P. Breuer and F. Petruccione, *The Theory of Open Quantum Systems* (Oxford University Press, Oxford, 2007).

[100] A. O. Caldeira and A. J. Leggett, "Path integral approach to quantum Brownian motion", Physica A: Statistical Mechanics and its Applications **121**, 587–616 (1983).

[101] A. O. Caldeira and A. J. Leggett, "Quantum tunnelling in a dissipative system", Annals of Physics **149**, 374–456 (1983).

[102] C. K. Law, "Effective Hamiltonian for the radiation in a cavity with a moving mirror and a time-varying dielectric medium", Physical Review A **49**, 433–437 (1994).

[103] C. K. Law, "Interaction between a moving mirror and radiation pressure: A Hamiltonian formulation", Physical Review A **51**, 2537–2541 (1995).

[104] J. D. Jackson, *Classical electrodynamics*, third edition (Wiley, Hoboken, New York, 1999).

[105] C. Baker, W. Hease, D.-T. Nguyen, A. Andronico, S. Ducci, G. Leo and I. Favero, "Photoelastic coupling in gallium arsenide optomechanical disk resonators", Optics Express **22**, 14072–14086 (2014).

[106] M. Hamoumi, "Vers l'optomécanique quantique en arséniure de gallium : dissipation nanomécanique et opération pulsée", PhD thesis (Sorbonne Paris Cité, 2018).

[107] P. F. Cohadon, A. Heidmann and M. Pinard, "Cooling of a Mirror by Radiation Pressure", Physical Review Letters **83**, 3174–3177 (1999).

[108] F. Marquardt, J. P. Chen, A. A. Clerk and S. M. Girvin, "Quantum Theory of Cavity-Assisted Sideband Cooling of Mechanical Motion", Physical Review Letters **99**, 093902 (2007).

[109] I. Wilson-Rae, N. Nooshi, W. Zwerger and T. J. Kippenberg, "Theory of Ground State Cooling of a Mechanical Oscillator Using Dynamical Backaction", Physical Review Letters **99**, 093901 (2007).

[110] C. Genes, D. Vitali, P. Tombesi, S. Gigan and M. Aspelmeyer, "Ground-state cooling of a micromechanical oscillator: Comparing cold damping and cavity-assisted cooling schemes", Physical Review A **77**, 033804 (2008).

[111] J. Restrepo, J. Gabelli, C. Ciuti and I. Favero, "Classical and quantum theory of photothermal cavity cooling of a mechanical oscillator", Comptes Rendus Physique, Nano- and Micro-Optomechanical Systems **12**, 860–870 (2011).

[112] C. H. Metzger and K. Karrai, "Cavity cooling of a microlever", Nature **432**, 1002–1005 (2004).

[113] S. Gigan, H. R. Böhm, M. Paternostro, F. Blaser, G. Langer, J. B. Hertzberg, K. C. Schwab, D. Bäuerle, M. Aspelmeyer and A. Zeilinger, "Self-cooling of a micromirror by radiation pressure", Nature **444**, 67–70 (2006).

[114] O. Arcizet, P.-F. Cohadon, T. Briant, M. Pinard and A. Heidmann, "Radiation-pressure cooling and optomechanical instability of a micromirror", Nature **444**, 71–74 (2006).

[115] A. Schliesser, P. Del'Haye, N. Nooshi, K. J. Vahala and T. J. Kippenberg, "Radiation Pressure Cooling of a Micromechanical Oscillator Using Dynamical Backaction", Physical Review Letters **97**, 243905 (2006).

[116] A. Schliesser, R. Rivière, G. Anetsberger, O. Arcizet and T. J. Kippenberg, "Resolved-sideband cooling of a micromechanical oscillator", Nature Physics **4**, 415–419 (2008).

[117] C. Metzger, I. Favero, A. Ortlieb and K. Karrai, "Optical self cooling of a deformable Fabry-Perot cavity in the classical limit", Physical Review B **78**, 035309 (2008).

[118] S. M. Barnett and D. T. Pegg, "Phase in quantum optics", Journal of Physics A: Mathematical and General **19**, 3849–3862 (1986).

[119] J. Lebreuilly, M. Wouters and I. Carusotto, "Towards strongly correlated photons in arrays of dissipative nonlinear cavities under a frequency-dependent incoherent pumping", Comptes Rendus Physique, Polariton Physics / Physique Des Polaritons **17**, 836–860 (2016).

[120] A. Xuereb, C. Genes, G. Pupillo, M. Paternostro and A. Dantan, "Reconfigurable long-range phonon dynamics in optomechanical arrays", Physical Review Letters **112**, 133604 (2014).

[121] A. Xuereb, A. Imparato and A. Dantan, "Heat transport in harmonic oscillator systems with thermal baths: application to optomechanical arrays", New Journal of Physics **17**, 055013 (2015).

[122] F. Marquardt, J. G. E. Harris and S. M. Girvin, "Dynamical Multistability Induced by Radiation Pressure in High-Finesse Micromechanical Optical Cavities", Physical Review Letters **96**, 103901 (2006).

[123] M. Ludwig, B. Kubala and F. Marquardt, "The optomechanical instability in the quantum regime", New Journal of Physics **10**, 095013 (2008).

[124] H. Rokhsari, T. J. Kippenberg, T. Carmon and K. J. Vahala, "Radiation-pressure-driven micro-mechanical oscillator", Optics Express **13**, 5293–5301 (2005).

[125] T. Carmon, H. Rokhsari, L. Yang, T. J. Kippenberg and K. J. Vahala, "Temporal Behavior of Radiation-Pressure-Induced Vibrations of an Optical Microcavity Phonon Mode", Physical Review Letters **94**, 223902 (2005).

[126] C. Metzger, M. Ludwig, C. Neuenhahn, A. Ortlieb, I. Favero, K. Karrai and F. Marquardt, "Self-Induced Oscillations in an Optomechanical System Driven by Bolometric Backaction", Physical Review Letters **101**, 133903 (2008).

[127] G. Heinrich, M. Ludwig, J. Qian, B. Kubala and F. Marquardt, "Collective Dynamics in Optomechanical Arrays", Physical Review Letters **107**, 043603 (2011).

[128] M. Ludwig and F. Marquardt, "Quantum Many-Body Dynamics in Optomechanical Arrays", Physical Review Letters **111**, 073603 (2013).

[129] A. Mari, A. Farace, N. Didier, V. Giovannetti and R. Fazio, "Measures of Quantum Synchronization in Continuous Variable Systems", Physical Review Letters **111**, 103605 (2013).

[130] T. Weiss, A. Kronwald and F. Marquardt, "Noise-induced transitions in optomechanical synchronization", New Journal of Physics **18**, 013043 (2016).

[131] M. Zhang, G. S. Wiederhecker, S. Manipatruni, A. Barnard, P. McEuen and M. Lipson, "Synchronization of Micromechanical Oscillators Using Light", Physical Review Letters **109**, 233906 (2012).

[132] M. Zhang, S. Shah, J. Cardenas and M. Lipson, "Synchronization and Phase Noise Reduction in Micromechanical Oscillator Arrays Coupled through Light", Physical Review Letters **115**, 163902 (2015).

[133] E. Gil-Santos, M. Labousse, C. Baker, A. Goetschy, W. Hease, C. Gomez, A. Lemaître, G. Leo, C. Ciuti and I. Favero, "Light-Mediated Cascaded Locking of Multiple Nano-Optomechanical Oscillators", Physical Review Letters **118**, 063605 (2017).

[134] M. F. Colombano, G. Arregui, N. E. Capuj, A. Pitanti, J. Maire, A. Griol, B. Garrido, A. Martinez, C. M. Sotomayor-Torres and D. Navarro-Urrios, "Synchronization of Optomechanical Nanobeams by Mechanical Interaction", Physical Review Letters **123**, 017402 (2019).

[135] J. Sheng, X. Wei, C. Yang and H. Wu, "Self-Organized Synchronization of Phonon Lasers", Physical Review Letters **124**, 053604 (2020).

[136] P. R. Rice and H. J. Carmichael, "Photon statistics of a cavity-QED laser: A comment on the laser–phase-transition analogy", Physical Review A **50**, 4318–4329 (1994).

[137] L. Ding, C. Baker, P. Senellart, A. Lemaitre, S. Ducci, G. Leo and I. Favero, "Wavelength-sized GaAs optomechanical resonators with gigahertz frequency", Applied Physics Letters **98**, 113108 (2011).

[138] J. Chan, A. H. Safavi-Naeini, J. T. Hill, S. Meenehan and O. Painter, "Optimized optomechanical crystal cavity with acoustic radiation shield", Applied Physics Letters **101**, 081115 (2012).

[139] M. H. Matheny, "Enhanced photon-phonon coupling via dimerization in one-dimensional optomechanical crystals", Applied Physics Letters **112**, 253104 (2018).

[140] S. M. Meenehan, J. D. Cohen, G. S. MacCabe, F. Marsili, M. D. Shaw and O. Painter, "Pulsed Excitation Dynamics of an Optomechanical Crystal Resonator near Its Quantum Ground State of Motion", Physical Review X **5**, 041002 (2015).

[141] P. Lacharmoise, A. Fainstein, B. Jusserand and V. Thierry-Mieg, "Optical cavity enhancement of light–sound interaction in acoustic phonon cavities", Applied Physics Letters **84**, 3274–3276 (2004).

[142] A. Fainstein, N. D. Lanzillotti-Kimura, B. Jusserand and B. Perrin, "Strong Optical-Mechanical Coupling in a Vertical GaAs/AlAs Microcavity for Subterahertz Phonons and Near-Infrared Light", Physical Review Letters **110**, 037403 (2013).

[143] G. Rozas, A. E. Bruchhausen, A. Fainstein, B. Jusserand and A. Lemaître, "Polariton path to fully resonant dispersive coupling in optomechanical resonators", Physical Review B **90**, 201302 (2014).

[144] B. Jusserand, A. N. Poddubny, A. V. Poshakinskiy, A. Fainstein and A. Lemaitre, "Polariton Resonances for Ultrastrong Coupling Cavity Optomechanics in GaAs/AlAs Multiple Quantum Wells", Physical Review Letters **115**, 267402 (2015).

[145] A. S. Kuznetsov, D. H. O. Machado, K. Biermann and P. V. Santos, "Electrically Driven Microcavity Exciton-Polariton Optomechanics at 20 GHz", Physical Review X **11**, 021020 (2021).

[146] S. Latini, U. De Giovannini, E. J. Sie, N. Gedik, H. Hübener and A. Rubio, "Phonoritons as Hybridized Exciton-Photon-Phonon Excitations in a Monolayer h-BN Optical Cavity", Physical Review Letters **126**, 227401 (2021).

[147] S. Richard, F. Aniel and G. Fishman, "Energy-band structure of Ge, Si, and GaAs: A thirty-band $\mathbf{k} \cdot \mathbf{p}$ method", Physical Review B **70**, 235204 (2004).

[148] N. Carlon Zambon, "Chirality and nonlinear dynamics in polariton microresonators", PhD thesis (Université Paris-Saclay, 2020).

[149] G. Bastard, *Wave mechanics applied to semiconductor heterostructures*, Monographies de Physique (EDP Science, 1992).

[150] L. C. Andreani, "Optical Transitions, Excitons, and Polaritons in Bulk and Low-Dimensional Semiconductor Structures", in *Confined Electrons and Photons*, Vol. 340, edited by E. Burstein and C. Weisbuch (Springer US, Boston, MA, 1995), pp. 57–112.

[151] V. Savona, L. C. Andreani, P. Schwendimann and A. Quattropani, "Quantum well excitons in semiconductor microcavities: Unified treatment of weak and strong coupling regimes", Solid State Communications **93**, 733–739 (1995).

[152] V. Savona, C. Piermarocchi, A. Quattropani, P. Schwendimann and F. Tassone, "Optical properties of microcavity polaritons", Phase Transitions **68**, 169–279 (1999).

[153] K. J. Moore, G. Duggan, K. Woodbridge and C. Roberts, "Observations and calculations of the exciton binding energy in (In,Ga)As/GaAs strained-quantum-well heterostructures", Physical Review B **41**, 1090–1094 (1990).

[154] R. S. Knox, *Theory of excitons* (Academic Press, New York, 1963).

[155] E. Hanamura and H. Haug, "Condensation effects of excitons", Physics Reports **33**, 209–284 (1977).

[156] C. Ciuti, V. Savona, C. Piermarocchi, A. Quattropani and P. Schwendimann, "Role of the exchange of carriers in elastic exciton-exciton scattering in quantum wells", Physical Review B **58**, 7926–7933 (1998).

[157] G. Rochat, C. Ciuti, V. Savona, C. Piermarocchi, A. Quattropani and P. Schwendimann, "Excitonic Bloch equations for a two-dimensional system of interacting excitons", Physical Review B **61**, 13856–13862 (2000).

[158] C. Ciuti, P. Schwendimann and A. Quattropani, "Theory of polariton parametric interactions in semiconductor microcavities", Semiconductor Science and Technology **18**, S279–S293 (2003).

[159] A. Verger, C. Ciuti and I. Carusotto, "Polariton quantum blockade in a photonic dot", Physical Review B **73**, 193306 (2006).

[160] R. Girlanda, A. Quattropani and P. Schwendimann, "Two-photon transitions to exciton states in semiconductors. Application to CuCl", Physical Review B **24**, 2009–2017 (1981).

[161] J. Bardeen and W. Shockley, "Deformation Potentials and Mobilities in Non-Polar Crystals", Physical Review **80**, 72–80 (1950).

[162] A. I. Ansel'm and I. A. Firsov, "The Mean Free Path of a Non-Localized Exciton in an Atomic Crystal", Journal of Experimental and Theoretical Physics **1**, 139–144 (1955).

[163] A. I. Ansel'm and I. A. Firsov, "The Free Path Length of a Nonlocalized Exciton in a Polar Crystal", Journal of Experimental and Theoretical Physics **3**, 564–567 (1956).

[164] C. Herring and E. Vogt, "Transport and deformation-potential theory for many-valley semiconductors with anisotropic scattering", Physical Review **101**, 944–961 (1956).

[165] G. L. Bir and G. E. Pikus, *Symmetry and strain-induced effects in semiconductors* (Wiley, New York, 1974).

[166] C. Piermarocchi, F. Tassone, V. Savona, A. Quattropani and P. Schwendimann, "Nonequilibrium dynamics of free quantum-well excitons in time-resolved photoluminescence", Physical Review B **53**, 15834–15841 (1996).

[167] C. M. Wolfe, G. E. Stillman and W. T. Lindley, "Electron Mobility in High-Purity GaAs", Journal of Applied Physics **41**, 3088–3091 (1970).

[168] S. Lee, J. Sanchez-Dehesa and J. D. Dow, "Theoretical investigation of the pressure dependences of energy gaps in semiconductors", Physical Review B **32**, 1152–1155 (1985).

[169] K. Rojan, Y. Léger, G. Morigi, M. Richard and A. Minguzzi, "Enhanced Second-Order Nonlinearity for THz Generation by Resonant Interaction of Exciton-Polariton Rabi Oscillations with Optical Phonons", Physical Review Letters **119**, 127401 (2017).

[170] A. Schliesser, G. Anetsberger, R. Rivière, O. Arcizet and T. J. Kippenberg, "High-sensitivity monitoring of micromechanical vibration using optical whispering gallery mode resonators", New Journal of Physics **10**, 095015 (2008).

[171] A. Schliesser and T. J. Kippenberg, "Chapter 5 - Cavity Optomechanics with Whispering-Gallery Mode Optical Micro-Resonators", in *Advances In Atomic, Molecular, and Optical Physics*, Vol. 58, edited by P. Berman, E. Arimondo and C. Lin, Advances In Atomic, Molecular, and Optical Physics (Academic Press, Jan. 2010), pp. 207–323.

[172] F. R. Lamberti, Q. Yao, L. Lanco, D. T. Nguyen, M. Esmann, A. Fainstein, P. Sesin, S. Anguiano, V. Villafañe, A. Bruchhausen, P. Senellart, I. Favero and N. D. Lanzillotti-Kimura, "Optomechanical properties of GaAs/AlAs micropillar resonators operating in the 18 GHz range", Optics Express **25**, 24437–24447 (2017).

[173] J. R. Klauder and E. C. G. Sudarshan, *Fundamentals of quantum optics* (Dover Publications, Mineola, NY, 2006).

[174] W.-M. Zhang, D. H. Feng and R. Gilmore, "Coherent states: Theory and some applications", Reviews of Modern Physics **62**, 867–927 (1990).

[175] R. J. Glauber, "Coherent and Incoherent States of the Radiation Field", Physical Review **131**, 2766–2788 (1963).

[176] M. Lax, "Formal Theory of Quantum Fluctuations from a Driven State", Physical Review **129**, 2342–2348 (1963).

[177] M. Lax, "Quantum Noise. X. Density-Matrix Treatment of Field and Population-Difference Fluctuations", Physical Review **157**, 213–231 (1967).

[178] C. Gardiner and P. Zoller, *Quantum Noise: A Handbook of Markovian and Non-Markovian Quantum Stochastic Methods with Applications to Quantum Optics*, third edition, Springer Series in Synergetics (Springer-Verlag, Berlin, Heidelberg, 2004).

[179] A. Metelmann and A. A. Clerk, "Nonreciprocal Photon Transmission and Amplification via Reservoir Engineering", Physical Review X **5**, 021025 (2015).

[180] A. Metelmann and A. A. Clerk, "Nonreciprocal quantum interactions and devices via autonomous feedforward", Physical Review A **95**, 013837 (2017).

[181] K. Fang, J. Luo, A. Metelmann, M. H. Matheny, F. Marquardt, A. A. Clerk and O. Painter, "Generalized non-reciprocity in an optomechanical circuit via synthetic magnetism and reservoir engineering", Nature Physics **13**, 465–471 (2017).

[182] Y. Huang and W. F. McColl, "Analytical inversion of general tridiagonal matrices", Journal of Physics A: Mathematical and General **30**, 7919–7933 (1997).

[183] H. M. Wiseman and G. J. Milburn, *Quantum Measurement and Control* (Cambridge University Press, Cambridge, 2009).

[184] D. J. Griffiths, *Introduction to electrodynamics*, fourth edition (Cambridge University Press, Cambridge, 2017).

[185] H. Bouchiat and G. Montambaux, "Persistent currents in mesoscopic rings : ensemble averages and half-flux-quantum periodicity", Journal de Physique (Paris) **50**, 2695–2707 (1989).

[186] M. Tinkham, *Introduction to superconductivity* (McGraw-Hill, New York, 1996).

[187] Á. Rivas and M. A. Martin-Delgado, "Topological heat transport and symmetry-protected boson currents", Scientific Reports **7**, 6350 (2017).

[188] M. Keck, D. Rossini and R. Fazio, "Persistent currents by reservoir engineering", Physical Review A **98**, 053812 (2018).

[189] F. Verstraete, M. M. Wolf and J. Ignacio Cirac, "Quantum computation and quantum-state engineering driven by dissipation", Nature Physics **5**, 633–636 (2009).

[190] J. Jin, A. Biella, O. Viyuela, L. Mazza, J. Keeling, R. Fazio and D. Rossini, "Cluster Mean-Field Approach to the Steady-State Phase Diagram of Dissipative Spin Systems", Physical Review X **6**, 031011 (2016).

[191] S. Barzanjeh, M. Aquilina and A. Xuereb, "Manipulating the Flow of Thermal Noise in Quantum Devices", Physical Review Letters **120**, 060601 (2018).

[192] H. Xu, L. Jiang, A. A. Clerk and J. G. E. Harris, "Nonreciprocal control and cooling of phonon modes in an optomechanical system", Nature (London) **568**, 65–69 (2019).

[193] M. Schmidt, S. Kessler, V. Peano, O. Painter and F. Marquardt, "Optomechanical creation of magnetic fields for photons on a lattice", Optica **2**, 635–641 (2015).

[194] A. McDonald, T. Pereg-Barnea and A. A. Clerk, "Phase-dependent chiral transport and effective non-hermitian dynamics in a bosonic Kitaev-Majorana chain", Physical Review X **8**, 041031 (2018).

[195] J. P. Mathew, J. del Pino and E. Verhagen, "Synthetic gauge fields for phonon transport in a nano-optomechanical system", Nature Nanotechnology **15**, 198–202 (2020).

[196] M. Bagheri, M. Poot, L. Fan, F. Marquardt and H. X. Tang, "Photonic Cavity Synchronization of Nanomechanical Oscillators", Physical Review Letters **111**, 213902 (2013).

[197] I. Favero and K. Karrai, "Optomechanics of deformable optical cavities", Nature Photonics **3**, 201–205 (2009).

[198] L. Ding, P. Senellart, A. Lemaitre, S. Ducci, G. Leo and I. Favero, "GaAs micronanodisks probed by a looped fiber taper for optomechanics applications", in Nanophotonics III, Vol. 7712 (2010), p. 771211.

[199] C. Baker, C. Belacel, A. Andronico, P. Senellart, A. Lemaitre, E. Galopin, S. Ducci, G. Leo and I. Favero, "Critical optical coupling between a GaAs disk and a nanowaveguide suspended on the chip", Applied Physics Letters **99**, 151117 (2011).

[200] E. Gil-Santos, C. Baker, A. Lemaître, S. Ducci, C. Gomez, G. Leo and I. Favero, "Scalable high-precision tuning of photonic resonators by resonant cavity-enhanced photoelectrochemical etching", Nature Communications **8**, 14267– (2017).

[201] K. W. Murch, K. L. Moore, S. Gupta and D. M. Stamper-Kurn, "Observation of quantum-measurement backaction with an ultracold atomic gas", Nature Physics **4**, 561–564 (2008).

[202] F. Brennecke, S. Ritter, T. Donner and T. Esslinger, "Cavity Optomechanics with a Bose-Einstein Condensate", Science **322**, 235–238 (2008).

[203] A. Seif, W. DeGottardi, K. Esfarjani and M. Hafezi, "Thermal management and non-reciprocal control of phonon flow via optomechanics", Nature Communications **9**, 1207 (2018).

[204] J. Dalibard, F. Gerbier, G. Juzeliūnas and P. Öhberg, "Colloquium: Artificial gauge potentials for neutral atoms", Reviews of Modern Physics **83**, 1523–1543 (2011).

[205] N. Goldman, G. Juzeliūnas, P. Öhberg and I. B. Spielman, "Light-induced gauge fields for ultracold atoms", Reports on Progress in Physics **77**, 126401 (2014).

[206] M. Aidelsburger, M. Atala, S. Nascimbène, S. Trotzky, Y.-A. Chen and I. Bloch, "Experimental Realization of Strong Effective Magnetic Fields in an Optical Lattice", Physical Review Letters **107**, 255301 (2011).

[207] M. Aidelsburger, M. Atala, M. Lohse, J. T. Barreiro, B. Paredes and I. Bloch, "Realization of the Hofstadter Hamiltonian with Ultracold Atoms in Optical Lattices", Physical Review Letters **111**, 185301 (2013).

[208] M. Cominotti, D. Rossini, M. Rizzi, F. Hekking and A. Minguzzi, "Optimal Persistent Currents for Interacting Bosons on a Ring with a Gauge Field", Physical Review Letters **113**, 025301 (2014).

[209] G. Arwas, D. Cohen, F. Hekking and A. Minguzzi, "Resonant persistent currents for ultracold bosons on a lattice ring", Physical Review A **96**, 063616 (2017).

[210] L. Kohn, P. Silvi, M. Gerster, M. Keck, R. Fazio, G. E. Santoro and S. Montangero, "Superfluid-to-Mott transition in a Bose-Hubbard ring: Persistent currents and defect formation", Physical Review A **101**, 023617 (2020).

[211] H. Weimer, A. Kshetrimayum and R. Orús, "Simulation methods for open quantum many-body systems", Reviews of Modern Physics **93**, 015008 (2021).

[212] W. Bao, D. Jaksch and P. A. Markowich, "Numerical solution of the Gross-Pitaevskii equation for Bose-Einstein condensation", Journal of Computational Physics **187**, 318–342 (2003).

[213] A. Minguzzi, S. Succi, F. Toschi, M. P. Tosi and P. Vignolo, "Numerical methods for atomic quantum gases with applications to Bose-Einstein condensates and to ultracold fermions", Physics Reports **395**, 223–355 (2004).

[214] X. Antoine, W. Bao and C. Besse, "Computational methods for the dynamics of the nonlinear Schrödinger/Gross-Pitaevskii equations", Computer Physics Communications **184**, 2621–2633 (2013).

[215] K. Sheshadri, H. R. Krishnamurthy, R. Pandit and T. V. Ramakrishnan, "Superfluid and Insulating Phases in an Interacting-Boson Model: Mean-Field Theory and the RPA", Europhysics Letters (EPL) **22**, 257–263 (1993).

[216] K. Sheshadri, H. R. Krishnamurthy, R. Pandit and T. V. Ramakrishnan, "Percolation-Enhanced Localization in the Disordered Bosonic Hubbard Model", Physical Review Letters **75**, 4075–4078 (1995).

[217] R. V. Pai, K. Sheshadri and R. Pandit, "Phases and transitions in the spin-1 Bose-Hubbard model: Systematics of a mean-field theory", Physical Review B **77**, 014503 (2008).

[218] A. Le Boité, G. Orso and C. Ciuti, "Steady-State Phases and Tunneling-Induced Instabilities in the Driven Dissipative Bose-Hubbard Model", Physical Review Letters **110**, 233601 (2013).

[219] V. Goblot, B. Rauer, F. Vicentini, A. Le Boité, E. Galopin, A. Lemaître, L. Le Gratiet, A. Harouri, I. Sagnes, S. Ravets, C. Ciuti, A. Amo and J. Bloch, "Nonlinear Polariton Fluids in a Flatband Reveal Discrete Gap Solitons", Physical Review Letters **123**, 113901 (2019).

[220] D. Witthaut, F. Trimborn, H. Hennig, G. Kordas, T. Geisel and S. Wimberger, "Beyond mean-field dynamics in open Bose-Hubbard chains", Physical Review A **83**, 063608 (2011).

[221] W. Casteels, S. Finazzi, A. L. Boité, F. Storme and C. Ciuti, "Truncated correlation hierarchy schemes for driven-dissipative multimode quantum systems", New Journal of Physics **18**, 093007 (2016).

[222] Z. Denis, A. Tiene, L. Salasnich and S. Wimberger, "Asymmetric many-body loss in a bosonic double well", Physical Review A **97**, 013602 (2018).

[223] Z. Denis and S. Wimberger, "Two-Time Correlation Functions in Dissipative and Interacting Bose-Hubbard Chains", Condensed Matter **3**, 2 (2018).

[224] A. Biella, J. Jin, O. Viyuela, C. Ciuti, R. Fazio and D. Rossini, "Linked cluster expansions for open quantum systems on a lattice", Physical Review B **97**, 035103 (2018).

[225] J. Huber, P. Kirton and P. Rabl, "Nonequilibrium magnetic phases in spin lattices with gain and loss", Physical Review A **102**, 012219 (2020).

[226] W. Casteels, R. M. Wilson and M. Wouters, "Gutzwiller Monte Carlo approach for a critical dissipative spin model", Physical Review A **97**, 062107 (2018).

[227] D. Huybrechts and M. Wouters, "Cluster methods for the description of a driven-dissipative spin model", Physical Review A **99**, 043841 (2019).

[228] K. Vogel and H. Risken, "Quasiprobability distributions in dispersive optical bistability", Physical Review A **39**, 4675–4683 (1989).

[229] A. Sinatra, C. Lobo and Y. Castin, "The truncated Wigner method for Bose-condensed gases: limits of validity and applications", Journal of Physics B: Atomic, Molecular and Optical Physics **35**, 3599–3631 (2002).

[230] F. Vicentini, F. Minganti, R. Rota, G. Orso and C. Ciuti, "Critical slowing down in driven-dissipative Bose-Hubbard lattices", Physical Review A **97**, 013853 (2018).

[231] J. Huber, P. Kirton and P. Rabl, "Phase-Space Methods for Simulating the Dissipative Many-Body Dynamics of Collective Spin Systems", SciPost Phys. **10**, 45 (2021).

[232] W. Verstraelen and M. Wouters, "Gaussian Quantum Trajectories for the Variational Simulation of Open Quantum-Optical Systems", Applied Sciences **8**, 1427 (2018).

[233] W. Verstraelen, R. Rota, V. Savona and M. Wouters, "Gaussian trajectory approach to dissipative phase transitions: The case of quadratically driven photonic lattices", Physical Review Research **2**, 022037 (2020).

[234] N. Shammah, S. Ahmed, N. Lambert, S. De Liberato and F. Nori, "Open quantum systems with local and collective incoherent processes: Efficient numerical simulations using permutational invariance", Physical Review A **98**, 063815 (2018).

[235] J. Dalibard, Y. Castin and K. Mølmer, "Wave-function approach to dissipative processes in quantum optics", Physical Review Letters **68**, 580–583 (1992).

[236] K. Mølmer, Y. Castin and J. Dalibard, "Monte Carlo wave-function method in quantum optics", Journal of the Optical Society of America B **10**, 524–538 (1993).

[237] K. Mølmer and Y. Castin, "Monte Carlo wavefunctions in quantum optics", Quantum and Semiclassical Optics: Journal of the European Optical Society Part B **8**, 49–72 (1996).

[238] R. Dum, P. Zoller and H. Ritsch, "Monte Carlo simulation of the atomic master equation for spontaneous emission", Physical Review A **45**, 4879–4887 (1992).

[239] H. Carmichael, *An Open Systems Approach to Quantum Optics: Lectures Presented at the Université Libre de Bruxelles, October 28 to November 4, 1991*, Lecture Notes in Physics Monographs (Springer-Verlag, Berlin, Heidelberg, 1993).

[240] M. B. Plenio and P. L. Knight, "The quantum-jump approach to dissipative dynamics in quantum optics", Reviews of Modern Physics **70**, 101–144 (1998).

[241] F. Vicentini, F. Minganti, A. Biella, G. Orso and C. Ciuti, "Optimal stochastic unraveling of disordered open quantum systems: Application to driven-dissipative photonic lattices", Physical Review A **99**, 032115 (2019).

[242] A. Nagy and V. Savona, "Driven-dissipative quantum Monte Carlo method for open quantum systems", Physical Review A **97**, 052129 (2018).

[243] C. Tsitouras, "Runge-Kutta pairs of order 5(4) satisfying only the first column simplifying assumption", Computers & Mathematics with Applications **62**, 770–775 (2011).

[244] F. Minganti, A. Biella, N. Bartolo and C. Ciuti, "Spectral theory of Liouvillians for dissipative phase transitions", Physical Review A **98**, 042118 (2018).

[245] J. Rang and L. Angermann, "New Rosenbrock W-Methods of Order 3 for Partial Differential Algebraic Equations of Index 1", BIT Numerical Mathematics **45**, 761–787 (2005).

[246] C. A. Kennedy and M. H. Carpenter, "Additive Runge-Kutta schemes for convection-diffusion-reaction equations", Applied Numerical Mathematics **44**, 139–181 (2003).

[247] J. R. Dormand and P. J. Prince, "A family of embedded Runge-Kutta formulae", Journal of Computational and Applied Mathematics **6**, 19–26 (1980).

[248] S. Krämer, D. Plankensteiner, L. Ostermann and H. Ritsch, "QuantumOptics.jl: A Julia framework for simulating open quantum systems", Computer Physics Communications **227**, 109–116 (2018).

[249] C. Rackauckas and Q. Nie, "DifferentialEquations.jl – A Performant and Feature-Rich Ecosystem for Solving Differential Equations in Julia", Journal of Open Research Software **5**, 15 (2017).

[250] K. Macieszczak, M. Guţă, I. Lesanovsky and J. P. Garrahan, "Towards a Theory of Metastability in Open Quantum Dynamics", Physical Review Letters **116**, 240404 (2016).

[251] G. L. G. Sleijpen and D. R. Fokkema, "BiCGstab(l) for linear equations involving unsymmetric matrices with complex spectrum.", ETNA. Electronic Transactions on Numerical Analysis **1**, 11–32 (1993).

[252] P. Sonneveld and M. B. van Gijzen, "IDR(s): A Family of Simple and Fast Algorithms for Solving Large Nonsymmetric Systems of Linear Equations", SIAM Journal on Scientific Computing **31**, 1035–1062 (2009).

[253] M. B. Van Gijzen and P. Sonneveld, "Algorithm 913: An elegant IDR(s) variant that efficiently exploits biorthogonality properties", ACM Transactions on Mathematical Software **38**, 5:1–5:19 (2011).

[254] N. N. Bogoliubov, "Kinetic Equations", Journal of Physics-USSR **10**, 265 (1946).

[255] M. Born and H. S. Green, "A general kinetic theory of liquids I. The molecular distribution functions", Proceedings of the Royal Society of London A **188**, 10–18 (1946).

[256] J. G. Kirkwood, "The Statistical Mechanical Theory of Transport Processes I. General Theory", The Journal of Chemical Physics **14**, 180–201 (1946).

[257] J. G. Kirkwood, "The Statistical Mechanical Theory of Transport Processes II. Transport in Gases", The Journal of Chemical Physics **15**, 72–76 (1947).

[258] J. Yvon and Y. Rocard, "La théorie statistique des fluides et l'équation d'état", Actualités scientifiques et industrielles **203** (1935).

[259] A. Vardi and J. R. Anglin, "Bose-Einstein Condensates beyond Mean Field Theory: Quantum Backreaction as Decoherence", Physical Review Letters **86**, 568–571 (2001).

[260] J. R. Anglin and A. Vardi, "Dynamics of a two-mode Bose-Einstein condensate beyond mean-field theory", Physical Review A **64**, 013605 (2001).

[261] I. Tikhonenkov, J. R. Anglin and A. Vardi, "Quantum dynamics of Bose-Hubbard Hamiltonians beyond the Hartree-Fock-Bogoliubov approximation: The Bogoliubov back-reaction approximation", Physical Review A **75**, 013613 (2007).

[262] P. C. Parks and V. Hahn, *Stability theory*, Prentice Hall International Series in Systems and Control Engineering (Prentice Hall, New York, 1993).

[263] D. Vitali, S. Gigan, A. Ferreira, H. R. Böhm, P. Tombesi, A. Guerreiro, V. Vedral, A. Zeilinger and M. Aspelmeyer, "Optomechanical Entanglement between a Movable Mirror and a Cavity Field", Physical Review Letters **98**, 030405 (2007).

[264] C. Genes, D. Vitali and P. Tombesi, "Emergence of atom-light-mirror entanglement inside an optical cavity", Physical Review A **77**, 050307 (2008).

[265] C. Genes, A. Mari, D. Vitali and P. Tombesi, "Chapter 2 Quantum Effects in Optomechanical Systems", in *Advances In Atomic, Molecular, and Optical Physics*, Vol. 57, Advances in Atomic Molecular and Optical Physics (Academic Press, Jan. 2009), pp. 33–86.

[266] C. Sommer and C. Genes, "Partial Optomechanical Refrigeration via Multimode Cold-Damping Feedback", Physical Review Letters **123**, 203605 (2019).

[267] I. Pietikäinen, O. Černotík and R. Filip, "Combining Floquet and Lyapunov techniques for time-dependent problems in optomechanics and electromechanics", New Journal of Physics **22**, 063019 (2020).

[268] W. P. Schleich, *Quantum Optics in Phase Space*, first edition (Wiley, Feb. 2001).

[269] E. Wigner, "On the Quantum Correction For Thermodynamic Equilibrium", Physical Review **40**, 749–759 (1932).

[270] K. Husimi, "Some Formal Properties of the Density Matrix", Proceedings of the Physico-Mathematical Society of Japan. 3rd Series **22**, 264–314 (1940).

[271] E. C. G. Sudarshan, "Equivalence of Semiclassical and Quantum Mechanical Descriptions of Statistical Light Beams", Physical Review Letters **10**, 277–279 (1963).

[272] H. J. Groenewold, "On the principles of elementary quantum mechanics", Physica **12**, 405–460 (1946).

[273] J. E. Moyal, "Quantum mechanics as a statistical theory", Mathematical Proceedings of the Cambridge Philosophical Society **45**, 99–124 (1949).

[274] K. E. Cahill and R. J. Glauber, "Ordered Expansions in Boson Amplitude Operators", Physical Review **177**, 1857–1881 (1969).

[275] K. E. Cahill and R. J. Glauber, "Density Operators and Quasiprobability Distributions", Physical Review **177**, 1882–1902 (1969).

[276] G. S. Agarwal and E. Wolf, "Calculus for Functions of Noncommuting Operators and General Phase-Space Methods in Quantum Mechanics. I. Mapping Theorems and Ordering of Functions of Noncommuting Operators", Physical Review D **2**, 2161–2186 (1970).

[277] G. S. Agarwal and E. Wolf, "Calculus for Functions of Noncommuting Operators and General Phase-Space Methods in Quantum Mechanics. II. Quantum Mechanics in Phase Space", Physical Review D **2**, 2187–2205 (1970).

[278] J. Restrepo, "Theory of quantum optomechanics with unconventional nonlinear coupling schemes", PhD thesis (Université Paris 7, Sorbonne Paris Cité, 2014).

[279] H. A. Kramers, "Brownian motion in a field of force and the diffusion model of chemical reactions", Physica **7**, 284–304 (1940).

[280] J. E. Moyal, "Stochastic Processes and Statistical Physics", Journal of the Royal Statistical Society B) **11**, 150–210 (1949).

[281] F. Vicentini, "Stochastic and Neural Network methods for critical phenomena in open quantum lattices", PhD thesis (Université de Paris, 2019).

[282] C. Rackauckas and Q. Nie, "Stability-Optimized High Order Methods and Stiffness Detection for Pathwise Stiff Stochastic Differential Equations", in 2020 IEEE High Performance Extreme Computing Conference (HPEC) (2020), pp. 1–8.

[283] J. R. Johansson, P. D. Nation and F. Nori, "QuTiP: An open-source Python framework for the dynamics of open quantum systems", Computer Physics Communications **183**, 1760–1772 (2012).

[284] J. R. Johansson, P. D. Nation and F. Nori, "QuTiP 2: A Python framework for the dynamics of open quantum systems", Computer Physics Communications **184**, 1234–1240 (2013).

[285] W. Krauth, *Statistical mechanics: algorithms and computations*, first edition, Oxford Master Series in Physics Statistical, Computational, and Theoretical Physics 13 (Oxford University Press, Oxford, 2010).

[286] R. Y. Rubinstein and D. P. Kroese, *Simulation and the Monte Carlo Method* (John Wiley & Sons, Inc., Hoboken, Nov. 2016).

[287] A. Blais, S. M. Girvin and W. D. Oliver, "Quantum information processing and quantum optics with circuit quantum electrodynamics", Nature Physics **16**, 247–256 (2020).

[288] C. D. Bruzewicz, J. Chiaverini, R. McConnell and J. M. Sage, "Trapped-ion quantum computing: Progress and challenges", Applied Physics Reviews **6**, 021314 (2019).

[289] F. Arute, K. Arya, R. Babbush, D. Bacon, J. C. Bardin, R. Barends, R. Biswas, S. Boixo, F. G. S. L. Brandao, D. A. Buell, B. Burkett, Y. Chen, Z. Chen, B. Chiaro, R. Collins, W. Courtney, A. Dunsworth, E. Farhi, B. Foxen, A. Fowler, C. Gidney, M. Giustina, R. Graff, K. Guerin, S. Habegger, M. P. Harrigan, M. J. Hartmann, A. Ho, M. Hoffmann, T. Huang, T. S. Humble, S. V. Isakov, E. Jeffrey, Z. Jiang, D. Kafri, K. Kechedzhi, J. Kelly, P. V. Klimov, S. Knysh, A. Korotkov, F. Kostritsa, D. Landhuis, M. Lindmark, E. Lucero, D. Lyakh, S. Mandrà, J. R. McClean, M. McEwen, A. Megrant, X. Mi, K. Michielsen, M. Mohseni, J. Mutus, O. Naaman, M. Neeley, C. Neill, M. Y. Niu, E. Ostby, A. Petukhov, J. C. Platt, C. Quintana, E. G. Rieffel, P. Roushan, N. C. Rubin, D. Sank, K. J. Satzinger, V. Smelyanskiy, K. J. Sung, M. D. Trevithick, A. Vainsencher, B. Villalonga, T. White, Z. J. Yao, P. Yeh, A. Zalcman, H. Neven and J. M. Martinis, "Quantum supremacy using a programmable superconducting processor", Nature **574**, 505–510 (2019).

[290] H.-S. Zhong, H. Wang, Y.-H. Deng, M.-C. Chen, L.-C. Peng, Y.-H. Luo, J. Qin, D. Wu, X. Ding, Y. Hu, P. Hu, X.-Y. Yang, W.-J. Zhang, H. Li, Y. Li, X. Jiang, L. Gan, G. Yang, L. You, Z. Wang, L. Li, N.-L. Liu, C.-Y. Lu and J.-W. Pan, "Quantum computational advantage using photons", Science **370**, 1460–1463 (2020).

[291] S. J. Devitt, W. J. Munro and K. Nemoto, "Quantum error correction for beginners", Reports on Progress in Physics **76**, 076001 (2013).

[292] B. P. Lanyon, J. D. Whitfield, G. G. Gillett, M. E. Goggin, M. P. Almeida, I. Kassal, J. D. Biamonte, M. Mohseni, B. J. Powell, M. Barbieri, A. Aspuru-Guzik and A. G. White, "Towards quantum chemistry on a quantum computer", Nature Chemistry **2**, 106–111 (2010).

[293] J. Biamonte, P. Wittek, N. Pancotti, P. Rebentrost, N. Wiebe and S. Lloyd, "Quantum machine learning", Nature **549**, 195–202 (2017).

[294]   R. Orús, S. Mugel and E. Lizaso, "Quantum computing for finance: Overview and prospects", Reviews in Physics **4**, 100028 (2019).

[295]   J. M. Martinis, "Qubit metrology for building a fault-tolerant quantum computer", npj Quantum Information **1**, 1–3 (2015).

[296]   R. Harper, S. T. Flammia and J. J. Wallman, "Efficient learning of quantum noise", Nature Physics **16**, 1184–1188 (2020).

[297]   I. H. Deutsch, "Harnessing the Power of the Second Quantum Revolution", PRX Quantum **1**, 020101 (2020).

[298]   A. W. Cross, L. S. Bishop, S. Sheldon, P. D. Nation and J. M. Gambetta, "Validating quantum computers using randomized model circuits", Physical Review A **100**, 032328 (2019).

[299]   D. Aharonov and M. Ben-Or, "Polynomial simulations of decohered quantum computers", in Proceedings of 37th Conference on Foundations of Computer Science (Oct. 1996), pp. 46–55.

[300]   S. Aaronson and D. J. Brod, "BosonSampling with lost photons", Physical Review A **93**, 012335 (2016).

[301]   A. W. Harrow and M. A. Nielsen, "Robustness of quantum gates in the presence of noise", Physical Review A **68**, 012308 (2003).

[302]   D. Koch, B. Martin, S. Patel, L. Wessing and P. M. Alsing, "Demonstrating NISQ era challenges in algorithm design on IBM's 20 qubit quantum computer", AIP Advances **10**, 095101 (2020).

[303]   R. LaRose, "Overview and Comparison of Gate Level Quantum Software Platforms", Quantum **3**, 130 (2019).

[304]   G. Vidal, "Efficient Classical Simulation of Slightly Entangled Quantum Computations", Physical Review Letters **91**, 147902 (2003).

[305]   Y. Zhou, E. M. Stoudenmire and X. Waintal, "What Limits the Simulation of Quantum Computers?", Physical Review X **10**, 041038 (2020).

[306]   K. Noh, L. Jiang and B. Fefferman, "Efficient classical simulation of noisy random quantum circuits in one dimension", Quantum **4**, 318 (2020).

[307]   J. Napp, R. L. La Placa, A. M. Dalzell, F. G. S. L. Brandao and A. W. Harrow, "Efficient classical simulation of random shallow 2D quantum circuits", arXiv: 2001.00021 (2020).

[308]   C. Oh, K. Noh, B. Fefferman and L. Jiang, "Classical simulation of lossy boson sampling using matrix product operators", arXiv: 2101.11234 (2021).

[309]   T. Jones, A. Brown, I. Bush and S. C. Benjamin, "QuEST and High Performance Simulation of Quantum Computers", Scientific Reports **9**, 10736 (2019).

[310]   D. Gottesman, "Fault-tolerant quantum computation with constant overhead", Quantum Information & Computation **14**, 1338–1372 (2014).

[311] Y. S. Weinstein, T. F. Havel, J. Emerson, N. Boulant, M. Saraceno, S. Lloyd and D. G. Cory, "Quantum process tomography of the quantum Fourier transform", The Journal of Chemical Physics **121**, 6117–6133 (2004).

[312] R. Klesse and S. Frank, "Quantum Error Correction in Spatially Correlated Quantum Noise", Physical Review Letters **95**, 230503 (2005).

[313] A. J. Daley, "Quantum trajectories and open many-body quantum systems", Advances in Physics **63**, 77–149 (2014).

[314] C. Le Bris and P. Rouchon, "Low-rank numerical approximations for high-dimensional Lindblad equations", Physical Review A **87**, 022125 (2013).

[315] Y.-T. Chen, C. Farquhar and R. M. Parrish, "Low-rank density-matrix evolution for noisy quantum circuits", npj Quantum Information **7**, 1–12 (2021).

[316] G. McCaul, K. Jacobs and D. I. Bondar, "Fast computation of dissipative quantum systems with ensemble rank truncation", Physical Review Research **3**, 013017 (2021).

[317] J. Guillaud and M. Mirrahimi, "Repetition Cat Qubits for Fault-Tolerant Quantum Computation", Physical Review X **9**, 041053 (2019).

[318] P. W. Shor, "Polynomial-Time Algorithms for Prime Factorization and Discrete Logarithms on a Quantum Computer", SIAM Journal on Computing **26**, 1484–1509 (1997).

[319] R. Cleve, A. Ekert, C. Macchiavello and M. Mosca, "Quantum algorithms revisited", Proceedings of the Royal Society of London A **454**, 339–354 (1998).

[320] M. Ettinger, P. Høyer and E. Knill, "The quantum query complexity of the hidden subgroup problem is polynomial", Information Processing Letters **91**, 43–48 (2004).

[321] C. Beck and F. Schögl, *Thermodynamics of Chaotic Systems: An Introduction*, Cambridge Nonlinear Science Series (Cambridge University Press, Cambridge, 1993).

[322] J. E. Gentle, *Matrix Algebra: Theory, Computations, and Applications in Statistics*, Springer Texts in Statistics (Springer-Verlag, New York, 2007).

[323] R. Horodecki, P. Horodecki, M. Horodecki and K. Horodecki, "Quantum entanglement", Reviews of Modern Physics **81**, 865–942 (2009).

[324] G. Wendin, "Quantum information processing with superconducting circuits: a review", Reports on Progress in Physics **80**, 106001 (2017).

[325] P. Krantz, M. Kjaergaard, F. Yan, T. P. Orlando, S. Gustavsson and W. D. Oliver, "A quantum engineer's guide to superconducting qubits", Applied Physics Reviews **6**, 021318 (2019).

[326] M. Kjaergaard, M. E. Schwartz, J. Braumüller, P. Krantz, J. I.-J. Wang, S. Gustavsson and W. D. Oliver, "Superconducting Qubits: Current State of Play", Annual Review of Condensed Matter Physics **11**, 369–395 (2020).

[327] M. Saffman, "Quantum computing with atomic qubits and Rydberg interactions: progress and challenges", Journal of Physics B: Atomic, Molecular and Optical Physics **49**, 202001 (2016).

[328] C. Monroe, D. M. Meekhof, B. E. King, W. M. Itano and D. J. Wineland, "Demonstration of a Fundamental Quantum Logic Gate", Physical Review Letters **75**, 4714–4717 (1995).

[329] R. Barends, J. Kelly, A. Megrant, A. Veitia, D. Sank, E. Jeffrey, T. C. White, J. Mutus, A. G. Fowler, B. Campbell, Y. Chen, Z. Chen, B. Chiaro, A. Dunsworth, C. Neill, P. O'Malley, P. Roushan, A. Vainsencher, J. Wenner, A. N. Korotkov, A. N. Cleland and J. M. Martinis, "Superconducting quantum circuits at the surface code threshold for fault tolerance", Nature **508**, 500–503 (2014).

[330] S. Sheldon, E. Magesan, J. M. Chow and J. M. Gambetta, "Procedure for systematically tuning up cross-talk in the cross-resonance gate", Physical Review A **93**, 060302 (2016).

[331] S. S. Hong, A. T. Papageorge, P. Sivarajah, G. Crossman, N. Didier, A. M. Polloreno, E. A. Sete, S. W. Turkowski, M. P. da Silva and B. R. Johnson, "Demonstration of a parametrically activated entangling gate protected from flux noise", Physical Review A **101**, 012302 (2020).

[332] J. Benhelm, G. Kirchmair, C. F. Roos and R. Blatt, "Towards fault-tolerant quantum computing with trapped ions", Nature Physics **4**, 463–466 (2008).

[333] K. R. Brown, A. C. Wilson, Y. Colombe, C. Ospelkaus, A. M. Meier, E. Knill, D. Leibfried and D. J. Wineland, "Single-qubit-gate error below 10^{-4} in a trapped ion", Physical Review A **84**, 030303 (2011).

[334] S. Debnath, N. M. Linke, C. Figgatt, K. A. Landsman, K. Wright and C. Monroe, "Demonstration of a small programmable quantum computer with atomic qubits", Nature **536**, 63–66 (2016).

[335] S. K. Moore, "IBM Edges Closer to Quantum Supremacy with 50-Qubit Processor", IEEE Spectrum (2017).

[336] Rigetti Computing, "Rigetti Computing introduces world's first scalable multi-chip quantum processor", Globe Newswire (2021).

[337] J. Hsu, "CES 2018: Intel's 49-Qubit Chip Shoots for Quantum Supremacy", IEEE Spectrum (2018).

[338] J. Hsu, "Google's Quantum Tech Milestone Excites Scientists and Spurs Rivals", IEEE Spectrum (2019).

[339] M. A. Nielsen and I. L. Chuang, *Quantum Computation and Quantum Information: 10th Anniversary Edition* (Cambridge University Press, Cambridge, 2010).

[340] D. M. Greenberger, M. A. Horne and A. Zeilinger, "Going Beyond Bell's Theorem", arXiv: 0712.0921 (2007).

[341] D. Bouwmeester, J.-W. Pan, M. Daniell, H. Weinfurter and A. Zeilinger, "Observation of Three-Photon Greenberger-Horne-Zeilinger Entanglement", Physical Review Letters **82**, 1345–1349 (1999).

[342] J.-W. Pan, D. Bouwmeester, M. Daniell, H. Weinfurter and A. Zeilinger, "Experimental test of quantum nonlocality in three-photon Greenberger–Horne–Zeilinger entanglement", Nature **403**, 515–519 (2000).

[343] G. Carleo and M. Troyer, "Solving the quantum many-body problem with artificial neural networks", Science **355**, 602–606 (2017).

[344] G. Carleo, Y. Nomura and M. Imada, "Constructing exact representations of quantum many-body systems with deep neural networks", Nature Communications **9**, 5322 (2018).

[345] N. Freitas, G. Morigi and V. Dunjko, "Neural network operations and Susuki–Trotter evolution of neural network states", International Journal of Quantum Information **16**, 1840008 (2018).

[346] M. Schmitt and M. Heyl, "Quantum Many-Body Dynamics in Two Dimensions with Artificial Neural Networks", Physical Review Letters **125**, 100503 (2020).

[347] O. Sharir, Y. Levine, N. Wies, G. Carleo and A. Shashua, "Deep Autoregressive Models for the Efficient Variational Simulation of Many-Body Quantum Systems", Physical Review Letters **124**, 020503 (2020).

[348] T. Fösel, P. Tighineanu, T. Weiss and F. Marquardt, "Reinforcement Learning with Neural Networks for Quantum Feedback", Physical Review X **8**, 031084 (2018).

[349] Y. X. Zeng, J. Shen, S. C. Hou, T. Gebremariam and C. Li, "Quantum control based on machine learning in an open quantum system", Physics Letters A **384**, 126886 (2020).

[350] J. Sun, X. Yuan, T. Tsunoda, V. Vedral, S. C. Benjamin and S. Endo, "Mitigating Realistic Noise in Practical Noisy Intermediate-Scale Quantum Devices", Physical Review Applied **15**, 034026 (2021).

[351] F. Nissen, J. M. Fink, J. A. Mlynek, A. Wallraff and J. Keeling, "Collective Suppression of Linewidths in Circuit QED", Physical Review Letters **110**, 203602 (2013).

[352] P. Ambs, "Optical Computing: A 60-Year Adventure", Advances in Optical Technologies **2010**, e372652 (2010).

[353] P. Mengert and T. T. Tanimoto, *Control apparatus*, US Patent 35,258,56, 1966.

[354] C. S. Weaver and J. W. Goodman, "A Technique for Optically Convolving Two Functions", Applied Optics **5**, 1248–1249 (1966).

[355] J. W. Goodman, A. R. Dias and L. M. Woody, "Fully parallel, high-speed incoherent optical method for performing discrete Fourier transforms", Opt. Lett. **2**, 1–3 (1978).

[356] A. Sawchuk and T. Strand, "Digital optical computing", Proceedings of the IEEE **72**, 758–779 (1984).

[357] A. Huang, "Architectural considerations involved in the design of an optical digital computer", Proceedings of the IEEE **72**, 780–786 (1984).

[358] A. Khan, A. Sohail, U. Zahoora and A. S. Qureshi, "A survey of the recent architectures of deep convolutional neural networks", Artif Intell Rev **53**, 5455–5516 (2020).

[359] M. M. Waldrop, "The chips are down for Moore's law", en, Nature News **530**, 144 (2016).

[360] E. Strubell, A. Ganesh and A. McCallum, "Energy and Policy Considerations for Deep Learning in NLP", in Proceedings of the 57th Annual Meeting of the Association for Computational Linguistics (2019), pp. 3645–3650.

[361] J. Dong, S. Gigan, F. Krzakala and G. Wainrib, "Scaling Up Echo-State Networks With Multiple Light Scattering", in 2018 IEEE Statistical Signal Processing Workshop (SSP) (2018), pp. 448–452.

[362] R. Ohana, J. Wacker, J. Dong, S. Marmin, F. Krzakala, M. Filippone and L. Daudet, "Kernel Computations from Large-Scale Random Features Obtained by Optical Processing Units", in ICASSP 2020 - 2020 IEEE International Conference on Acoustics, Speech and Signal Processing (ICASSP) (2020), pp. 9294–9298.

[363] D. Schneider, "Lightmatter's Mars Chip Performs Neural-Network Calculations at the Speed of Light: MIT spinoff harnesses optical computing to make neural-networks run faster and more efficiently", IEEE Spectrum (2020).

[364] D. Schneider, "Deep Learning at the Speed of Light: Lightmatter bets that optical computing can solve AI's efficiency problem", IEEE Spectrum **58**, 28–29 (2021).

[365] G. Wetzstein, A. Ozcan, S. Gigan, S. Fan, D. Englund, M. Soljačić, C. Denz, D. A. B. Miller and D. Psaltis, "Inference in artificial intelligence with deep optics and photonics", Nature **588**, 39–47 (2020).

[366] X. Lin, Y. Rivenson, N. T. Yardimci, M. Veli, Y. Luo, M. Jarrahi and A. Ozcan, "All-optical machine learning using diffractive deep neural networks", Science **361**, 1004–1008 (2018).

[367] M. Miscuglio, Z. Hu, S. Li, J. K. George, R. Capanna, H. Dalir, P. M. Bardet, P. Gupta and V. J. Sorger, "Massively parallel amplitude-only Fourier neural network", Optica **7**, 1812–1819 (2020).

[368] J. Feldmann, N. Youngblood, M. Karpov, H. Gehring, X. Li, M. Stappers, M. Le Gallo, X. Fu, A. Lukashchuk, A. S. Raja, J. Liu, C. D. Wright, A. Sebastian, T. J. Kippenberg, W. H. P. Pernice and H. Bhaskaran, "Parallel convolutional processing using an integrated photonic tensor core", Nature **589**, 52–58 (2021).

[369] M. D. Zeiler and R. Fergus, "Visualizing and Understanding Convolutional Networks", in Computer Vision – ECCV 2014, edited by D. Fleet, T. Pajdla, B. Schiele and T. Tuytelaars, Lecture Notes in Computer Science (2014), pp. 818–833.

[370] Y. Lecun, L. Bottou, Y. Bengio and P. Haffner, "Gradient-based learning applied to document recognition", Proc. IEEE **86**, 2278–2324 (1998).

[371] A. Trask, D. Gilmore and M. Russell, "Modeling Order in Neural Word Embeddings at Scale", in International Conference on Machine Learning (2015), pp. 2266–2275.

[372] V. Sanh, L. Debut, J. Chaumond and T. Wolf, "DistilBERT, a distilled version of BERT: smaller, faster, cheaper and lighter", arXiv: 1910.01108 (2020).

[373] H. Jaeger, "The "echo state" approach to analysing and training recurrent neural networks", Bonn, Germany: German National Research Center for Information Technology GMD Technical Report **148** (2001).

[374]   H. Jaeger and H. Haas, "Harnessing Nonlinearity: Predicting Chaotic Systems and Saving Energy in Wireless Communication", en, Science **304**, 78–80 (2004).

[375]   D. Verstraeten, B. Schrauwen, D. Stroobandt and J. Van Campenhout, "Isolated word recognition with the Liquid State Machine: a case study", Information Processing Letters, Applications of Spiking Neural Networks **95**, 521–528 (2005).

[376]   D. Verstraeten, B. Schrauwen and D. Stroobandt, "Reservoir-based techniques for speech recognition", The 2006 IEEE International Joint Conference on Neural Network Proceedings (2006).

[377]   M. Lukoševičius and H. Jaeger, "Reservoir computing approaches to recurrent neural network training", en, Computer Science Review **3**, 127–149 (2009).

[378]   K. Nakajima, "Physical reservoir computing—an introductory perspective", en, Japanese Journal of Applied Physics **59**, 060501 (2020).

[379]   A. Rodan and P. Tino, "Minimum Complexity Echo State Network", IEEE Transactions on Neural Networks **22**, 131–144 (2011).

[380]   G. V. der Sande, D. Brunner and M. C. Soriano, "Advances in photonic reservoir computing", Nanophotonics **6**, 561–576 (2017).

[381]   K. Vandoorne, P. Mechet, T. Van Vaerenbergh, M. Fiers, G. Morthier, D. Verstraeten, B. Schrauwen, J. Dambre and P. Bienstman, "Experimental demonstration of reservoir computing on a silicon photonics chip", Nature Communications **5**, 3541 (2014).

[382]   F. Denis-Le Coarer, M. Sciamanna, A. Katumba, M. Freiberger, J. Dambre, P. Bienstman and D. Rontani, "All-Optical Reservoir Computing on a Photonic Chip Using Silicon-Based Ring Resonators", IEEE Journal of Selected Topics in Quantum Electronics **24**, 1–8 (2018).

[383]   M. S. Kulkarni and C. Teuscher, "Memristor-based reservoir computing", in 2012 IEEE/ACM International Symposium on Nanoscale Architectures (NANOARCH) (July 2012), pp. 226–232.

[384]   C. Du, F. Cai, M. A. Zidan, W. Ma, S. H. Lee and W. D. Lu, "Reservoir computing using dynamic memristors for temporal information processing", en, Nature Communications **8**, 2204 (2017).

[385]   S. Boyn, J. Grollier, G. Lecerf, B. Xu, N. Locatelli, S. Fusil, S. Girod, C. Carrétéro, K. Garcia, S. Xavier, J. Tomas, L. Bellaiche, M. Bibes, A. Barthélémy, S. Saïghi and V. Garcia, "Learning through ferroelectric domain dynamics in solid-state synapses", Nature Communications **8**, 14736 (2017).

[386]   D. Marković, N. Leroux, M. Riou, F. Abreu Araujo, J. Torrejon, D. Querlioz, A. Fukushima, S. Yuasa, J. Trastoy, P. Bortolotti and J. Grollier, "Reservoir computing with the frequency, phase, and amplitude of spin-torque nano-oscillators", Applied Physics Letters **114**, 012409 (2019).

[387]   K. Vandoorne, W. Dierckx, B. Schrauwen, D. Verstraeten, R. Baets, P. Bienstman and J. V. Campenhout, "Toward optical signal processing using Photonic Reservoir Computing", Optics Express **16**, 11182–11192 (2008).

[388] Y. Paquot, J. Dambre, B. Schrauwen, M. Haelterman and S. Massar, "Reservoir computing: a photonic neural network for information processing", in Nonlinear Optics and Applications IV, Vol. 7728 (2010), 77280B.

[389] L. Appeltant, M. C. Soriano, G. Van der Sande, J. Danckaert, S. Massar, J. Dambre, B. Schrauwen, C. R. Mirasso and I. Fischer, "Information processing using a single dynamical node as complex system", Nature Communications **2**, 468 (2011).

[390] K. Vandoorne, J. Dambre, D. Verstraeten, B. Schrauwen and P. Bienstman, "Parallel Reservoir Computing Using Optical Amplifiers", IEEE Transactions on Neural Networks **22**, 1469–1481 (2011).

[391] F. Duport, B. Schneider, A. Smerieri, M. Haelterman and S. Massar, "All-optical reservoir computing", Optics Express **20**, 22783–22795 (2012).

[392] Y. Paquot, F. Duport, A. Smerieri, J. Dambre, B. Schrauwen, M. Haelterman and S. Massar, "Optoelectronic Reservoir Computing", Scientific Reports **2**, 287 (2012).

[393] L. Larger, M. C. Soriano, D. Brunner, L. Appeltant, J. M. Gutierrez, L. Pesquera, C. R. Mirasso and I. Fischer, "Photonic information processing beyond Turing: an optoelectronic implementation of reservoir computing", Optics Express **20**, 3241–3249 (2012).

[394] M. C. Soriano, S. Ortín, D. Brunner, L. Larger, C. R. Mirasso, I. Fischer and L. Pesquera, "Optoelectronic reservoir computing: tackling noise-induced performance degradation", Optics Express **21**, 12–20 (2013).

[395] R. M. Nguimdo, G. Verschaffelt, J. Danckaert and G. Van der Sande, "Simultaneous Computation of Two Independent Tasks Using Reservoir Computing Based on a Single Photonic Nonlinear Node With Optical Feedback", IEEE Transactions on Neural Networks and Learning Systems **26**, 3301–3307 (2015).

[396] S. Ortín, M. C. Soriano, L. Pesquera, D. Brunner, D. San-Martín, I. Fischer, C. R. Mirasso and J. M. Gutiérrez, "A Unified Framework for Reservoir Computing and Extreme Learning Machines based on a Single Time-delayed Neuron", Scientific Reports **5**, 14945 (2015).

[397] L. Larger, A. Baylón-Fuentes, R. Martinenghi, V. S. Udaltsov, Y. K. Chembo and M. Jacquot, "High-Speed Photonic Reservoir Computing Using a Time-Delay-Based Architecture: Million Words per Second Classification", Physical Review X **7**, 011015 (2017).

[398] Y. K. Chembo, "Machine learning based on reservoir computing with time-delayed optoelectronic and photonic systems", Chaos **30**, 013111 (2020).

[399] A. Opala, S. Ghosh, T. C. Liew and M. Matuszewski, "Neuromorphic Computing in Ginzburg-Landau Polariton-Lattice Systems", Physical Review Applied **11**, 064029 (2019).

[400] D. Ballarini, A. Gianfrate, R. Panico, A. Opala, S. Ghosh, L. Dominici, V. Ardizzone, M. De Giorgi, G. Lerario, G. Gigli, T. C. H. Liew, M. Matuszewski and D. Sanvitto, "Polaritonic Neuromorphic Computing Outperforms Linear Classifiers", Nano Letters **20**, 3506–3512 (2020).

[401] R. Mirek, A. Opala, P. Comaron, M. Furman, M. Król, K. Tyszka, B. Seredyński, D. Ballarini, D. Sanvitto, T. C. H. Liew, W. Pacuski, J. Suffczyński, J. Szczytko, M. Matuszewski and B. Piętka, "Neuromorphic Binarized Polariton Networks", Nano Letters **21**, 3715–3720 (2021).

[402] J. Dong, M. Rafayelyan, F. Krzakala and S. Gigan, "Optical Reservoir Computing Using Multiple Light Scattering for Chaotic Systems Prediction", IEEE Journal of Selected Topics in Quantum Electronics **26**, 1–12 (2020).

[403] M. Rafayelyan, J. Dong, Y. Tan, F. Krzakala and S. Gigan, "Large-Scale Optical Reservoir Computing for Spatiotemporal Chaotic Systems Prediction", Physical Review X **10**, 041037 (2020).

[404] J. von Neumann, "First draft of a report on the EDVAC", IEEE Annals of the History of Computing **15**, 27–75 (1993).

[405] J. Backus, "Software I: Function-level computing: A new programming method, linked to radically different architectures, may greatly simplify software development", IEEE Spectrum **19**, 22–27 (1982).

[406] N. R. Mahapatra and B. Venkatrao, "The processor-memory bottleneck: problems and solutions", XRDS: Crossroads, The ACM Magazine for Students **5**, 2–es (1999).

[407] K.-H. Kim, S. Gaba, D. Wheeler, J. M. Cruz-Albrecht, T. Hussain, N. Srinivasa and W. Lu, "A Functional Hybrid Memristor Crossbar-Array/CMOS System for Data Storage and Neuromorphic Applications", Nano Letters **12**, 389–395 (2012).

[408] J. J. Yang, D. B. Strukov and D. R. Stewart, "Memristive devices for computing", en, Nature Nanotechnology **8**, 13–24 (2013).

[409] M. Prezioso, F. Merrikh-Bayat, B. D. Hoskins, G. C. Adam, K. K. Likharev and D. B. Strukov, "Training and operation of an integrated neuromorphic network based on metal-oxide memristors", en, Nature **521**, 61–64 (2015).

[410] M. Hu, J. P. Strachan, Z. Li, E. M. Grafals, N. Davila, C. Graves, S. Lam, N. Ge, J. J. Yang and R. S. Williams, "Dot-product engine for neuromorphic computing: Programming 1T1M crossbar to accelerate matrix-vector multiplication", in 2016 53nd ACM/EDAC/IEEE Design Automation Conference (DAC) (June 2016), pp. 1–6.

[411] D. S. Jeong, K. M. Kim, S. Kim, B. J. Choi and C. S. Hwang, "Memristors for Energy-Efficient New Computing Paradigms", en, Advanced Electronic Materials **2**, 1600090 (2016).

[412] N. Ge, J. H. Yoon, M. Hu, E. J. Merced-Grafals, N. Davila, J. P. Strachan, Z. Li, H. Holder, Q. Xia, R. S. Williams, X. Zhou and J. J. Yang, "An efficient analog Hamming distance comparator realized with a unipolar memristor array: a showcase of physical computing", en, Scientific Reports **7**, 40135 (2017).

[413] P. Yao, H. Wu, B. Gao, S. B. Eryilmaz, X. Huang, W. Zhang, Q. Zhang, N. Deng, L. Shi, H.-S. P. Wong and H. Qian, "Face classification using electronic synapses", en, Nature Communications **8**, 15199 (2017).

[414] M. A. Zidan, J. P. Strachan and W. D. Lu, "The future of electronics based on memristive systems", en, Nature Electronics **1**, 22–29 (2018).

[415] M. Hu, C. E. Graves, C. Li, Y. Li, N. Ge, E. Montgomery, N. Davila, H. Jiang, R. S. Williams, J. J. Yang, Q. Xia and J. P. Strachan, "Memristor-Based Analog Computation and Neural Network Classification with a Dot Product Engine", en, Advanced Materials **30**, 1705914 (2018).

[416] C. Li, M. Hu, Y. Li, H. Jiang, N. Ge, E. Montgomery, J. Zhang, W. Song, N. Dávila, C. E. Graves, Z. Li, J. P. Strachan, P. Lin, Z. Wang, M. Barnell, Q. Wu, R. S. Williams, J. J. Yang and Q. Xia, "Analogue signal and image processing with large memristor crossbars", en, Nature Electronics **1**, 52–59 (2018).

[417] C. Li, Y. Li, H. Jiang, W. Song, P. Lin, Z. Wang, J. J. Yang, Q. Xia, M. Hu, E. Montgomery, J. Zhang, N. Dávila, C. E. Graves, Z. Li, J. P. Strachan, R. S. Williams, N. Ge, M. Barnell and Q. Wu, "Large Memristor Crossbars for Analog Computing", in 2018 IEEE International Symposium on Circuits and Systems (ISCAS) (May 2018), pp. 1–4.

[418] Y. Kim, W. H. Jeong, S. B. Tran, H. C. Woo, J. Kim, C. S. Hwang, K.-S. Min and B. J. Choi, "Memristor crossbar array for binarized neural networks", AIP Advances **9**, 045131 (2019).

[419] A. Sengupta, Y. Shim and K. Roy, "Proposal for an All-Spin Artificial Neural Network: Emulating Neural and Synaptic Functionalities Through Domain Wall Motion in Ferromagnets", IEEE Transactions on Biomedical Circuits and Systems **10**, 1152–1160 (2016).

[420] J. Grollier, D. Querlioz and M. D. Stiles, "Spintronic Nanodevices for Bioinspired Computing", Proceedings of the IEEE **104**, 2024–2039 (2016).

[421] J. Torrejon, M. Riou, F. A. Araujo, S. Tsunegi, G. Khalsa, D. Querlioz, P. Bortolotti, V. Cros, K. Yakushiji, A. Fukushima, H. Kubota, S. Yuasa, M. D. Stiles and J. Grollier, "Neuromorphic computing with nanoscale spintronic oscillators", Nature **547**, 428–431 (2017).

[422] M. Romera, P. Talatchian, S. Tsunegi, F. Abreu Araujo, V. Cros, P. Bortolotti, J. Trastoy, K. Yakushiji, A. Fukushima, H. Kubota, S. Yuasa, M. Ernoult, D. Vodenicarevic, T. Hirtzlin, N. Locatelli, D. Querlioz and J. Grollier, "Vowel recognition with four coupled spin-torque nano-oscillators", Nature **563**, 230–234 (2018).

[423] J. Grollier, D. Querlioz, K. Y. Camsari, K. Everschor-Sitte, S. Fukami and M. D. Stiles, "Neuromorphic spintronics", en, Nature Electronics **3**, 360–370 (2020).

[424] S. H. Jo, T. Chang, I. Ebong, B. B. Bhadviya, P. Mazumder and W. Lu, "Nanoscale Memristor Device as Synapse in Neuromorphic Systems", Nano Letters **10**, 1297–1301 (2010).

[425] S. Yu, Y. Wu, R. Jeyasingh, D. Kuzum and H.-S. P. Wong, "An Electronic Synapse Device Based on Metal Oxide Resistive Switching Memory for Neuromorphic Computation", IEEE Transactions on Electron Devices **58**, 2729–2737 (2011).

[426] Y. Yang, B. Chen and W. D. Lu, "Memristive Physically Evolving Networks Enabling the Emulation of Heterosynaptic Plasticity", Advanced Materials **27**, 7720–7727 (2015).

[427] S. Kim, C. Du, P. Sheridan, W. Ma, S. Choi and W. D. Lu, "Experimental Demonstration of a Second-Order Memristor and Its Ability to Biorealistically Implement Synaptic Plasticity", Nano Letters **15**, 2203–2211 (2015).

[428] M. Chu, B. Kim, S. Park, H. Hwang, M. Jeon, B. H. Lee and B.-G. Lee, "Neuromorphic Hardware System for Visual Pattern Recognition With Memristor Array and CMOS Neuron", IEEE Transactions on Industrial Electronics **62**, 2410–2419 (2015).

[429] C.-C. Hsieh, A. Roy, Y.-F. Chang, D. Shahrjerdi and S. K. Banerjee, "A sub-1-volt analog metal oxide memristive-based synaptic device with large conductance change for energy-efficient spike-based computing systems", Applied Physics Letters **109**, 223501 (2016).

[430] Z. Wang, S. Joshi, S. E. Savel'ev, H. Jiang, R. Midya, P. Lin, M. Hu, N. Ge, J. P. Strachan, Z. Li, Q. Wu, M. Barnell, G.-L. Li, H. L. Xin, R. S. Williams, Q. Xia and J. J. Yang, "Memristors with diffusive dynamics as synaptic emulators for neuromorphic computing", en, Nature Materials **16**, 101–108 (2017).

[431] J. H. Yoon, Z. Wang, K. M. Kim, H. Wu, V. Ravichandran, Q. Xia, C. S. Hwang and J. J. Yang, "An artificial nociceptor based on a diffusive memristor", en, Nature Communications **9**, 417 (2018).

[432] Z. Wang, S. Joshi, S. Savel'ev, W. Song, R. Midya, Y. Li, M. Rao, P. Yan, S. Asapu, Y. Zhuo, H. Jiang, P. Lin, C. Li, J. H. Yoon, N. K. Upadhyay, J. Zhang, M. Hu, J. P. Strachan, M. Barnell, Q. Wu, H. Wu, R. S. Williams, Q. Xia and J. J. Yang, "Fully memristive neural networks for pattern classification with unsupervised learning", en, Nature Electronics **1**, 137–145 (2018).

[433] C. Li, D. Belkin, Y. Li, P. Yan, M. Hu, N. Ge, H. Jiang, E. Montgomery, P. Lin, Z. Wang, W. Song, J. P. Strachan, M. Barnell, Q. Wu, R. S. Williams, J. J. Yang and Q. Xia, "Efficient and self-adaptive in-situ learning in multilayer memristor neural networks", en, Nature Communications **9**, 2385 (2018).

[434] Y. Kim, Y. J. Kwon, D. E. Kwon, K. J. Yoon, J. H. Yoon, S. Yoo, H. J. Kim, T. H. Park, J.-W. Han, K. M. Kim and C. S. Hwang, "Nociceptive Memristor", en, Advanced Materials **30**, 1704320 (2018).

[435] D. S. Jeong and C. S. Hwang, "Nonvolatile Memory Materials for Neuromorphic Intelligent Machines", en, Advanced Materials **30**, 1704729 (2018).

[436] A. Afifi, A. Ayatollahi and F. Raissi, "Implementation of biologically plausible spiking neural network models on the memristor crossbar-based CMOS/nano circuits", in 2009 European Conference on Circuit Theory and Design (2009), pp. 563–566.

[437] D. Querlioz, O. Bichler and C. Gamrat, "Simulation of a memristor-based spiking neural network immune to device variations", in The 2011 International Joint Conference on Neural Networks (2011), pp. 1775–1781.

[438] D. Querlioz, O. Bichler, P. Dollfus and C. Gamrat, "Immunity to Device Variations in a Spiking Neural Network With Memristive Nanodevices", IEEE Transactions on Nanotechnology **12**, 288–295 (2013).

[439] G. Srinivasan, A. Sengupta and K. Roy, "Magnetic Tunnel Junction Based Long-Term Short-Term Stochastic Synapse for a Spiking Neural Network with On-Chip STDP Learning", Scientific Reports **6**, 29545 (2016).

[440] K. Roy, A. Jaiswal and P. Panda, "Towards spike-based machine intelligence with neuromorphic computing", Nature **575**, 607–617 (2019).

[441] A. Sengupta, Y. Ye, R. Wang, C. Liu and K. Roy, "Going Deeper in Spiking Neural Networks: VGG and Residual Architectures", Frontiers in Neuroscience **13** (2019).

[442] M. Ernoult, J. Grollier, D. Querlioz, Y. Bengio and B. Scellier, "Updates of Equilibrium Prop Match Gradients of Backprop Through Time in an RNN with Static Input", arXiv: 1905.13633 (2019).

[443] M. Ernoult, J. Grollier, D. Querlioz, Y. Bengio and B. Scellier, "Equilibrium Propagation with Continual Weight Updates", arXiv: 2005.04168 (2020).

[444] A. Laborieux, M. Ernoult, B. Scellier, Y. Bengio, J. Grollier and D. Querlioz, "Scaling Equilibrium Propagation to Deep ConvNets by Drastically Reducing Its Gradient Estimator Bias", Frontiers in Neuroscience **15** (2021).

[445] J. Laydevant, M. Ernoult, D. Querlioz and J. Grollier, "Training Dynamical Binary Neural Networks with Equilibrium Propagation", arXiv: 2103.08953 (2021).

[446] E. Martin, M. Ernoult, J. Laydevant, S. Li, D. Querlioz, T. Petrisor and J. Grollier, "EqSpike: Spike-driven equilibrium propagation for neuromorphic implementations", iScience **24**, 102222 (2021).

[447] T. Krisnanda, S. Ghosh, T. Paterek and T. C. H. Liew, "Creating and concentrating quantum resource states in noisy environments using a quantum neural network", Neural Networks **136**, 141–151 (2021).

[448] B. E. Boser, I. M. Guyon and V. N. Vapnik, "A training algorithm for optimal margin classifiers", in Proceedings of the fifth annual workshop on Computational learning theory, COLT '92 (1992), pp. 144–152.

[449] B. Schölkopf and A. J. Smola, *Learning with kernels: Support vector machines, regularization, optimization, and beyond* (MIT Press, Cambridge, Massachusetts, USA, 2001).

[450] T. Hastie, R. Tibshirani and J. Friedman, *The Elements of Statistical Learning*, Springer Series in Statistics (Springer New York, New York, 2009).

[451] I. Goodfellow, Y. Bengio and A. Courville, *Deep learning* (MIT Press, 2016).

[452] M. J. D. Powell, "Radial basis functions for multivariable interpolation : A review", Algorithms for Approximation (1987).

[453] D. S. Broomhead and D. Lowe, "Multivariable Functional Interpolation and Adaptive Networks", Complex Systems **2**, 321–355 (1988).

[454] T. van Gestel, J. A. Suykens, B. Baesens, S. Viaene, J. Vanthienen, G. Dedene, B. de Moor and J. Vandewalle, "Benchmarking Least Squares Support Vector Machine Classifiers", Machine Learning **54**, 5–32 (2004).

[455] M. Schuld and N. Killoran, "Quantum Machine Learning in Feature Hilbert Spaces", Physical Review Letters **122**, 040504 (2019).

[456] K. Bartkiewicz, C. Gneiting, A. Černoch, K. Jiráková, K. Lemr and F. Nori, "Experimental kernel-based quantum machine learning in finite feature space", Scientific Reports **10**, 12356 (2020).

[457] V. Havlíček, A. D. Córcoles, K. Temme, A. W. Harrow, A. Kandala, J. M. Chow and J. M. Gambetta, "Supervised learning with quantum-enhanced feature spaces", Nature **567**, 209–212 (2019).

[458] T. Kusumoto, K. Mitarai, K. Fujii, M. Kitagawa and M. Negoro, "Experimental quantum kernel trick with nuclear spins in a solid", npj Quantum Information **7**, 1–7 (2021).

[459] Y. Liu, S. Arunachalam and K. Temme, "A rigorous and robust quantum speed-up in supervised machine learning", arXiv: 2010.02174 (2020).

[460] M. Schuld, "Supervised quantum machine learning models are kernel methods", arXiv: 2101.11020 (2021).

[461] C. Williams and M. Seeger, "Using the Nyström Method to Speed Up Kernel Machines", in Advances in Neural Information Processing Systems 13 (2001), pp. 682–688.

[462] B. Schölkopf, A. Smola and K.-R. Müller, "Kernel principal component analysis", in Advances in Kernel Methods - Support Vector Learning (1999), pp. 327–352.

[463] S. Mika, B. Schölkopf, A. Smola, K. R. Müller, M. Scholz and G. Rätsch, "Kernel PCA and de-noising in feature spaces", in Advances in Neural Information Processing Systems 11 - Proceedings of the 1998 Conference, NIPS 1998 (1999), pp. 536–542.

[464] S. Rosset, J. Zhu and T. Hastie, "Margin maximizing loss functions", in Proceedings of the 16th International Conference on Neural Information Processing Systems, NIPS'03 (Dec. 2003), pp. 1237–1244.

[465] R. Zhang and W. Wang, "Facilitating the applications of support vector machine by using a new kernel", Expert Systems with Applications **38**, 14225–14230 (2011).

[466] M. Udell, K. Mohan, D. Zeng, J. Hong, S. Diamond and S. Boyd, "Convex optimization in Julia", in Proceedings of the 1st First Workshop for High Performance Technical Computing in Dynamic Languages, HPTCDL '14 (Nov. 2014), pp. 18–28.

[467] J. C. Platt, "Probabilistic Outputs for Support Vector Machines and Comparisons to Regularized Likelihood Methods", in Advances in Large Margin Classifiers (1999), pp. 61–74.

[468] A. Kronwald, F. Marquardt and A. A. Clerk, "Arbitrarily large steady-state bosonic squeezing via dissipation", Physical Review A **88**, 063833 (2013).

[469] A. Kronwald, F. Marquardt and A. A. Clerk, "Dissipative optomechanical squeez-
       ing of light", New Journal of Physics **16**, 063058 (2014).

[470] A. E. Niederle, G. Morigi and H. Rieger, "Ultracold bosons with cavity-mediated
       long-range interactions: A local mean-field analysis of the phase diagram", Physical
       Review A **94**, 033607 (2016).

[471] J. T. Young, A. V. Gorshkov, M. Foss-Feig and M. F. Maghrebi, "Nonequilibrium
       Fixed Points of Coupled Ising Models", Physical Review X **10**, 011039 (2020).

[472] S. Julià-Farré, T. Salamon, A. Riera, M. N. Bera and M. Lewenstein, "Bounds on
       the capacity and power of quantum batteries", Physical Review Research **2**, 023113
       (2020).

[473] D. Rossini, G. M. Andolina, D. Rosa, M. Carrega and M. Polini, "Quantum Ad-
       vantage in the Charging Process of Sachdev-Ye-Kitaev Batteries", Physical Review
       Letters **125**, 236402 (2020).